

DISSERTATION

CHARACTERIZING POROUS PROTEIN CRYSTAL MATERIALS FOR APPLICATIONS
IN NANOMEDICINE AND NANOBIO TECHNOLOGY

Submitted by

Luke Fredrick Hartje

Department of Biochemistry and Molecular Biology

In partial fulfillment of the requirements

For the Degree of Doctor of Philosophy

Colorado State University

Fort Collins, Colorado

Summer 2018

Doctoral Committee:

Advisor: Christopher D. Snow

P. Shing Ho
Olve B. Peersen
Martin McCullagh

Copyright by Luke Fredrick Hartje 2018

All Rights Reserved

ABSTRACT

CHARACTERIZING POROUS PROTEIN CRYSTAL MATERIALS FOR APPLICATIONS IN NANOMEDICINE AND BIONANOTECHNOLOGY

Protein crystals are biologically derived, self-assembling, porous structures that have been used for decades in structure determination *via* X-ray diffraction. Recently, however, there has been increased interest in utilizing protein crystals for their unique material properties—most notably, their highly ordered porous structure, innate biocompatibility, and chemical plasticity. The diverse topologies of protein crystals and the relative ease with which their chemical properties can be altered *via* genetic mutation or chemical modification offers a wider and more dynamic design palette than existing chemically-synthesized nanoporous frameworks. These traits make protein crystals an attractive new material for applications in nanomedicine and nanobiotechnology.

The intent of this project is to demonstrate the application potential of porous protein crystal materials for use in nanostructured devices. This work highlights our efforts to: experimentally and computationally investigate macromolecular transport and interaction energies within a large-pore protein crystal environment using time-lapse confocal microscopy, bulk equilibrium adsorption, and hindered diffusion simulation; assess the cytocompatibility of various cross-linking chemistries for the production of biostable protein crystal materials for use in biologically sensitive environments; and create multifunctional textiles by covalently attaching various cross-linked protein crystals to cellulose fibers in woven cotton fabrics. By pursuing this research, we hope to better understand porous protein crystal materials and leverage that knowledge to design advanced nanostructured devices for applications in medicine and biotechnology.

ACKNOWLEDGEMENTS

There have been so many people who have helped me get to this point, offering words of encouragement, thoughtful discussion, and challenging criticisms. From faculty advisors and collaborators who have patiently answered countless questions and offered world-class advice to fellow graduate students, friends, and family who have happily given their time to provide hands-on expertise, a fresh perspective, or to simply share a pint in celebration of small victories.

Chief among those to thank is my advisor, Christopher Snow, a dedicated, patient, and approachable mentor who has been instrumental in my graduate career. His passion for biomolecular engineering is contagious and his ability to inspire creativity and drive in others has motivated me to become a better scientist and teacher. I thank my committee members P. Shing Ho, Olve Peersen, and Martin McCullagh for their service and commitment to my graduate studies and development as a scientist. Additionally, I thank P. Shing Ho and Olve Peersen for allowing me the opportunity to serve with them as a teaching assistant for their Physical Biochemistry class; working with these two professors afforded me the chance to learn first-hand what it means to be a great teacher, as such, I am truly grateful. I must also thank my collaborators, first and foremost, Brian Munsky for spending countless hours teaching me the basics of finite element modeling and Vivian Li for not only providing unique insights into the world of textile science but also offering lab space and equipment to do my laundry.

I would not be here if it weren't for the tremendous support I received from my family and friends. My parents, Kevin and Deena, who instilled in me their faith and Christian values, an ethic of hard work, and a heart to serve others; for this they have my utmost respect and thanks. My siblings and oldest friends, Kaleb and Maggie, for their constant encouragement, much needed

hugs, and comedic relief. I would also like to thank my dear friend, Nick Gregoire, for his unwavering optimism and cheer and for being a rock in difficult and uncertain times. Above all, I thank my loving and brilliant wife, Rhea Kay. Her patience and scientific insights have truly been a blessing. There is no one I would rather share this adventure with.

TABLE OF CONTENTS

ABSTRACT.....	ii
ACKNOWLEDGMENTS	iii
CHAPTER1: PROTEIN CRYSTAL BASED MATERIALS FOR NANOSCALE	
APPLICATIONS IN MEDICINE AND BIOTECHNOLOGY	1
1.1 Summary.....	1
1.2 Introduction.....	1
1.3 Protein Crystals.....	4
1.3.1 Crystal Growth.....	4
1.3.2 Stability and Bioconjugation.....	6
1.3.3 Porosity and Guest Transport.....	15
1.3.4 Engineering Protein Crystals	19
1.4 Applications in Nanomedicine.....	25
1.4.1 Pharmaceutical Formulations.....	25
1.4.2 Vaccine Delivery	26
1.4.3 Drug Delivery	27
1.5 Applications in Biotechnology	30
1.5.1 Catalysis.....	30
1.5.2 Biotemplating	31
1.5.3 Biosensing	31
1.5.4 Chromatography	35
1.6 Conclusions.....	36

CHAPTER 2: ADSORPTION-COUPLED DIFFUSION OF GOLD NANOCCLUSERS

WITHIN A LARGE-PORE PROTEIN CRYSTAL SCAFFOLD	38
2.1 Summary	38
2.2 Introduction.....	39
2.3 Theory	42
2.3.1 Determining Diffusion Coefficient	42
2.3.2 Adsorption Model	43
2.3.3 One Dimensional Hindered Diffusion Model.....	44
2.4 Experimental Section	46
2.4.1 Materials	46
2.4.2 Protein Expression	46
2.4.3 Crystallization and Cross-Linking.....	47
2.4.4 Nanocluster Preparation.....	47
2.4.5 Equilibrium Adsorption Experiments	48
2.4.6 Confocal Imaging Experiments	48
2.4.7 Hindered Diffusion Finite Element Model	49
2.5 Results and Discussion	49
2.5.1 Adsorption Isotherm	49
2.5.2 Processing Confocal Images	50
2.5.3 Fit Experimental Data to Hindered Diffusion.....	53
2.6 Conclusions.....	55
2.7 Recognition.....	58
2.8 Term Definitions.....	58

CHAPTER 3: CHARACTERIZING THE CYTOCOMPATIBILITY OF VARIOUS CROSS-LINKING CHEMISTRIES FOR THE PRODUCTION OF BIOSTABLE LARGE-PORE PROTEIN CRYSTAL MATERIALS	60
3.1 Summary	60
3.2 Introduction.....	61
3.3 Results and Discussion	62
3.4 Conclusions.....	71
3.5 Recognition.....	73
CHAPTER 4: TEXTILE FUNCTIONALIZATION BY POROUS PROTEIN CRYSTAL CONJUGATION AND GUEST MOLECULE LOADING.....	74
4.1 Summary	74
4.2 Introduction.....	75
4.3 Results and Discussion	76
4.4 Conclusions.....	84
4.5 Recognition.....	85
CHAPTER 5: SUMMARY AND FUTURE PROSPECTIVE.....	86
5.1 Summary.....	86
5.1.1 Improving Techniques for the Study of Absorption-Coupled Diffusion within the Confined Pores of Protein Crystal Materials	87
5.1.2 Understanding the Effects of Various Cross-Linking Chemistries on Protein Crystal Stability and Biocompatibility	88
5.1.3 Assessing Bioconjugation Techniques for the Immobilization of Protein Crystal Reservoirs for the Production of Multifunctional Materials.....	89

5.2 Future Prospective	90
5.2.1 DNA Guest Molecule Loading for Information Storage	90
5.2.2 Crystal Functionalization by Covalent Guest Capture.....	91
REFERENCES	93
APPENDIX I: SUPPORTING INFORMATION FOR CHAPTER 2.....	117
APPENDIX II: SUPPORTING INFORMATION FOR CHAPTER 3	140
APPENDIX III: SUPPORTING INFORMATION FOR CHAPTER 4.....	164

CHAPTER 1

PROTEIN CRYSTAL BASED MATERIALS FOR NANOSCALE APPLICATIONS IN MEDICINE AND BIOTECHNOLOGY¹

© 1.1 SUMMARY

The porosity, order, biocompatibility, and chirality of protein crystals has motivated interest from diverse research domains including materials science, biotechnology, and medicine. Porous protein crystals have the unusual potential to organize guest molecules within highly ordered scaffolds enabling applications ranging from biotemplating and catalysis to biosensing and drug delivery. Significant research has therefore been directed toward characterizing protein crystal materials in hopes of optimizing crystallization, scaffold stability, and application efficacy. In this overview article, we describe recent progress in the field of protein crystal materials with special attention given to applications in nanomedicine and nanobiotechnology.

© 1.2 INTRODUCTION

Proteins are important biological macromolecules responsible for many catalytic, signaling, and structural functions within cells and tissues. The diverse functions of proteins and their innate biocompatibility are attractive qualities for applications in nanomedicine and nanobiotechnology. As such, a wide variety of peptide- and protein-based nanomaterials have been reported, ranging from peptide nanofibrils, nanotubes, and nanospheres to smart biomaterials derived from collagen, elastin, and resilin.^{1,2} Compared to alternative materials, protein crystals offer unparalleled

¹ The work in this chapter is formatted as an overview article for *WIREs Nanomedicine and Nanobiotechnology*. C.D.S. and I conceived and wrote the manuscript.

Hartje, L. F., Snow, C. D. Protein Crystal Based Materials for Nanoscale Applications in Medicine and Bionanotechnology. *Wiley Interdiscip. Rev. Nanomed. Nanobiotechnol.* Formatted for submission.

volumetric density and precisely repetitive 3D geometric presentation of constituent proteins (Figure 1.1). From a materials perspective, it can also be quite useful to focus on the negative space defined by excluding the protein matrix portion of the crystal. The remaining solvent channel arrays typically consist of interconnected porous networks of varying geometric configuration with pores ranging in size from 0.3 nm to 10 nm^{3,4} and in rare cases have been shown to be even larger (Figure 1.1B & 1.1C).^{5,6} The solvent content of protein crystals is most commonly found to vary between 27-65%,³ commensurate to zeolites and metal organic frameworks, both of which have widely reported utility for medical, catalytic, and sorption applications.⁷⁻⁹ One goal for this chapter is to assess the application prospects for engineered protein crystals in these domains.

Historically, protein crystals have been used both for protein purification and structure determination *via* X-ray diffraction (XRD). While the former application has been widely replaced by chromatography techniques, protein crystal growth continues to be the dominant method for determining 3D protein structure. As a result, the Protein Data Bank (PDB)¹⁰ currently contains over 120,000 X-ray structures encompassing myriad packing arrangements and solvent channel geometries/topologies. With few exceptions, each such crystal represents an unexplored material since the structural biologists who grew the crystals were, in most cases, only interested in the detailed structure of the constituent molecules. This chapter will focus on the exceptions to this rule, *i.e.* the number of research studies that have noted the material advantages of solid-state crystalline proteins or have otherwise sought to repurpose protein crystals for diverse material applications.

We begin by first providing a minimal general background on protein crystallization methods and the structural properties of the resultant crystals. We will then proceed with an overview of

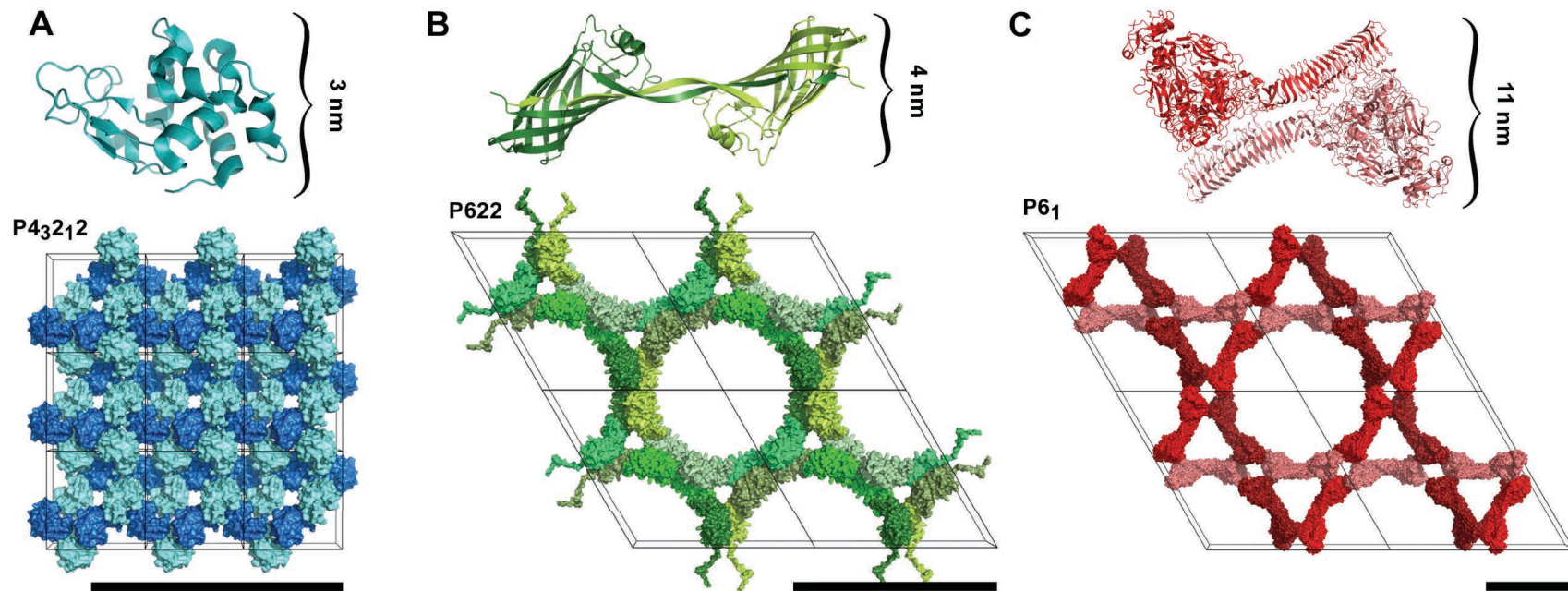


Figure 1.1. Various protein structures (*Top*) and their corresponding crystal scaffolds (*Bottom*) illustrating the diversity of pore sizes and geometries within this class of material; boxes delineate unit cells; *Scale bars:* 20 nm (A) tetragonal Hen Egg White Lysozyme (HEWL) (PDB Code: 2HTX) (B) CJ-1 protein (PDB Code: 5W17). (C) Major Tropism Determinant P1 (Mtd-P1) complexed with Pertactin extracellular domain (Prn-E) (PDB Code: 2IOU). Images created using PyMOL v1.7.4.4, Schrödinger, LLC.

and historical contributions made to the field of protein crystal materials, giving special attention to applications in nanomedicine and nanobiotechnology.

☉ 1.3 PROTEIN CRYSTALS

☉ 1.3.1 Crystal Growth

The science of growing protein crystals has a rich history, dating back to the mid-1800s when Hünefeld first formed hemoglobin crystals by slowly drying the blood of an earthworm between two glass slides.¹¹ The process of slow drying caused hemoglobin proteins to move from an undersaturated stable-state to a supersaturated metastable-state and eventually inducing hemoglobin nucleation. As the crystals nucleate and grow, they fall out of solution thereby lowering the soluble protein concentration and moving the saturation point back into the metastable region where crystal growth occurs without further nucleation (Figure 1.2).¹² Since Hünefeld's experiments, crystallization techniques have improved dramatically with the advent of easy-to-use crystal screening kits and high-throughput micropipetting robotics; however, the scientific principles behind protein crystallization remain the same. In general, protein crystals form when individual growth units self-assemble into an ordered crystalline scaffold through the formation of non-covalent interactions. This process occurs under precise conditions of reduced protein solubility which can be achieved by a variety of methods, the most commonly used being dialysis, vapor diffusion, or batch crystallization.

Dialysis: Precipitating agents can be slowly introduced to a protein solution *via* dialysis. A protein solution is placed in a vessel separated by a dialysis membrane from a larger reservoir containing a higher concentration of precipitating agent. The concentration of precipitating agent surrounding the protein gradually increases thereby reducing the protein solubility and eventually leading to nucleation (Figure 1.2A).

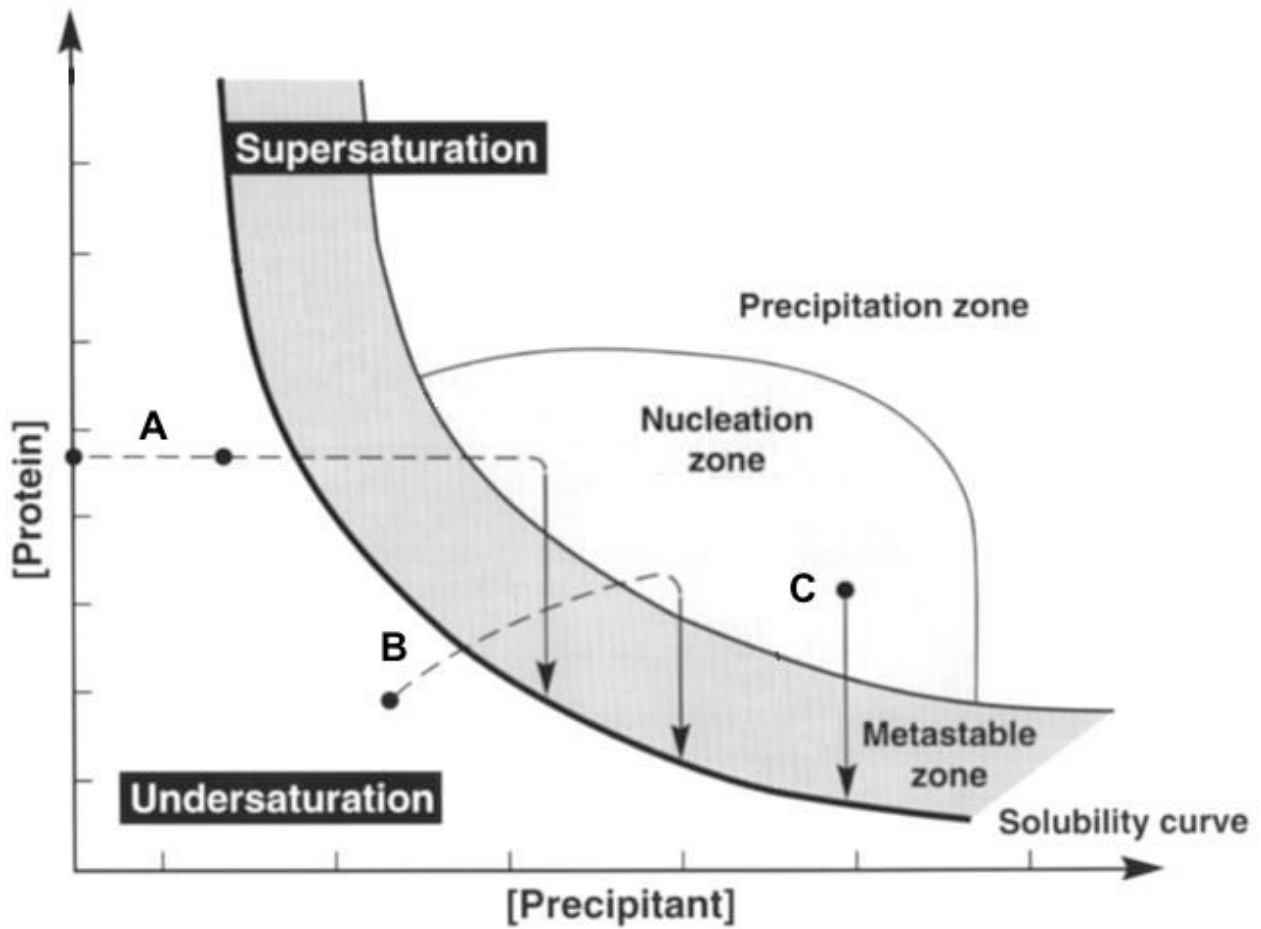


Figure 1.2. A protein crystallization phase diagram based on varied protein and precipitant concentrations. Three commonly used crystallization methods are highlighted showing the path each method takes to produce crystals. Note that all paths need to reach the same destination, namely the nucleation zone, after which they make their way through the metastable zone, where crystal growth takes place, and eventually arrive at the solubility curve. • represents possible starting conditions. (A) Dialysis. (B) Vapor diffusion. (C) Batch crystallization. Reproduced from Chayen. *Acta Crystallogr. D Biol. Crystallogr.* 1998, 54 (1), 8–15 with permission of the International Union of Crystallography.

Vapor Diffusion: The method of vapor diffusion crystallization can be generally divided into two categories: sitting drop and hanging drop. Both categories accomplish protein supersaturation by the same general principle. An aqueous protein solution droplet containing insufficient precipitant for crystallization is setup apart from a larger reservoir containing a high concentration of precipitant in a sealed vessel. Over time, the droplet is equilibrated with the reservoir *via* vapor diffusion of water and other volatile components. Loss of water increases both the protein and precipitate concentrations in the droplet leading to supersaturation (Figure 1.2B). This method is often favored by structural biologists for growing large single crystals with high diffraction quality.

Batch Crystallization: Batch crystallization is achieved by adding precipitating agents directly to a concentrated protein sample so as to shift the solubility curve directly into the nucleation zone. In other words, the protein and precipitant are mixed at their final concentrations to achieve nucleation (Figure 1.2C). Due to the relative ease with which batch crystallization can be scaled up, this method is preferred for industrial scale applications in which many protein crystals are required.

☉ 1.3.2 Stability and Bioconjugation

One factor that has historically limited the material application of protein crystals is their relative mechanical and thermal instability compared to other nanoporous materials such as zeolites. Protein crystals are highly fragile due to several factors. First, the irregular shape of the constituent proteins generally leads to non-specific packing arrangements with high solvent content and relatively small interfacial contacts ($\sim 570 \text{ \AA}^2$ on average) when compared to known specific interactions ($\sim 1,600 \text{ \AA}^2$ on average).^{13,14} Second, these interfaces generally include adventitious and solvent-dependent interfacial contacts that are weak and non-covalent. Third, shifts in solvent conditions can destroy desirable properties of the crystals in several ways:

i) solvents that increase solubility can simply dissolve the crystal; ii) solvents that decrease the solubility can drive disordered aggregation on the crystal surfaces; iii) even solvents that are compatible with an essentially isomorphous crystalline form can shatter the crystal if the solvent is introduced in a way that induces stress associated with crystal structure gradients.

In sum, protein crystals grown in their mother liquor possess inadequate stability for most conceivable applications. To solve this stability problem, many groups have turned to chemical cross-linking to introduce covalent linkages, thereby generating extended bond networks throughout the protein crystal matrix. This method has proven to be effective, enabling protein crystals to withstand solution conditions well outside their crystallization environments.^{15–18}

Cross-linking and Bioconjugation Chemistries: Protein crystals are comprised of individual proteins (or complexes thereof) which are in turn composed of polymerized amino acids. There are 20 common amino acids bearing a variety of unique chemical functionalities. The most useful amino acids for cross-linking and bioconjugation chemistries are those with ionizable side chains: aspartic acid, glutamic acid, lysine, arginine, cysteine, histidine, and tyrosine (Figure 1.3).¹⁹ This collection of amino acids includes primary amines, thiols, and carboxylates—common chemical group targets for post-crystallization bioconjugation. The bioconjugation field is quite broad, but well established, with many research articles, reviews, and books dedicated to diverse bioconjugation chemistries directed at improving biomaterial stability, compatibility, or functionality; the book by Hermanson, in particular, is highly recommended.^{19,20} Here, we will briefly introduce the aldehyde and carbodiimide reagents most commonly used in current protein crystal material applications.

Aldehyde cross-linkers (Figure 1.4A) have been widely used throughout history to stabilize biological specimens by covalently linking proximal primary amine groups. Examples include

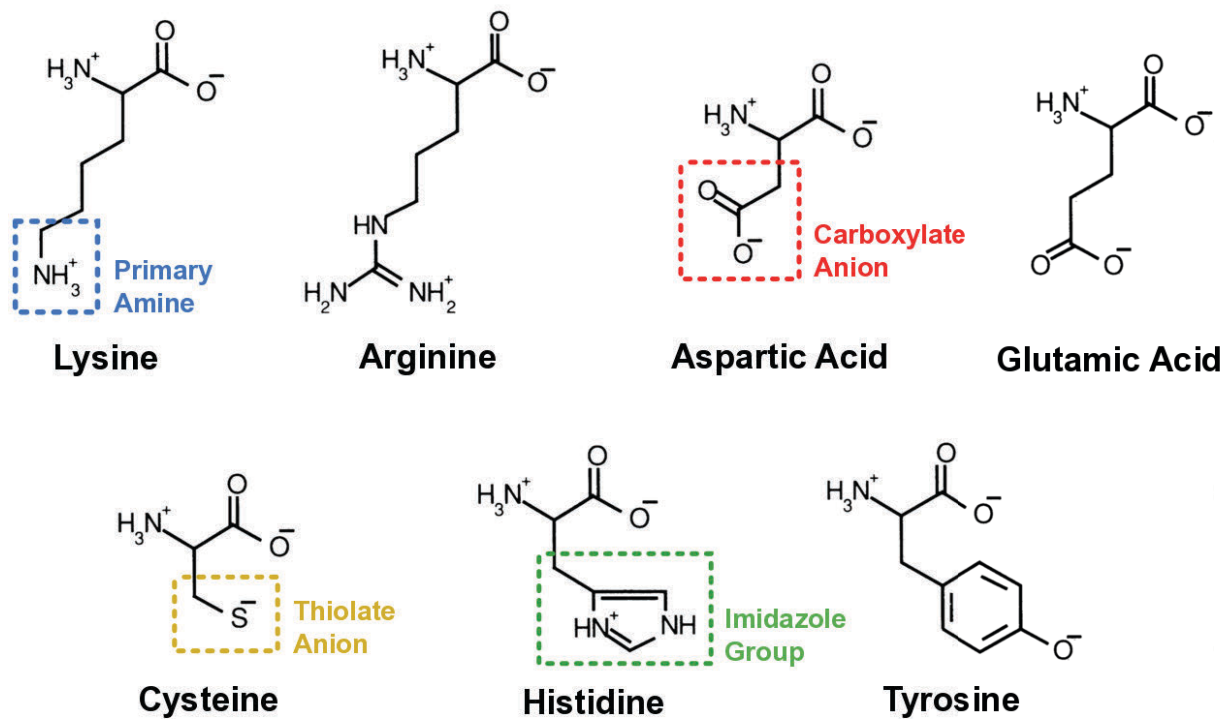


Figure 1.3. Various functional groups associated with ionizable amino acids found in protein crystal materials.

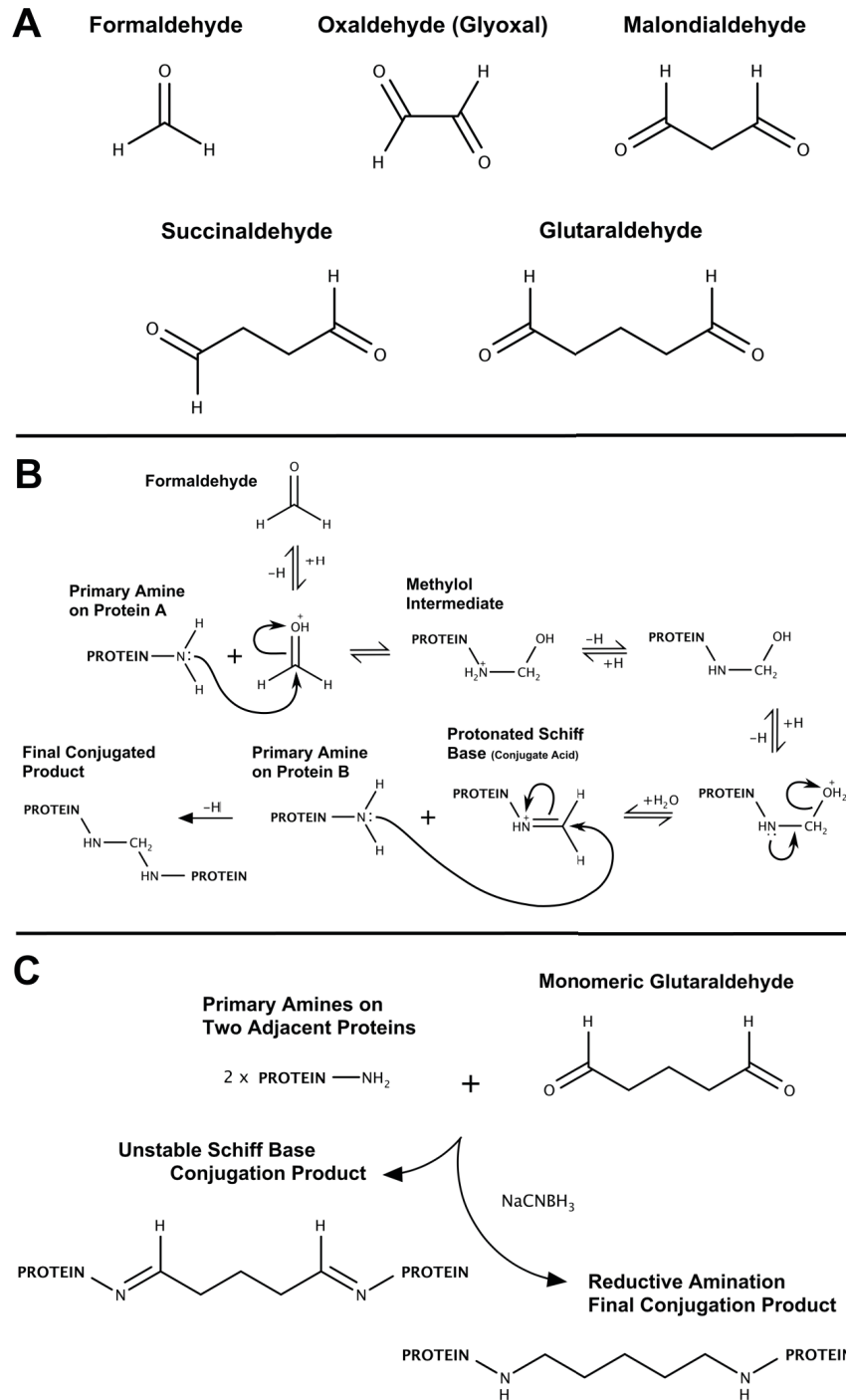


Figure 1.4. (A) Aldehydes of varying length. (B) Formaldehyde cross-linking leads to a stable final conjugation product. (C) Monomeric glutaraldehyde cross-linking results in unstable Schiff base formation unless a reducing agent (*e.g.* NaCNBH_3) is added, which leads to reductive amination.

early embalming chemistries, leather tanning, and more recently chromatin immunoprecipitation and cell fixation techniques.²¹ In 1964, Quioco and Richards were the first to use glutaraldehyde (GA) to improve carboxypeptidase-A crystal stability in diffraction experiments.²² Soon after, they demonstrated the enzymatic activity of glutaraldehyde cross-linked carboxypeptidase-A crystals in aqueous solutions different from that of the mother liquor.²³ Since then, aldehydes (Figure 1.4A), specifically glutaraldehyde, have been the dominant cross-linking agents for the stabilization of protein crystals.^{24–26} Despite the ubiquity of glutaraldehyde cross-linking, the chemical basis is incompletely understood. In principle, formyl groups in aldehydes undergo nucleophilic attack by primary amines producing a Schiff base. In the case of formaldehyde (Figure 1.4B), this Schiff base can undergo a second nucleophilic attack by another primary amine to complete the cross-linking reaction.²¹ However, in the case of monomeric glutaraldehyde, two Schiff bases are formed *via* nucleophilic attack, but are not reduced (Figure 1.4C).¹⁹ Notably, Schiff base formation is reversible, leading to cross-link reversal, particularly in acidic conditions; reducing agents such as sodium cyanoborohydride (NaCNBH_3) may be used to induce reductive amination leading to a stable final product. Intriguingly however, the actual glutaraldehyde cross-linking end products appear to be stable even in acidic conditions without the addition of reducing agents.²⁷ Thus, other chemical mechanisms, aside from Schiff base formation, are likely responsible for the exceptional stability of glutaraldehyde cross-linked materials. Migneault *et al.* outlined 13 known aqueous states of glutaraldehyde, which can range from monomeric to highly polymerized; these different forms of glutaraldehyde can interact with proteins by way of 8 different reaction mechanisms.²⁸ More recently, Yariv Wine and coworkers attempted to resolve the predominant reaction mechanism of glutaraldehyde cross-linking in hen egg white lysozyme (HEWL) crystals (Figure 1.1A) under acidic and alkaline conditions using X-ray diffraction and

mass- spectrometry analysis.²⁹ They were able to resolve two distinct glutaraldehyde cross-links within HEWL crystals at different pH conditions. Both resolved cross-links were consistent with polymeric glutaraldehyde forms serving as the active species.

Carbodiimide agents catalyze the formation of amide bonds between amines and carboxyl groups (Figure 1.5).¹⁹ Unlike aldehydes, carbodiimides are “zero-length” cross-linkers, meaning they do not add additional atoms between the two conjugated molecules. This process has been utilized to produce stable collagen matrices,³⁰ and protein-based nanoparticles,³¹ crystals,³² and macrocomplexes,³³ as well as conjugate enzymes to cellulose-based materials.^{34–36} 1-Ethyl-3-(3-dimethylaminopropyl)-carbodiimide (EDC) is the most commonly used carbodiimide agent for protein conjugation, primarily due to its solubility in aqueous solutions. The other commonly available water-soluble carbodiimide is 1-cyclohexyl-3-(2-morpholinoethyl)carbodiimide (CMC). Most other carbodiimides, such as dicyclohexyl carbodiimide (DCC) and diisopropyl carbodiimide (DIC) are water-insoluble, making their use in protein conjugation more limited—though they are widely used in organic synthesis of peptides.¹⁹

Biocompatibility of Protein Crystal Materials: Numerous alternative bioconjugation chemistries for the stabilization and functionalization of protein crystal materials are briefly outlined by Alexey Margolin and Manuel Navia.¹⁶ However, any chemical additive may have the unintended potential to negatively impact biocompatibility. In broad terms, a biocompatible material has low propensity to cause biological damage to the host upon contact. This damage may take the form of direct cell or tissue death (cytotoxicity), unintended immune responses (immunogenicity), or genetic mutations (genotoxicity).³⁷ Decreased biocompatibility due to cross-linking has been observed in various protein-based materials including collagen fibers³⁸ and protein nanoparticles.³¹

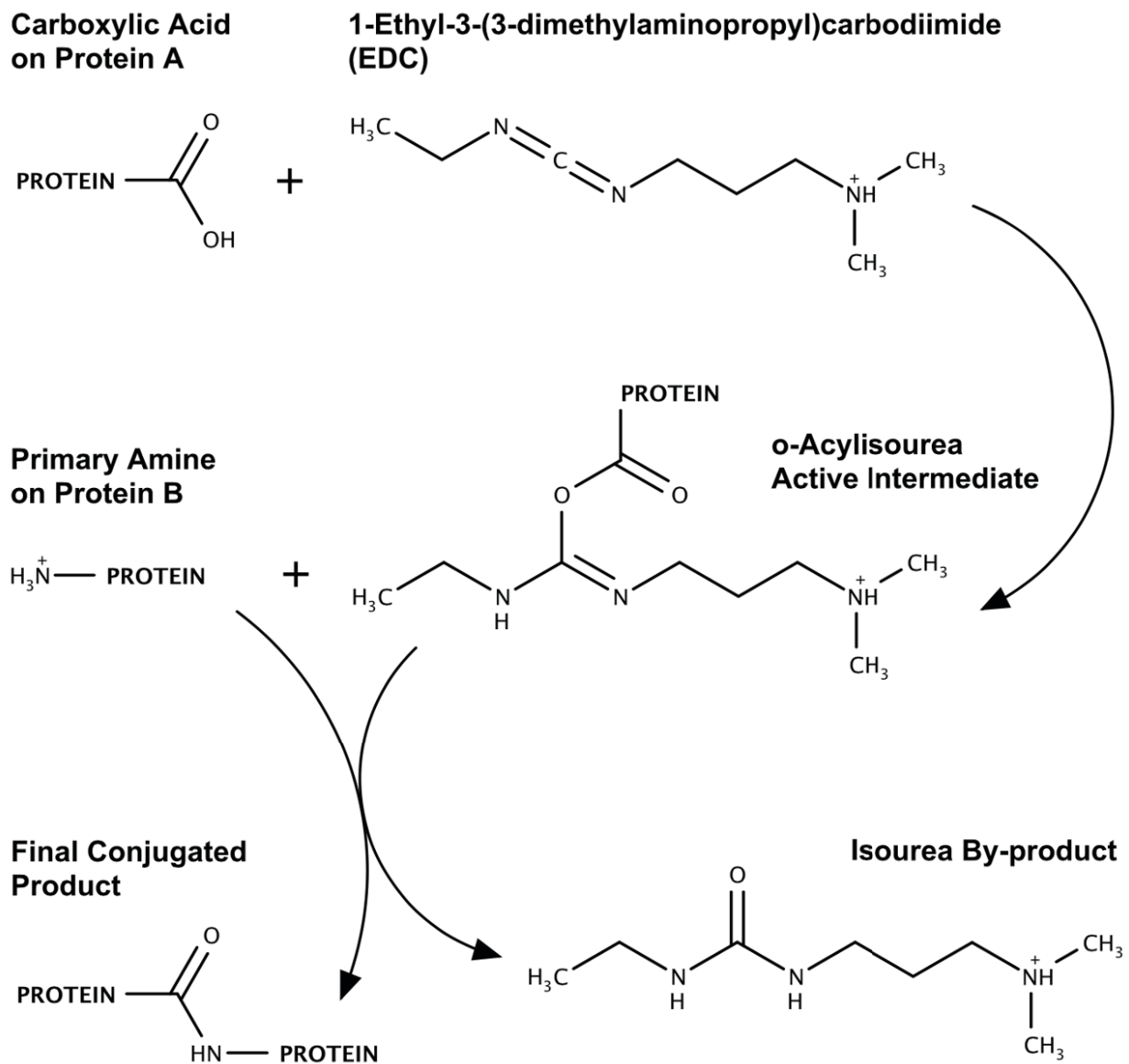


Figure 1.5. EDC reacts with carboxylic acids to create an active-ester intermediate. In the presence of an amine nucleophile, an amide bond is formed with release of an isourea by-product.

Biocompatibility testing of cross-linked protein crystal materials has only recently been pursued as protein crystal applications in nanomedicine become more widely apparent. For instance, Takafumi Ueno's work on cross-linked hen egg white lysozyme crystals impregnated with ruthenium carbonyl complexes (Ru•Cl-HEWL) motivated their preliminary testing of cytocompatibility against human embryonic kidney cells.³⁹ Using a solution of 0.5% trypan blue as an indicator of cell viability, they found no measurable cytotoxicity after 24 hours at the single concentration tested (2.0×10^5 crystals/well). More recently, our group has assessed the stability and biocompatibility of various cross-linking agents on two distinct protein crystal scaffolds: HEWL (Figure 1.1A) and CJ (Figure 1.1B).³² The cell viability of each cross-linked protein crystal material was assessed at varying concentrations (1, 50, 100, 200, and 400 $\mu\text{g/mL}$) against two human cell lines: adult human dermal fibroblasts (HDFa) and human macrophages (MV-4-11). Viability was quantified using a lactate dehydrogenase assay (Figure 1.6A, B, D) and qualitatively confirmed *via* live dead staining (Figure 1.6C). Results indicate that cell cultures subjected to high concentrations of glutaraldehyde cross-linked protein crystal materials (100 – 400 $\mu\text{g/mL}$) suffered noticeable loss in cell viability. However, no substantial loss in cell viability was observed in cell cultures subjected to protein crystal materials cross-linked by oxaldehyde (OA) or EDC. These results suggest that researchers should consider alternatives to glutaraldehyde when stabilizing protein crystal materials, particularly if the application requires biological amity.

Existing studies have only scratched the surface with respect to evaluating the biocompatibility of engineered protein crystals in the context of nanomedicine and nanobiotechnology. Future work that focuses on genotoxicity and immunogenicity is needed to understand the biological responses to these novel materials and to determine when alternative chemistries for the production of stable protein crystal materials will be needed.

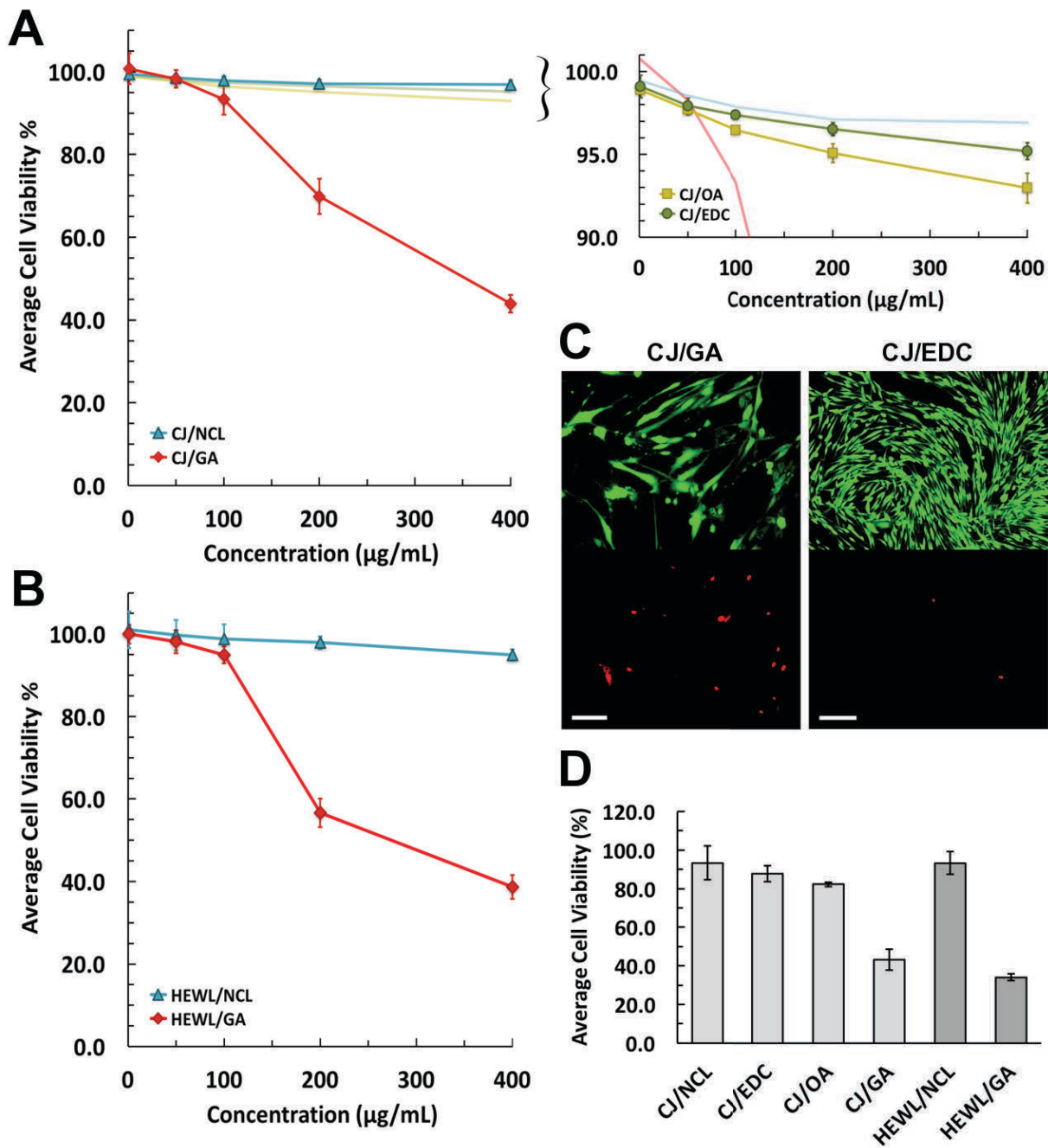


Figure 1.6. (A) HDFa cell viability under varying concentrations of cross-linked CJ crystal materials; *Error Bars*: standard deviation, $n=3$. (B) HDFa cell viability under varying concentrations of fragmented HEWL protein crystal materials; *Error Bars*: standard deviation, $n=3$. (C) HDFa cells incubated with 400 $\mu\text{g/mL}$ protein crystal material; *Top*: green fluorescent live cell stain (calcein); *Bottom*: red fluorescent dead cell stain (ethidium homodimer); *Left*: CJ/GA, *Scale Bar*: 100 μm ; *Right*: CJ/EDC, *Scale Bar*: 300 μm . (D) MV-4-11 cell viability when incubated with various protein crystal materials at a concentration of 400 $\mu\text{g/mL}$; *Error Bars*: standard deviation, $n=3$. Adapted from Hartje *et al.* *ACS Biomater. Sci. Eng.*, 2018, 4 (3), 826–831 and reprinted with permission from The American Chemical Society.

© 1.3.3 Porosity and Guest Transport

Myriad applications for engineered protein crystals depend on transport rates and/or molecular interactions between guest molecules and the pore surfaces of scaffold materials. For instance, enzyme crystal biocatalysis applications are sensitive to the ratio of crystalline pore size to the size of the substrates and products, as mass-transfer rates can limit the net activity for cross-linked enzyme crystals of sufficient size.^{40,41,23} Similarly, in the case of chromatography, the separation capability of protein crystals is dependent on three modes of physical segregation: adsorption, diffusion, and size exclusion—all of which are influenced by mass transport. Therefore, understanding transport within protein crystals is an important first step in advancing their material applications. To this end, many groups have sought to quantify the transport of solvent, small molecules, and macromolecules within the pore networks of various protein crystals. In this section, we will review some of the more common experimental and computational techniques utilized to study pore networks and guest transport within protein crystals.

Experimental Approaches: One of the earliest studies of diffusion within protein crystals was reported in 1941 by Sam Granick who showed guinea pig hemoglobin crystals to be permeable to ferricyanide and hydrosulfite by monitoring oxidative colorimetric changes caused by the hemoglobin oxygen.⁴² Granick's work helped to confirm the porous nature of protein crystals well before the first protein crystal structure was solved in 1958 by John C. Kendrew and coworkers using X-ray diffraction (XRD).⁴³ Over two decades later, in 1968, quantitative diffusion studies of bromine-containing solutes within cross-linked β -lactoglobulin crystals was performed by William H. Bishop and Fredric M. Richards using X-ray fluorescence measurements.⁴⁴ By understanding the material properties of protein crystals, Bishop and Richards generated quantitative transport data as a function of time and estimated the effective pore size of the solvated

channels. Their work not only advanced our understanding of hydration shells surrounding biomolecules, it also emphasized the usefulness of protein crystals as model systems to study transport phenomena. Since then, other quantitative methods, such as video absorbance spectroscopy⁴⁵ and fluorescence microscopy⁴⁶ have been implemented to study time resolved transport of guest molecules into protein crystals.

One major limitation of these early transport experiments was the inability to accurately resolve the precise position of guest molecules within the path length of the crystal. More recent confocal microscopy methods overcome these limitations and observe transport in protein crystals as a function of both time and position. Confocal microscopes can illuminate specific focal planes within protein crystals and thereby resolve the relative concentration of fluorophores within spatial slices. In the early 2000's, Aleksandar Cvetkovic and coworkers were the first to use 3D confocal microscopy to study small molecule transport within protein crystals.^{47,48} Their early work monitored the 3D diffusion of fluorescein within tetragonal, orthorhombic, and triclinic HEWL crystals. Later, they applied this technique to quantify the binary diffusion of fluorescein and rhodamine B within HEWL crystals (Figure 1.7A).⁴⁹ Using confocal microscopy data, they fit their observations to anisotropic diffusion models and found that transport diffusivities were strongly related to pore size (Figure 1.7B). By linking mathematical models for guest molecule transport to experimental confocal data, Cvetkovic and associates provided valuable insights and tools to understand complex systems where the functional properties depend on the intra-crystal transport of one or more guest molecules.

Mathematical transport models are limited by the requirement to reduce model complexity. In the case of guest molecule transport inside porous host materials, this is often done by assuming non-interacting spherical guests diffusing within hard cylindrical pores. These geometric

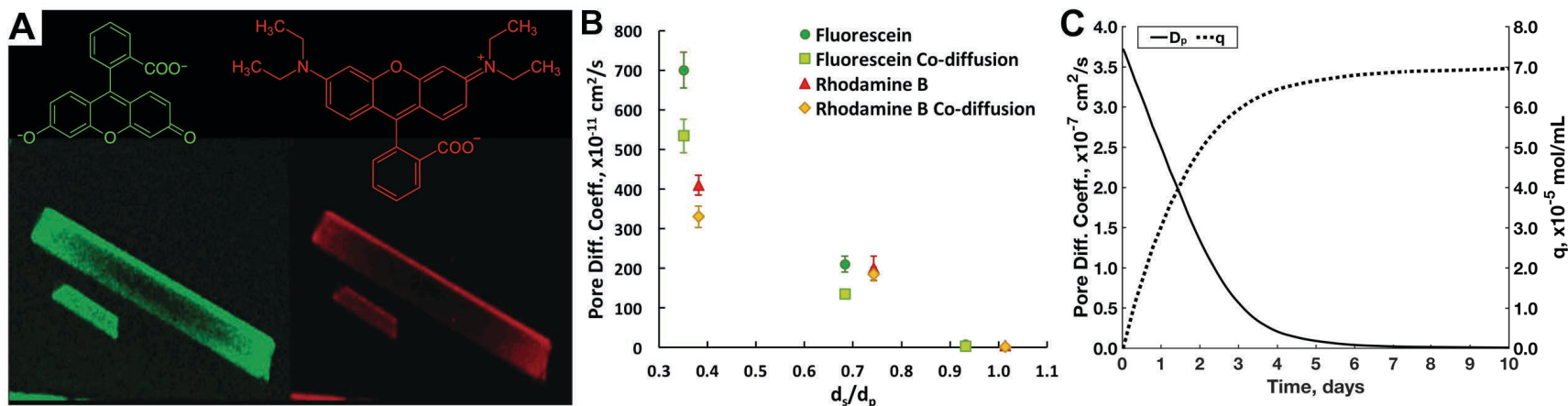


Figure 1.7. (A) Co-diffusion of fluorescein (*left*) and rhodamine B (*right*) in a cross-linked HEWL crystal. (B) The pore diffusion coefficient (D_p) is related to the ratio of guest substrate diameter (d_s) to pore diameter (d_p). A & B adapted from Cvetkovic *et al. J. Phys. Chem. B*, 2005, 109 (21), 10561–10566 and reprinted with permission from The American Chemical Society. (C) The adsorbed guest concentration (q) causes occlusion of the scaffold pore leading to attenuation of D_p . Reprinted from Hartje *et al. J. Phys. Chem. B*, 2017, 121 (32), 7652–7659 with permission from The American Chemical Society.

assumptions represent significant over-simplifications for most actual crystal scaffold host-guest systems. Furthermore, adsorption of guest molecules can occlude small pores. As one would intuitively expect, strong adsorption can greatly attenuate the diffusion coefficient when pore occlusion reduces the effective pore diameter so as to only permit single-file guest diffusion (Figure 1.7C).⁵⁰⁻⁵² Thus, accurate modeling of diffusion must account for adsorption, thereby further complicating any mathematical model of diffusion within the context of porous protein crystals. To alleviate some of the complexities and assumptions associated with mathematical diffusion modelling within protein crystal systems, a number of research groups have instead turned to numerical simulations that embrace the complex details of the guest molecule and pore structures.

Computational Approaches: Molecular simulation of guest transport within protein crystal pores can more accurately account for the complex environment of protein crystal solvent channels. The increased realism comes with a price; atomistic simulations are much more computationally costly than the simplified mathematical models. Atomistic simulations have therefore been severely limited in their ability to generate enough trajectory data for accurate representations of the statistical ensembles describing transport phenomena. However, with modern advancements in computer science, atomistic simulation of small molecule guest transport has become more attainable. Brownian dynamics,^{53,54} Monte Carlo,^{55,56} and molecular dynamics^{54,57-61} approaches have all been used to investigate small molecule transport within protein crystals. Kouros Malek has put together a comprehensive two-part review that details the various simulation techniques used to model diffusion within protein crystal materials.^{62,63} We will therefore not cover these techniques in detail here. Notably, these methods have not yet been extended to study macromolecular guest transport over long timescales.

Given the expense of molecular simulation, it can be useful to also perform a static analysis of the crystal structure. In particular, understanding the solvent channel environment of protein crystals is critically important for diverse protein crystal applications including catalysis, chromatography, biotemplating, and drug delivery. Multiple software packages have been created to aid in the identification of pores, channels, and cavities and better model their physiochemical environments. In 1994, Oleg Kisljuk and coworkers developed CHANNEL, a software package designed to identify channels within protein crystals by building up a spatial graph of intersecting spheres of defined radii to elucidate interconnected cavities within the unit cell.⁶⁴ More recently, Douglas Juers and Jon Ruffin have developed MAP_CHANNELS, a computational tool designed to aid in the visualization of solvent channels in macromolecular crystals and to quantitatively characterize those channels with metrics relevant for the study of guest molecule transport.⁶⁵

© 1.3.4 Engineering Protein Crystals

The chemical versatility of proteins, combined with the intrinsic porosity of protein crystal scaffolds suggests that protein crystals can be engineered to become useful biologically derived nanomaterials. In this section, we will discuss the many efforts to engineer protein crystal scaffolds to optimize stability, biocompatibility, transport dynamics, and surface functionality. Modification of the scaffold constituent proteins by site directed mutagenesis can be a particularly powerful engineering tool to direct desired chemical functional groups to specific locations within the scaffold. For example, crystal interfaces can conceivably be engineered to incorporate cysteine or histidine residues to promote disulfide bond formation or metal coordination, respectively, at protein contacts within the crystal. Below, we will review engineering studies that utilized these functional groups to generate protein crystal scaffolds with intriguing characteristics for applications in nanomedicine and nanobiotechnology.

Engineering Scaffold Interfaces: Novel protein crystal scaffolds can be generated by synthetic symmetrization of the crystal component proteins. Symmetrization of component proteins can be achieved by adding disulfide linkages or metal binding sites to direct oligomerization prior to crystallization. For example, in 2006, Rey Bonatao and coworkers in Todd Yeates' lab generated three single-cysteine mutant variants of T4 lysozyme (T4L) prepared as symmetric dimers through a disulfide linkage.⁶⁶ These three mutant dimers were shown to form six novel protein crystal scaffolds. In similar fashion, the Yeates group went on to create symmetric structures through metal coordination with engineered histidine or cysteine residues on both T4L and maltose binding protein (MBP).⁶⁷ Oligomeric states were generated upon addition of metal ions: copper (Cu^{2+}), nickel (Ni^{2+}), or zinc (Zn^{2+}). These symmetric oligomers were shown to form sixteen unique crystal lattices. This method, metal-mediated synthetic symmetrization, has the potential to expand the known crystal structure repertoire and could help crystallize proteins that have proven difficult to grow using conventional methods.

Engineered disulfide bonds and metal coordination can also be used to increase crystal stability without relying on the addition of chemical cross-linking agents, thereby potentially increasing overall crystal biocompatibility. An early successful introduction of disulfide cross-links at protein-protein interfaces was reported in 2000 by Yang *et al.*⁶⁸ In this case, the crystallographic interfaces within T4L was used to model cysteine mutants that would create disulfide cross-links. Polymers of T4L were then made both from lysozyme in solution and crystallized lysozyme mutants by exposing the protein to oxygen. The yield of polymers was much higher from oxidized crystals than oxidized monomers in solution. Interestingly, these polymers were exploited as a means of studying monomer unfolding by mechanical stress through scanning force microscopy (SFM)

A couple years later, in 2002, Srinivasan *et al.* promoted disulfide cross-linked protein crystals as a way to form protein fibers which they called crystine.⁶⁹ The disulfide modeling program MODIP was used to predict sites in 15 crystallographic interfaces that would support disulfide cross-linking. Only one out of three designs produced was successfully crystallized. The authors noted that even though the cross-linking was only one-dimensional, the crystals were difficult to dissolve. Dissolution of these crystals resulted in bundled fibers with diameters up to 7 nm in which several cross-linked chains were held together by non-covalent interactions. In contrast to the random three-dimensional network produced by glutaraldehyde cross-linking, disulfide cross-links preserved the order of a protein crystal at specific sites along crystal interfaces. In 2014, Esben Quistgaard demonstrated the use of disulfide cross-linking within crystals composed of vDED coiled-coil domain dimers from human BAP29.⁷⁰ These crystals form honeycomb-like scaffolds with complete disulfide cross-links along the c-axis (PDB Code: 3W7Y, Figure 1.8A). Per MAP_CHANNELS, the major axial pores are large enough to accommodate 1D diffusion of 7 nm diameter guest spheres, though the short unit cell height (3.1 nm) would preclude some applications. Finally, Heinz and Mathews reported that designed intermolecular disulfide cross-links in T4L resulted in more rapid crystallization.⁷¹

Similarly, protein crystal scaffold interfaces can be engineered to display surface histidine (or histidine motifs) that can coordinate metal ions and stabilize the crystal lattice. In 2010, Robert Radford and others working in Akif Tezcan's group implemented a bottom-up strategy to direct protein self-assembly using supramolecular metal coordination chemistry in the production of a porous protein crystal framework.⁷² Their engineered protein (MBPPhen2) was derived from a four-helix bundle heme protein (cytochrome *cb*₅₆₂) and was shown to readily crystallize in the presence of Ni²⁺ or Zn²⁺ ions (Figure 1.8B). The resulting scaffold (PDB Code: 3NMK) contains

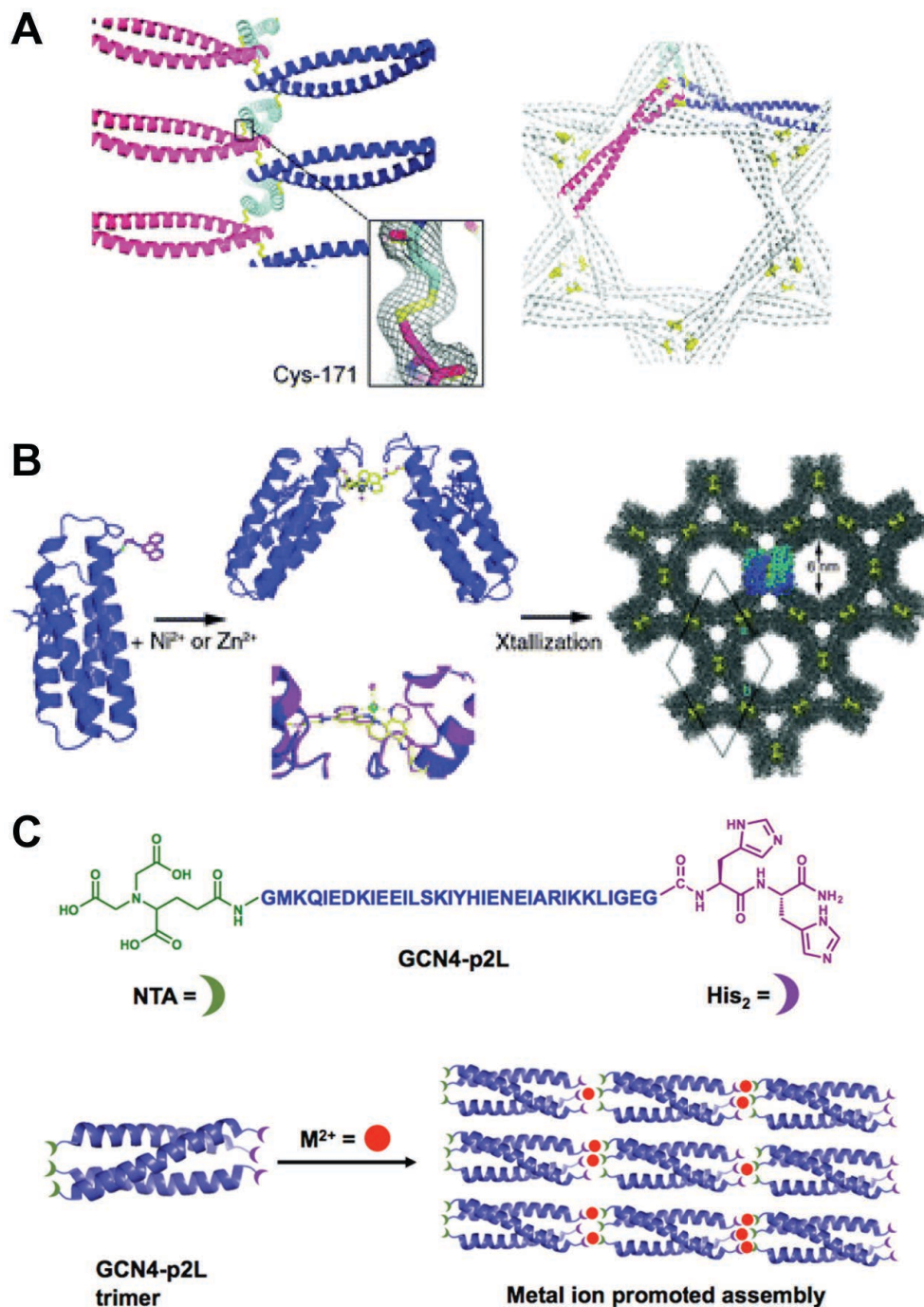


Figure 1.8. (A) disulfide linkages within a porous protein crystal scaffold. Adapted from Quistgaard. *Chem Commun* 2014, 50 (95), 14995–14997 with permission from The Royal Society of Chemistry. (B) Schematic of zinc mediated crystal formation of MBPPhen2 illustrating resultant lattice porosity. Reproduced from Radford *et al.* *Chem. Commun.* 2010, 47 (1), 313–315 with permission from The Royal Society of Chemistry. (C) Schematic of metal mediated coiled-coil crystal assembly. Reproduced from Nepal. *J. Am. Chem. Soc.* 2016, 138 (34), 11051–11057 with permission from The American Chemical Society.

hexagonal pores, the largest of which could accommodate a spherical guest with 4.6 nm diameter (per MAP_CHANNELS). More recently, metal-coordination has been used to direct coiled-coil self-assembly in the production of crystal scaffolds. Both Jean Chmielewski's group (Figure 1.8C)⁷³ and Seth Horne's group⁷⁴ have used peptide engineering and metal-coordination to produce self-assembling crystalline scaffolds with tunable morphologies.

Other methods of engineering scaffold interfaces include hydrophobic patch design, ligand-mediated crystallization, and natural dimer and trimer fusion proteins. All of these approaches have led to unique artificial protein crystals. These methods and others are reviewed in detail by Satoshi Abe and Takafumi Ueno.⁷⁵

Engineering Crystal Surfaces and Pore Environments: Site-specific modifications of protein constituents can improve or expand protein crystal functionality, producing novel scaffolds with uniquely desirable traits. For instance, surface modification of protein crystals with secondary molecules capable of binding cell surface markers could prove beneficial in directing crystals to specific tissue types in drug delivery applications. Takafumi Ueno's group has shown the ability to decorate the surface of polyhedral crystals (PhC) with Lewis X (LeX) carbohydrate by modifying surface cysteine residues using established maleimide and click chemistry (Figure 1.9A).⁷⁶ Alternatively, the Chmielewski metal-coordination driven coiled-coil assembly that was described above (Figure 1.8C) was also shown to direct guest molecules to distinct crystal surfaces (Figure 1.9B).⁷³

Other crystal engineering efforts have focused on modification of the interior surfaces. Pore structure and the physicochemical character of the interior crystal surfaces are critically important for the overall performance properties of protein crystal materials that include guest molecules.

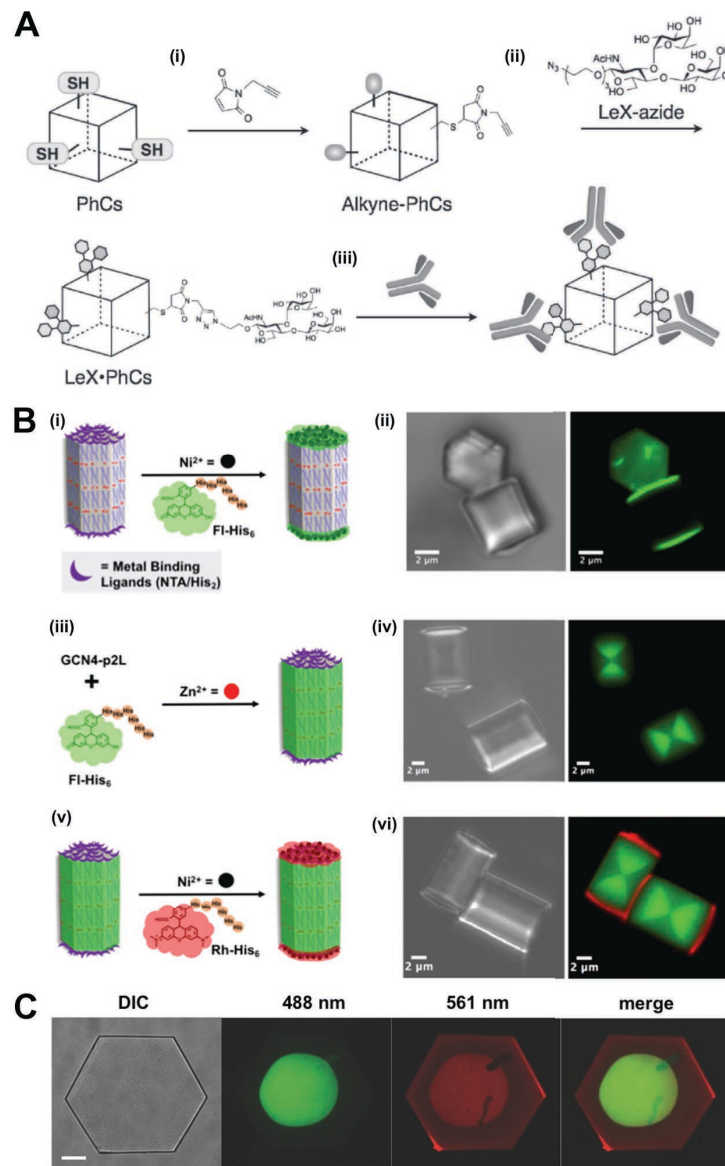


Figure 1.9. (A) Schematic representation of LeX immobilization on the surface of PhC: (i) cysteine residues of PhC modified with propargyl maleimide; (ii) acetylene moieties modified with LeX-azide *via* copper-catalyzed azide-alkyne cycloaddition; (iii) antibody-antigen reaction on the surface of modified PhCs. Reproduced from Abe *et al. Chem. Lett.* 2014, 44 (1), 29–31 with permission from The Chemical Society of Japan (B) Schematic representations for directing His-tagged fluorophore guests to protein crystals: (i) on the surface after crystal formation, (iii) within the crystal during formation, or (v) at both the surface and within crystals. (ii, iv, vi) Bright-field (left) and confocal (right) microscopy images. Reproduced from Nepal *et al. J. Am. Chem. Soc.* 2016, 138 (34), 11051–11057 with permission from The American Chemical Society. (C) Confocal imaging of an interior plane within a highly porous CJ crystal, demonstrating spatially segregated macromolecular guests (mNeonGreen and mCherry) immobilized with Zn^{2+} . Reproduced from Huber *et al. Small* 2017, 13 (7), 1602703 with permission from The Royal Society of Chemistry.

Accordingly, there have been multiple attempts to modify protein scaffolds to optimize specific properties related to transport, catalysis, and templating. In 2009 & 2011, Felix Frolow and Amihay Freeman's group used both systematic mutation of pore surface residues to alter the porosity of HEWL crystals in the interest of biotemplating applications.⁷⁷ They furthermore investigated the possibility of utilizing metal-mediated crystal-packing to affect the pore size of HEWL crystals *via* simple addition of various metal ions (Co^{2+} , Ni^{2+} , Cu^{2+} , Zn^{2+} , Cd^{2+}) to the crystal growth environment. However, this approach resulted in limited changes to crystal packing and overall porosity.⁷⁸

Our group has recently engineered metal coordination sites on the interior pore surfaces of CJ protein crystals (Figure 1.1B), to exert spatial and temporal control over macromolecular guest installation within the crystal scaffold (Figure 1.9C).^{79,80} We used stepwise guest loading and EDTA as a metal chelator to demonstrate secure immobilization and precise segregation. These results illustrate the capacity of protein crystal materials to organize trillions of guest molecules in 3D with robust control over localization and release. Efforts to modify surface and pore functionality of protein crystal scaffolds have enhanced the prospects for using engineered protein crystals as host matrices for drug storage, delivery, and release with exciting implications for the future of nanomedicine.

☉ 1.4 APPLICATIONS IN NANOMEDICINE

☉ 1.4.1 Pharmaceutical Formulations

The simplest route through which protein crystals can benefit nanomedicine is the use of non-cross-linked protein crystal formulations for drug delivery. Alexey Margolin and Manuel Navia have outlined several significant advantages crystallization can offer from a therapeutic perspective: i) crystallization can streamline the manufacturing process by providing a means of

protein purification; ii) crystals are the most concentrated form of proteins, which is beneficial for high-dose delivery; iii) crystal dissolution is dependent on crystal morphology, which enables optimization of a slow dose release regimen by altering the crystal size and shape; iv) lastly, dry crystal formulations are known to have improved physical and thermal stability over their soluble or amorphous counterparts.⁸¹ In 2003, Alexey Margolin's group went on to demonstrate the feasibility of crystallizing monoclonal antibodies (mAbs) in large quantities using batch crystallization methods.⁸² Their work generated functional crystalline suspensions of three approved therapeutic mAbs with yields of 85-95%. Crystal morphologies could be tuned by manipulation of the batch crystallization protocol to generate optimal formulations for subcutaneous delivery in high concentrations. They have subsequently written an expert opinion piece focusing on the use of protein crystals for the delivery of biopharmaceuticals, which describes the benefits, challenges, and techniques associated with this technology.⁸¹ In addition to this work, experimental⁸³⁻⁸⁶ and computational⁸⁷⁻⁹⁴ studies have characterized batch crystallization techniques for the generation of monodisperse sub-micron protein crystals of specific morphologies in the interest of industrial scale pharmaceutical formulations and drug delivery. We also note that microcrystalline suspensions offer potential advantages in terms of shelf-stability⁹⁵ and decreased viscosity which could enable delivery *via* smaller needles.⁸¹

☉ 1.4.2 Vaccine Delivery

Subunit vaccines are ideally composed of highly purified and well characterized antigenic molecules that can be manufactured through chemical synthesis or recombinant DNA expression systems.⁹⁶ Furthermore, subunit vaccine formulations provide superior safety over live-attenuated vaccines and thus may be administered to patients with weakened immune systems.⁹⁷ The high purity and regularity of protein crystals, along with their biodegradability may provide significant

advantages over soluble subunit vaccine formulations by improving the immune response and limiting the need for additional adjuvants. For instance, in 1997 Wade-Evans *et al.* demonstrated 70% reduction in mortality in mice immunized with a crystalline vaccine composed of the major outer core protein of African horse sickness virus, VP7.⁹⁸ Protection was slightly improved (90%) when the VP7 protein crystal vaccine was administered along with Freund's complete adjuvant. Both outcomes demonstrated significant improvement over the dramatic 80-100% mortality in non-immunized mice. In 1999, Nancy St. Clair working with Alexey Margolin and coworkers used cross-linked protein crystals composed of human serum albumin (HSA) to elicit an immune response in rats.⁹⁹ They compared the HSA crystal vaccination response to that of soluble HSA and observed that cross-linked crystals were significantly more immunogenic as assessed using antibody titer counts. While this early work demonstrated the utility of protein crystals for use in vaccine delivery, recent progress on improving subunit vaccine immune responses has been primarily pursued by groups focusing on other forms of supramacromolecular structures, such as protein nanoparticles, cages, and viral-like particles.¹⁰⁰⁻¹⁰³

☉ 1.4.3 Drug Delivery

Drug delivery is a broad field with tremendous impact on the future of nanomedicine. Aside from the previously mentioned pharmaceutical formulations, there are numerous drug delivery vehicles ranging from various nanoparticles^{101,104} to protein cages and artificial virus-like particles.^{105,106} One drug delivery avenue where protein crystal materials have been of recent use is in the delivery of gas signaling molecules. Carbon monoxide (CO) is a cell signaling molecule that mediates anti-inflammatory and vasoactive responses.¹⁰⁷ Hiroyasu Tabe and associates working in Takafumi Ueno's group used cross-linked HEWL crystals as a scaffold to immobilize ruthenium carbonyls, creating ruthenium carbonyl-incorporated cross-linked hen egg white

lysozyme crystals (Ru•CL-HEWL) with CO-releasing properties.³⁹ They demonstrated the efficacy of Ru•CL-HEWL for the extracellular delivery of CO by treating cells with Ru•CL-HEWL crystals and assaying the cellular response to CO (Figure 1.10A). Specifically, they implemented a luciferase reporter assay to monitor nuclear factor kappa B activity. Similar cellular responses were generated using non-cross-linked polyhedral crystals (PhCs) spontaneously grown within, and purified from, insect cells.¹⁰⁸ Ueno's group went on to demonstrate photoactivatable release of CO from manganese carbonyl groups immobilized on non-cross-linked PhCs (Figure 1.10B).¹⁰⁹ This body of work illustrates the potential for porous protein crystal materials to be used as extracellular matrices for the metered delivery of signaling gases. Future work in this area may focus on alternate protein crystal scaffolds engineered to release a variety of biologically relevant gas molecules, such as NO, which has many therapeutic uses including antimicrobial and anticancer properties.^{110,111}

Multifunctional fibrous matrices offer another path for the delivery of therapeutics. Electrospun non-wovens have demonstrated the capacity for controlled release of therapeutic molecules—offering an intriguing drug delivery method with applications in wound dressings, transdermal delivery, and post-surgical intervention. Certain electrospun materials, such as those derived from poly-ε-caprolactone (PCL), can be both biocompatible and biodegradable and can deliver a wide range of drugs from small molecules like antibiotics to biomacromolecules like protein drugs and nucleic acids for gene delivery.^{112,113} However, one challenge in electrospinning protein therapeutics into non-woven matrices is the common requirement to use organic solvents in the electrospinning process, which can lead to protein denaturation or aggregation. Recall however, that crystals often offer some additional protection with respect to solvent conditions—

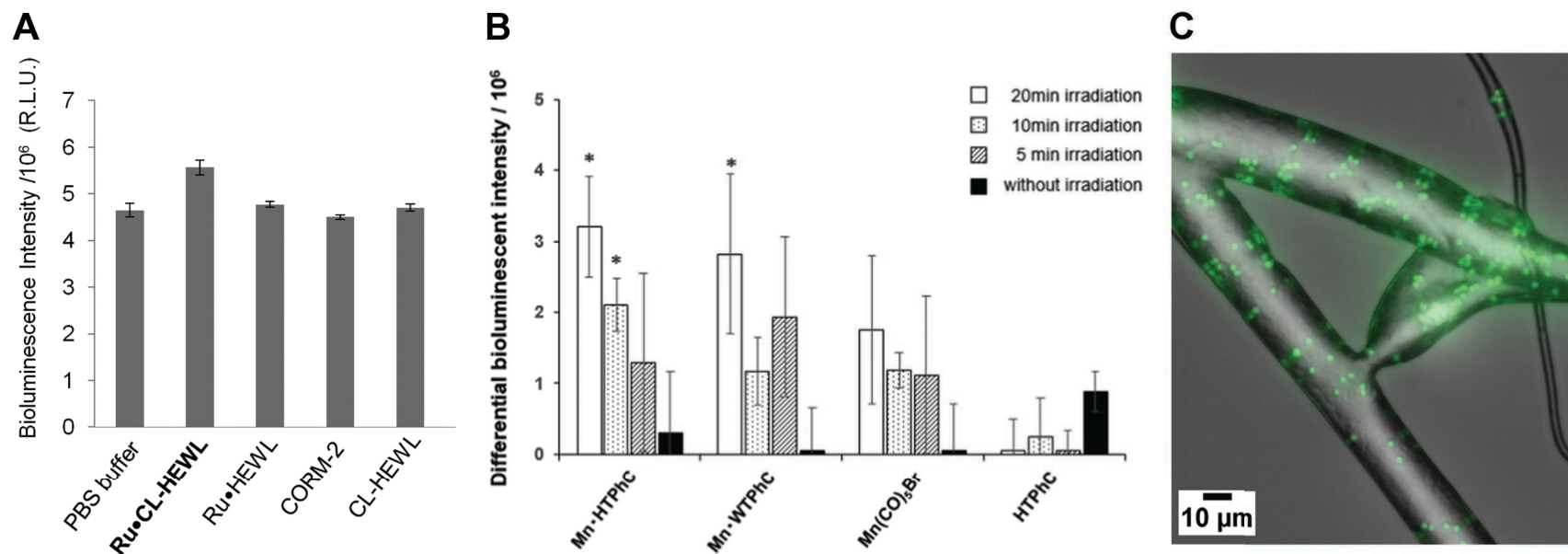


Figure 1.10. (A) Bioluminescence intensity in the luciferase reporter assay for evaluation of NF- κ B activity of HEK293/ κ B-Fluc cells in the presence of 1.0 ng/mL TNF- α after incubation with PBS buffer (as control), Ru-CL-HEWL, Ru-HEWL, CORM-2, and CL-HEWL for 24 h. Reproduced from Tabe *et al. Inorg. Chem.* 2015, 54 (1), 215–220 with permission from The American Chemical Society. (B) Luminescence intensity in the luciferase reporter assay for the evaluation of NF- κ B activity of HEK293/ κ B-Fluc cells in the presence of 10 ng/mL TNF- α after incubation for 12 hours with Mn-HTPhC, Mn-WTPPhC, MnCO₅Br and HTPPhC, with the light irradiation for 20 min (white), 10 min (dot), 5 min (slashed) and without the light irradiation (black). Reproduced from Tabe *et al. Chem. Commun.* 2016, 52 (24), 4545–4548 with permission from the Royal Society of Chemistry. (C) Distribution of FITC-labeled lysozyme crystals in a PCL non-woven prepared using ~2 μ m lysozyme crystals, a 25% PCL solution, and a drug loading of 5%. Reproduced from Puhl *et al. Mol. Pharm.* 2014, 11 (7), 2372–2380 with permission from The American Chemical Society.

demonstrating superior stability in aqueous-organic solvents than their non-crystalline counterparts. Sebastian Puhl *et al.* utilized the superior stability of protein crystals in the electrospinning process.¹¹⁴ Specifically, they incorporated non-cross-linked HEWL crystals into non-woven matrices *via* PCL electrospinning (Figure 1.10C) as a proof of principle for improved protein incorporation and release from electrospun non-woven matrices. In this case, dissolution of HEWL crystals could provide a sustained release of the constituent enzymes. Future work in the development of multifunctional fabrics may alternatively focus on using bioconjugation chemistries to directly and covalently attach porous protein crystals to pre-existing textiles.

☉ 1.5 APPLICATIONS IN BIOTECHNOLOGY

☉ 1.5.1 Catalysis

After Quioco and Richards' studies on glutaraldehyde cross-linked carboxypeptidase-A crystals in the 1960's,^{22,23} subsequent studies of cross-linked enzyme crystals (CLECs) progressed rather slowly with only a handful of studies in the 1970s that investigated glutaraldehyde cross-linked subtilisin crystals¹¹⁵ as well as crystals of carboxypeptidase A¹¹⁶ and B.¹¹⁷ It wasn't until the early 1990s that CLEC technologies became widely considered for industrial applications when Nancy St. Clair and Manuel Navia published their work on thermolysin CLECs.¹¹⁸ Their study looked at the catalytic activity and stability of thermolysin CLECs in a broad range of aqueous-organic solvents that would normally cause non-crystalline enzymes to denature and lose activity. The superior stability of crystalline enzymes (after chemical cross-linking) allowed CLECs to operate well outside normal biological conditions. In 1995, Alexey Margolin's group demonstrated that cross-linked crystals of lipase derived from *Candida rugose* could be used for enantioselective hydrolysis of chiral racemic esters.¹¹⁹ Their work showed lipase CLECs to have superior enantioselectivity over crude lipase extracts. Many examples of CLECs have since been

reported in the literature,^{15,120–128} providing new opportunities for biocatalysis. Today, CLEC catalysis has a notable role in industrial scale synthesis.^{129–131}

☉ 1.5.2 Biotemplating

Biology is replete with complex and intricate systems that exhibit ordered structures on the nanoscale level. As nanotechnology advances, researchers are increasingly turning to biological systems to aid in the construction of synthetic devices. Biotemplating is the process by which biological scaffolds such as proteins, DNA, viruses, and bacteria can help control the size and shape of inorganic nanostructures during synthesis. Protein crystal scaffolds have been identified as intriguing biotemplating candidates on account of their highly-porous regular structure. In 2006, Cohen-Hadar *et al.* assessed the feasibility of using cross-linked protein crystals as a biotemplating scaffold.²⁵ To do this, they used cross-linked lysozyme crystals to template the assembly of a synthetic hydrogel while monitoring the gel synthesis process and crystal stability *via* X-ray diffraction. In addition to templating hydrogels, protein crystals have been used as molds during the synthesis of both quantum dots¹³² and carbon dots¹³³ with tunable fluorescence, or to grow and coordinate gold nanoclusters^{134–137,80} and luminescent lanthanide complexes.¹³⁸ There have been many other accounts of stabilized protein crystals being utilized as effective biotemplating scaffolds and catalytic vessels for the assembly of organometallic complexes and biohybrid materials. These efforts have been thoroughly reviewed by Takafumi Ueno's group.^{139–143}

☉ 1.5.3 Biosensing

Detecting biologically relevant molecules has become an important aspect of many scientific disciplines, including the biomedical and biotechnology industries as well as environmental protection. Biosensors, a term coined in 1977 by Karl Camman, describes analytical devices that monitor changes in biological analytes including metabolites, biomolecules, supramolecular

structures, and whole cells.¹⁴⁴ Most such devices can be analyzed in terms of three components that each handle a specific task: i) analyte recognition, usually performed by a biological element such as cell receptors, proteins/enzymes, or DNA; ii) signal transduction elements, that transform the detection event into a measurable electrical or optical signal; iii) signal detection, which converts the electrical or optical signal into a readable result. The efficacy and performance of biosensors are often limited by the affinity and selectivity of the initial biomolecular recognition event. Thus, biomolecular recognition sensitivity limitations can bottleneck the biosensor performance.

As discussed above, protein crystals are highly concentrated, regularly repeating structures that can be either engineered or cross-linked to become remarkably stable. Furthermore, CLECs possess high specific activity toward their reactants, even under very low reactant concentrations,¹¹⁸ thereby enabling CLECs to perform well as biorecognition elements within biosensing devices. In 1999, Manuel Navia and Nancy St. Clair filed a patent for the use of glutaraldehyde cross-linked protein crystals as biosensors, providing evidence for thermolysin, elastase, asparaginase, lysozyme, lipase, and urease CLEC stability and catalytic activity.¹⁴⁵ A fully realized example of a CLEC biosensor was later presented in 2001 by Arkady Karyakin's group, in which they evaluated a glucose biosensor based on Prussian Blue and CLECs derived from glucose oxidase.¹⁴⁶ Their study compared the performance of a commercially available glucose oxidase biosensor to their glucose oxidase CLEC sensor in terms of sensitivity, linear range, and operational stability. They found that glucose oxidase CLECs had remarkable selectivity and improved sensing and stability over the commercially available biosensor, establishing the potential for future devices to incorporate protein crystals when diagnosing and treating diabetes.

Protein crystal based biosensors have also been implemented in detecting organic pollutants in the interest of environmental science and conservation. In 2004, Jegan Roy and coworkers developed a biosensor based on a laccase CLEC for the detection of phenols.¹⁴⁷ This study found that laccase CLEC biosensors possessed high activity and sensitivity over a 3-month period towards a variety of phenols: catechin, catechol, pyrogallol, guaiacol, ferulic acid, and 2-amino phenol. Their sensor could be useful in the detection of antioxidant phenols in foods and phenolic pollutants in wastewater. In 2008, Thanaporn Laothanachareon and associates used organophosphate hydrolase (OPH) CLECs to create a biosensor for the detection of organophosphorus compounds.¹⁴⁸ Their design utilized crude OPH CLECs as opposed to more costly purified OPH. Notably, the OPH CLECs demonstrated similar sensitivity to biosensors that used pure OPH. This work established that relaxed purity requirements could facilitate economically viable crystal production for biosensors.

Microfluidic and nanowell devices, with their small scale and highly tunable transport properties, have been widely used for screening protein crystal growth conditions, study crystallization kinetics, and develop crystallization phase diagrams.^{149–153} Interestingly, nanowell devices have also been used to better understand protein nucleation and growth in the formation of sub-micrometer protein crystals for applications in pharmaceutical formulation and biosensing; Liying Wang and coworkers developed a method of crystallizing proteins in patterned nanowells (Figure 1.11A).¹⁵⁴ Their work demonstrated control over the localization of submicron crystals. Advancements in microwell protein crystallization has allowed for novel applications in microfluidic biosensing. For instance, Conejero-Muriel *et al.* have shown the feasibility of using CLECs for continuous analyte detection; their platform, termed OCER (optofluidic CELC-based

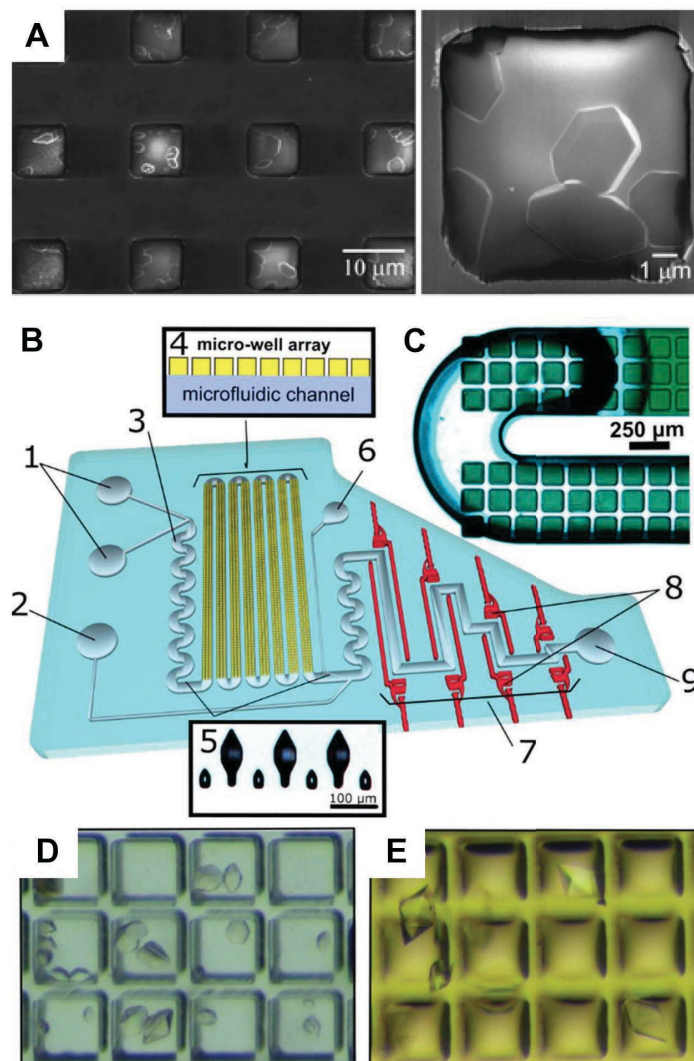


Figure 1.11. (A) SEM images of lysozyme crystals grown in 10- μm wells. Reproduced from Wang *et al. J. Am. Chem. Soc.* 2008, 130 (7), 2142–2143 with permission from The American Chemical Society. (B) (a) Schematic of the OCER platform: (1) inlet ports, (2) extra inlet port for injecting analytic solutions; (3) passive zigzag micromixer; (4) serpentine channel for droplet storage and cross-section depicting the layout of the solution-storage array; (5) image of the structures located before and after the serpentine channel to prevent any mobile crystal/aggregate from being dragged by the injected solutions; (6) outlet port for the crystallization and cross-linking solution to avoid any contamination of the sensing region; (7) multiple path configuration for the photonic detection system, allowing a large concentration range to be explored while maintaining the absorbance linear range; (8) 2D microlenses with air mirrors along the interrogation channel; (9) outlet port for the product solutions. (C) Operation of the solution trapping system during the injection of a green dyed solution. The meniscus of the flowing solution is observed when emptying the microfluidic device, while the solution trapping system retains nanoliter-sized droplets in the microwell array. (D) Lipase crystals obtained in the OCER platform and (E) after being cross-linked with glutaraldehyde. Reproduced from Conejero-Muriel *et al. Anal. Chem.* 2016, 88 (23), 11919–11923 with permission from The American Chemical Society.

enzymatic reactor), has implications in cost-effective next-generation lab on a chip applications (Figure 1.11B).¹⁵⁵

☉ 1.5.4 Chromatography

Chromatography is a widely-used technique for purifying both small molecules and biomacromolecules. The earliest example of using protein crystal scaffolds as chromatography media was presented in 1998 by Lev Vilenchick working with Alexey Margolin and associates.⁴ In this seminal paper, they use macromolecular porosimetry to study the fully hydrated pore structures of various cross-linked protein crystal scaffolds. This technique utilizes size exclusion chromatography (SEC) experiments to estimate the apparent pore size distribution of porous media. In their study, they investigated cross-linked protein crystal slurries of thermolysin, two forms of lipase (derived from *Candida rugose* and *Pseudomonas cepacia*), as well as bovine and human serum albumins (BSA and HSA) in packed chromatography columns. Their results demonstrate the ability of protein crystal materials to repeatedly separate molecules based on size, chemical structure, and chirality without significant loss in separation efficiency or structural integrity. Other groups have since demonstrated myriad separation applications for various protein crystal scaffolds.^{156–158}

One challenge in the field of chromatography is enantioselective separation of racemic mixtures. The Vilenchick *et al.* results highlight the inherently chiral nature of protein crystals as a distinct advantage over other porous materials. Proteins and enzymes are composed of purely L-amino acids resulting in the potential for enantioselective guest interactions. One of the most extensible schemes for enantiomer separations involving protein crystal scaffolds relies on antibody crystals. Antibody proteins possess high affinity and specificity toward their antigens; thus, antibody crystals could conceivably also possess high affinity and specificity toward their

antigen leading to the ability to distinguish chiral racemates. This idea was confirmed by Antti Vuolanto and coworkers in 2003 and 2004 when they demonstrated chiral separations using crystalline chromatography media derived from antibody Fab fragments.^{159,160}

Later, in 2009, Zhongqiao Hu and Jianwen Jiang utilized molecular dynamics simulations to explain the ability of protein crystals to separate chiral molecules. They first modeled the transport of various amino acids (Arg, Phe, and Trp) inside glucose isomerase crystals, providing insight into the relative velocities of each amino acid during separation.⁶⁰ Later, they simulated chiral separation of racemic phenylglycines within thermolysin crystals, predicting the ability of non-antibody protein crystals to separate chiral mixtures.⁶¹

◎ 1.6 CONCLUSIONS

The exceptional properties of proteins can be harnessed in the form of crystal scaffolds to generate advanced nanostructured devices and materials. Recent advancements in protein crystal material research and engineering have opened the door to intriguing applications. The controlled growth of protein crystals with defined size and shape has facilitated the synthesis of next generation materials. As we have discussed, cross-linked protein crystals are remarkably stable against mechanical disruption, solvent changes, and pH extremes. CLEC catalysts have been remarkably active and specific, even at elevated temperature and in aqueous-organic solvents. These properties have allowed CLECs to be successfully used as catalysts for industrial synthesis, organometallic complexes and biohybrid materials, as well as detectors and transducers in biosensing technologies.

Future studies of protein crystal material applications should assess the economics of this technology. In 2012, Harvey Blanch and coworkers evaluated the best-case scenario for highly optimized enzyme expression, estimating the baseline production cost to be \$10.14/kg.¹⁶¹ In the

case of protein crystal materials, the cost of bulk purification and crystallization would have to be included, thereby increasing this floor. The economics may nonetheless be favorable for high-value per gram applications such as biomolecular sensing, pharmaceutical formulations, and drug delivery. In the short-term, protein crystals may still be too precious for bulk material applications, such as chromatography media, in which hundreds of kilograms of crystalline material may be needed.

CHAPTER 2

ADSORPTION-COUPLED DIFFUSION OF GOLD NANOCCLUSERS WITHIN A LARGE-PORE PROTEIN CRYSTAL SCAFFOLD²

◎ 2.1 SUMMARY

Large-pore protein crystals (LPCs) are ordered biologically derived nanoporous materials exhibiting pore diameters greater than 8 nm. These substantial pores distinguish LPCs from typical nanoporous scaffolds, enabling engineered LPC materials to readily uptake, immobilize, and release macromolecular guests. In this study, macromolecular transport within an LPC environment was experimentally and computationally investigated by studying adsorption-coupled diffusion of Au₂₅(glutathione)₁₈ nanoclusters within a cross-linked LPC scaffold *via* time-lapse confocal microscopy, bulk equilibrium adsorption, and hindered diffusion simulation. Equilibrium adsorption data is congruent with a Langmuir adsorption model, exhibiting strong binding behavior between nanoclusters and the scaffold. The standard Gibbs free energy of binding is equivalent to -37.2 kJ/mol, and the maximum binding capacity of 1.25×10^3 mg/g corresponds to approximately 29 nanoclusters per LPC unit cell. The hindered diffusion model showed good agreement with experimental data, revealing a pore diffusion coefficient of 3.7×10^{-7} cm²/s under low nanocluster concentration. Furthermore, the model was sufficient to

² The work in this chapter was published in 2017 in *The Journal of Physical Chemistry B*. C.D.S. and I conceived and wrote the manuscript. I expressed, purified, and crystallized CJ protein, cross-linked CJ crystals, and performed the adsorption equilibrium, confocal loading, and dynamic light scattering experiments. B.M. and I developed the finite element model.

Hartje, L. F., Munsky, B., Ni, T. W., Ackerson, C. J. & Snow, C. D. Adsorption-Coupled Diffusion of Gold Nanoclusters within a Large-Pore Protein Crystal Scaffold. *J. Phys. Chem. B*, 2017, 121, 7652–7659.

determine adsorption and desorption kinetic values for k_a and k_d equal to $13 \text{ cm}^3/\text{mol}\cdot\text{s}$ and $1.7 \times 10^{-7} \text{ s}^{-1}$, respectively. At higher nanocluster concentrations, the simulated pore diffusion coefficient could be reduced by 3 orders of magnitude to $3.4 \times 10^{-10} \text{ cm}^2/\text{s}$ due to the effects of pore occlusion. This study demonstrates a strategy to analyze adsorption-coupled diffusion data to better understand complex transport of fluorescent macromolecules into LPCs. This approach fits the observable fluorescence data to the key molecular details and will benefit downstream efforts to engineer LPC-based nanoporous materials.

◎ 2.2 INTRODUCTION

Conventional nanoporous materials derived from mesoporous silica, zeolites and metal-organic frameworks (MOFs) have long been used in applications involving molecular separations, adsorbents, catalysis, and molecular storage—all of which rely on mass transport through the material void space. Thus, characterizing transport within nanoporous materials has historically been a critical step in engineering and optimizing new constructs. Experimental and computational diffusion studies of small molecules, solvents, and gasses within conventional nanoporous materials have been looked at extensively in the literature.^{162–167} In contrast, highly porous protein crystals represent a less explored class of self-assembling nanoporous materials that is chemically and structurally divergent from these more characterized antecedents. As such, large-pore protein crystals (LPCs) pose an exciting new area for nanoporous material research.

Composed of numerous chiral constituents, protein crystals are biologically derived and can be engineered to contain varying functional groups by means of genetic mutation or post-translational modification. Furthermore, chemical crosslinking has been shown to stabilize and reinforce protein crystals thereby increasing their tolerance to harsh conditions.^{15–18} The chemical diversity, functional versatility, and imbued stability of crosslinked protein crystals make them

promising targets for use as nano-structured scaffolds with potential applications in drug delivery,^{81,168,169} catalysis,^{16,170–172} biosensing,^{146–148} enantiomer separations^{4,61,157–159,173} and biotemplating.^{25,174–176}

While diffusion of low molecular weight solutes within protein crystals has been the subject of a handful of studies,^{44–49,177–179} to date, we are unaware of any quantitative experimental or computational characterization of macromolecular guest transport within porous protein crystals. This is due in large part to the restrictive size of typical protein crystal pores, which have been reported to range from 0.3–10.0 nm in diameter.^{4,16,44} However, pore sizes greater than 8.0 nm are considered highly atypical, generally requiring a less-common high-symmetry space group. The protein crystal used in this study is composed of CJ monomers, a modified form of a putative periplasmic isoprenoid-binding protein from *Campylobacter jejuni*. CJ derived large-pore protein crystals (CJ-LPCs) adopt the P622 space group, with unit cell dimensions of $a, b = 179.59 \text{ \AA}$, and $c = 50.58 \text{ \AA}$ (Protein Data Bank ID: 2fgs), they also exhibit axial pore diameters of 13 nm and < 3 nm diameter lateral pores (Figure 2.1). The uncommonly large pore structure of the CJ-LPC scaffold permits passive diffusion of diverse macromolecular guests such as gold nanoclusters⁸⁰ as well as various enzymes and fluorescent proteins.⁷⁹

Transport within nanoporous materials is known to be sensitive to the relative size and shape of both the scaffold pore and guest molecules; such that the diffusion coefficient declines rapidly as the guest diameter increases¹⁸⁰. The aim of this study is to understand the transport characteristics of macromolecular guests within LPC materials. For this purpose, the adsorption-coupled diffusion of $\text{Au}_{25}(\text{GSH})_{18}$ nanoclusters within a CJ-LPC scaffold is investigated *via* confocal microscopy and equilibrium adsorption measurements. Intriguingly, CJ-LPC axial pores can be adequately modeled as parallel non-intersecting cylinders (Figure 2.1D) while $\text{Au}_{25}(\text{GSH})_{18}$

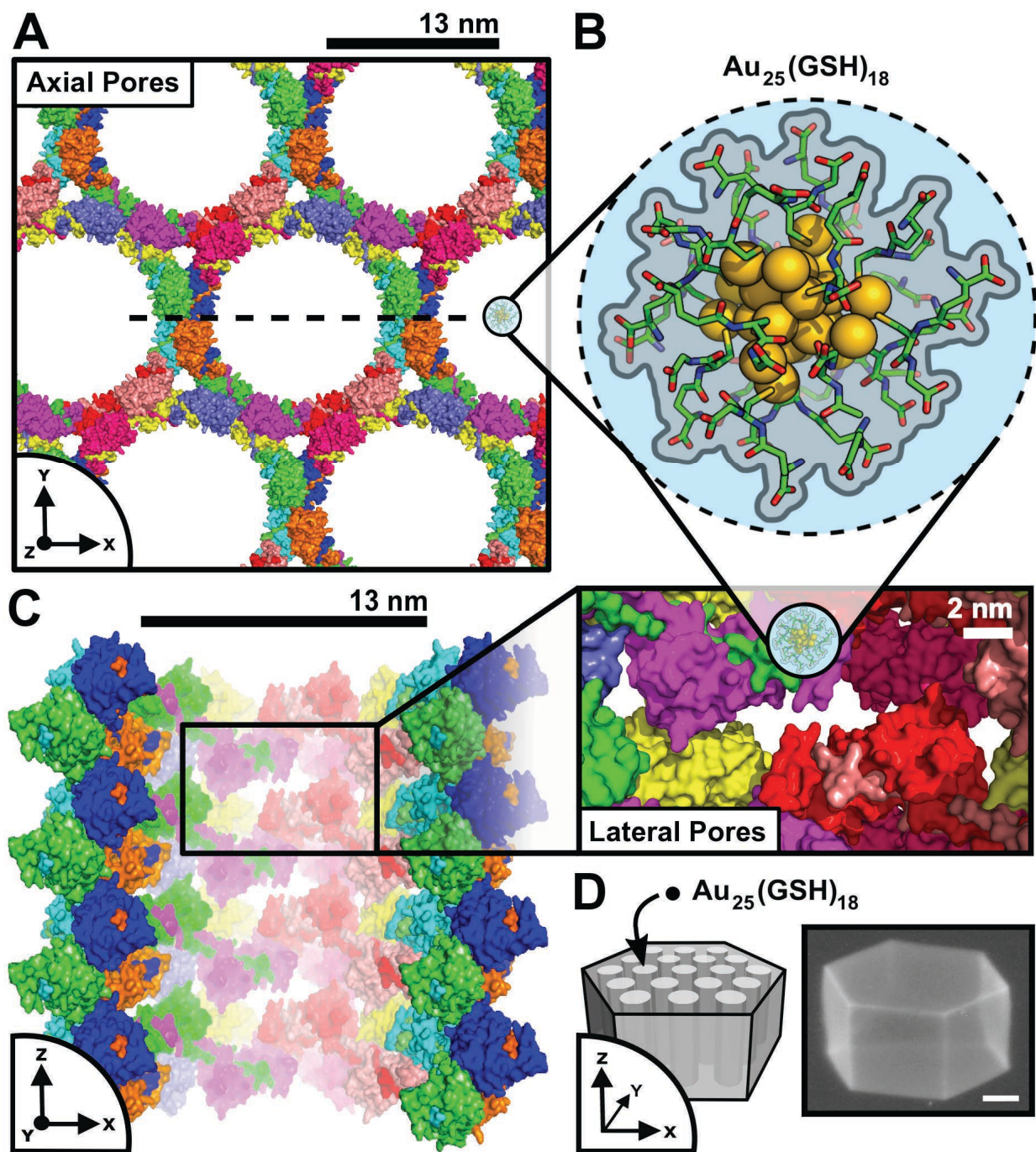


Figure 2.1. (A.) CJ-LPC 13 nm diameter z-axial pores; *Dashes*: cross-section depicted in C. (B.) $\text{Au}_{25}(\text{GSH})_{18}$ nanocluster; ^{181}CPK spheres and sticks represent gold atoms and glutathione (GSH), respectively; *Dashes*: 3.38 nm hydrodynamic diameter determined by dynamic light scattering (APPENDIX I). (C.) Cross-section of single z-axial pore; *Panel*: < 3 nm diameter lateral pores. (D.) *Left*: CJ-LPC model depicting parallel non-intersecting cylindrical pores and guest $\text{Au}_{25}(\text{GSH})_{18}$ nanocluster (not to scale). *Right*: CJ-LPC showing hexagonal morphology; *Scale bar*: 20 μm .

nanoclusters are intrinsically fluorescent and essentially spherical (Figure 2.1B), thereby making this host-guest pair an attractive model system for mass transport studies and enabling the experimental data to be fit to a dynamic transport model that includes a porosity-dependent variable diffusion coefficient as well as dynamic adsorption-desorption.

⊙ 2.3 THEORY

⊙ 2.3.1 Determining Diffusion Coefficients

Macromolecular transport within nanoporous materials is a complex process involving both diffusion and guest-scaffold interactions. These interactions tend to decrease transport by means of adsorption and hindrance. Thus, to appropriately model guest transport, the continuity equation must incorporate a pore diffusion coefficient, D_p , representing the free-solution diffusion coefficient reduced by finite interstitial volume and hindrance effects and two species of guest concentration—diffusive (mobile), C , and adsorbed (immobile), q :

$$\frac{\partial C}{\partial t} + \frac{\partial q}{\partial t} = \nabla \cdot (D_p \nabla C) \quad (\text{Eq. 2.1})$$

However, the relationship between adsorption and diffusion can be difficult to experimentally determine. For instance, while fluorescence microscopy has been used to monitor the rate of fluorescent guest infusion into lysozyme crystals,^{46,49,182} this method alone does not provide a means of separating the diffusive and adsorbed concentrations seen in the fluorescence intensity profiles. If all intensity values were assumed to be in the diffusive phase (C) Equation 2.1 would reduce to the following:

$$\frac{\partial C}{\partial t} = D_e \nabla^2 C \quad (\text{Eq. 2.2})$$

Here, the effective diffusion coefficient, D_e , represents an averaged diffusivity that does not explicitly account for adsorption or hindrance effects and can therefore misrepresent the details of the transport process.

One way to obtain accurate values for D_p , is to perform fluorescence microscopy experiments under conditions in which adsorption is negligible ($\partial q/\partial t \simeq 0$) whereupon D_e approaches D_p . However, if Equation 2.2 is utilized under adsorbing conditions, the actual interstitial pore diffusivity can be underestimated. Essentially, adsorption coupled to rapid diffusion can be mistaken for slow diffusion. Here, we demonstrate an alternative method to decouple fluorescence signals into diffusive and adsorbed guest pools using equilibrium adsorption data and a hindered diffusion model that incorporates adsorption kinetics and a variable pore diffusion coefficient.

☉ 2.3.2 Adsorption Model

We began this study by quantifying the adsorption equilibrium between $\text{Au}_{25}(\text{GSH})_{18}$ and the host crystal. There are multiple models explaining various types of adsorption processes, the most commonly used is Langmuir adsorption^{183,184}. The following Langmuir equation can be used to fit equilibrium adsorption data¹⁸⁴:

$$q = q_{max} \frac{K_L C_0}{(1 + K_L C_0)} \quad (\text{Eq. 2.3})$$

where q_{max} is the maximum concentration capable of being adsorbed onto a given amount of host material and C_0 is the free-solution concentration at equilibrium. The Langmuir adsorption equilibrium constant, K_L , is related to the adsorption, k_a , and desorption, k_d , rate constants ($K_L = k_a/k_d$). Furthermore, K_L can be used to calculate ΔG° , the change in standard Gibbs free energy of adsorption:^{185,186}

$$\Delta G^\circ = -RT \ln(55.5 K_L W_g) \quad (\text{Eq. 2.4})$$

where R is the ideal gas constant, T is temperature in Kelvin, and W_g is the molecular weight of the adsorbed guest. Multiplication by the molarity of water (55.5 mol/L) results in a dimensionless quantity within the logarithmic function (APPENDIX I).

Additionally, we can use the kinetic rate constants to determine the change in the adsorbed concentration over time by implementing the Langmuir adsorption kinetic equation:¹⁸⁴

$$\frac{dq}{dt} = k_a C(q_{max} - q) - k_d q \quad (Eq. 2.5)$$

To determine the adsorption rate constants (k_a and k_d) from the fixed parameter K_L , we used a hindered diffusion model to fit these parameters to experimental confocal loading data.

⊙ 2.3.3 One-Dimensional Hindered Diffusion Model

It is well known that guest molecule diffusion in nanoporous materials is reduced by a combination of guest-scaffold hydrodynamic interactions and steric confinement¹⁸⁰. This hindrance is dependent on the proximity of the guest to the pore wall and increases with decreasing pore size. Furthermore, guest molecules adsorbed to the scaffold take up pore volume, thereby effectively decreasing the pore size. Therefore, the process of adsorption leads to increased hindrance and the attenuation of $D_p(q)$.

Various models in the literature explain the relation between pore diffusivity and free-solution diffusivity as a function of λ , where λ is the ratio of molecular guest radius over effective pore radius ($\lambda = R/R_p$).^{180,187-189} Dechadilok and Deen¹⁸⁰ showed the following relationship to be within 2% of empirical observation for diffusion of spheres in cylindrical pores in which $\lambda < 0.95$:

$$\begin{aligned} D_p = D_0 & (1 + 1.125\lambda(\ln \lambda) - 1.56034\lambda + 0.528155\lambda^2 \\ & + 1.91521\lambda^3 - 2.81903\lambda^4 + 0.270788\lambda^5 \\ & + 1.10115\lambda^6 - 0.435933\lambda^7) \end{aligned} \quad (Eq. 2.6)$$

In the present work, the guest molecular radius (R) is computationally approximated from the known guest molecular structure using a hydrodynamic bead model (HYDROPRO),¹⁹⁰ while the free-solution diffusion coefficient, D_0 , is calculated using the Stokes-Einstein relationship:

$$D_0 = \frac{k_B T}{6\pi\eta R_h} \quad (Eq. 2.7)$$

Where k_B is Boltzmann's constant, T is the temperature in Kelvin, η is the solution viscosity (0.01 g/cm · s), and R_h is the guest hydrodynamic radius obtained *via* dynamic light scattering (APPENDIX I). The effective pore radius is ascertained for each location along the pore over time from the quantity of locally adsorbed guest molecules:

$$R_p = R_{p_o} \left[1 - \left(\frac{4}{3} \pi R^3 \right) q N_A \right]^{0.5} \quad (\text{Eq. 2.8})$$

where N_A is Avogadro's number and the internal term estimates the volume consumed per adsorbed guest (APPENDIX I).

If transport is assumed to only occur in the interstitial pore volume along the z -axis, Equation 2.1 can be simplified to a single dimension. Combining Equations 2.1 and 2.5 produces the final continuity equation describing adsorption-coupled hindered diffusion for spherical guest transport within a one-dimensional cylindrical pore:

$$\frac{\partial c}{\partial t} = \frac{\partial}{\partial z} \left(D_p \frac{\partial c}{\partial z} \right) - k_a C (q_{max} - q) + k_d q \quad (\text{Eq. 2.9})$$

Here, the effect of reduced interstitial volume and hindrance factors is represented by a temporally and spatially varying pore diffusion coefficient, $D_p(q)$, calculated from Equation 2.6.

To describe diffusion into an empty crystal, initial conditions are set such that when $t = 0$, $q = 0$. Furthermore, Robin boundary conditions are set at the crystal surfaces ($z = 0, L$):

$$D_p \frac{\partial c}{\partial z} = -k_m (C_{0_e} - C) \quad (\text{Eq. 2.10})$$

where k_m is the external mass transfer rate of the guest, C_{0_e} is the effective free-solution guest concentration at the crystal surface interface, and C is the diffusive intrapore guest concentration just inside the crystal at the surface interface. L is the total size of the crystal along the z -axis and transport occurs from the surfaces of the crystal ($z = 0, L$) toward the interior midplane ($z = L/2$).

◎ 2.4 EXPERIMENTAL SECTION

◎ 2.4.1 Materials

The following chemicals were purchased and used without further purification. From Sigma-Aldrich: dimethylamine borane complex (DMAB). From Acros Organics: glyoxal solution (40% in H₂O). From Alfa Aesar: hydroxylamine solution (50% in H₂O). From Promega: analytical low melting point agarose. From VWR: HEPES. From Fisher Scientific: NaCl. From J.T. Baker: citric acid. Other reagents from Thermo Scientific and Sigma-Aldrich were used to make mTacsimate™: 1.83 M malonic acid, 0.25 M sodium citrate, 0.12 M succinic acid, 0.3 M D-L malic acid, 0.4 M acetic acid, 0.5 M sodium formate, and 0.16 M sodium tartrate—titrated to pH 7.5. mTacsimate™ is a modified blend of Tacsimate™ from Hampton Research that removes ammonium from the solution, which contains primary amines that interfere with protein crystal crosslinking.

◎ 2.4.2 Protein Expression

The target gene CJ was modified from the gene vector encoding protein CJ0 obtained from the Protein Structure Initiative: Biology-Materials Repository (Genebank ID: cj0420, Protein Data Bank ID: 2fgs). For ease of uniform expression and purification, the CJ0 gene was codon optimized and the periplasmic signaling peptide deleted thereby yielding CJ. The CJ gene was encoded in expression vector pSB3 with a C-terminal 6xHis tag and expressed in *Escherichia coli* BL21(DE3) pLysS cells using a glucose/lactose induction system¹⁹¹ at 17° C for 36 hours. Cells were lysed by sonication and the CJ protein purified *via* nickel affinity capture on a HisTrap HP™ column (GE Healthcare). A single chromatography step provided sufficient purity for crystallization. Purified CJ protein was buffer exchanged into 0.15 M NaCl, 10 mM HEPES, and 10% glycerol at pH 7.5, concentrated to 15 mg/mL, and stored at -30° C until used.

⊙ 2.4.3 Crystallization and Crosslinking

CJ-LPCs were grown overnight by sitting drop vapor diffusion at 20° C in 85-90% mTacsimateTM and 10% glycerol at pH 7.5. Prior to crosslinking, crystals were washed by loop transferring them into a 90% mTacsimateTM, 10% glycerol mixture at pH 7.5 for 16-24 hours. Crystals were then transferred into a fresh mixture of 90% mTacsimateTM, 10% glycerol at pH 7.5, and crosslinked for 2-4 hours by the direct addition of 1% glyoxal and 25 mM DMAB. The crosslinking reaction was quenched by transferring CJ-LPCs into a solution of 0.3 M hydroxylamine, 25 mM DMAB, 0.15 M NaCl, and 0.1 M citric acid at pH 5.0 for 2-4 hours. After crosslinking and quenching, crystals appear clear with hexagonal morphology (Figure 2.1D).

⊙ 2.4.4 Nanocluster Preparation

Au₂₅(GSH)₁₈ was synthesized and purified according to a previously published procedure.⁸⁰ Glutathione (308.1 mg, 1x10⁻³ mol) was added to a solution of HAuCl₄ (98.7 mg, 2.5x10⁻⁴ mol) in 50 mL methanol and stirred to combine. Initially the mixture is a yellow cloudy suspension, but turns clear and colorless after approximately five minutes of magnetic stirring. The mixture is then cooled at 0° C while stirring for 30 minutes. To this, a solution of NaBH₄ (94.3 mg, 2.5x10⁻³ mol) in 12.5 mL ice H₂O was added rapidly while stirring. The reaction was allowed to mix for one hour at room temperature. The precipitate was then spun down at 4,000 rpm in 200 μL of methanol containing 5.0 M NH₄OAc and the supernatant discarded. The precipitate was washed twice more in the same solution. Au₂₅(GSH)₁₈ was then purified using a 24% polyacrylamide gel. Au₂₅(GSH)₁₈ nanoclusters were extracted from the polyacrylamide using H₂O and subsequently precipitated in 200 μL of methanol containing 5.0 M NH₄OAc. Finally, Au₂₅(GSH)₁₈ was dried and stored at 4° C. The hydrodynamic radius, R_h , of these Au₂₅(GSH)₁₈ nanoclusters was evaluated *via* dynamic light scattering in 20 mM HEPES pH 8.0 at 20° C (APPENDIX I).

☉ 2.4.5 Equilibrium Adsorption Experiments

To determine the binding affinity of $\text{Au}_{25}(\text{GSH})_{18}$ to the CJ-LPC pore walls the adsorption isotherm was determined by constant volume bulk equilibrium adsorption. Four replicate adsorption equilibrium experiments were set up as follows: multiple large (100-400 μm diameter) crosslinked CJ-LPC crystals of known volume (and by extension known dry weight) were transferred into 5 μL of 20 mM HEPES pH 8.0 containing varying concentrations of $\text{Au}_{25}(\text{GSH})_{18}$ nanoclusters. Samples were sealed and lightly shaken for several days. The absorbance of $\text{Au}_{25}(\text{GSH})_{18}$ nanoclusters in the free-solution was measured at 235 nm on a Take3TM micro-volume plate using an EpochTM spectrophotometer (BioTek Instruments) before and after the incubation. The concentrations were obtained by comparison to an absorbance standard (APPENDIX I). The adsorbed concentration of $\text{Au}_{25}(\text{GSH})_{18}$ nanoclusters on CJ-LPC at equilibrium was determined *via* mass conservation and normalized to the total mass of CJ-LPC present.

☉ 2.4.6 Confocal Imaging Experiments

Quantifiable time-lapse diffusion data was obtained by monitoring $\text{Au}_{25}(\text{GSH})_{18}$ nanocluster uptake within crosslinked CJ-LPCs *via* confocal microscopy. Individual crystals were loop transferred into a 20 μL total volume microwell containing 2.0 μL of 0.4% low melting point agarose to prevent crystal movement during imaging (APPENDIX I Figure I.6). After immobilization, the remaining volume (18 μL) was filled with 1.5 mg/mL $\text{Au}_{25}(\text{GSH})_{18}$ suspended in 20 mM HEPES pH 8.0. A vacuum greased coverslip was placed over the well to prevent desiccation. Images were taken such that the z-axis fell within the image focal plane to monitor fluorescence intensity changes through the crystal over time. All diffusion experiments were performed in triplicate on an Olympus IX81 spinning-disk confocal microscope with Photometrics

Cascade II camera, a 20×/0.5 numerical aperture objective with a 1x magnification changer, and an Intelligent Imaging Innovations (3i) phasor holographic photoactivation system. Excitation was achieved with a 561 nm diode laser and 692 ± 12.5 nm single bandpass emission filter. Freshly crosslinked and quenched CJ-LPCs were imaged to ensure the crystals were intrinsically non-fluorescent prior to $\text{Au}_{25}(\text{GSH})_{18}$ infusion. All images were acquired with SlideBook 6.0 software (3i) and exported in tagged image file format (.tiff). Images were quantitatively processed using MATLAB version 9.1.0 software (Natick, MA).

☉ 2.4.7 Hindered Diffusion Finite Element Model

Confocal images and equilibrium adsorption data were used to fit the k_a and k_d parameters contributing to the final continuity equation (Eq. 2.9) using a finite element model (FEM). The value for, C_{0_e} , in the boundary conditions (Eq. 2.10) gradually increases during early infusion as $\text{Au}_{25}(\text{GSH})_{18}$ diffuses through the 0.4% agarose gel toward the crystal, eventually reaching the constant C_0 value of 1.43×10^{-7} mol/mL (1.5 mg/mL). This behavior was modeled using the error-function complement for one-dimensional diffusion in a semi-infinite bath (APPENDIX I). The spatial dimension within the crystal (distance along the crystal z-axis) was discretized into one-dimensional elements resulting in a set of ordinary differential equations (ODEs) in time, which were solved by an implicit ODE solver (ode15s) in MATLAB version 9.1.0 (Natick, MA). See Table 2.1 for all other parameters used.

☉ 2.5 RESULTS AND DISCUSSION

☉ 2.5.1 Adsorption Isotherm

To quantify the binding affinity of $\text{Au}_{25}(\text{GSH})_{18}$ to CJ-LPC pore walls, an adsorption isotherm was generated from equilibrium adsorption experimental data. After fitting the experimental data to both Langmuir and Freundlich isotherm models *via* least squares, it was determined that the

Langmuir model (Eq. 2.3) demonstrated slightly superior fit (Figure. 2.2, APPENDIX I Figure I.12).

The Langmuir fit resulted in an adsorption equilibrium constant (K_L) of 7.51 L/g, revealing strong binding behavior between nanoclusters and the scaffold—from Equation 2.4: $\Delta G^\circ = -37.2$ kJ/mol. The maximum binding capacity (q_{max}) was found to be 1.25×10^3 mg/g or approximately 29 nanoclusters per LPC unit cell. Remarkably, the apparent 29 nanoclusters per unit cell corresponds closely to the expected number for a close-packed, adsorbed monolayer (APPENDIX I). K_L and q_{max} were later used as fixed parameters (Table 2.1), when tuning the free parameter k_a to best fit the observable confocal fluorescence data (*i.e.* the temporally and spatially varying sum of q and C). Note that k_d was determined using K_L and k_a ($k_d = k_a/K_L$).

☉ 2.5.2 Processing Confocal Images

Images obtained by confocal microscopy were taken with the confocal image plane passing through the crystal along the z-axis of diffusion; schematic illustration found in Figure 2.3A. Digital images of a single crystal being infused with $\text{Au}_{25}(\text{GSH})_{18}$ nanoclusters were recorded at intervals of 2 min for the duration of 1 hour, representative images shown in Figure 2.3B. To increase the fluorescence signal-to-noise ratio, intensity values from a 150 μm tall horizontal slice through the center of the crystal were taken at each time point and collapsed into one dimension by averaging the pixel values in each column, thereby creating a mean fluorescence ray-trace along the axis of diffusion (Figure 2.3C). The crystal boundaries ($z = 0, L$) were determined using canny edge detection in MATLAB version 9.1.0 (Natick, MA). Intra-crystal fluorescence intensity profiles at representative time points are shown in Figure 2.4C.

Lateral diffusion across the xy-plane was not observed in the confocal data, which is consistent with the steric confinement prediction of parallel non-intersecting cylindrical pores (Figure 2.1).

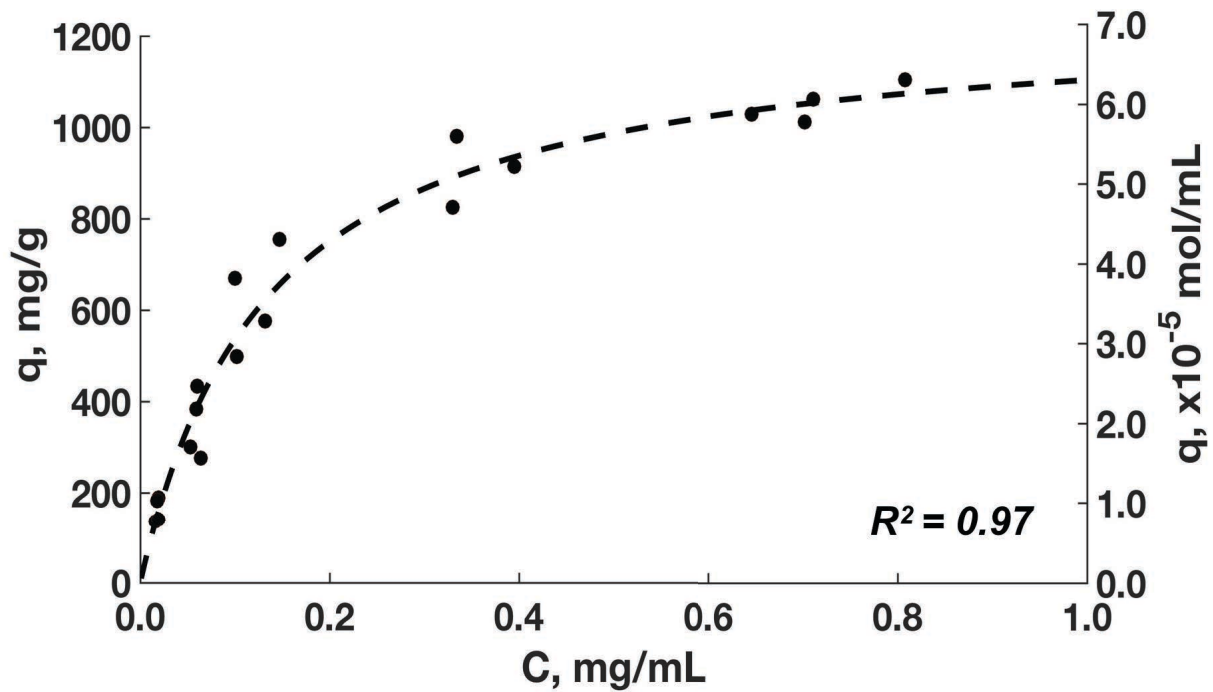


Figure 2.2. Adsorption experimental data fit to a Langmuir isotherm model (Eq. 2.3). The conversion from mg/g (left) to mol/mL (right) assumes ideal 13 nm diameter pores.

Table 2.1. FEM Fixed Parameters

Parameter	Value
C_0	1.43×10^{-7} mol/mL
D_0	1.27×10^{-6} cm ² /s
k_m	4.81×10^{-3} cm/s
* K_L	7.85×10^7 cm ³ /mol
* q_{max}	7.16×10^{-5} mol/mL
R	1.54×10^{-7} cm
R_{p_0}	6.50×10^{-7} cm
T	293 K

* Converted to appropriate units from equilibrium adsorption isotherm parameters assuming ideal 13 nm cylindrical pores.

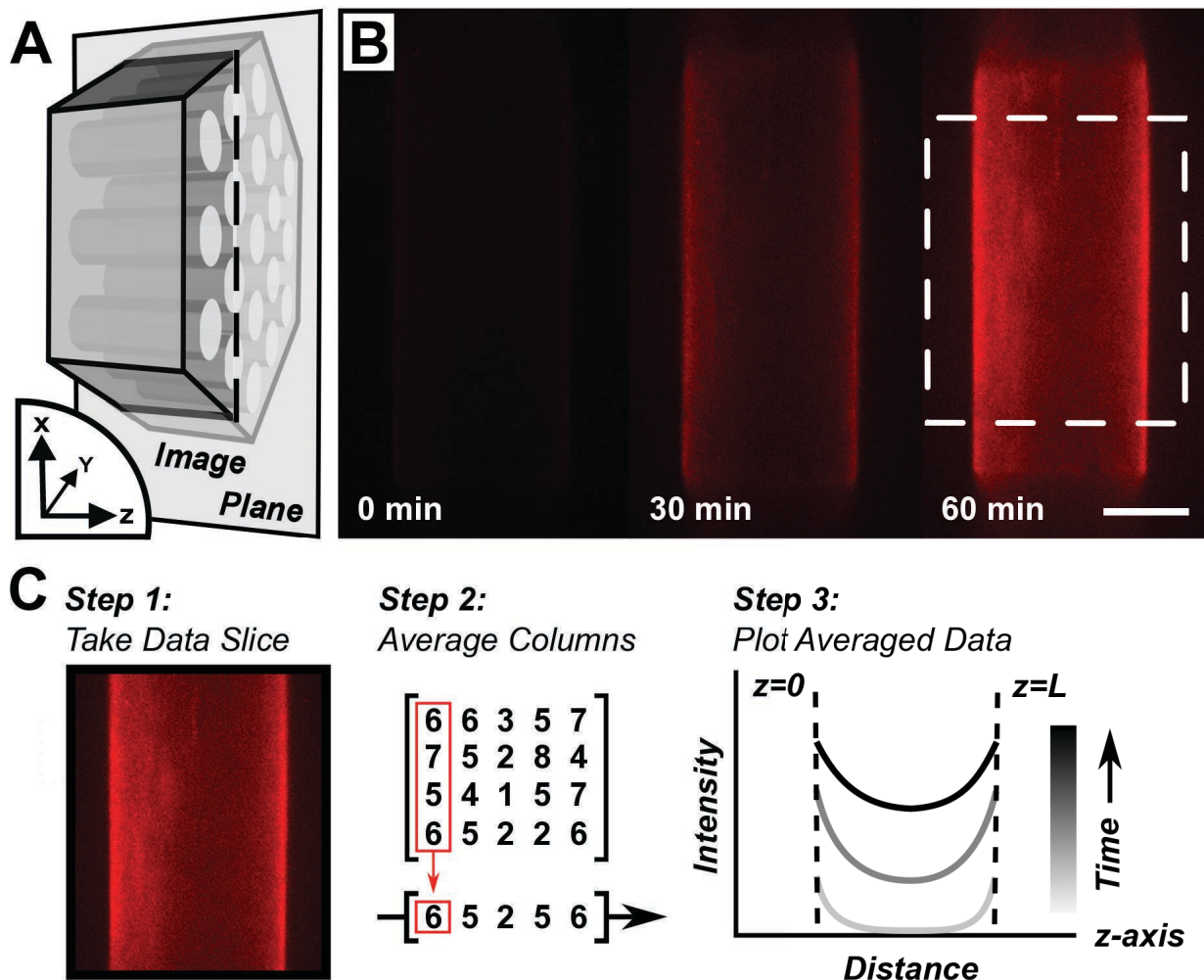


Figure 2.3. (A) Schematic depicting orientation of the confocal image plane with respect to the crystal axes (not to scale). (B.) Representative images of fluorescent $\text{Au}_{25}(\text{GSH})_{18}$ nanoclusters diffusing along the z-axis into an initially non-fluorescent CJ-LPC scaffold over the course of 1 hour; *Scale bar:* 40 μm ; *Dashed box:* 150 μm tall data slice. (C.) Schematic depicting the averaging of the columns in the data slice to obtain the processed fluorescence intensity distribution (not to scale), this process is repeated for every time point to generate a complete intensity profile.

Prior to calculating the pore diffusion coefficient, the fluorescence intensity values in Figure 2.4C were converted to units of concentration *via* fluorescence standard (Figure 2.4A-B). In addition, as the infusion from the two halves of the crystal should be symmetric given ideal external $\text{Au}_{25}(\text{GSH})_{18}$ transport, the right and left sides of the concentration profiles were averaged together resulting in a final symmetric distribution (Figure 2.4D). Not only does the $\text{Au}_{25}(\text{GSH})_{18}$ concentration increase with time, but the distribution profile also changes, exhibiting a minimum in the center of the crystal that increases over time. Modest deviations in intrapore guest concentration between crystal replicates and asymmetric loading into the opposing faces of the same crystal may be explained by small differences in the free-solution concentration observed at each surface caused by imperfect external transport (*e.g.* due to irregularities in the agarose gel density)

© 2.5.3 Fit Experimental Data to Hindered Diffusion

The specific kinetic coefficients (k_a and k_d) cannot be directly determined from the Langmuir adsorption equilibrium constant (K_L) obtained from the equilibrium adsorption isotherm. Instead, to decouple the time-lapsed confocal fluorescence signal into diffusive (mobile) and adsorbed (immobile) nanocluster pools and simulate adsorption-coupled diffusion, we used the Langmuir kinetic model combined with a one-dimensional pore diffusion equation (*Eq.* 2.9). To determine these parameters, the adsorption-coupled hindered diffusion model was fit using the sum of squared deviations integrated over time and position for three sets of confocal loading data gathered from three different crystals. The fixed parameters used in the model were either obtained from the adsorption experimental data, DLS measurements, or were calculated based on the known structure of $\text{Au}_{25}(\text{GSH})_{18}$ and CJ-LPC pores; these parameters can be found in Table 2.1.

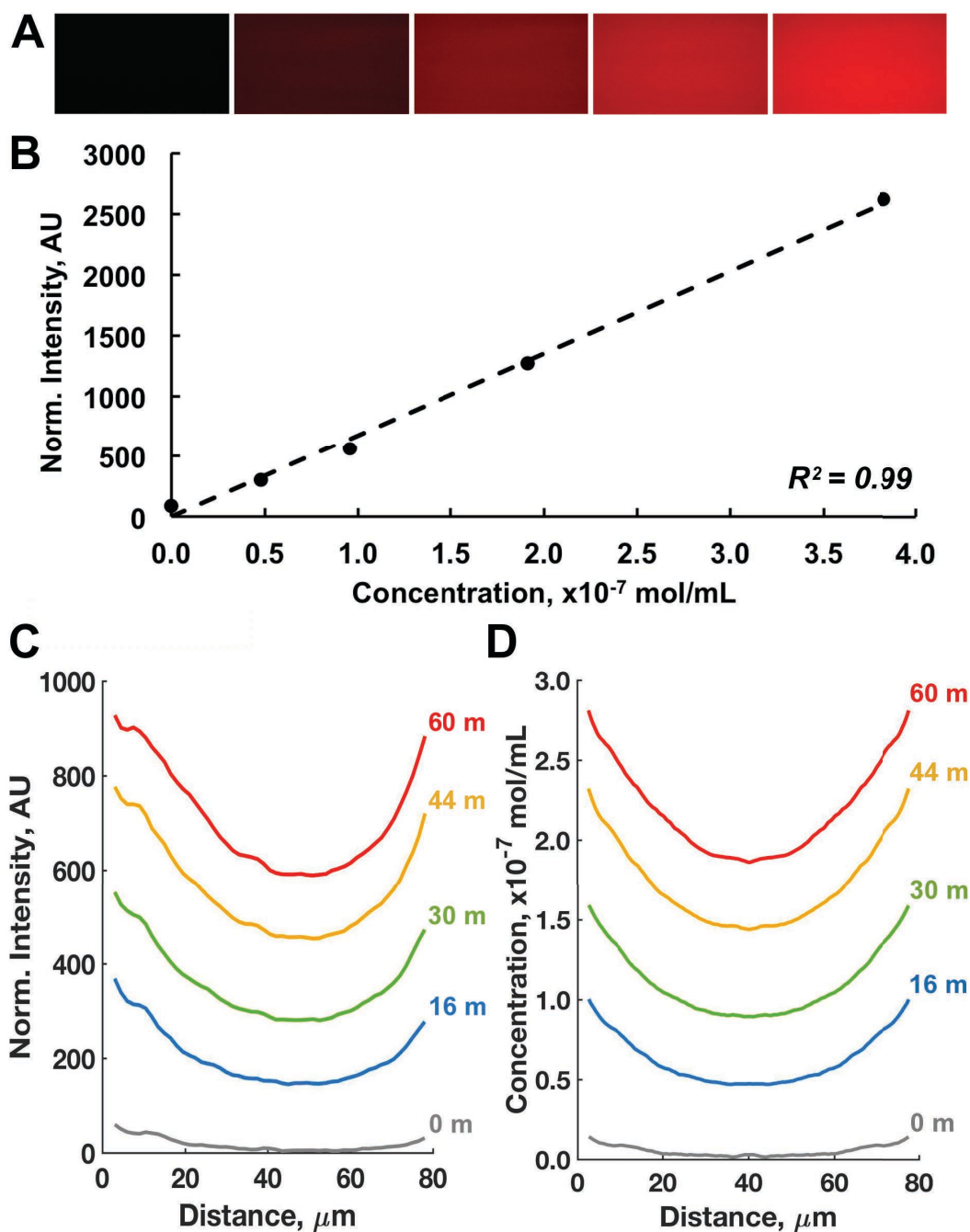


Figure 2.4. (A) Confocal images of $\text{Au}_{25}(\text{GSH})_{18}$ nanocluster concentrations in free-solution: 0.0, 0.5, 1.0, 2.0, and 4.0 mg/mL from left to right. (B.) Fluorescence standard created by averaging fluorescence intensities in A and converting to mol/mL. (C.) Processed loading data plotted as fluorescence intensity distributions at various time points. (D.) Example of symmetric concentration distribution data used to fit the hindered diffusion model; Intensity values from C were averaged across the central axis of symmetry ($z = L/2$), converted to units of concentration *via* the fluorescence standard, and corrected for scaffold-occluded volume by dividing by the CJ-LPC void fraction of 0.476, which assumes unit cells with a volume of 1411.83 nm^3 and a single ideal cylindrical nanopore with a radius of 13.0 nm and height of 5.058 nm.

The values obtained for k_a and k_d were found to be similar for all three crystals (Table 2.2, APPENDIX I Figure I.15). Next, we used the mean k_a and k_d parameters to simulate Au₂₅(GSH)₁₈ nanocluster loading over the course of one hour with external concentration $C_0 = 1.43 \times 10^{-7}$ mol/mL. The resulting simulated concentration profiles combined both the adsorbed (q) and free (C) concentrations and were in good agreement with the experimental observation (Figure 2.5). As transport progresses, the quantity of Au₂₅(GSH)₁₈ adsorbed to the pore wall increases towards an equilibrium maximum adsorbed state. The total amount of Au₂₅(GSH)₁₈ adsorbed at equilibrium is dependent on the free-solution concentration (C_0) as can be seen in the equilibrium adsorption isotherm (Figure 2.2). Furthermore, as adsorption increases the pore diffusion coefficient (D_p) decreases due to pore occlusion. Thus, under higher free solution concentrations, $D_p(q)$ will see greater attenuation. The results of simulating diffusion for 10 days using a high external concentration of 9.56×10^{-7} mol/mL (10 mg/mL) reveals a pore diffusion coefficient at the crystal surface that gradually dropped from 3.7×10^{-7} cm²/s to 3.4×10^{-10} cm²/s (Figure 2.6), which is far lower than the free-solution diffusion coefficient ($D_0 = 1.27 \times 10^{-6}$ cm²/s).

© 2.6 CONCLUSIONS

In summary, the investigation of Au₂₅(GSH)₁₈ nanocluster transport within CJ-LPC pores using confocal microscopy in combination with hindered diffusion simulation and adsorption equilibrium data can significantly advance the comprehension of macromolecular diffusion and adsorption in Large-pore protein crystal materials. The hindered diffusion simulation coincides well with confocal observation enabling kinetic parameters to be ascertained from the equilibrium adsorption data. This approach provides a suitable method to calculate the pore diffusion coefficient under conditions involving adsorption-coupled diffusion whereby the adsorbate constr-

Table 2.2. FEM Fit Parameters

Replicate	k_a (cm ³ /mol · s)	k_d (s ⁻¹)
1	12.9	1.66 x 10 ⁻⁷
2	13.2	1.70 x 10 ⁻⁷
3	12.9	1.66 x 10 ⁻⁷
Mean	13	1.7 x 10 ⁻⁷

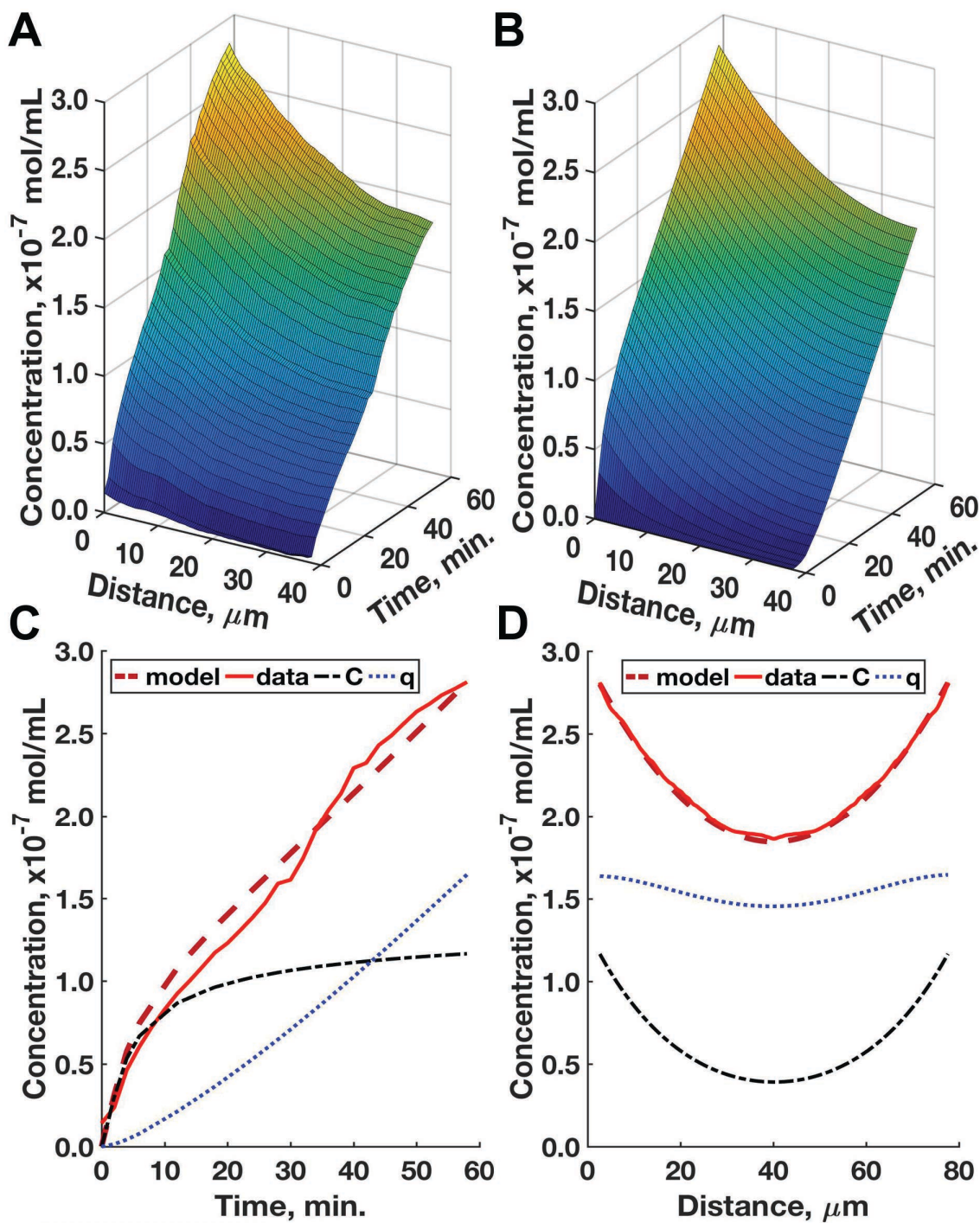


Figure 2.5. (A, B) Concentration, distance, and time surface plots of the left-hand half ($z = 0$ to $z = L/2$) of a 60-minute diffusion profile showing confocal data and FEM simulated data, respectively. (C.) Comparison of FEM data and experimental confocal data taken just inside the crystal at the surface ($z = 0$) over 60-minutes, the model line represents the sum of C and q . (D.) Comparison of FEM data and experimental confocal data taken at the 60-minute time point over the entire crystal ($z = 0$ to $z = L$).

icts the pore causing an increase in hindrance effects which attenuate the pore diffusivity. We see a decrease in the pore diffusion coefficient over time as more nanoclusters adsorb and occlude the crystal pores thus hindering diffusion. This effect is maximized at higher free-solution concentrations that lead to a higher adsorbed state within the pores. These finding will benefit downstream efforts to better engineer large-pore protein crystal based nanoporous materials to serve as new and unique tools in bionanotechnology.

© 2.7 RECOGNITION

The authors would like to recognize Thaddaus R. Huber for graciously providing advanced access to protein materials and crosslinking protocols used in this study and others^{79,80} Mark W. Lunt for contributions to the FEM diffusion model, and Ann Kowalski for coordinating with the Ackerson group in the procurement of gold nanoclusters. This research was supported in part by the CSU Microscope Imaging Network Foundational Core facility.

© 2.8 TERM DEFINITIONS

- C : Mobile phase concentration in pore (mol/mL)
- C_0 : Concentration in surrounding solution (mol/mL)
- C_{0e} : Effective concentration at the surface (mol/mL)
- D_e : Effective diffusion coefficient (cm²/s)
- D_p : Pore diffusion coefficient (cm²/s)
- D_0 : Diffusion coefficient in free-solution (cm²/s)
- G° : Standard Gibbs free energy (kJ/mol)
- k_a : Adsorption coefficient (cm³/mol · s)
- k_d : Desorption coefficient (s⁻¹)
- k_m : External mass transfer coefficient (cm/s)
- k_B : Boltzmann's constant (1.3806 x 10⁻¹⁶ cm² g/s² · K)
- K_L : Langmuir adsorption equilibrium coefficient
- L : Pore length (cm)
- N_A : Avogadro's number (6.022 x 10²³ mol⁻¹)
- q : Adsorbed concentration (mol/mL)
- q_{max} : Maximum adsorbed concentration

- R_p : Effective pore radius (cm)
 R_{p_0} : Initial pore radius (cm)
 R : Au₂₅(GSH)₁₈ molecular radius (cm)
 T : Adsorption temperature (K)
 W_G : Au₂₅(GSH)₁₈ molecular weight (10456 g/mol)
 λ : Ratio of Au₂₅(GSH)₁₈ and pore diameter (R_g/R_{p_0})
 η : Solution viscosity (g/cm · s)

CHAPTER 3

CHARACTERIZING THE CYTOTOXICITY OF VARIOUS CROSS-LINKING CHEMISTRIES FOR THE PRODUCTION OF BIOSTABLE LARGE-PORE PROTEIN CRYSTAL MATERIALS³

◎ 3.1 SUMMARY

With rapidly growing interest in therapeutic macromolecules, targeted drug delivery, and *in vivo* biosensing comes the need for new nanostructured biomaterials capable of macromolecule storage and metered release that exhibit robust stability and cytocompatibility. One novel possibility for such a material are engineered large-pore protein crystals (LPCs). Here, various chemically-stabilized LPC derived biomaterials were generated using three cross-linking agents: glutaraldehyde, oxaldehyde, and 1-Ethyl-3-(3-dimethylaminopropyl)carbodiimide. LPC biostability and *in vitro* mammalian cytocompatibility was subsequently evaluated and compared to similarly cross-linked tetragonal hen egg white lysozyme crystals. This study demonstrates the ability of various cross-linking chemistries to physically stabilize the molecular structure of LPC materials—increasing their tolerance to challenging conditions while exhibiting minimal cytotoxicity. This approach produces LPC derived biomaterials with promising utility for diverse applications in biotechnology and nanomedicine.

³ The work in this chapter was published in 2018 in ACS Biomaterials Science and Engineering. C.D.S., S.P.J., H.T.B. and I conceived of the experiments. C.D.S. and I wrote the manuscript. I expressed and purified the protein, and performed XRD, SEM, endotoxin and nitrite analyses. D.A.A. and I grew and cross-linked the crystals aided by methods developed by T.R.H. H.T.B. and I maintained the cell cultures and performed the LDH assay, live/dead staining, and all microscopy imaging.

L. F. Hartje, H. T. Bui, D. A. Andales, S. P. James, T. R. Huber and C. D. Snow. Characterizing the Cytocompatibility of Various Cross-Linking Chemistries for the Production of Biostable Large-Pore Protein Crystal Materials. *ACS Biomater. Sci. Eng.*, 2018, 4, 826–831.

◎ 3.2 INTRODUCTION

Protein crystals, typically evaluated solely for the elucidation of three-dimensional protein structure through X-ray diffraction, have unique chemical and material qualities—most notably, their self-assembling, homochiral, highly-ordered nanoporous structure. Intriguingly, the chemical properties of protein crystal materials can be readily engineered through genetic or chemical modification of their monomeric protein constituents. A common example of protein crystal modification involves the introduction of covalent bonds between adjacent monomers using bifunctional reagents.¹⁶ This chemical cross-linking has been shown to greatly improve overall crystal stability,^{15,17} thereby broadening the potential for protein crystals to be used in diverse material applications.²⁶

One distinct advantage of protein crystals over chemically synthesized nanoporous scaffolds, such as zeolites and metal organic frameworks, is their biological origin; biologically derived nanoporous materials have been recognized as attractive scaffolds for applications in which biodegradability and/or biocompatibility is preferred. Some of these applications include: drug delivery,^{81,169} vaccinations,⁹⁹ environmental remediation,¹⁹² and biosensing.^{146–148} However, stabilizing biologically derived materials with chemical cross-linkers can lead to increases in cytotoxicity.^{31,38,193} Despite this risk, we are unaware of any studies that have quantified the cytotoxicity and stability of various chemically cross-linked protein crystal materials. Therefore, the extent of any toxic effects the cross-linking process may impart to protein crystal materials is unclear, nor is it clear whether the nanostructure of these biomaterials can survive in contact with living cells or tissues.

To demonstrate the feasibility of utilizing chemically-stabilized protein crystal materials in biological and environmental applications in which both toxicity and material stability is a

concern, we investigated the efficacy of various cross-linking reagents to stabilize the molecular structure of two distinct protein crystal variants while minimizing cytotoxicity. The first crystal variant used in this study is a large-pore protein crystal (LPC) composed of CJ monomers (Figure 3.1A & 3.1C).

CJ is a modified form of a putative periplasmic isoprenoid binding protein derived from *Campylobacter jejuni*. Our lab has shown that CJ derived large-pore protein crystals (CJ-LPCs) have properties uniquely suited for programmable organization of macromolecular guests at distinct sites within hundreds of millions of precisely defined pores.^{50,79,80} The combination of high theoretical capacity for guest macromolecules and the mechanical strength of a cross-linked honeycomb lattice make CJ-LPCs attractive molecular depots for use in various biomedical and environmental applications. As a point of comparison, the second crystal variant studied was tetragonal hen egg white lysozyme (HEWL), which represents a more comprehensively studied protein crystal system with archetypal pore sizes (Figure 3.1B & 3.1D).

◎ 3.3 RESULTS AND DISCUSSION

Large (100–500 μm diameter) CJ-LPCs were grown by sitting drop vapor diffusion at 20° C in 3.3–3.6 M $(\text{NH}_4)_2\text{SO}_4$, 100 mM bis-tris at pH 7.0 (Figure 3.1C). Tetragonal HEWL crystals were grown per a modified version of a previously described batch crystallization protocol¹⁹⁴ (Figure 3.1D). Prior to cross-linking, crystals were washed in buffered high-salt solutions to remove residual protein monomers without compromising the integrity of the crystal. Washed crystals were then cross-linked using one of three chemical cross-linkers: 1-Ethyl-3-(3-dimethylaminopropyl)carbodiimide (EDC), glutaraldehyde (GA), or oxaldehyde (OA) to introduce covalent attachments between adjacent monomers, thereby generating various chemically stabilized protein crystal materials. In all cases, cross-linking was performed in solut-

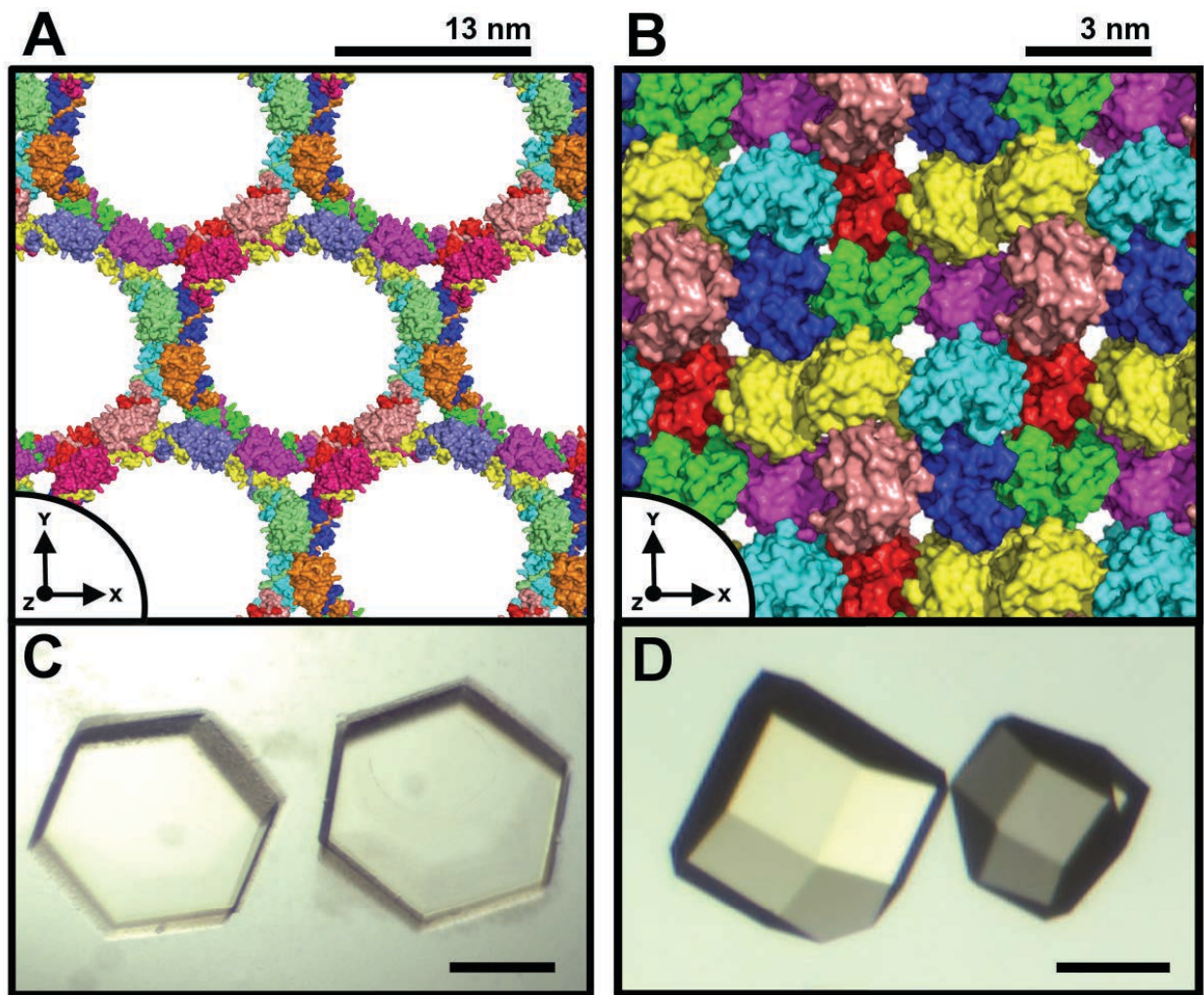


Figure 3.1. (A) CJ-LPC crystal lattice (PDB Code: 5W17) showing large (13 nm) pores. (B) Tetragonal HEWL crystal lattice (PDB Code: 2HTX) showing much smaller and more typical pore sizes (<2 nm). (C) CJ-LPCs in growth well. *Scale bar:* 200 μm. (D) HEWL crystals in growth well. *Scale bar:* 100 μm.

ions intended to mimic the mother liquor to mitigate crystal degradation. Protein expression, purification, crystallization, and cross-linking are described in more detail in APPENDIX II.

The efficacy of various cross-linking chemistries in stabilizing protein crystals on a macroscopic level was investigated using stereomicroscopy. Images were taken of crystals in high-salt conditions directly after cross-linking (*pre-incubation*) and again after 24-hour incubation with adult human dermal fibroblast (HDFa) cells at 37° C (*post-incubation*). Pre-incubation images of cross-linked CJ-LPC materials (CJ/GA, CJ/OA, CJ/EDC) demonstrate similar macroscopic crystal quality as the washed non-cross-linked CJ-LPCs (CJ/NCL) (Figure 3.2A *pre-incubation*), thus indicating these cross-linking methods do not overtly lead to CJ-LPC deterioration. As expected, the comparatively low salt and high temperature environment associated with HDFa cell culture caused CJ/NCL crystals to completely dissolve within 24-hours. Conversely, all chemically stabilized CJ-LPCs continued to show no loss of crystal quality despite being transferred away from their high-salt crystallization environment (Figure 3.2A *post-incubation*). Therefore, all three cross-linking chemistries are shown to be independently sufficient and necessary to preserve the short-term macroscopic structure of CJ-LPCs in the presence of living cells. Complementary images of cross-linked HEWL crystals taken prior to incubation with HDFa cells reveal HEWL/GA crystals to have similar quality as the washed HEWL/NCL crystals; however, images of HEWL/OA and HEWL/EDC crystals show moderate to severe surface deformation and cracking (Figure 3.2B *pre-incubation*). Post-incubation images of HEWL/GA crystals continue to evince no loss of crystal quality while images of HEWL/OA reveal increased cracking and severe crystal deterioration—HEWL/EDC and HEWL/NCL crystals completely dissolved (Figure 3.2B *post-incubation*). These results suggest that the cross-linking methods for HEWL/EDC and

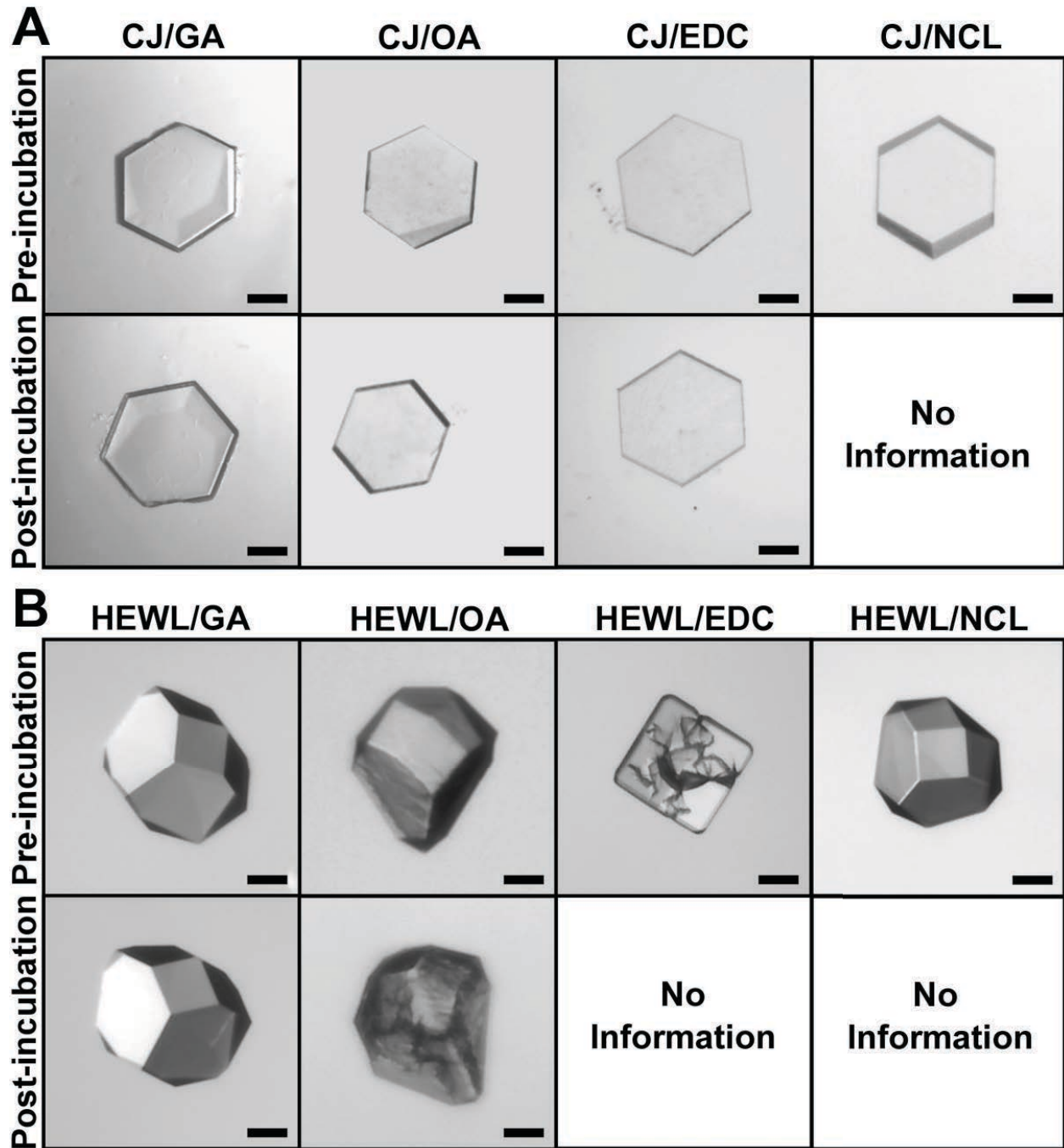


Figure 3.2. Microscopy images of protein crystals taken both before (*pre-incubation*) and after (*post-incubation*) 24-hour incubation with HDFa cells. (A) CJ-LPCs; *Scale bar*: 100 μm . (B) HEWL crystals; *Scale bar*: 50 μm . Note: ‘No Information’ indicates the crystals dissolved during incubation.

HEWL/OA were not sufficient to stabilize the macroscopic structure of tetragonal HEWL, resulting in severe crystal degradation and/or disintegration.

To further examine cross-linked crystal stability, the molecular order of sufficiently cross-linked protein crystal materials (CJ/GA, CJ/OA, CJ/EDC, HEWL/GA) was analyzed both pre- and post-incubation with HDFa cells by X-ray diffraction (XRD) on a Rigaku HomeLab (Figure 3.3). Pre-incubation CJ/OA and CJ/EDC crystals achieved diffraction out to approximately 3.7 and 3.1 Å respectively, which is comparable to the washed pre-incubation CJ/NCL crystal diffraction of 3.0 Å. Intriguingly however, while GA cross-linking did not overtly disrupt CJ-LPC crystal quality when observed on a macroscopic level *via* stereomicroscopy, it did disrupt the molecular order as observed by XRD; GA cross-linked CJ-LPCs demonstrated markedly reduced pre-incubation molecular order—to the point that the XRD data could not be comparatively indexed and scaled. These results indicate the molecular order of CJ/OA and CJ/EDC crystals was maintained throughout the cross-linking method, while GA cross-linked crystals became more disordered. Conversely, GA was the only cross-linking agent capable of stabilizing tetragonal HEWL crystals, both on a macroscopic level, as seen by stereomicroscopy, and on a molecular level, yielding a post-cross-linking diffraction resolution of 2.0 Å.

To monitor short-term stability differences, the same cross-linked crystals were subsequently subjected to HDFa cell culture for 24 hours after which the post-incubation retention of molecular order was measured again using XRD. All cross-linked CJ-LPCs as well as the HEWL/GA crystals exhibited post-incubation resolution comparable to their respective pre-incubation resolution estimates (Figure 3.3 *Table*)—suggesting these cross-linked protein crystal materials can retain their molecular order in environments well outside their crystallization condition and in the presence of HDFa cells.

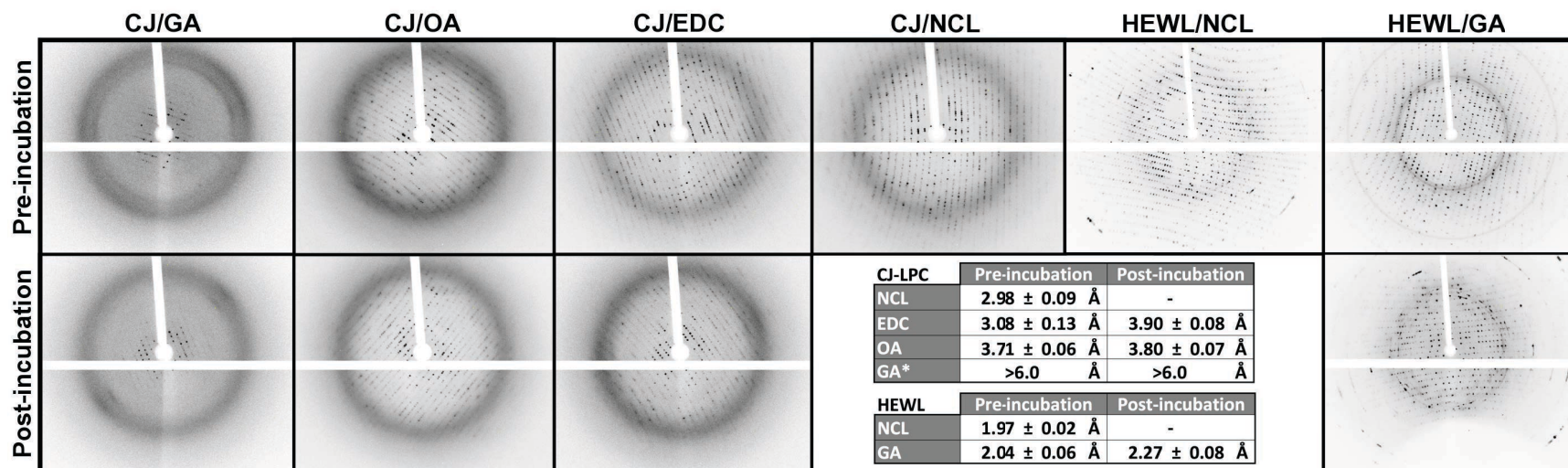


Figure 3.3. Representative XRD diffraction patterns both pre- and post-incubation with HDF cells. *Tables:* High-resolution estimates for each diffraction set. See APPENDIX II for XRD replicate data and resolution estimate details. *Note:* there is no resolution estimate for post-incubation NCL crystals due to the crystals dissolving when transferred outside their respective crystallization conditions. *The high-resolution estimate ($>6.0 \text{ \AA}$) for CJ/GA crystals is a qualitative estimate based on observable spots—the reflection data could not be comparatively indexed and scaled due to poor diffraction.

Potential cytotoxic effects from GA, OA, or EDC cross-linking was investigated by measuring the viability of HDFa and human macrophage (MV-4-11) cells when subjected to cross-linked protein crystal materials. Prior to cross-linking and incubation with human cells, large CJ-LPCs and HEWL crystals were first fragmented by sonication to increase their surface area and thereby maximize the potential cytotoxic response¹⁹⁵ (APPENDIX II). The particle size distribution of fragmented CJ-LPCs was observed *via* scanning electron microscopy (SEM). SEM images were processed using image stitching and particle detection packages in Fiji^{196,197} and quantified *via* histogram plotting tools in MATLAB version 9.1.0 (Natick, MA). The mean particle size was found to be $5.8 \pm 3.9 \mu\text{m}$ with a mode of about $3.3 \mu\text{m}$ (APPENDIX II Figure II.1).

To prepare for incubation with HDFa cell culture, cross-linked fragmented protein crystal materials were sterilized in high-salt buffers containing 20% ethanol, washed in sterile PBS pH 7.5, and transferred to sterile supplemented cell culture medium (APPENDIX II). HDFa cells were plated at a density of 150,000 cells/mL within a 96 well plate and allowed to adhere for 24 hours. After the initial 24-hour period, the old medium was evacuated and replaced with new supplemented medium containing the various fragmented protein crystal materials in a range of concentrations (1, 50, 100, 200, and 400 $\mu\text{g/mL}$) determined by Bradford assay. Cells were incubated in the presence of protein crystal materials for an additional 24 hours, after which, cell viability was measured using the PierceTM lactate dehydrogenase (LDH) cytotoxicity assay kit (Figure 3.4A & 3.4B). While HEWL/NCL sample wells maintained very high cell viability across all concentrations, HEWL/GA materials prompted a precipitous decline in cell viability corresponding to increasing material concentration—suggesting a toxic response to GA. Similarly, CJ/GA materials also triggered a dramatic decrease in cell viability corresponding to increasing material concentration. Conversely, CJ/OA, CJ/EDC, and CJ/NCL materials preserved cell viabil-

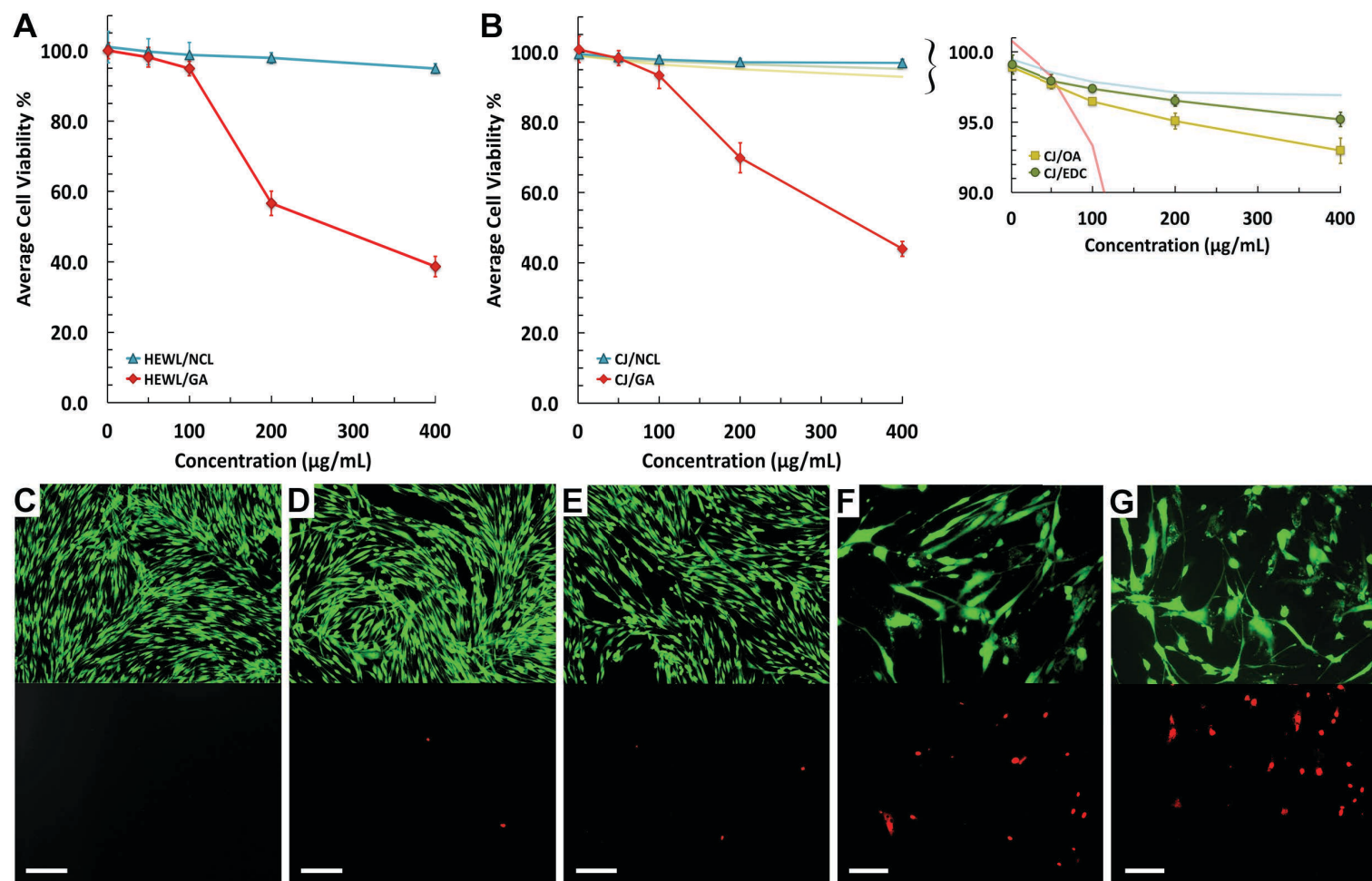


Figure 3.4. (A) HDFa cell viability under varying concentrations of fragmented HEWL protein crystal materials; *Error Bars*: standard deviation, $n=3$. (B) HDFa cell viability under varying concentrations of fragmented CJ-LPC materials; *Error Bars*: standard deviation, $n=3$. (C) Control HDFa cells with no material added to the medium; *Scale Bar*: 300 μm ; *Top*: green fluorescent live cell stain (calcein); *Bottom*: red fluorescent dead cell stain (ethidium homodimer). (D) HDFa cells incubated with 400 $\mu\text{g/mL}$ CJ/EDC; *Scale Bar*: 300 μm . (E) HDFa cells incubated with 400 $\mu\text{g/mL}$ CJ/OA; *Scale Bar*: 300 μm . (F) HDFa cells incubated with 400 $\mu\text{g/mL}$ CJ/GA; *Scale Bar*: 100 μm . (G) HDFa cells incubated with 400 $\mu\text{g/mL}$ HEWL/GA; *Scale Bar*: 100 μm .

ity despite high material concentrations (up to 400 $\mu\text{g}/\text{mL}$). We suspect the slightly diminished viability seen in CJ/NCL sample wells compared to HEWL/NCL samples is due to trace quantities of endotoxin, which is progressively removed during CJ-LPC material purification, crystallization, and subsequent wash steps (APPENDIX II Figure II.3). The more pronounced reduction in cell viability for GA cross-linked crystals can likely be attributed to unreacted GA that has leached from the crystals into the growth medium.

The HDFa viability quantified by LDH activity was qualitatively confirmed by live/dead staining (Figure 3.4C-3.4G); calcein (green) was used as the live cell stain while dead cells were visualized using ethidium homodimer (red). Control cells, not subjected to any materials, were compared to cells incubated with 400 $\mu\text{g}/\text{mL}$ of various cross-linked protein crystal materials. The cell counts for control cells as well as cells incubated with CJ/EDC and CJ/OA crystals show minimal cell death, while cells incubated with CJ/GA and HEWL/GA materials appear to suffer approximately 50% cell death. These images agree with quantitative data from the LDH assay—indicating minimal loss of cell viability for EDC and OA cross-linked protein crystal materials and a much higher loss of viability for protein crystal materials cross-linked by GA. More details concerning the LDH, endotoxin, and live/dead staining assays can be found in APPENDIX II.

To prepare for incubation with MV-4-11 cell culture, cross-linked fragmented protein crystal materials were sterilized in high-salt buffers containing 20% ethanol, washed in sterile PBS pH 7.5, and transferred to sterile double deionized water (APPENDIX II). Fragmented crystal materials were transferred to an empty 96-well plate at a concentration of 400 $\mu\text{g}/\text{mL}$ and allowed to dry overnight. MV-4-11 cell suspension was then added to the dried material at a density of 150,000 cells/mL. Cells were then incubated in the presence of the fragmented protein crystal materials for 24 hours, after which the cell viability (Figure 3.5A) and nitrite concentration was

determined (Figure 3.5B). The viability trend for MV-4-11 cultures is commensurate to HDFa cells, showing high viability for both NCL crystals as well as OA and EDC cross-linked protein crystal materials, while both CJ/GA and HEWL/GA materials engendered low cell viability. All samples tested demonstrated low nitrite concentration relative to the negative control (cells only), indicating these materials do not appear to promote human macrophage activation.

◎ 3.4 CONCLUSIONS

A priori it was not known if chemically modifying CJ-LPC interfaces would substantially degrade diffraction quality. While GA, the cross-linking agent primarily used to stabilize protein crystals, generated robust CJ-LPCs on a macroscopic level when tested against HDFa cell culture, it exhibited the greatest initial loss in molecular order upon cross-linking. Migneault *et al.* details the complex solution properties of GA and lists 13 proposed forms ranging from monomeric to highly polymerized.²⁸ Thus, in this case, the heterogeneous nature of GA is likely at odds with preserving molecular order at the lysine rich interfaces of CJ-LPCs. Surprisingly, the seldom used cross-linkers, OA and EDC, generated CJ-LPC materials capable of retaining molecular order post-incubation while suffering minimal loss of diffraction upon cross-linking.

Conversely, cross-linking tetragonal HEWL with GA was shown to be effective at both stabilizing the crystal and preserving diffraction quality; these results support previous findings.²⁹ To date, neither OA nor EDC has been effective at stabilizing HEWL crystals. This is not surprising considering the small number of amines at HEWL crystal interfaces as well as a lack of proximal amine to carboxylic acid pairs at crystal interfaces. OA is the shortest dialdehyde and primarily monomeric, which may limit its ability to be effective.¹⁹⁸ In this case, the ability to polymerize may enable GA to sufficiently cross-link HEWL crystals.

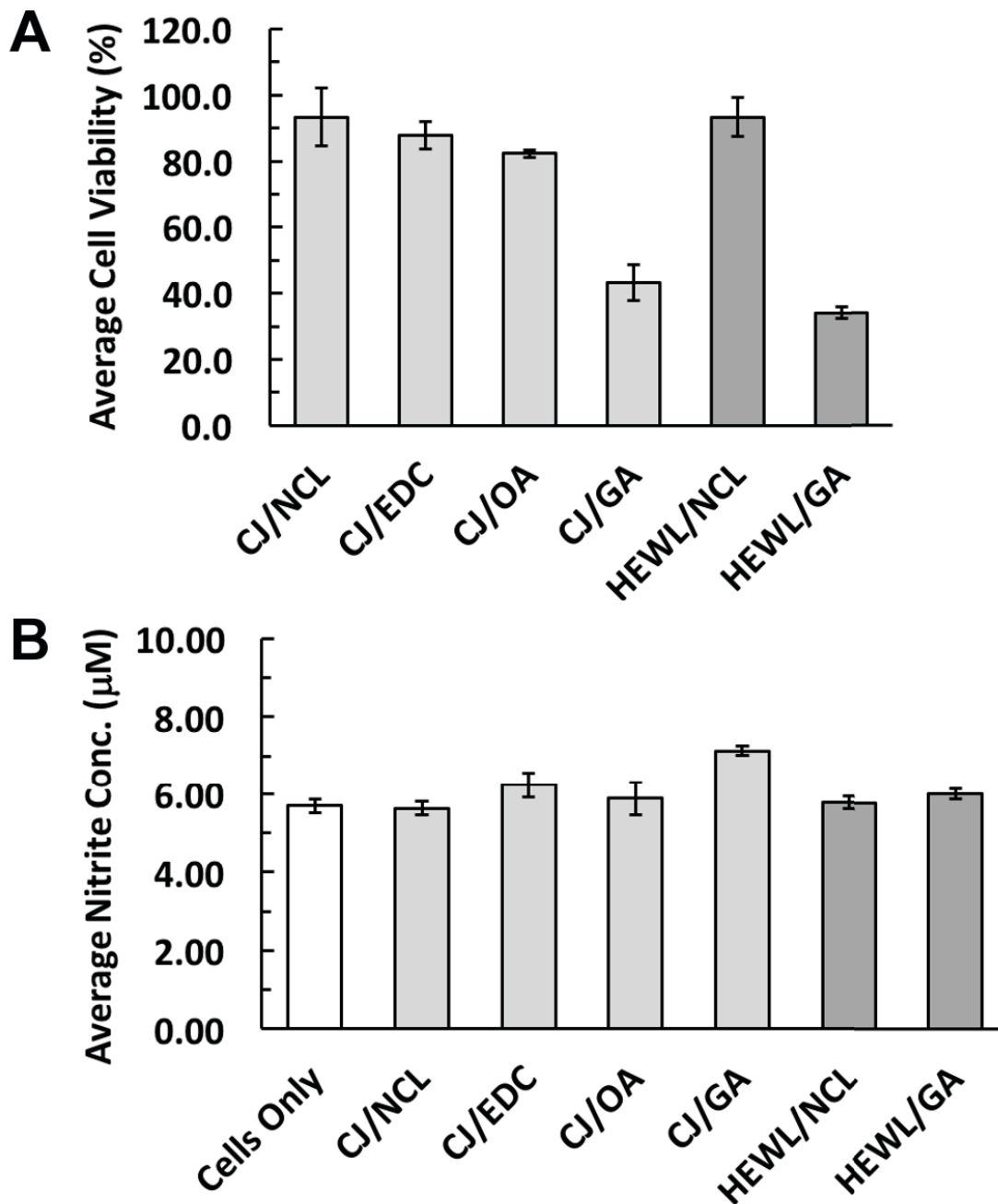


Figure 3.5. (A) MV-4-11 cell viability when incubated with various protein crystal materials at a concentration of 400 µg/mL; *Error Bars*: standard deviation, n=3. (B) Nitrite concentration released from MV-4-11 cells incubated with 400 µg/mL of various protein crystal materials.; *Error Bars*: standard deviation, n=3.

The results of the stability and toxicity tests suggest that both OA and EDC cross-linked CJ-LPC materials are superior to protein crystals cross-linked by GA, demonstrating both promising molecular stability and cytocompatibility when tested in the short-term against HDFa and MV-4-11 cells. These materials may be particularly well suited for use in biocatalysis, drug delivery, biosensing, and environmental remediation. Further genotoxicity, and immunogenicity studies should be done to determine long-term biocompatibility toward a more diverse set of tissue types. By pursuing this research, we hope to better understand protein crystal materials and leverage that knowledge to design advanced nanostructured devices for applications in biotechnology and nanomedicine.

© 3.5 RECOGNITION

The authors would like to thank Morgan Hawker for her aid in SEM training, Aidan Friederich for assistance with the LDH cytotoxicity assay, and finally Matt Kipper, Ellen Fisher, and Ketul Popat for thoughtful discussion. This research was supported in part by the Compatible Polymer Network project funded by the Colorado State University Office of the Vice President for Research and by the National Science Foundation grant number 1506219. The authors declare no competing financial interest.

CHAPTER 4

TEXTILE FUNCTIONALIZATION BY POROUS PROTEIN CRYSTAL CONJUGATION AND GUEST MOLECULE LOADING⁴

◎ 4.1 SUMMARY

Protein crystals are versatile nanostructured materials that can be readily engineered for applications in nanomedicine and nanobiotechnology. Despite their versatility, the minute size of individual protein crystals presents challenges for macroscale applications. One way to overcome this limitation is by immobilizing protein crystals onto larger substrates. Cotton is composed primarily of cellulose, the most common natural fiber in the world, and is routinely used in numerous material applications including textiles, explosives, paper, and bookbinding. Here, HEWL and CJ protein crystals were conjugated to the cellulosic substrate of cotton fabric using a 1,1'-carbonyldiimidazole/aldehyde mediated coupling protocol. The efficacy of this attachment was assessed *via* accelerated laundering and quantified by fluorescence imaging. The ability to load guest molecules of varying sizes into the scaffold structure of the conjugated protein crystals was also assessed. This work demonstrates the potential to create multifunctional textiles by incorporating diverse protein crystal scaffolds which can be infused with a multiplicity of useful guest molecules.

⁴ The work in this chapter is formatted for an *ACS journal*. C.D.S., L.B.J., and I conceived of the experiments. C.D.S., D.A.A., and I wrote the manuscript. D.A.A. and I performed all of the experiments and I processed the data. L.P.G performed preliminary experiments.

Hartje L.F., Andales D.A., Gintner L.P., Johnson L.B., Li Y.V., Snow C.D. Textile Functionalization by Porous Protein Crystals Conjugation and Guest Molecule Loading. Formatted for submission.

◎ 4.2 INTRODUCTION

Protein crystal materials are alternative porous scaffolds to traditional non-biological nanoporous materials such as zeolites or metal organic frameworks (MOFs). Efforts to characterize protein crystals have led to advancements in crystal production, stabilization, and design—increasing their appeal for material applications. Protein crystal materials are attractive for many reasons: they are self-assembling, exhibit a highly ordered porous structure, have been shown to be biodegradable and biocompatible,^{32,109} and can be engineered with relative ease through genetic modification or chemical conjugation. Protein crystal materials have been utilized in a variety of disciplines for various applications ranging from biocatalysis^{15,120–128} and chromatography^{4,199,157–160} to drug delivery^{81,114,108,39} and biosensing.^{146–148,155} Here, we propose implementing protein crystals as tunable porous scaffolds for the organization and containment of diverse functional guest molecules in the interest of producing multifunctional textile materials.

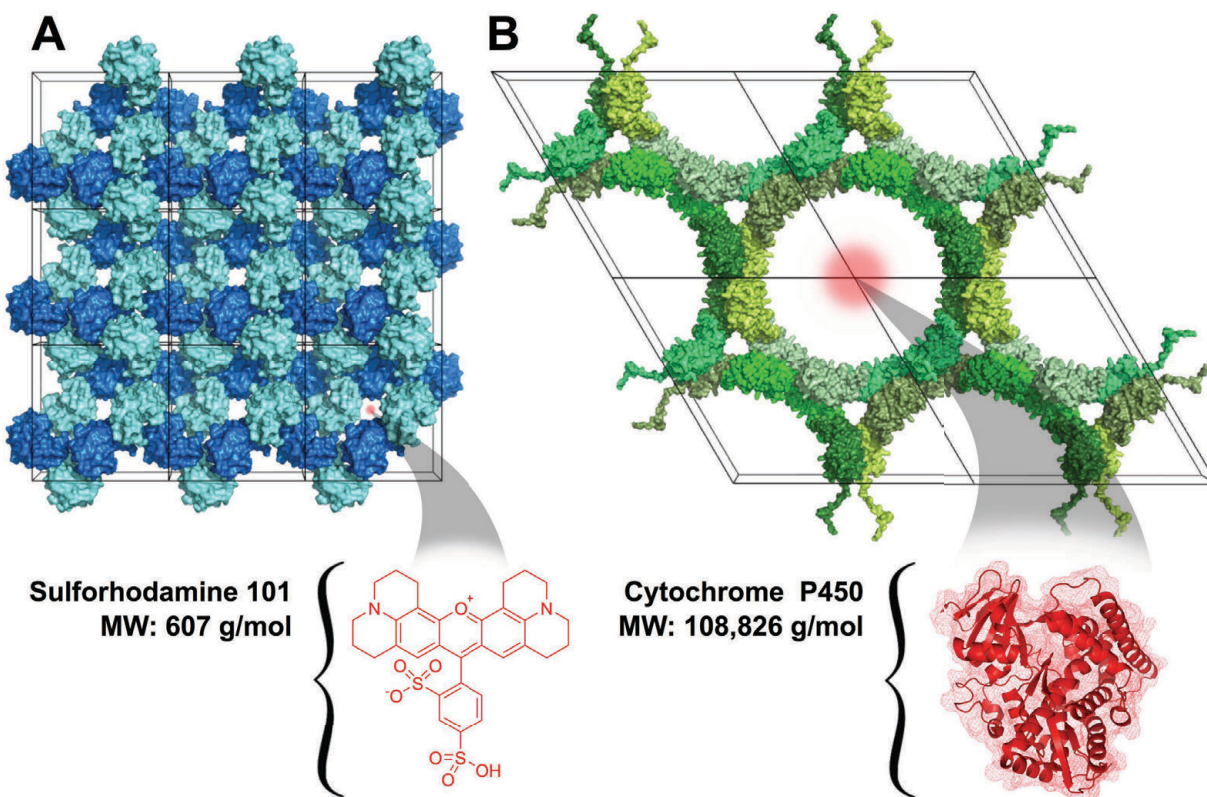
A typical protein crystal contains uniform solvent-filled channels ranging from 30 to 60% of the total crystal volume.³ These pores can be employed as a reservoir for guest molecules of assorted size and functionality, including various small molecules, enzymes, therapeutic proteins and DNA, as well as nanoparticles and organometallic compounds. Despite their remarkable qualities, usage of protein crystals in conventional macroscale material science applications is limited due to their small size (commonly <1 mm). This limitation may be overcome by devising methods for integrating protein crystals into larger host materials. Textiles are inexpensive and widely used across many industries, making them attractive host materials for protein crystal bioconjugation. By conjugating crystals to textiles, a multifunctional macroscale nanoporous scaffold material can be realized.

We investigated two distinct protein crystal variants each with dramatically different pore size distributions, geometries, and luminal environments. The first crystal variant tested was tetragonal hen egg white lysozyme (HEWL), a relatively inexpensive and well characterized protein (Figure 4.1A). Cvetkovic et al. determined that the pores of cross-linked tetragonal HEWL crystals accept small molecule guests with molecular weights below 1,000 g/mol.⁴⁷⁻⁴⁹ In contrast, CJ protein crystals, our second crystal variant, are a member of the large-pore protein crystal (LPC) class—possessing axial pores measuring 13 nm in diameter which enables the accommodation of macromolecular guests (Figure 4.1B). Typical CJ derived large-pore protein crystals (CJ-LPCs) possess hundreds of millions of pores and can be engineered with capture sites within the lumen for the purpose of organizing macromolecular guests at distinct sites.^{50,79,80,5} The combination of high theoretical capacity for guest molecules and the mechanical strength of cross-linking make porous protein crystals attractive molecular depots for use in multifunctional macroscale nanoporous scaffold materials.

© 4.3 RESULTS AND DISCUSSION

To demonstrate the feasibility of attaching protein crystals to textiles *via* chemical conjugation, we first investigated the retention properties of two conjugation strategies designed to link primary amine groups on HEWL crystals to cellulose fibers within 100% cotton fabric. Small (10 – 100 μm diameter) tetragonal HEWL crystals were grown per a modified version of a previously described batch crystallization protocol.¹⁹⁴ Prior to cross-linking, crystals were washed in buffered high-salt solutions to remove residual protein monomers without compromising the integrity of the crystals.

Washed crystals were then stabilized *via* cross-linking by direct addition of glutaraldehyde (GA), which covalently links primary amine groups on adjacent protein monomers within the crystal



scaffold. To reintroduce amines to the crystal surface, GA cross-linking intermediates were quenched with carbohydrazide. Finally, crystals were trace labeled with NHS-fluorescein. Refer to APPENDIX III for more details concerning HEWL crystallization and cross-linking.

Fabric activation was achieved by introducing carboxylic acid groups onto cellulose fibers within the cotton fabric using a sodium hypophosphite and citric acid (CA) treatment adapted from previous methods developed by Edwards *et al.*^{34,35} (Figure 4.2A). Oxidized cotton was then incubated with 1,1'-carbonyldiimidazole (CDI) in a non-aqueous environment as detailed by Hermanson;¹⁹ this process formed an intermediate allowing for direct chemical attachment of amine containing substituents to the textile surface. From this CDI intermediate, short-length attachment (CDI-only) was achieved by direct addition of protein crystals to the textile (Figure 4.2B). Alternatively, to form a somewhat extended molecular interface for crystal attachment, CDI-intermediate textile was treated with adipic acid dihydrazide (AAD). Long-length attachment (CDI+AAD+GA) to the textile was therefore achieved by cross-linking the primary amine from the AAD treated textile to the protein crystal using GA (Figure 4.2C). Fabric treatment, and HEWL attachment protocols are described in more detail in APPENDIX III

The effectiveness of the CDI-only and CDI+AAD+GA conjugation schemes was assessed using an accelerated laundering protocol based on the American Association of Textile Chemists and Colorists (AATCC) Test Method 61 section 1A.²⁰⁰ Standard 1"x1" cotton test fabric swatches containing five evenly distributed areas (~12 mm diameter, Figure 4.3A) of attached protein crystal material were subjected to a total of 60 minutes of wash time in an accelerated laundering machine. HEWL crystal retention was quantified every 15 minutes by removing the samples and imaging them on a Typhoon FLA 7000 fluorescent scanner using an excitation wavelength of 473 nm at 10 µm resolution. Images were analyzed using the Fiji software package¹⁹⁷ to detect and count

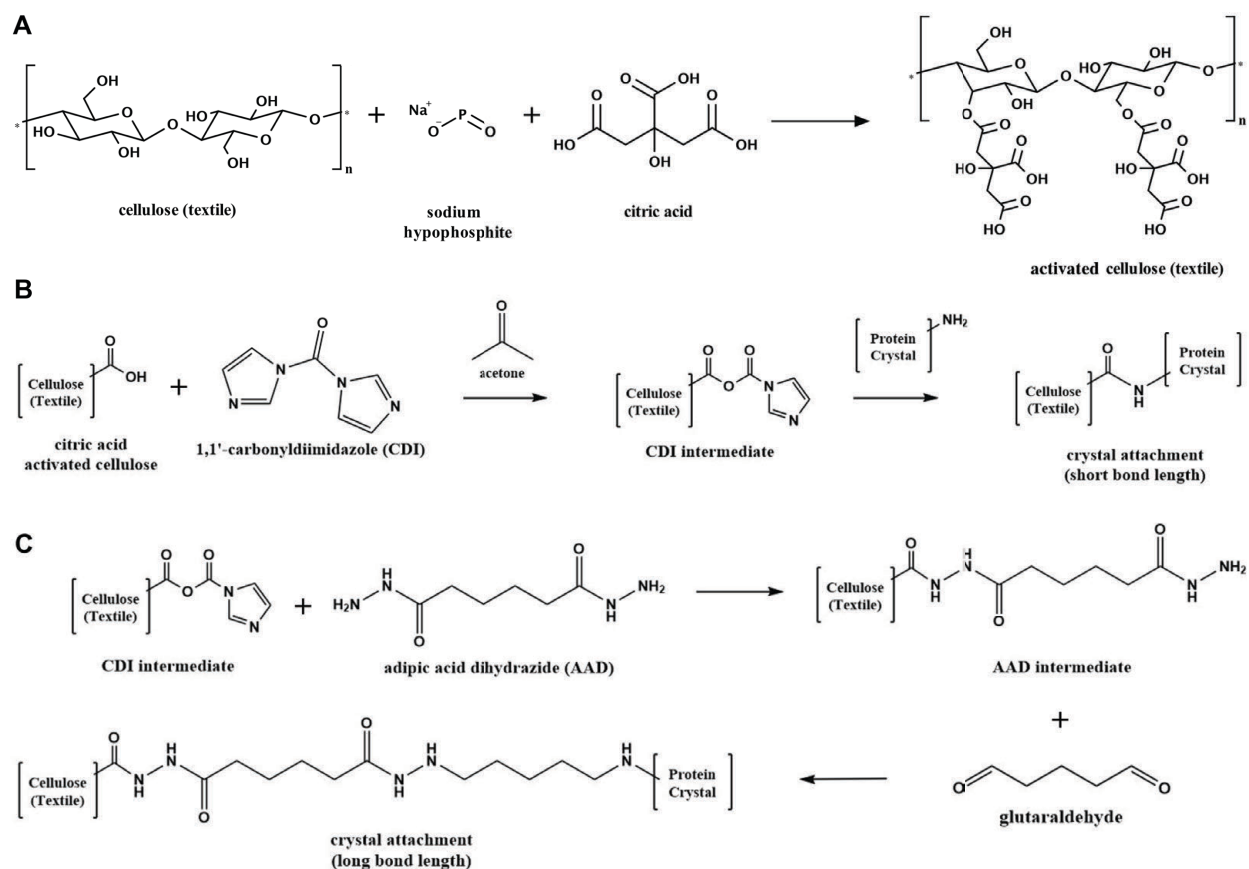


Figure 4.2. Protein crystal to fabric attachment chemistries. (A) Formation of surface carboxylic acid groups on cellulose fabric. (B) Formation of CDI intermediate and crystal attachment *via* pre-existing primary amines on the crystal surface. (C) Attachment of AAD linker arm to CDI intermediate followed by crystal attachment to AAD intermediate textile *via* glutaraldehyde cross-linking.

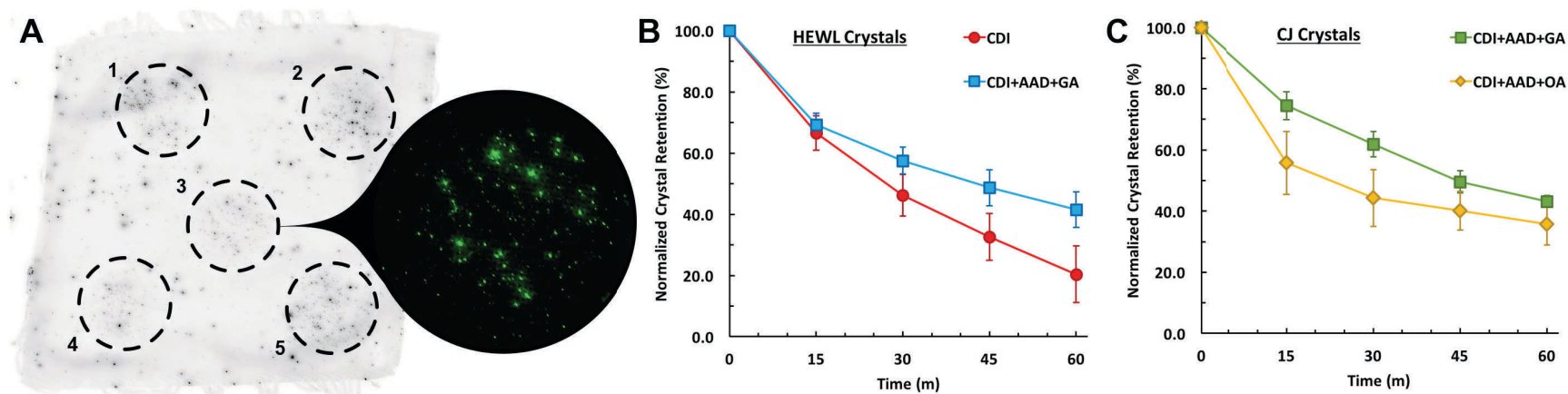


Figure 4.3. Results of the accelerated wash tests. (A) Cotton test swatch containing 5 areas of HEWL crystal attachment at time zero in the accelerated wash protocol.; *Inset*: magnified view of the center application area demonstrating fluorescent puncta used to normalize the percent retention of protein crystals throughout the wash cycles. (B) Comparison of short-length and long-length attachment reaction schemes for HEWL crystals over 60 minutes of accelerated laundering time; *Error Bars*: standard deviation, n=5. (C) Comparison of GA and OA cross-linked CJ-LPC retention over 60 minutes of accelerated laundering time; *Error Bars*: standard deviation, n=5.

fluorescent puncta corresponding to retained trace-labeled crystals. In initial testing using HEWL crystals, the CDI+AAD+GA conjugation scheme performed significantly better than that of the CDI-only treatment (Figure 4.3B). Approximately 40% of HEWL crystals were retained on CDI+AAD+GA treated fabric, while just over 20% of HEWL crystals were retained on CDI-only treated fabric after one hour of accelerated laundering. In contrast, control swatches that either were not decorated with carboxylic acid groups or did not receive CDI showed near-zero crystal retention after rinsing in pure H₂O (APPENDIX III Figure III.3). These results suggest that the fabric activation by CA treatment is necessary for CDI installment of protein crystals. We hypothesize that the increased linker arm length created by the addition of AAD and GA results in a greater number of covalent bonds across the crystal-to-fabric interface, thereby improving overall retention. Because the CDI+AAD+GA treatment showed a marked improvement over CDI-only, the former was chosen as the preferred method for testing CJ-LPC attachment. However, it has previously been shown that oxaldehyde (OA) cross-linked CJ crystals retain diffraction better than crystals cross-linked with GA.⁵⁰ In light of this, OA cross-linked crystals and a final CDI+AAD+OA conjugation step were implemented alongside GA treatments for CJ-LPC attachment tests.

Small (10 – 100 μm diameter) CJ-LPCs were grown by batch crystallization in 3.4-3.6 M (NH₄)₂SO₄, 40 mM bis-tris pH 6.5 at 15° C. Crystals were cross-linked with either GA or OA, quenched with carbonyldiimidazole, and trace labeled with NHS-fluorescein implementing the same procedures used for tetragonal HEWL crystals. After cross-linking, crystals were conjugated to the cotton fabric either by a CDI+AAD+GA scheme or CDI+AAD+OA scheme. CJ protein expression, purification, crystallization, fabric treatment, and cross-linking methods are detailed in APPENDIX III. As with HEWL, approximately 40% of CJ-LPC crystals were retained on

CDI+AAD+GA treated fabric after one hour of accelerated laundering (Figure 4.3C). However, this retention rate dropped slightly to 35% for OA cross-linked CJ-LPC crystals on CDI+AAD+OA treated fabric. We suspect that this discrepancy is caused by GA's propensity for polymerization.²⁸ Polymerization of GA between the AAD primary amines and the CJ-LPC primary amines may result in longer conjugation linkages than theorized in Figure 4.2C thus providing a more extensively bonded crystal-to-fabric interface when compared to a similarly structured bifunctional cross-linking agent such as OA.

After successful demonstration of attachment, protein crystal conjugated cotton was loaded with guest molecules of varying sizes to demonstrate the wide range of guest functionalization. Separate fabric swatches containing either CDI+AAD+GA conjugated HEWL crystals or CDI+AAD+GA conjugated CJ crystals were first washed for 15-minutes in pure water to remove excess non-covalently attached crystals from the fabric surface. Cotton samples conjugated with HEWL crystals were added to 500 μ L sulforhodamine 101 (Figure 4.1A) in a sealed vessel and incubated for 24 hours protected from light. After incubation, the fabric was briefly rinsed with pure water to remove residual guest molecules. Differential interference contrast (DIC) and fluorescent (488 nm & 561 nm) confocal images taken both before and after incubation with sulforhodamine 101 demonstrate HEWL crystal attachment and co-localization with the small molecule guests (Figure 4.4A). Similarly, CJ-LPC conjugated fabric was soaked in 500 μ L of sulforhodamine-labeled cytochrome P450 heme domain to demonstrate the potential for enzyme loading. The cytochrome P450 heme domain used as a model guest enzyme was a synthetic homolog to the soluble P450s of *Bacillus megaterium* and *Bacillus subtilis*.²⁰¹ Specifically, we used a purified aliquot of chimera 21311331, where each numeral indicates the parent enzyme (1: CYP102A1, Figure 4.1B, 2: CYP102A2, 3: CYP102A3). Images were taken on a fluorescent

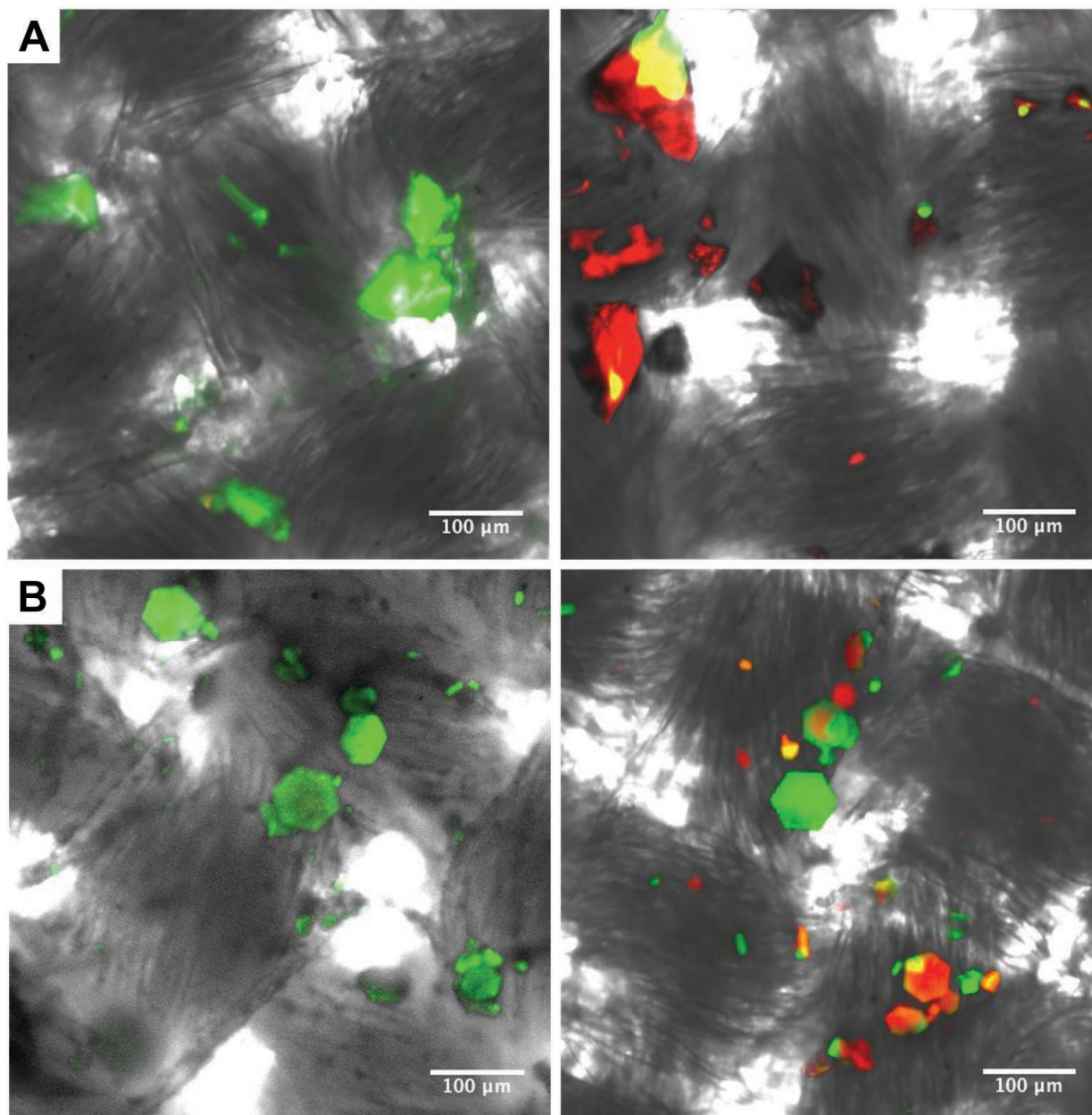


Figure 4.4. Composite confocal images of protein crystals conjugated to cotton fabric (DIC, 488nm and 561nm). (A) *Left:* empty fluorescein-labeled HEWL crystals (green). *Right:* HEWL crystals (green) after 24-hour incubation with sulforhodamine 101 (red). (B) *Left:* empty fluorescein-labeled CJ-LPCs (green); *Right:* CJ-LPCs (green) after 36-minute incubation with sulforhodamine-labeled P450 (red).

confocal microscope at 488 nm and 561 nm every 2 minutes for 36 minutes (APPENDIX III Figure III.4). Diffusion of P450 enzyme into CJ-LPC pores was observed throughout this time-lapse. After loading, the fabric was briefly rinsed with pure water to remove residual P450 enzyme. DIC and fluorescent (488 nm & 561 nm) confocal images were then taken, demonstrating CJ-LPC attachment and co-localization with the macromolecular guests (Figure 4.4B). These results indicate that a range of guest molecules can be loaded into different porous protein crystal scaffolds that have been conjugated to cellulose fibers in cotton textiles. More information regarding guest loading can be found in APPENDIX III.

◎ 4.4 CONCLUSIONS

The myriad topologies of protein crystals provide a wide range of pore structures and dimensions. As such, these materials can accommodate adsorbates of varying size, from small molecules to macromolecular guests. Here we have demonstrated that versatile guest molecule storage materials may be created from inexpensive cotton fabrics functionalized by conjugated protein crystals. There is a clear separation of timescales in guest retention between the bare textile and the protein crystal reservoirs, with reservoirs achieving superior retention. Furthermore, the loading times required for each guest molecule depends on the host crystal. By rationally selecting the host crystal pore structure, one could conceivably optimize the storage or transport kinetics of guest molecules based on size, charge, or hydrophobicity. Furthermore, multi-species guest loading and release may be possible by conjugating a variety of protein crystal reservoirs, each optimized for a specific guest molecule.

This method of loading guest molecules into the void space of protein crystals conjugated to textiles may prove a reliable method for the extended, metered release of a variety of molecules. We have previously demonstrated guest molecule release in response to changes in pH;^{79,80} thus,

it may be feasible to trigger release of guest molecules from textile bound protein crystal reservoirs using environmental cues such as pH or exposure to analytes. Characterizing guest loading and release kinetics under varying environmental conditions may be an attractive follow up study. Applications of this technology range from medical wound dressing to multifunctional textiles exhibiting anti-microbial and anti-malarial properties.

© 4.5 RECOGNITION

This material is based upon work supported by the National Science Foundation under Grant No. 1506219. This specific project was initiated with support from the Natick Soldier Research Development and Engineering Center. The authors thank the following NSRDEC members for materials and helpful discussions: Shaun Filocamo, June Lum, Shalli Sherman, and Laura Place.

CHAPTER 5

SUMMARY AND FUTURE PROSPECTIVE

© 5.1 SUMMARY

Nanostructured devices of the future will improve upon existing technology in numerous regards, incorporating multiple components into smaller, integrated devices that are sufficiently economical, robust, and biodegradable. Porous protein crystals are unique materials that may be used as novel nanostructured host-guest devices. The stability, long-term biodegradability, and small size of cross-linked porous protein crystals could enable otherwise infeasible applications in biosensing, drug delivery, biotemplating and catalysis—providing new tools for the advancement of human health and technology. The work presented in this dissertation helps demonstrate the application potential of porous protein crystal based host-guest nanostructured systems; we not only made steps toward better understanding host-guest biochemical interactions and transport dynamics, but also made progress in characterizing the biocompatibility, physical stability, and chemical versatility of these materials and their guest molecules.

Typical pore diameters of protein crystals have been reported to range from 0.3 – 10.0 nm.³ However, we demonstrate here a recently identified class of porous protein crystals exhibiting pore diameters greater than 10 nm. These large-pore protein crystals (LPCs) are capable of macromolecular uptake, allowing them to be used as novel host scaffolds. The primary protein crystal used in this study was composed of CJ monomers, a modified form of a putative periplasmic isoprenoid-binding protein derived from *Campylobacter jejuni*. CJ derived large-pore protein crystals (CJ-LPCs) exhibit an axial pore diameter of 13 nm and less than 3 nm diameter lateral pores. The aim of this dissertation work was to provide foundational data that will improve

our understanding of host-guest transport phenomena within these unique LPC materials as well as characterize their chemical versatility, physical stability, and biological compatibility with respect to other more archetypal protein crystal scaffolds, such as tetragonal HEWL. By pursuing this research, we hope to better understand LPC materials and leverage that knowledge to intelligently design advanced nanodevices for use in medicine and biotechnology.

⊙ **5.1.1 Improving Techniques for the Study of Adsorption-Coupled Diffusion within the Confined Pores of Protein Crystal Materials**

We developed methods for quantifying hindered diffusion of $\text{Au}_{25}(\text{glutathione})_{18}$ nanoclusters in the presence of strong adsorption within an LPC pore environment. This was achieved by first determining the equilibrium adsorption coefficient by performing constant volume bulk equilibrium adsorption experiments. Next, we monitored macromolecular $\text{Au}_{25}(\text{GSH})_{18}$ nanocluster transport within CJ-LPC pores using confocal microscopy. In our confocal loading studies, we observed a decrease in the pore diffusion coefficient over time as more nanoclusters adsorb and occlude the crystal pores, thus hindering diffusion. This effect was maximized at higher free-solution concentrations, which lead to a higher adsorbed state within the pores. We developed a hindered diffusion simulation model that coincides well with our transport observations. This model enabled kinetic parameters to be ascertained from equilibrium adsorption data, providing a suitable method to calculate transport phenomena involving adsorption-coupled diffusion whereby the adsorbate constricts the pore causing an increase in hindrance effects which attenuate the pore diffusivity. These finding may benefit downstream efforts to better engineer large-pore protein crystal based nanoporous materials to serve as new and unique tools in bionanotechnology.

⊙ 5.1.2 Understanding the Effects of Various Cross-linking Chemistries on Protein Crystal Stability and Biocompatibility

To demonstrate the feasibility of utilizing chemically-stabilized protein crystal materials in biological and environmental applications in which both toxicity and material stability is a concern, we investigated the efficacy of various cross-linking reagents to stabilize the molecular structure of two distinct protein crystal variants (tetragonal HEWL and CJ-LPC) while seeking to minimize cytotoxicity. We crosslinked HEWL crystals and CJ-LPCs with glutaraldehyde (GA), oxaldehyde (OA), and 1-Ethyl-3-(3-dimethylaminopropyl)carbodiimide (EDC). The retention of molecular order of these materials was investigated using X-ray diffraction both after cross-linking and after incubation with adult human dermal fibroblast (HDFa) cells. While GA has been widely shown to stabilize HEWL crystals without loss in diffraction,²⁹ it was not initially known if chemically modifying CJ-LPC interfaces would substantially degrade diffraction quality. While GA, the cross-linking agent primarily used to stabilize protein crystals, generated robust CJ-LPCs on a macroscopic level when tested against HDFa cell culture, it exhibited the greatest initial loss in molecular order upon cross-linking. We hypothesized that, in this case, the heterogeneous nature of GA²⁸ was likely at odds with preserving molecular order at the lysine rich interfaces of CJ-LPCs. Surprisingly, the seldom used cross-linkers, OA and EDC, generated CJ-LPC materials capable of retaining molecular order while suffering minimal loss of diffraction upon cross-linking and incubation with human cell culture.

Potential cytotoxic effects from GA, OA, or EDC cross-linking was investigated by measuring the viability of HDFa and human macrophage (MV-4-11) cells when subjected to cross-linked protein crystal materials. Cells were incubated in the presence of protein crystal materials for 24 hours, after which, cell viability was quantified by monitoring lactate dehydrogenase activity.

While non-cross-linked crystal materials maintained very high cell viability across all concentrations, GA cross-linked HEWL and CJ-LPC materials prompted a precipitous decline in cell viability corresponding to increasing material concentration—suggesting a toxic response to GA. Conversely, OA and EDC cross-linked CJ-LPC materials preserved cell viability despite high material concentrations (up to 400 $\mu\text{g/mL}$). The more pronounced reduction in cell viability for GA cross-linked crystals can likely be attributed to unreacted GA species that had leached from the crystals into the growth medium.

The results of the stability and toxicity tests suggest that both OA and EDC cross-linked CJ-LPC materials are superior to protein crystals cross-linked by GA, demonstrating both promising molecular stability and cytocompatibility when tested in the short-term against HDFa and MV-4-11 cells. These materials may be particularly well suited for use in biocatalysis, drug delivery, biosensing, and environmental remediation. Further genotoxicity, and immunogenicity studies should be done to determine long-term biocompatibility toward a more diverse set of tissue types.

⊙ 5.1.3 Assessing Bioconjugation Techniques for the Immobilization of Protein Crystal Reservoirs for the Production of Multifunctional Materials

We demonstrated that the pores or protein crystals can be employed as a reservoir for guest molecules of assorted size and functionality. This work suggests that these materials may have the potential to retain various small molecules, enzymes, therapeutic proteins and DNA, as well as nanoparticles and organometallic compounds. Historically, despite their remarkable qualities, usage of porous protein crystals in conventional macroscale material science applications has been limited due to their small size (commonly <1 mm). Here, we presented methods to overcome this limitation by integrating protein crystals into larger, inexpensive textile host materials.

Tetragonal HEWL crystals and CJ-LPCs were conjugated to the cellulosic substrate of cotton fabric using a carbodiimide-mediated coupling reaction. The efficacy of this attachment was assessed *via* accelerated laundering and quantified by fluorescence imaging. The ability to load guest molecules of varying sizes into the scaffold structure of the conjugated protein crystals was also assessed. This work demonstrates engineered LPC materials to be attractive candidates for the uptake, immobilization, and controlled release of macromolecular guests making them promising targets for use as nanostructured scaffolds. By conjugating crystals to textiles, multifunctional macroscale nanoporous scaffold materials can be realized which may be uniquely suited for applications in wound dressing and textile science.

◎ 5.2 FUTURE PROSPECTIVE

◎ 5.2.1 DNA Guest Molecule Loading for Information Storage

The work in this dissertation illustrates the propensity for large-pore protein crystals, such as CJ-LPCs, to accommodate macromolecular guest molecules within their interior void spaces either through passive diffusion or adsorption. This feature may be exploited for various applications in guest molecule storage. Recent unpublished results provide a proof-of-principle for loading protein crystals with short, exogenous oligonucleotides. Confocal microscopy was used to observe the transport and adsorption of 6FAM-labeled 15-mer DNA to the interior of oxaldehyde (OA) cross-linked CJ-LPCs. Remarkably, preliminary results indicate guest DNA remains adsorbed in a wide variety of conditions including high salt aqueous solutions and aqueous-organic DMSO solutions. (data not shown). Further research is needed to determine the reproducibility of these results and to optimize experimental loading and unloading conditions. It will be important to quantify the adsorption capacity of CJ-LPCs and to determine if there are size limitations for the guest DNA. We will additionally evaluate the resulting host-guest crystals for information storage and

barcoding applications—assessing the propensity of the host crystals to protect guest DNA under challenging conditions (*i.e.* from degradation in the environment). To these ends, a recent member of the Snow lab, Julius Stuart, will conduct additional confocal microscopy and adsorption isotherm experiments with fluorescently labeled oligonucleotides of varying size in a wide range of solution conditions. Microscopic information repositories such as this may have a variety of long-term analytical, forensic, and environmental applications.

⊙ 5.2.2 Crystal Functionalization by Covalent Guest Capture

Our lab has recently shown the ability to install small molecule guests onto the pore surface of CJ-LPCs by way of engineered solvent-exposed cysteine residues.⁵ This covalent guest capture could be used to add novel functionality to host crystals by enabling site-specific modification of the luminal environment.

Lanthanide Complex Assembly and Capture: Our collaborators in China have recently published work on the assembly of lanthanide complexes within cross-linked hen egg white lysozyme (HEWL) crystals.¹³⁸ This research was conducted in the interest of next-generation photonic applications; the authors claim organized arrays of lanthanide complexes to be compelling design targets for a variety of reasons: i) unlike other metals, lanthanides can provide unique photophysical properties to a material, depending on their coordination sphere. Long-lived luminescence from lanthanide centers can compete favorably with the properties of fluorescent proteins or small molecules; ii) incorporation into porous scaffolds, such as protein crystals, would result in a three-dimensional array of emitters, which should ultimately allow superior performance compared to uncontrolled lanthanide complex aggregates; iii) the photophysical properties of the resulting lanthanide lattice may be improved by the detailed structure of the crystal host scaffold, thereby enabling a new class of sensors in which the long-lived luminescence of the lanthanide

sites can be used to eliminate background; iv) as heavy atoms, lanthanide sites will be easy to validate *via* single-crystal X-ray diffraction. However, one limitation facing this technology is the slow leakage of lanthanides from the HEWL crystal scaffold (*i.e.* limited capture capability). To address this issue, it may be advantageous to install chemical groups, such as phenanthroline, that are capable of coordinating lanthanides at specific locations within an LPC environment thereby facilitating lanthanide retention and a longer luminescent lifetime of the material.

Nitric Oxide Releasing Protein Crystal Materials: In addition to lanthanide-based photonic applications, small molecule capture could provide advancements in drug delivery. For instance, nitric oxide (NO) is a cell signaling gas with many therapeutic uses including antimicrobial and anticancer properties.^{110,111} As such, NO-releasing materials have garnered increasing interest for medicinal applications.²⁰² Melissa Reynolds' group here at Colorado State University has demonstrated sustained NO-release from an S-nitrosothiol-based bioerodible coating and produced metal-organic frameworks (MOFs) capable of catalyzing NO-production from endogenous S-nitrosothiols.^{203,204} S-nitrosoglutathione (GSNO), is an S-nitrosothiol with remarkably high NO retention leading to steady, long-term NO release when compared to other S-nitrosothiols such as S-nitrosocysteine.^{205,206} Engineered CJ-LPCs could conceivably be functionalized with GSNO molecules by way of cysteine capture sites to produce a novel NO-releasing material, one with potentially superior biocompatibility over current MOF materials.

REFERENCES

- (1) Feyzizarnagh, H.; Yoon, D. Y.; Goltz, M.; Kim, D. S. Peptide Nanostructures in Biomedical Technology. *Wiley Interdiscip. Rev. Nanomed. Nanobiotechnol.* **2016**, 8 (5), 730–743.
- (2) Desai, M. S.; Lee, S. W. Protein-Based Functional Nanomaterial Design for Bioengineering Applications. *Wiley Interdiscip. Rev. Nanomed. Nanobiotechnol.* **2015**, 7 (1), 69–97.
- (3) Matthews, B. W. Solvent Content of Protein Crystals. *J. Mol. Biol.* **1968**, 33 (2), 491–497.
- (4) Vilenchik, L. Z.; Griffith, J. P.; St. Clair, N.; Navia, M. A.; Margolin, A. L. Protein Crystals as Novel Microporous Materials. *J Am Chem Soc* **1998**, 120 (18), 4290–4294.
- (5) Huber, T. R.; McPherson, E. C.; Keating, C. E.; Snow, C. D. Installing Guest Molecules at Specific Sites within Scaffold Protein Crystals. *Bioconjug. Chem.* **2018**, 29 (1), 17–22.
- (6) Miller, J. L.; Coq, J. L.; Hodes, A.; Barbalat, R.; Miller, J. F.; Ghosh, P. Selective Ligand Recognition by a Diversity-Generating Retroelement Variable Protein. *PLOS Biol.* **2008**, 6 (6), e131.
- (7) Auerbach, S. M.; Carrado, K. A.; Dutta, P. K. *Handbook of Zeolite Science and Technology*; CRC Press, 2003.
- (8) Horcajada, P.; Gref, R.; Baati, T.; Allan, P. K.; Maurin, G.; Couvreur, P.; Férey, G.; Morris, R. E.; Serre, C. Metal–Organic Frameworks in Biomedicine. *Chem. Rev.* **2012**, 112 (2), 1232–1268.
- (9) Furukawa, H.; Cordova, K. E.; O’Keeffe, M.; Yaghi, O. M. The Chemistry and Applications of Metal-Organic Frameworks. *Science* **2013**, 341 (6149), 1230444.

- (10) Berman, H. M.; Westbrook, J.; Feng, Z.; Gilliland, G.; Bhat, T. N.; Weissig, H.; Shindyalov, I. N.; Bourne, P. E. The Protein Data Bank. *Nucleic Acids Res.* **2000**, *28* (1), 235–242.
- (11) McPherson, A. A Brief History of Protein Crystal Growth. *J. Cryst. Growth* **1991**, *110* (1), 1–10.
- (12) Chayen, N. E. Comparative Studies of Protein Crystallization by Vapour-Diffusion and Microbatch Techniques. *Acta Crystallogr. D Biol. Crystallogr.* **1998**, *54* (1), 8–15.
- (13) Pifat-Mrzljak, G. *Supramolecular Structure and Function 9*; Springer Science & Business Media, 2007.
- (14) Janin, J.; Rodier, F. Protein-Protein Interaction at Crystal Contacts. *Proteins* **1995**, *23* (4), 580–587.
- (15) Noritomi, H.; Koyama, K.; Kato, S.; Nagahama, K. Increased Thermostability of Cross-Linked Enzyme Crystals of Subtilisin in Organic Solvents. *Biotechnol. Tech.* *12* (6), 467–469.
- (16) Margolin, A. L.; Navia, M. A. Protein Crystals as Novel Catalytic Materials. *Angew. Chem. Int. Ed.* **2001**, *40* (12), 2204–2222.
- (17) Lee, T. S.; Turner, M. K.; Lye, G. J. Mechanical Stability of Immobilized Biocatalysts (CLECs) in Dilute Agitated Suspensions. *Biotechnol. Prog.* **2002**, *18* (1), 43–50.
- (18) Ayala, M.; Horjales, E.; Pickard, M. A.; Vazquez-Duhalt, R. Cross-Linked Crystals of Chloroperoxidase. *Biochem. Biophys. Res. Commun.* **2002**, *295* (4), 828–831.
- (19) Hermanson, G. T. *Bioconjugate Techniques*; Academic Press, 2013.
- (20) Wong, S. S.; Jameson, D. M.; Wong, S. S. *Chemistry of Protein and Nucleic Acid Cross-Linking and Conjugation*, 2nd ed.; Taylor & Francis/CRC Press: Boca Raton, 2012.

- (21) Hoffman, E. A.; Frey, B. L.; Smith, L. M.; Auble, D. T. Formaldehyde Crosslinking: A Tool for the Study of Chromatin Complexes. *J. Biol. Chem.* **2015**, *290* (44), 26404–26411.
- (22) Quioco, F. A.; Richards, F. M. Intermolecular Cross Linking of a Protein in the Crystalline State: Carboxypeptidase-A. *Proc. Natl. Acad. Sci.* **1964**, *52* (3), 833–839.
- (23) Quioco, F. A.; Richards, F. M. The Enzymic Behavior of Carboxypeptidase-A in the Solid State. *Biochemistry (Mosc.)* **1966**, *5* (12), 4062–4076.
- (24) Khalaf, N. K.; Margolin, A. L.; Persichetti, R. A.; Shenoy, B. C.; St, C. N. L.; Inc, A. B. *Controlled Dissolution Cross-Linked Protein Crystals*; 1998.
- (25) Cohen-Hadar, N.; Wine, Y.; Nachliel, E.; Huppert, D.; Gutman, M.; Frolow, F.; Freeman, A. Monitoring the Stability of Crosslinked Protein Crystals Biotemplates: A Feasibility Study. *Biotechnol. Bioeng.* **2006**, *94* (5), 1005–1011.
- (26) Yan, E. K.; Cao, H. L.; Zhang, C. Y.; Lu, Q. Q.; Ye, Y. J.; He, J.; Huang, L. J.; Yin, D. C. Cross-Linked Protein Crystals by Glutaraldehyde and Their Applications. *RSC Adv.* **2015**, *5* (33), 26163–26174.
- (27) Vaghjiani, J. D.; Lee, T. S.; Lye, G. J.; Turner, M. K. Production and Characterisation of Cross-Linked Enzyme Crystals (Clecs®) for Application as Process Scale Biocatalysts. *Biocatal. Biotransformation* **2000**, *18* (2), 151–175.
- (28) Migneault, I.; Dartiguenave, C.; Bertrand, M. J.; Waldron, K. C. Glutaraldehyde: Behavior in Aqueous Solution, Reaction with Proteins, and Application to Enzyme Crosslinking. *BioTechniques* **2004**, *37* (5), 790–796, 798–802.

- (29) Wine, Y.; Cohen-Hadar, N.; Freeman, A.; Frolow, F. Elucidation of the Mechanism and End Products of Glutaraldehyde Crosslinking Reaction by X-Ray Structure Analysis. *Biotechnol. Bioeng.* **2007**, *98* (3), 711–718.
- (30) Park, S. N.; Lee, H. J.; Lee, K. H.; Suh, H. Biological Characterization of EDC-Crosslinked Collagen–Hyaluronic Acid Matrix in Dermal Tissue Restoration. *Biomaterials* **2003**, *24* (9), 1631–1641.
- (31) Niknejad, H.; Mahmoudzadeh, R. Comparison of Different Crosslinking Methods for Preparation of Docetaxel-Loaded Albumin Nanoparticles. *Iran. J. Pharm. Res. IJPR* **2015**, *14* (2), 385–394.
- (32) Hartje, L. F.; Bui, H. T.; Andales, D. A.; James, S. P.; Huber, T. R.; Snow, C. D. Characterizing the Cytocompatibility of Various Cross-Linking Chemistries for the Production of Biostable Large-Pore Protein Crystal Materials. *ACS Biomater. Sci. Eng.* **2018**.
- (33) Lepvrier, E.; Doigneaux, C.; Moullintraffort, L.; Nazabal, A.; Garnier, C. Optimized Protocol for Protein Macrocomplexes Stabilization Using the EDC, 1-Ethyl-3-(3-(Dimethylamino)Propyl)Carbodiimide, Zero-Length Cross-Linker. *Anal. Chem.* **2014**, *86* (21), 10524–10530.
- (34) Edwards, J. V.; Prevost, N. T.; Condon, B.; French, A. Covalent Attachment of Lysozyme to Cotton/Cellulose Materials: Protein Verses Solid Support Activation. *Cellulose* **2011**, *18* (5), 1239–1249.
- (35) Edwards, J. V.; Prevost, N.; Condon, B.; Sethumadhavan, K.; Ullah, J.; Bopp, A. Immobilization of Lysozyme on Cotton Fabrics: Synthesis, Characterization, and Activity. *ARS USDA Submiss.* **2011**.

- (36) Edwards, J. V.; Prevost, N. T.; Condon, B.; French, A.; Wu, Q. Immobilization of Lysozyme-Cellulose Amide-Linked Conjugates on Cellulose I and II Cotton Nanocrystalline Preparations. *Cellulose* **2012**, *19* (2), 495–506.
- (37) Wnek, G. E.; Bowlin, G. L. *Encyclopedia of Biomaterials and Biomedical Engineering* -; Taylor & Francis, 2004.
- (38) Amri, M. A.; Firdaus, M. a. B.; Fauzi, M. B.; Chowdhury, S. R.; Fadilah, N. R.; Wan Hamirul, W. K.; Reusmaazran, M. Y.; Aminuddin, B. S.; Ruszymah, B. H. I. Cytotoxic Evaluation of Biomechanically Improved Crosslinked Ovine Collagen on Human Dermal Fibroblasts. *Biomed. Mater. Eng.* **2014**, *24* (4), 1715–1724.
- (39) Tabe, H.; Fujita, K.; Abe, S.; Tsujimoto, M.; Kuchimaru, T.; Kizaka-Kondoh, S.; Takano, M.; Kitagawa, S.; Ueno, T. Preparation of a Cross-Linked Porous Protein Crystal Containing Ru Carbonyl Complexes as a CO-Releasing Extracellular Scaffold. *Inorg. Chem.* **2015**, *54* (1), 215–220.
- (40) Chance, B.; Ravilly, A.; Rumen, N. Reaction Kinetics of a Crystalline Hemoprotein: An Effect of Crystal Structure on Reactivity of Ferrimyoglobin. *J. Mol. Biol.* **1966**, *17* (2), 525–534.
- (41) Doscher, M. S.; Richards, F. M. The Activity of an Enzyme in the Crystalline State: Ribonuclease S. *J. Biol. Chem.* **1963**, *238* (7), 2399–2406.
- (42) Granick, S. Some Properties of Crystalline Guinea Pig Hemoglobin. *J. Gen. Physiol.* **1942**, *25* (4), 571–578.
- (43) Kendrew, J. C.; Bodo, G.; Dintzis, H. M.; Parrish, R. G.; Wyckoff, H.; Phillips, D. C. A Three-Dimensional Model of the Myoglobin Molecule Obtained by X-Ray Analysis. *Nature* **1958**, *181* (4610), 662–666.

- (44) Bishop, W. H.; Richards, F. M. Properties of Liquids in Small Pores: Rates of Diffusion of Some Solutes in Cross-Linked Crystals of β -Lactoglobulin. *J. Mol. Biol.* **1968**, *38* (3), 315–328.
- (45) O'Hara, P.; Goodwin, P.; Stoddard, B. L. Direct Measurement of Diffusion Rates in Enzyme Crystals by Video Absorbance Spectroscopy. *J. Appl. Crystallogr.* **1995**, *28* (6), 829–834.
- (46) Velev, O. D.; Kaler, E. W.; Lenhoff, A. M. Surfactant Diffusion into Lysozyme Crystal Matrices Investigated by Quantitative Fluorescence Microscopy. *J. Phys. Chem. B* **2000**, *104* (39), 9267–9275.
- (47) Cvetkovic, A.; Straathof, A. J. J.; Hanlon, D. N.; van der Zwaag, S.; Krishna, R.; van der Wielen, L. A. M. Quantifying Anisotropic Solute Transport in Protein Crystals Using 3-D Laser Scanning Confocal Microscopy Visualization. *Biotechnol. Bioeng.* **2004**, *86* (4), 389–398.
- (48) Cvetkovic, A.; Picioreanu, C.; Straathof, A. J. J.; Krishna, R.; van der Wielen, L. A. M. Relation between Pore Sizes of Protein Crystals and Anisotropic Solute Diffusivities. *J. Am. Chem. Soc.* **2005**, *127* (3), 875–879.
- (49) Cvetkovic, A.; Picioreanu, C.; Straathof, A. J. J.; Krishna, R.; van der Wielen, L. A. M. Quantification of Binary Diffusion in Protein Crystals. *J. Phys. Chem. B* **2005**, *109* (21), 10561–10566.
- (50) Hartje, L. F.; Munsky, B.; Ni, T. W.; Ackerson, C. J.; Snow, C. D. Adsorption-Coupled Diffusion of Gold Nanoclusters within a Large-Pore Protein Crystal Scaffold. *J. Phys. Chem. B* **2017**, *121* (32), 7652–7659.

- (51) Gutenwik, J.; Nilsson, B.; Axelsson, A. Effect of Hindered Diffusion on the Adsorption of Proteins in Agarose Gel Using a Pore Model. *J. Chromatogr. A* **2004**, *1048* (2), 161–172.
- (52) Gutenwik, J.; Nilsson, B.; Axelsson, A. Coupled Diffusion and Adsorption Effects for Multiple Proteins in Agarose Gel. *AIChE J.* **2004**, *50* (12), 3006–3018.
- (53) Morozov, V. N.; Kachalova, G. S. Permeability of Lysozyme Tetragonal Crystals to Water. *N. Y.* **1995**, *24*, 43212–43212.
- (54) Malek, K.; Coppens, M.-O. Molecular Simulations of Solute Transport in Xylose Isomerase Crystals. *J. Phys. Chem. B* **2008**, *112* (5), 1549–1554.
- (55) Malek, K.; Odijk, T.; Coppens, M.-O. Diffusion in Protein Crystals—A Computer Simulation. *ChemPhysChem* **2004**, *5* (10), 1596–1599.
- (56) Hu, Z.; Jiang, J.; Sandler, S. I. Water in Hydrated Orthorhombic Lysozyme Crystal: Insight from Atomistic Simulations. *J. Chem. Phys.* **2008**, *129* (7), 075105.
- (57) Malek, K.; Odijk, T.; Coppens, M. O. Diffusion of Water and Sodium Counter-Ions in Nanopores of a β -Lactoglobulin Crystal: A Molecular Dynamics Study. *Nanotechnology* **2005**, *16* (7), S522-530.
- (58) Malek, K. Solute Transport in Orthorhombic Lysozyme Crystals: A Molecular Simulation Study. *Biotechnol. Lett.* **2007**, *29* (12), 1865–1873.
- (59) Hu, Z.; Jiang, J. Molecular Dynamics Simulations for Water and Ions in Protein Crystals. *Langmuir ACS J. Surf. Colloids* **2008**, *24* (8), 4215–4223.
- (60) Hu, Z.; Jiang, J. Separation of Amino Acids in Glucose Isomerase Crystal: Insight from Molecular Dynamics Simulations. *J. Chromatogr. A* **2009**, *1216* (26), 5122–5129.

- (61) Hu, Z.; Jiang, J. Chiral Separation of Racemic Phenylglycines in Thermolysin Crystal: A Molecular Simulation Study. *J. Phys. Chem. B* **2009**, *113* (48), 15851–15857.
- (62) Malek, K. Transport in Protein Crystals, Part I: Insights from Molecular Simulations. *Comput. Sci. Eng.* **2007**, *9* (5), 90–95.
- (63) Malek, K. Transport in Protein Crystals, Part II - Diffusion Simulation and Chiral Recognition. *Comput. Sci. Eng.* **2007**, *9* (6), 70–75.
- (64) Kisljuk, O. S.; Kachalova, G. S.; Lanina, N. P. An Algorithm to Find Channels and Cavities within Protein Crystals. *J. Mol. Graph.* **1994**, *12* (4), 305–307, 296.
- (65) Juers, D. H.; Ruffin, J. MAP_CHANNELS: A Computation Tool to Aid in the Visualization and Characterization of Solvent Channels in Macromolecular Crystals. *J. Appl. Crystallogr.* **2014**, *47* (6), 2105–2108.
- (66) Banatao, D. R.; Cascio, D.; Crowley, C. S.; Fleissner, M. R.; Tienson, H. L.; Yeates, T. O. An Approach to Crystallizing Proteins by Synthetic Symmetrization. *Proc. Natl. Acad. Sci.* **2006**, *103* (44), 16230–16235.
- (67) Laganowsky Arthur; Zhao Minglei; Soriaga Angela B.; Sawaya Michael R.; Cascio Duilio; Yeates Todd O. An Approach to Crystallizing Proteins by Metal-mediated Synthetic Symmetrization. *Protein Sci.* **2011**, *20* (11), 1876–1890.
- (68) Yang, G.; Cecconi, C.; Baase, W. A.; Vetter, I. R.; Breyer, W. A.; Haack, J. A.; Matthews, B. W.; Dahlquist, F. W.; Bustamante, C. Solid-State Synthesis and Mechanical Unfolding of Polymers of T4 Lysozyme. *Proc. Natl. Acad. Sci. U. S. A.* **2000**, *97* (1), 139–144.

- (69) Srinivasan, U.; Iyer, G. H.; Przybycien, T. A.; Samsonoff, W. A.; Bell, J. A. Crystine: Fibrous Biomolecular Material from Protein Crystals Cross-Linked in a Specific Geometry. *Protein Eng.* **2002**, *15* (11), 895–902.
- (70) Quistgaard, E. M. A Disulfide Polymerized Protein Crystal. *Chem Commun* **2014**, *50* (95), 14995–14997.
- (71) Heinz, D. W.; Matthews, B. W. Rapid Crystallization of T4 Lysozyme by Intermolecular Disulfide Cross-Linking. *Protein Eng.* **1994**, *7* (3), 301–307.
- (72) Radford, R. J.; Lawrenz, M.; Nguyen, P. C.; McCammon, J. A.; Tezcan, F. A. Porous Protein Frameworks with Unsaturated Metal Centers in Sterically Encumbered Coordination Sites. *Chem. Commun.* **2010**, *47* (1), 313–315.
- (73) Nepal, M.; Sheedlo, M. J.; Das, C.; Chmielewski, J. Accessing Three-Dimensional Crystals with Incorporated Guests through Metal-Directed Coiled-Coil Peptide Assembly. *J. Am. Chem. Soc.* **2016**, *138* (34), 11051–11057.
- (74) Tavenor, N. A.; Murnin, M. J.; Horne, W. S. Supramolecular Metal-Coordination Polymers, Nets, and Frameworks from Synthetic Coiled-Coil Peptides. *J. Am. Chem. Soc.* **2017**, *139* (6), 2212–2215.
- (75) Abe, S.; Ueno, T. Design of Protein Crystals in the Development of Solid Biomaterials. *RSC Adv.* **2015**, *5* (27), 21366–21375.
- (76) Abe, S.; Tokura, Y.; Pal, R.; Komura, N.; Imamura, A.; Matsumoto, K.; Ijiri, H.; Sanghamitra, N. J. M.; Tabe, H.; Ando, H.; et al. Surface Functionalization of Protein Crystals with Carbohydrate Using Site-Selective Bioconjugation. *Chem. Lett.* **2014**, *44* (1), 29–31.

- (77) Wine, Y.; Cohen-Hadar, N.; Lamed, R.; Freeman, A.; Frolow, F. Modification of Protein Crystal Packing by Systematic Mutations of Surface Residues: Implications on Biotemplating and Crystal Porosity. *Biotechnol. Bioeng.* **2009**, *104* (3), 444–457.
- (78) Wine, Y.; Cohen-Hadar, N.; Lagziel-Simis, S.; Dror, Y.; Frolow, F.; Freeman, A. Adjustment of Protein Crystal Porosity for Biotemplating: Chemical and Protein Engineering Tools. *AIP Conf. Proc.* **2010**, *1254* (1), 198–203.
- (79) Huber Thaddaus R.; Hartje Luke F.; McPherson Eli C.; Kowalski Ann E.; Snow Christopher D. Programmed Assembly of Host–Guest Protein Crystals. *Small* **2017**, *13* (7), 1602703.
- (80) Kowalski, A. E.; Huber, T. R.; Ni, T. W.; Hartje, L. F.; Appel, K. L.; Yost, J. W.; Ackerson, C. J.; Snow, C. D. Gold Nanoparticle Capture within Protein Crystal Scaffolds. *Nanoscale* **2016**, *8* (25), 12693–12696.
- (81) Basu, S. K.; Govardhan, C. P.; Jung, C. W.; Margolin, A. L. Protein Crystals for the Delivery of Biopharmaceuticals. *Expert Opin. Biol. Ther.* **2004**, *4* (3), 301–317.
- (82) Yang, M. X.; Shenoy, B.; Disttler, M.; Patel, R.; McGrath, M.; Pechenov, S.; Margolin, A. L. Crystalline Monoclonal Antibodies for Subcutaneous Delivery. *Proc. Natl. Acad. Sci. U. S. A.* **2003**, *100* (12), 6934–6939.
- (83) Martin, R. W.; Zilm, K. W. Preparation of Protein Nanocrystals and Their Characterization by Solid State NMR. *J. Magn. Reson.* **2003**, *165* (1), 162–174.
- (84) Falkner, J. C.; Al-Somali, A. M.; Jamison, J. A.; Zhang, J.; Adrianse, S. L.; Simpson, R. L.; Calabretta, M. K.; Radding, W.; Phillips; Colvin, V. L. Generation of Size-Controlled, Submicrometer Protein Crystals. *Chem. Mater.* **2005**, *17* (10), 2679–2686.

- (85) Hebel, D.; Huber, S.; Stanislawski, B.; Hekmat, D. Stirred Batch Crystallization of a Therapeutic Antibody Fragment. *J. Biotechnol.* **2013**, *166* (4), 206–211.
- (86) Hekmat, D. Large-Scale Crystallization of Proteins for Purification and Formulation. *Bioprocess Biosyst. Eng.* **2015**, *38* (7), 1209–1231.
- (87) Shi, D.; Mhaskar, P.; El-Farra, N. H.; Christofides, P. D. Predictive Control of Crystal Size Distribution in Protein Crystallization. *Nanotechnology* **2005**, *16* (7), S562.
- (88) Liu, J. J.; Ma, C. Y.; Hu, Y. D.; Wang, X. Z. Modelling Protein Crystallisation Using Morphological Population Balance Models. *Chem. Eng. Res. Des.* **2010**, *88* (4), 437–446.
- (89) Liu, J. J.; Ma, C. Y.; Hu, Y. D.; Wang, X. Z. Effect of Seed Loading and Cooling Rate on Crystal Size and Shape Distributions in Protein Crystallization—A Study Using Morphological Population Balance Simulation. *Comput. Chem. Eng.* **2010**, *34* (12), 1945–1952.
- (90) Nayhouse, M.; Sang-Il Kwon, J.; Christofides, P. D.; Orkoulas, G. Crystal Shape Modeling and Control in Protein Crystal Growth. *Chem. Eng. Sci.* **2013**, *87*, 216–223.
- (91) Liu, J. J.; Hu, Y. D.; Wang, X. Z. Optimization and Control of Crystal Shape and Size in Protein Crystallization Process. *Comput. Chem. Eng.* **2013**, *57*, 133–140.
- (92) Kwon, J. S. I.; Nayhouse, M.; Christofides, P. D.; Orkoulas, G. Modeling and Control of Protein Crystal Shape and Size in Batch Crystallization. *AIChE J.* **2013**, *59* (7), 2317–2327.
- (93) Kwon, J. S. I.; Nayhouse, M.; Christofides, P. D.; Orkoulas, G. Modeling and Control of Crystal Shape in Continuous Protein Crystallization. *Chem. Eng. Sci.* **2014**, *107*, 47–57.

- (94) Kwon, J. S. I.; Nayhouse, M.; Christofides, P. D.; Orkoulas, G. Protein Crystal Shape and Size Control in Batch Crystallization: Comparing Model Predictive Control with Conventional Operating Policies. *Ind. Eng. Chem. Res.* **2014**, *53* (13), 5002–5014.
- (95) Shenoy, B.; Wang, Y.; Shan, W.; Margolin, A. L. Stability of Crystalline Proteins. *Biotechnol. Bioeng.* **2001**, *73* (5), 358–369.
- (96) Hansson Marianne; Nygren Per-Åke; Ståhl Stefan. Design and Production of Recombinant Subunit Vaccines. *Biotechnol. Appl. Biochem.* **2010**, *32* (2), 95–107.
- (97) Moyle, P. M.; Toth, I. Modern Subunit Vaccines: Development, Components, and Research Opportunities. *ChemMedChem* **2013**, *8* (3), 360–376.
- (98) Wade-Evans, A. M.; Pullen, L.; Hamblin, C.; O’Hara, R.; Burroughs, J. N.; Mertens, P. P. African Horsesickness Virus VP7 Sub-Unit Vaccine Protects Mice against a Lethal, Heterologous Serotype Challenge. *J. Gen. Virol.* **1997**, *78* (7), 1611–1616.
- (99) Clair, N. S.; Shenoy, B.; Jacob, L. D.; Margolin, A. L. Cross-Linked Protein Crystals for Vaccine Delivery. *Proc. Natl. Acad. Sci.* **1999**, *96* (17), 9469–9474.
- (100) Roy, P.; Noad, R. Virus-Like Particles as a Vaccine Delivery System: Myths and Facts. In *Pharmaceutical Biotechnology; Advances in Experimental Medicine and Biology*; Springer, New York, NY, 2009; pp 145–158.
- (101) Wilczewska, A. Z.; Niemirowicz, K.; Markiewicz, K. H.; Car, H. Nanoparticles as Drug Delivery Systems. *Pharmacol. Rep. PR* **2012**, *64* (5), 1020–1037.
- (102) López-Sagaseta, J.; Malito, E.; Rappuoli, R.; Bottomley, M. J. Self-Assembling Protein Nanoparticles in the Design of Vaccines. *Comput. Struct. Biotechnol. J.* **2016**, *14*, 58–68.
- (103) Heddle, J. G.; Chakraborti, S.; Iwasaki, K. Natural and Artificial Protein Cages: Design, Structure and Therapeutic Applications. *Curr. Opin. Struct. Biol.* **2017**, *43*, 148–155.

- (104) Couvreur, P. Nanoparticles in Drug Delivery: Past, Present and Future. *Adv. Drug Deliv. Rev.* **2013**, *65* (1), 21–23.
- (105) Somiya, M.; Liu, Q.; Kuroda, S. Current Progress of Virus-Mimicking Nanocarriers for Drug Delivery. *Nanotheranostics* **2017**, *1* (4), 415–429.
- (106) Rohovie, M. J.; Nagasawa, M.; Swartz, J. R. Virus-like Particles: Next-Generation Nanoparticles for Targeted Therapeutic Delivery. *Bioeng. Transl. Med.* **2017**, *2* (1), 43–57.
- (107) Gullotta, F.; di Masi, A.; Ascenzi, P. Carbon Monoxide: An Unusual Drug. *IUBMB Life* **2012**, *64* (5), 378–386.
- (108) Tabe, H.; Shimoi, T.; Fujita, K.; Abe, S.; Ijiri, H.; Tsujimoto, M.; Kuchimaru, T.; Kizaka-Kondo, S.; Mori, H.; Kitagawa, S.; et al. Design of a CO-Releasing Extracellular Scaffold Using in Vivo Protein Crystals. *Chem. Lett.* **2014**, *44* (3), 342–344.
- (109) Tabe, H.; Shimoi, T.; Boudes, M.; Abe, S.; Coulibaly, F.; Kitagawa, S.; Mori, H.; Ueno, T. Photoactivatable CO Release from Engineered Protein Crystals to Modulate NF-KB Activation. *Chem. Commun.* **2016**, *52* (24), 4545–4548.
- (110) Schairer, D. O.; Chouake, J. S.; Nosanchuk, J. D.; Friedman, A. J. The Potential of Nitric Oxide Releasing Therapies as Antimicrobial Agents. *Virulence* **2012**, *3* (3), 271–279.
- (111) Korde Choudhari, S.; Chaudhary, M.; Bagde, S.; Gadbaile, A. R.; Joshi, V. Nitric Oxide and Cancer: A Review. *World J. Surg. Oncol.* **2013**, *11*, 118.
- (112) Meinel, A. J.; Germershaus, O.; Luhmann, T.; Merkle, H. P.; Meinel, L. Electrospun Matrices for Localized Drug Delivery: Current Technologies and Selected Biomedical Applications. *Eur. J. Pharm. Biopharm.* **2012**, *81* (1), 1–13.

- (113) Dash, T. K.; Konkimalla, V. B. Poly-ε-Caprolactone Based Formulations for Drug Delivery and Tissue Engineering: A Review. *J. Controlled Release* **2012**, *158* (1), 15–33.
- (114) Puhl, S.; Li, L.; Meinel, L.; Germershaus, O. Controlled Protein Delivery from Electrospun Non-Wovens: Novel Combination of Protein Crystals and a Biodegradable Release Matrix. *Mol. Pharm.* **2014**, *11* (7), 2372–2380.
- (115) Tüchsen, E.; Ottesen, M. Kinetic Properties of Subtilisin Type Carlsberg in the Crystalline State. *Carlsberg Res. Commun.* **1977**, *42* (5), 407–420.
- (116) Spilburg, C. A.; Bethune, J. L.; Vallee, B. L. Kinetic Properties of Crystalline Enzymes. Carboxypeptidase A. *Biochemistry (Mosc.)* **1977**, *16* (6), 1142–1150.
- (117) Alter, G. M.; Leussing, D. L.; Neurath, H.; Vallee, B. L. Kinetic Properties of Carboxypeptidase B in Solutions and Crystals. *Biochemistry (Mosc.)* **1977**, *16* (16), 3663–3668.
- (118) Nancy L. St. Clair, M. A. N. Cross-Linked Enzyme Crystals as Robust Biocatalysts. *J. Am. Chem. Soc.* **1992**, *114* (18).
- (119) Lalonde, J. J.; Govardhan, C.; Khalaf, N.; Martinez, A. G.; Visuri, K.; Margolin, A. L. Cross-Linked Crystals of *Candida Rugosa* Lipase: Highly Efficient Catalysts for the Resolution of Chiral Esters. *J Am Chem Soc* **1995**, *117* (26), 6845–6852.
- (120) Sobolov, S. B.; Bartoszko-Malik, A.; Oeschger, T. R.; Montelbano, M. M. Cross-Linked Enzyme Crystals of Fructose Diphosphate Aldolase: Development as a Biocatalyst for Synthesis. *Tetrahedron Lett.* **1994**, *35* (42), 7751–7754.
- (121) Sobolov, S. B.; Leonida, M. D.; Bartoszko-Malik, A.; Voivodov, K. I.; McKinney, F.; Kim, J.; Fry, A. J. Cross-Linked LDH Crystals for Lactate Synthesis Coupled to Electroenzymatic Regeneration of NADH. *J. Org. Chem.* **1996**, *61* (6), 2125–2128.

- (122) Khalaf, N.; Govardhan, C. P.; Lalonde, J. J.; Persichetti, R. A.; Wang, Y. F.; Margolin, A. L. Cross-Linked Enzyme Crystals as Highly Active Catalysts in Organic Solvents. *J. Am. Chem. Soc.* **1996**, *118* (23), 5494–5495.
- (123) Xu, K.; Klibanov, A. M. PH Control of the Catalytic Activity of Cross-Linked Enzyme Crystals in Organic Solvents. *J. Am. Chem. Soc.* **1996**, *118* (41), 9815–9819.
- (124) Wang, Y. F.; Yakovlevsky, K.; Zhang, B.; Margolin, A. L. Cross-Linked Crystals of Subtilisin: Versatile Catalyst for Organic Synthesis. *J. Org. Chem.* **1997**, *62* (11), 3488–3495.
- (125) Visuri, K.; Pastinen, O.; Wu, X.; Mäkinen, K.; Leisola, M. Stability of Native and Cross-linked Crystalline Glucose Isomerase. *Biotechnol. Bioeng.* **1999**, *64* (3), 377–380.
- (126) St Clair, N.; Wang, Y. F.; Margolin, A.L. Cofactor-Bound Cross-Linked Enzyme Crystals (CLEC) of Alcohol Dehydrogenase. *Angew. Chem. Int. Ed Engl.* **2000**, *39* (2), 380–383.
- (127) Roy J Jegan; Abraham T Emilia. Continuous Biotransformation of Pyrogallol to Purpurogallin Using Cross-linked Enzyme Crystals of Laccase as Catalyst in a Packed-bed Reactor. *J. Chem. Technol. Biotechnol.* **2006**, *81* (11), 1836–1839.
- (128) Lopez, S.; Rondot, L.; Leprêtre, C.; Marchi-Delapierre, C.; Ménage, S.; Cavazza, C. Cross-Linked Artificial Enzyme Crystals as Heterogeneous Catalysts for Oxidation Reactions. *J. Am. Chem. Soc.* **2017**, *139* (49), 17994–18002.
- (129) Zaks, A. Industrial Biocatalysis. *Curr. Opin. Chem. Biol.* **2001**, *5* (2), 130–136.
- (130) Jegan Roy, J.; Emilia Abraham, T. Strategies in Making Cross-Linked Enzyme Crystals. *Chem. Rev.* **2004**, *104* (9), 3705–3722.
- (131) Vos, D. D.; Vankelecom, I. F. J.; Jacobs, P. A. *Chiral Catalyst Immobilization and Recycling*; John Wiley & Sons, 2008.

- (132) Wei, H.; House, S.; Wu, J.; Zhang, J.; Wang, Z.; He, Y.; Gao, E. J.; Gao, Y.; Robinson, H.; Li, W.; et al. Enhanced and Tunable Fluorescent Quantum Dots within a Single Crystal of Protein. *Nano Res.* **2013**, *6* (9), 627–634.
- (133) England, M. W.; Patil, A. J.; Mann, S. Synthesis and Confinement of Carbon Dots in Lysozyme Single Crystals Produces Ordered Hybrid Materials with Tuneable Luminescence. *Chem. – Eur. J.* **2015**, *21* (25), 9008–9013.
- (134) Wei, H.; Wang, Z.; Zhang, J.; House, S.; Gao, Y. G.; Yang, L.; Robinson, H.; Tan, L. H.; Xing, H.; Hou, C.; et al. Time-Dependent, Protein-Directed Growth of Gold Nanoparticles within a Single Crystal of Lysozyme. *Nat. Nanotechnol.* **2011**, *6* (2), 93–97.
- (135) Wei, H.; Lu, Y. Catalysis of Gold Nanoparticles within Lysozyme Single Crystals. *Chem. Asian J.* **2012**.
- (136) Liang, M.; Wang, L.; Liu, X.; Qi, W.; Su, R.; Huang, R.; Yu, Y.; He, Z. Cross-Linked Lysozyme Crystal Templated Synthesis of Au Nanoparticles as High-Performance Recyclable Catalysts. *Nanotechnology* **2013**, *24* (24), 245601.
- (137) Liu, M.; Wang, L.; Huang, R.; Yu, Y.; Su, R.; Qi, W.; He, Z. Superior Catalytic Performance of Gold Nanoparticles Within Small Cross-Linked Lysozyme Crystals. *Langmuir* **2016**, *32* (42), 10895–10904.
- (138) Zhang, Y.; Zhang, X.; Tang, J.; Snow, C. D.; Sun, G.; Kowalski, A. E.; Hartje, L. F.; Zhao, N.; Wang, Y.; Belfiore, L. A. Synthesis of Luminescent Lanthanide Complexes within Crosslinked Protein Crystal Matrices. *CrystEngComm* **2018**.
- (139) Ueno, T. Porous Protein Crystals as Reaction Vessels. *Chem. Weinh. Bergstr. Ger.* **2013**, *19* (28), 9096–9102.

- (140) Tabe, H.; Abe, S.; Hikage, T.; Kitagawa, S.; Ueno, T. Porous Protein Crystals as Catalytic Vessels for Organometallic Complexes. *Chem. Asian J.* **2014**, *9* (5), 1373–1378.
- (141) Abe, S.; Maity, B.; Ueno, T. Design of a Confined Environment Using Protein Cages and Crystals for the Development of Biohybrid Materials. *Chem. Commun.* **2016**, *52* (39), 6496–6512.
- (142) Maity, B.; Ueno, T. Design of Bioinorganic Materials at the Interface of Coordination and Biosupramolecular Chemistry. *Chem. Rec.* **2017**, *17* (4), 383–398.
- (143) Abe, S.; Maity, B.; Ueno, T. Functionalization of Protein Crystals with Metal Ions, Complexes and Nanoparticles. *Curr. Opin. Chem. Biol.* **2018**, *43*, 68–76.
- (144) Lisdat, F. *Biosensing for the 21st Century*; Springer, 2007.
- (145) US Patent for Biosensors, extracorporeal devices and methods for detecting substances using crosslinked protein crystals Patent (Patent # 6,004,768 issued December 21, 1999) - Justia Patents Search <https://patents.justia.com/patent/6004768> (accessed Apr 17, 2018).
- (146) Luiz de Mattos, I.; Lukachova, L. V.; Gorton, L.; Laurell, T.; Karyakin, A. A. Evaluation of Glucose Biosensors Based on Prussian Blue and Lyophilised, Crystalline and Cross-Linked Glucose Oxidases (CLEC(R)). *Talanta* **2001**, *54* (5), 963–974.
- (147) Roy, J. J.; Abraham, T. E.; Abhijith, K. S.; Kumar, P. V. S.; Thakur, M. S. Biosensor for the Determination of Phenols Based on Cross-Linked Enzyme Crystals (CLEC) of Laccase. *Biosens. Bioelectron.* **2005**, *21* (1), 206–211.
- (148) Laothanachareon, T.; Champreda, V.; Sritongkham, P.; Somasundrum, M.; Surareungchai, W. Cross-Linked Enzyme Crystals of Organophosphate Hydrolase for

- Electrochemical Detection of Organophosphorus Compounds. *World J. Microbiol. Biotechnol.* **2008**, *24* (12), 3049–3055.
- (149) Zheng, B.; Roach, L. S.; Ismagilov, R. F. Screening of Protein Crystallization Conditions on a Microfluidic Chip Using Nanoliter-Size Droplets. *J. Am. Chem. Soc.* **2003**, *125* (37), 11170–11171.
- (150) Hansen, C. L.; Classen, S.; Berger, J. M.; Quake, S. R. A Microfluidic Device for Kinetic Optimization of Protein Crystallization and in Situ Structure Determination. *J. Am. Chem. Soc.* **2006**, *128* (10), 3142–3143.
- (151) Sauter, C.; Dhouib, K.; Lorber, B. From Macrofluidics to Microfluidics for the Crystallization of Biological Macromolecules. *Cryst. Growth Des.* **2007**, *7* (11), 2247–2250.
- (152) Lau, B. T. C.; Baitz, C. A.; Dong, X. P.; Hansen, C. L. A Complete Microfluidic Screening Platform for Rational Protein Crystallization. *J. Am. Chem. Soc.* **2007**, *129* (3), 454–455.
- (153) Abdallah, B. G.; Roy-Chowdhury, S.; Fromme, R.; Fromme, P.; Ros, A. Protein Crystallization in an Actuated Microfluidic Nanowell Device. *Cryst. Growth Des.* **2016**, *16* (4), 2074–2082.
- (154) Wang, L.; Barton, J.; Hughes, L.; Odom, T. W. Shape-Control of Protein Crystals in Patterned Microwells. *J. Am. Chem. Soc.* **2008**, *130* (7), 2142–2143.
- (155) Conejero-Muriel, M.; Rodríguez-Ruiz, I.; Verdugo-Escamilla, C.; Llobera, A.; Gavira, J. A. Continuous Sensing Photonic Lab-on-a-Chip Platform Based on Cross-Linked Enzyme Crystals. *Anal. Chem.* **2016**, *88* (23), 11919–11923.

- (156) Pastinen, O.; Visuri, K.; Leisola, M. Xylitol Purification by Cross-Linked Glucose Isomerase Crystals. *Biotechnol. Techniques*. **1998**, 12 (7), 557–560.
- (157) Pastinen, O.; Jokela, J.; Eerikäinen, T.; Schwabe, T.; Leisola, M. Cross-Linked Glucose Isomerase Crystals as a Liquid Chromatographic Separation Material. *Enzyme Microb. Technol.* **2000**, 26 (7), 550–558.
- (158) Leisola, M.; Jokela, J.; Finell, J.; Pastinen, O. Simultaneous Catalysis and Product Separation by Cross-Linked Enzyme Crystals. *Biotechnol. Bioeng.* **2001**, 72 (4), 501–505.
- (159) Vuolanto, A.; Kiviharju, K.; Nevanen, T. K.; Leisola, M.; Jokela, J. Development of Cross-Linked Antibody Fab Fragment Crystals for Enantioselective Separation of a Drug Enantiomer. *Cryst. Growth Des.* **2003**, 3 (5), 777–782.
- (160) Vuolanto, A.; Leisola, M.; Jokela, J. Enantioselective Affinity Chromatography of a Chiral Drug by Crystalline and Carrier-Bound Antibody Fab Fragment. *Biotechnol. Prog.* **2004**, 20 (3), 771–776.
- (161) Klein-Marcuschamer, D.; Oleskowicz-Popiel, P.; Simmons, B. A.; Blanch, H. W. The Challenge of Enzyme Cost in the Production of Lignocellulosic Biofuels. *Biotechnol. Bioeng.* **2012**, 109 (4), 1083–1087.
- (162) Sholl, D. S. Understanding Macroscopic Diffusion of Adsorbed Molecules in Crystalline Nanoporous Materials via Atomistic Simulations. *Acc. Chem. Res.* **2006**, 39 (6), 403–411.
- (163) Dubbeldam, D.; Snurr, R. Q. Recent Developments in the Molecular Modeling of Diffusion in Nanoporous Materials. *Mol. Simul.* **2007**, 33 (4–5), 305–325.

- (164) Keskin, S.; Liu, J.; Rankin, R. B.; Johnson, J. K.; Sholl, D. S. Progress, Opportunities, and Challenges for Applying Atomically Detailed Modeling to Molecular Adsorption and Transport in Metal–Organic Framework Materials. *Ind. Eng. Chem. Res.* **2009**, *48* (5), 2355–2371.
- (165) Jiang, J.; Babarao, R.; Hu, Z. Molecular Simulations for Energy, Environmental and Pharmaceutical Applications of Nanoporous Materials: From Zeolites, Metal–Organic Frameworks to Protein Crystals. *Chem Soc Rev* **2011**, *40* (7), 3599–3612.
- (166) Keil, F. J.; Krishna, R.; Coppens, M. O. Modeling of Diffusion in Zeolites. *Rev. Chem. Eng.* **2011**, *16* (2), 71–197.
- (167) Kärger, J.; Ruthven, D. M. Diffusion in Nanoporous Materials: Fundamental Principles, Insights and Challenges. *New J. Chem.* **2016**, *40* (5), 4027–4048.
- (168) Shi, K.; Jiang, Y.B.; Yang, L. L.; Cui, F. Progress in the Development of Crystallized Proteins as Drug Delivery System. *Yao Xue Xue Bao* **2009**, *44* (8), 845–851.
- (169) Zhang, Y.; Chan, H. F.; Leong, K. W. Advanced Materials and Processing for Drug Delivery: The Past and the Future. *Adv. Drug Deliv. Rev.* **2013**, *65* (1), 104–120.
- (170) Alexey L., M. Novel Crystalline Catalysts. *Trends Biotechnol.* **1996**, *14* (7), 223–230.
- (171) Abe, S.; Tsujimoto, M.; Yoneda, K.; Ohba, M.; Hikage, T.; Takano, M.; Kitagawa, S.; Ueno, T. Porous Protein Crystals as Reaction Vessels for Controlling Magnetic Properties of Nanoparticles. *Small Wein. Bergstr. Ger.* **2012**, *8* (9), 1314–1319.
- (172) A. L. Margolin. Cross-Linked Enzyme Crystals as Novel Materials for Catalysis and Chromatography. *Chimia* **1996**, *50* (9), 423–424.

- (173) Jouni Jokela, O. P. Isomerization of Pentose and Hexose Sugars by an Enzyme Reactor Packed with Cross-Linked Xylose Isomerase Crystals. *Enzyme Microb. Technol.* **2002**, *31* (1–2), 67–76.
- (174) Lagziel-Simis, S.; Cohen-Hadar, N.; Moscovich-Dagan, H.; Wine, Y.; Freeman, A. Protein-Mediated Nanoscale Biotemplating. *Curr. Opin. Biotechnol.* **2006**, *17* (6), 569–573.
- (175) Cohen-Hadar, N.; Wine, Y.; Lagziel-Simis, S.; Moscovich-Dagan, H.; Dror, Y.; Frolow, F.; Freeman, A. Protein Crystal-Mediated Biotemplating. *J. Porous Media* **2009**, *12* (3), 213–220.
- (176) Cohen-Hadar, N.; Lagziel-Simis, S.; Wine, Y.; Frolow, F.; Freeman, A. Re-Structuring Protein Crystals Porosity for Biotemplating by Chemical Modification of Lysine Residues. *Biotechnol. Bioeng.* **2011**, *108* (1), 1–11.
- (177) Wyckoff, H. W.; Doscher, M.; Tsernoglou, D.; Inagami, T.; Johnson, L. N.; Hardman, K. D.; Allewell, N. M.; Kelly, D. M.; Richards, F. M. Design of a Diffractometer and Flow Cell System for X-Ray Analysis of Crystalline Proteins with Applications to the Crystal Chemistry of Ribonuclease-S. *J. Mol. Biol.* **1967**, *27* (3), 563–578.
- (178) Alber, T.; Petsko, G. A.; Tsernoglou, D. Crystal Structure of Elastase-Substrate Complex at -- 55 Degrees C. *Nature* **1976**, *263* (5575), 297–300.
- (179) Westbrook, E. M.; Sigler, P. B. Enzymatic Function in Crystals of Delta 5-3-Ketosteroid Isomerase. Catalytic Activity and Binding of Competitive Inhibitors. *J. Biol. Chem.* **1984**, *259* (14), 9090–9095.
- (180) Dechadilok, P.; Deen, W. M. Hindrance Factors for Diffusion and Convection in Pores. *Ind. Eng. Chem. Res.* **2006**, *45* (21), 6953–6959.

- (181) Rojas-Cervellera, V.; Rovira, C.; Akola, J. How Do Water Solvent and Glutathione Ligands Affect the Structure and Electronic Properties of Au₂₅(SR)₁₈? *J. Phys. Chem. Lett.* **2015**, *6* (19), 3859–3865.
- (182) Cvetkovic, A.; Straathof, A. J. J.; Hanlon, D. N.; van der Zwaag, S.; Krishna, R.; van der Wielen, L. a. M. Quantifying Anisotropic Solute Transport in Protein Crystals Using 3-D Laser Scanning Confocal Microscopy Visualization. *Biotechnol. Bioeng.* **2004**, *86* (4), 389–398.
- (183) Langmuir, I. THE ADSORPTION OF GASES ON PLANE SURFACES OF GLASS, MICA AND PLATINUM. *J. Am. Chem. Soc.* **1918**, *40* (9), 1361–1403.
- (184) Masel, R. I. *Principles of Adsorption and Reaction on Solid Surfaces*; Wiley series in chemical engineering; Wiley: New York, 1996.
- (185) Milonjić, S. K. A Consideration of the Correct Calculation of Thermodynamic Parameters of Adsorption. *J. Serbian Chem. Soc.* **2007**, *72* (12), 1363–1367.
- (186) Zhou, X.; Zhou, X. The Unit Problem in the Thermodynamic Calculation of Adsorption Using the Langmuir Equation. *Chem. Eng. Commun.* **2014**, *201* (11), 1459–1467.
- (187) Ferry, J. D. Statistical Evaluation of Sieve Constants in Ultrafiltration. *J. Gen. Physiol.* **1936**, *20* (1), 95–104.
- (188) Renkin, E. M. Filtration, Diffusion, and Molecular Sieving through Porous Cellulose Membranes. *J. Gen. Physiol.* **1954**, *38* (2), 225–243.
- (189) Ogston, A. G.; Preston, B. N.; Wells, J. D. On the Transport of Compact Particles Through Solutions of Chain-Polymers. *Proc. R. Soc. Lond. Math. Phys. Eng. Sci.* **1973**, *333* (1594), 297–316.

- (190) Ortega, A.; Amorós, D.; García de la Torre, J. Prediction of Hydrodynamic and Other Solution Properties of Rigid Proteins from Atomic- and Residue-Level Models. *Biophys. J.* **2011**, *101* (4), 892–898.
- (191) Studier, F. W. Protein Production by Auto-Induction in High Density Shaking Cultures. *Protein Expr. Purif.* **2005**, *41* (1), 207–234.
- (192) Hoskin, F. C.; Walker, J. E.; Stote, R. Degradation of Nerve Gases by CLECS and Cells: Kinetics of Heterogenous Systems. *Chem. Biol. Interact.* **1999**, *119–120*, 439–444.
- (193) Speer, D. P.; Chvapil, M.; Eskelson, C. D.; Ulreich, J. Biological Effects of Residual Glutaraldehyde in Glutaraldehyde-Tanned Collagen Biomaterials. *J. Biomed. Mater. Res.* **1980**, *14* (6), 753–764.
- (194) Hekmat, D.; Hebel, D.; Schmid, H.; Weuster-Botz, D. Crystallization of Lysozyme: From Vapor Diffusion Experiments to Batch Crystallization in Agitated MI-Scale Vessels. *Process Biochem.* **2007**, *42* (12), 1649–1654.
- (195) Ducheyne, P.; Healy, K.; Hutmacher, D. E.; Grainger, D. W.; Kirkpatrick, C. J. *Comprehensive Biomaterials*; Newnes, **2015**.
- (196) Preibisch, S.; Saalfeld, S.; Tomancak, P. Globally Optimal Stitching of Tiled 3D Microscopic Image Acquisitions. *Bioinformatics* **2009**, *25* (11), 1463–1465.
- (197) Schindelin, J.; Arganda-Carreras, I.; Frise, E.; Kaynig, V.; Longair, M.; Pietzsch, T.; Preibisch, S.; Rueden, C.; Saalfeld, S.; Schmid, B.; et al. Fiji: An Open-Source Platform for Biological-Image Analysis. *Nat. Methods* **2012**, *9* (7), 676–682.
- (198) Whipple, E. B. Structure of Glyoxal in Water. *J. Am. Chem. Soc.* **1970**, *92* (24), 7183–7186.

- (199) Pastinen, O.; Visuri, K.; Leisola, M. Xylitol Purification by Cross-Linked Glucose Isomerase Crystals. *Biotechnol. Tech.* **1998**, *12* (7), 557–560.
- (200) AATCC Test Method 61, Colorfastness to Laundering: Accelerated. *AATCC Tech Man.* **2013**.
- (201) Otey, C. R.; Landwehr, M.; Endelman, J. B.; Hiraga, K.; Bloom, J. D.; Arnold, F. H. Structure-Guided Recombination Creates an Artificial Family of Cytochromes P450. *PLoS Biol.* **2006**, *4* (5), e112.
- (202) Seabra, A. B.; Justo, G. Z.; Haddad, P. S. State of the Art, Challenges and Perspectives in the Design of Nitric Oxide-Releasing Polymeric Nanomaterials for Biomedical Applications. *Biotechnol. Adv.* **2015**, *33* (6 Pt 3), 1370–1379.
- (203) Lutzke, A.; Tapia, J. B.; Neufeld, M. J.; Reynolds, M. M. Sustained Nitric Oxide Release from a Tertiary S-Nitrosothiol-Based Polyphosphazene Coating. *ACS Appl. Mater. Interfaces* **2017**, *9* (3), 2104–2113.
- (204) Neufeld, M. J.; Lutzke, A.; Jones, W. M.; Reynolds, M. M. Nitric Oxide Generation from Endogenous Substrates Using Metal-Organic Frameworks: Inclusion within Poly(Vinyl Alcohol) Membranes To Investigate Reactivity and Therapeutic Potential. *ACS Appl. Mater. Interfaces* **2017**, *9* (41), 35628–35641.
- (205) Singh, S. P.; Wishnok, J. S.; Keshive, M.; Deen, W. M.; Tannenbaum, S. R. The Chemistry of the S-Nitrosoglutathione/Glutathione System. *Proc. Natl. Acad. Sci.* **1996**, *93* (25), 14428–14433.
- (206) Bradley, S. A.; Steinert, J. R. Characterisation and Comparison of Temporal Release Profiles of Nitric Oxide Generating Donors. *J. Neurosci. Methods* **2015**, *245* (Supplement C), 116–124.

APPENDIX I

SUPPORTING INFORMATION

FOR CHAPTER 2

SUPPORTING INFORMATION

ADSORPTION-COUPLED DIFFUSION OF GOLD NANOCCLUSERS WITHIN A LARGE- PORE PROTEIN CRYSTAL SCAFFOLD

© I.1 PORE VOLUMES AND NUMBER OF NANOCCLUSERS PER UNIT CELL

Considering the known crystalline nanostructure of CJ-LPC pores, the Langmuir isotherm seems to be a reasonable choice. The periodicity of the crystal increases the realism of the Langmuir assumption that the binding sites are equivalent. Also, the Langmuir isotherm capacity of a single adsorption monolayer is fairly realistic, in that the nanopores could not physically accommodate more than 2 layers for guests with a diameter of ~ 3 nm, and the formation of such a second layer would prevent further transport into the crystal (Figure I.1). Additionally, the volumetric capacity of a hypothetical second layer would be reduced. Specifically, the volume of the outer ~ 3 nm shell would be $h\pi(6.5^2 - 3.5^2) = 477 \text{ nm}^3$, while the second shell would only be $h\pi(3.5^2 - 0.5^2) = 191 \text{ nm}^3$, or only 40% of the capacity of the outer layer before taking into account discrete particle effects.

Analytical lower bound: hard spheres in a hard cylinder:

We can provide an analytical lower bound for the maximum capacity of the adsorbed nanocluster layer if we consider $\text{Au}_{25}(\text{GSH})_{18}$ nanoclusters to be hard spheres with a diameter of 3.08 nm (HYDROPRO¹ prediction) and the pores to be hard cylinders of diameter 13.0 nm:

$$\text{maximum \# Au}_{25}(\text{GSH})_{18} \text{ in first layer} = \eta \frac{h\pi R_{p_0}^2 - h\pi(R_{p_0} - 2R)^2}{\frac{4}{3}\pi R^3} \quad (\text{Eq. I.1})$$

Where η is the packing fraction, h is the height of the unit cell (5.0577 nm), R_{p_0} is the initial pore radius (6.5 nm) and R is the radius of a $\text{Au}_{25}(\text{GSH})_{18}$ nanocluster (1.54 nm). Therefore, the right-hand side numerator corresponds to the idealized volume of the first adsorbed layer ($V_{\text{first layer}}$)

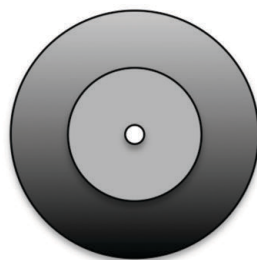


Figure I.1. Diagram demonstrating the Au₂₅(GSH)₁₈ adsorption layers within a single pore of CJ: a 1 nm disc, inscribed within a 7 nm disc, inscribed within a 13 nm disc.

while the denominator corresponds to the volume of a $\text{Au}_{25}(\text{GSH})_{18}$ nanocluster sphere ($V_{\text{Au}_{25}(\text{GSH})_{18}}$). Thus, Equation A1.1 can be written as:

$$\text{maximum \# Au}_{25}(\text{GSH})_{18} \text{ in first layer} = \eta \left(\frac{V_{\text{first layer}}}{V_{\text{Au}_{25}(\text{GSH})_{18}}} \right) \quad (\text{Eq. I.2})$$

If we use the maximum 3-dimensional packing fraction for spheres of 0.74 we find the maximum number of $\text{Au}_{25}(\text{GSH})_{18}$ nanoclusters in the first adsorbed layer to be approximately 23. If we use a more conservative 2-dimensional hexagonal packing fraction of 0.60 (subtracting $1/6^{\text{th}}$ of the volume for three spheres inset on an equilateral triangular prism, see Figure I.2), we obtain a modest 19 nanoclusters per unit cell. Both estimates appear to underestimate the number of nanoparticles that can adsorb to the crystal. However, as outlined below, a single adsorption layer is still consistent with the data.

Numerical estimate for adsorbed layer volume: To more accurately estimate the volume that is accessible to the nanoclusters in the pores, and adsorbed to the scaffold crystal, we turn to numerical estimates. By explicitly modeling possible nanocluster binding, and quantifying accessible volume elements using a grid (see Kowalski *et al.* Supporting Information)² we observe that the ideal 13 nm diameter cylinder underestimates the volume available for nanocluster occupancy. In Figure I.3, we use orange spheres to mark grid points that are accessible to some portion of $\text{Au}_{25}(\text{GSH})_{18}$ nanoclusters, when such nanoclusters are docked throughout the protein matrix. Numerically, the adsorbed layer volume is approximately 563 nm^3 , 18% larger than the idealized outer cylindrical shell.

Numerical estimate for nanocluster volume: We can additionally use numerical methods to more accurately assess the volume consumed per nanocluster. To estimate the nanocluster volume we used the software package MSMS.³ With default atomic radii, and a solvent probe radius of 0.15 nm, we obtained a numerical solvent-excluded volume (sesV) of 6.05 nm^3 within the triangul-

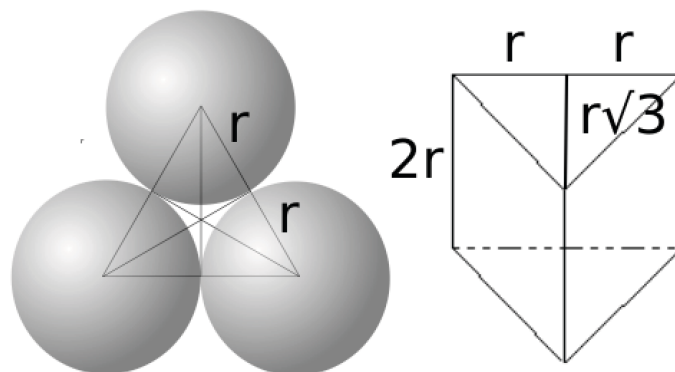


Figure I.2. Diagram demonstrating 2-dimensional hexagonal packing fraction of 0.6, a value obtained by subtracting $1/6^{\text{th}}$ of the volume for three spheres inset on an equilateral triangular prism.

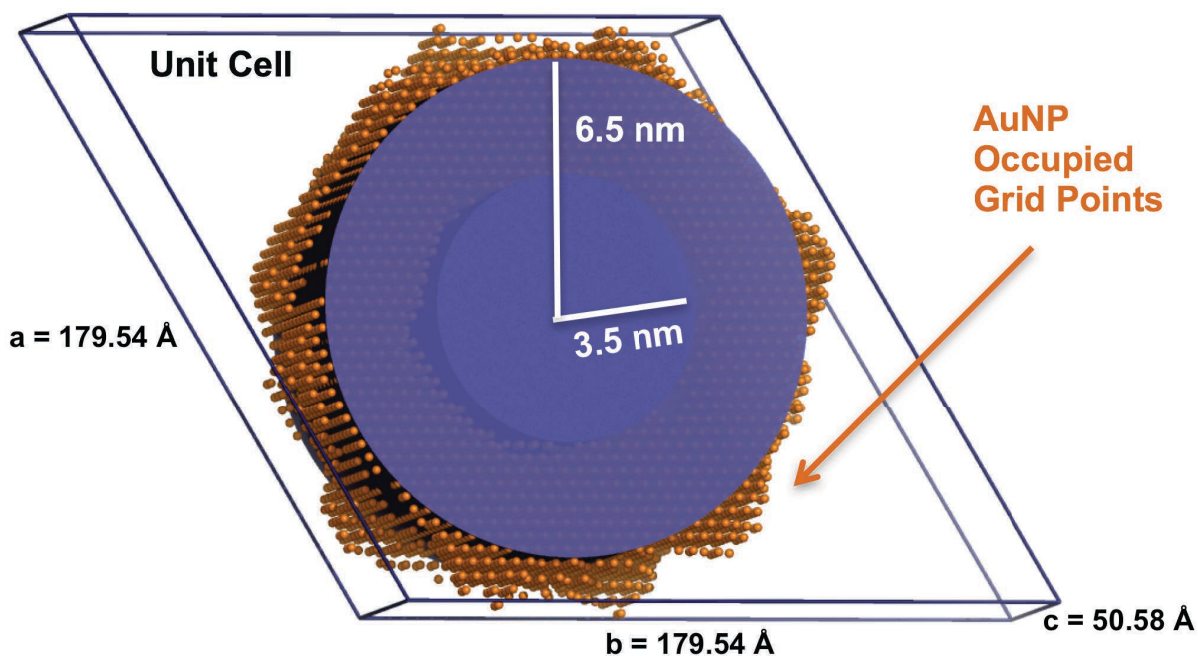


Figure I.3. Diagram demonstrating that the ideal 13 nm diameter cylinder (purple circle) assumed for CJ-LPC pores underestimates the total volume available for nanocluster occupancy. Orange spheres mark grid points that are accessible to some portion of $\text{Au}_{25}(\text{GSH})_{18}$ nanoclusters; numerically, the adsorbed layer volume is approximately 563 nm^3 or 18% larger than the idealized outer cylindrical shell.

ated surface mesh. A sphere with this volume has a radius of only 1.13 nm. Figure I.4 shows the triangulated surface mesh for $\text{Au}_{25}(\text{GSH})_{18}$, and a comparison between the atomic coordinates for $\text{Au}_{25}(\text{GSH})_{18}$ and a sphere of the same net volume (radius=1.13 nm).

Maximum observed packing fraction: To estimate the actual packing fraction (η), we use the numerical estimate for the maximum adsorbed layer volume ($V_{\text{first layer}}$) of 563 nm^3 per unit cell and the numerical minimum excluded volume per nanocluster ($V_{\text{Au}_{25}(\text{GSH})_{18}}$) of 6.05 nm^3 , and the experimentally observed maximum concentration of adsorbed nanoclusters of ~ 29 per unit cell. Solving for η in Equation I.2, we obtain a packing fraction of only 0.31, well under the theoretical maximum of 0.6 for a hexagonally close-packed sphere monolayer (see above).

Implied inter-nanocluster spacing for maximum adsorbed layer: If we assume that 29 guest nanoclusters are arranged in a typical unit cell (q_{max}), then the portion of the adsorbed layer volume available for a typical nanocluster would be 19.4 nm^3 . If we model the packing arrangement as a hexagonal monolayer (packing fraction of 0.6), we can imagine individual nanoclusters as spheres of 11.65 nm^3 with inter-molecule spacing of 2.8 nm. Figure I.5, shows an image of two $\text{Au}_{25}(\text{GSH})_{18}$ nanoclusters, with a 2.8 nm displacement. This level of spacing appears to be sufficient for the adsorbed layer to retain solvent (and counterions) between the nanoclusters.

© I.2 EXTERNAL FREE-SOLUTION CONCENTRATION AT THE BOUNDARY

$\text{Au}_{25}(\text{GSH})_{18}$ nanoclusters are added to the upper well of a the microwell chip (Figure I.6) at a known concentration (C_0). However, $\text{Au}_{25}(\text{GSH})_{18}$ nanoclusters must diffuse through some distance (x) of low percentage agarose gel separating the upper well from the confocal plane located in the lower well. Thus, at early times the effective concentration of nanoclusters in free

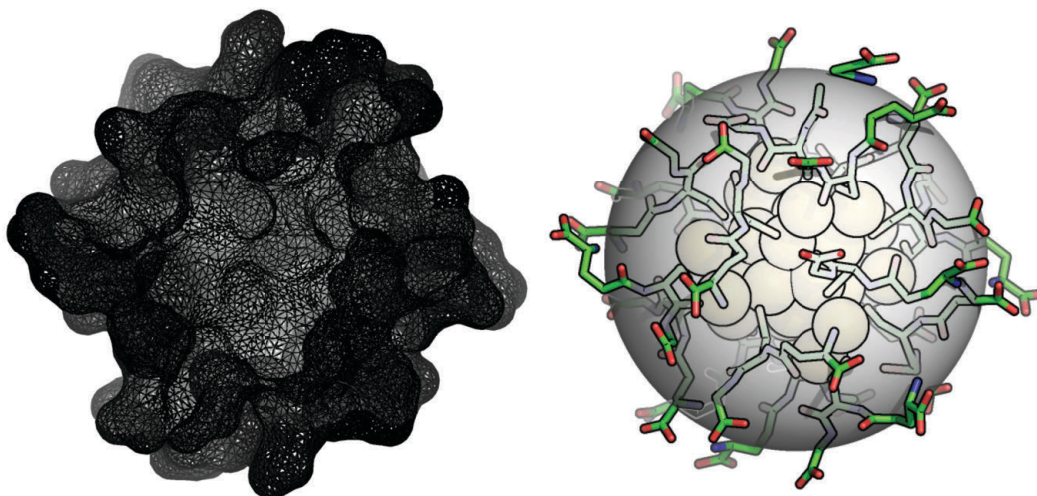


Figure I.4. Diagram demonstrating the structural volume of Au₂₅(GSH)₁₈. (Left) Triangulated surface mesh for Au₂₅(GSH)₁₈. (Right) Comparison between the atomic coordinates for Au₂₅(GSH)₁₈ and a sphere of radius 1.13 nm, which equates to the numerically estimated solvent excluded volume of 6.05 nm³.

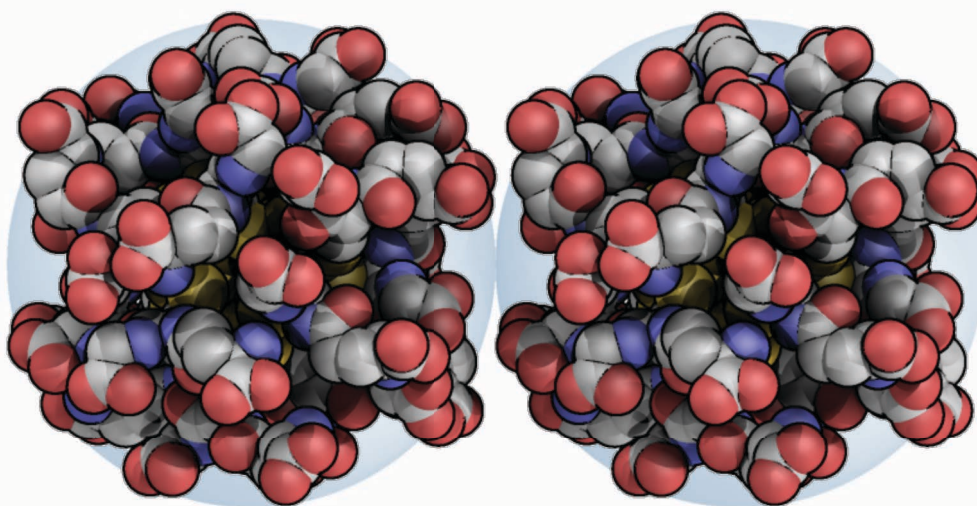


Figure I.5. Diagram of two Au₂₅(GSH)₁₈ nanoclusters displaced by 2.8 nm, blue circles represent the radius of a sphere with volume 11.65 nm³.

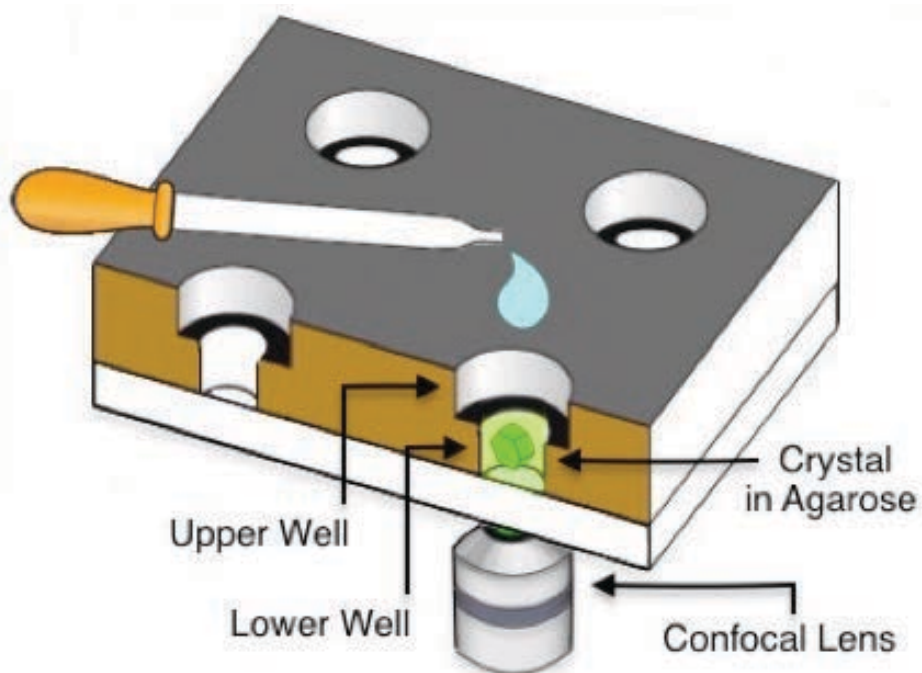


Figure I.6. Schematic illustration of the microwell chip used for confocal imaging (not to scale). The crystal is immobilized in the lower well (2 μL volume) using 0.4% low melting point agarose gel while the larger upper well (18 μL volume) is reserved for the guest solution.

solution at the boundary is lower than C_0 and can be approximated using the error-function compliment for a semi-infinite medium:⁴

$$C_{0_e}(t) = C_0 \operatorname{erfc} \left(\frac{x}{2\sqrt{D_0 t}} \right) \quad (\text{I.3})$$

Where C_{0_e} is the effective free-solution concentration at the boundary at any given time, t , and is used in the boundary conditions (CHAPTER 2 Eq. 2.10). As time progresses C_{0_e} approaches C_0 . For all confocal replicates: $C_0 = 1.43 \times 10^{-7}$ mol/mL and $D_0 = 1.27 \times 10^{-6}$ cm²/s. See Figure I.14 for comparison of the Equation I.3 model to confocal experimental data.

☉ I.3 CONTINUITY EQUATION DERIVATION

The one-dimensional pore diffusion equation can be derived by mass balance for the contents of a slice of crystal perpendicular to the six-fold crystal axis (\hat{z}). Here, the axis \hat{z} points from the crystal midline ($z = L/2$) towards the crystal surface ($z = L$).

Step A. The continuity equation for the mobile guest can be derived from mass balance. The accumulation of mobile guest into a z -slice of the crystal, of width Δz and cross-section area, A , (Figure I.7) must be equal to the difference in flux at the two boundaries, in addition to reduction in the mobile guest concentration due to adsorption (conversion to the bound state) as well as increases in the mobile guest concentration due to desorption (conversion from the bound state).

$$\text{Mobile Guest Accumulation} = \text{Influx} - \text{Outflux} - \text{Adsorption} + \text{Desorption} \quad (\text{Eq. I.4})$$

$$\text{Mobile Guest Accumulation} = \int_V \frac{\partial C}{\partial t} dV = \int_z^{z+\Delta z} \frac{\partial C}{\partial t} A dz = A \frac{\partial C}{\partial t} \Delta z + O(\Delta z^2) \quad (\text{Eq. I.5})$$

The rate of change for the quantity of mobile guest in the slice is simply the volume of the slice V times the rate of change of the concentration of the mobile guest C . The volume of the slice, V , is the cross-section area, A , times the width Δz . Since the mobile guest molecules can only diffuse

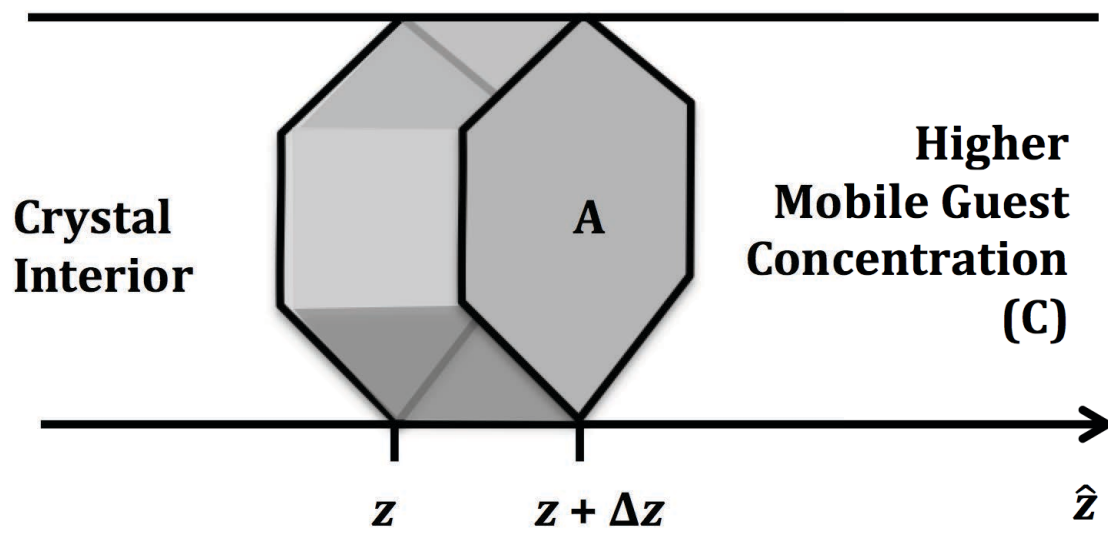


Figure I.7. Diagram of the diffusion axis.

along \hat{z} , the flux across the boundaries of the slice is in accord with Fick's first law in one dimension.

$$Influx = \left(D_p(q(z)) \cdot A \frac{\partial C}{\partial z} \right) \Big|_{z+\Delta z} \quad (Eq. I.6)$$

$$Outflux = \left(D_p(q(z)) \cdot A \frac{\partial C}{\partial z} \right) \Big|_z \quad (Eq. I.7)$$

The change in the local concentration of adsorbed guests with respect to time, $\frac{\partial q}{\partial t}$, is equal to the difference in the rate of adsorption and the rate of desorption. The rate of change for the concentration of adsorbed species is the kinetic adsorption coefficient, k_a , times the concentration of free guest, $C(z)$, times the concentration of available binding sites, $(q_{max} - q(z))$.

$$Adsorption = k_a \cdot C \cdot (q_{max} - q(z)) \cdot A \cdot \Delta z + O(\Delta z^2) \quad (Eq. I.8)$$

$$Desorption = k_d \cdot q(z) \cdot A \cdot \Delta z + O(\Delta z^2) \quad (Eq. I.9)$$

Combining Equations I.5, I.6, I.7, I.8, and I.9, and suppressing the z -dependence of q and the q -dependence of D_p for brevity:

$$A \frac{\partial C}{\partial t} \Delta z = \left(D_p A \frac{\partial C}{\partial z} \right) \Big|_{z+\Delta z} - \left(D_p A \frac{\partial C}{\partial z} \right) \Big|_z - k_a C (q_{max} - q) A \Delta z + k_d q A \Delta z + O(\Delta z^2) \quad (Eq. I.10)$$

Dividing by Δz :

$$A \frac{\partial C}{\partial t} = \frac{\left(D_p A \frac{\partial C}{\partial z} \right) \Big|_{z+\Delta z} - \left(D_p A \frac{\partial C}{\partial z} \right) \Big|_z}{\Delta z} - k_a C (q_{max} - q) A + k_d q A + O(\Delta z) \quad (Eq. I.11)$$

Taking the limit of infinitesimal Δz , the first term on the right-hand side becomes a derivative, per the following standard definition of a derivative:

$$\frac{\partial(\mathcal{F})}{\partial z} = \lim_{\Delta z \rightarrow 0} \frac{\mathcal{F}(z+\Delta z) - \mathcal{F}(z)}{\Delta z} \quad (Eq. I.12)$$

Therefore, as Δz goes to 0:

$$A \frac{\partial C}{\partial t} = \frac{\partial}{\partial z} \left(D_p A \frac{\partial C}{\partial z} \right) - k_a C (q_{max} - q) A + k_d q A \quad (Eq. I.13)$$

Since A is a constant, we divide by A, and restore the notation indicating the q -dependence of D_p :

$$\frac{\partial c}{\partial t} = \frac{\partial}{\partial z} \left(D_p(q) \frac{\partial c}{\partial z} \right) - k_a C(q_{max} - q) + k_d q \quad (\text{Eq. I.14})$$

Here we recover the final continuity equation for the mobile species (CHAPTER 2 Eq. 2.9).

Step B. The continuity equation for the bound guest can also be derived from mass balance.

The derivation is similar, but lacking in diffusion terms:

$$\text{Bound Guest Accumulation} = \text{Adsorption} - \text{Desorption} \quad (\text{Eq. I.15})$$

$$\text{Bound Guest Accumulation} = \int_V \frac{\partial q}{\partial t} dV = \int_z^{z+\Delta z} \frac{\partial Aq}{\partial t} dz = A \frac{\partial q}{\partial t} \Delta z + O(\Delta z^2) \quad (\text{Eq. I.16})$$

$$\text{Adsorption} = k_a \cdot C \cdot (q_{max} - q(z)) \cdot A \cdot \Delta z + O(\Delta z^2) \quad (\text{Eq. I.17})$$

$$\text{Desorption} = k_d \cdot q(z) \cdot A \cdot \Delta z + O(\Delta z^2) \quad (\text{Eq. I.18})$$

Combining these, and suppressing the z -dependence of q for brevity,

$$A \frac{\partial q}{\partial t} \Delta z = k_a C (q_{max} - q) A \Delta z - k_d q A \Delta z + O(\Delta z^2) \quad (\text{Eq. I.19})$$

Dividing by $A \cdot \Delta z$, and taking the limit as Δz goes to 0:

$$\frac{\partial q}{\partial t} = k_a C (q_{max} - q) - k_d q \quad (\text{Eq. I.20})$$

Here, we recover the Langmuir adsorption kinetic equation (CHAPTER 2 Eq. 2.5).

© I.4 PORE DIFFUSION COEFFICIENT

The nanopores are described using two radii. Whereas R_{p_o} is the radius of the original, unobstructed nanopores, R_p is the effective radius due to adsorption (the bound species has concentration q), see Figure I.8.

$$\text{Free volume fraction} = \frac{\pi R_p^2 L}{\pi R_{p_o}^2 L} \quad (\text{Eq. I.21})$$

$$1 - \text{Consumed volume fraction} = \frac{R_p^2}{R_{p_o}^2} \quad (\text{Eq. I.22})$$

$$1 - \frac{[\text{volume}]}{[\text{particle}]} \frac{[\text{moles}]}{[\text{volume}]} \frac{[\text{particle}]}{[\text{moles}]} = \frac{R_p^2}{R_{p_o}^2} \quad (\text{Eq. I.23})$$

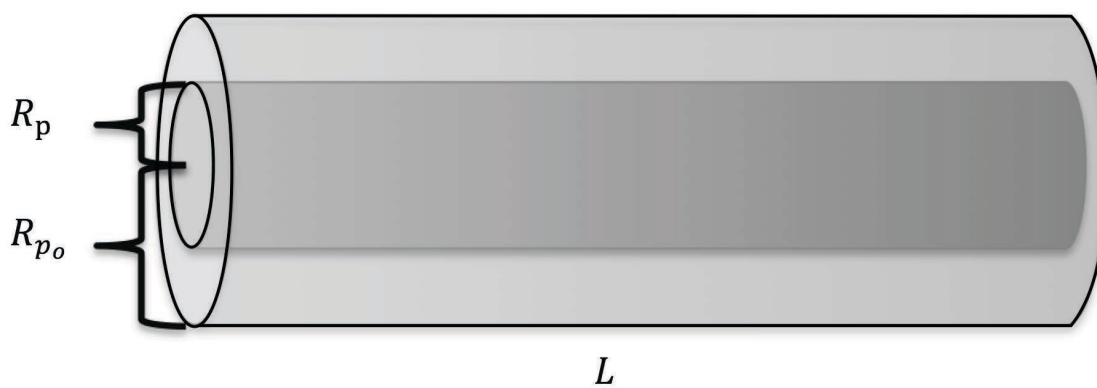


Figure I.8. Diagram of the initial pore radii (R_{p_0}) and the effective pore radii (R_p) reduced by adsorption of guest $\text{Au}_{25}(\text{GSH})_{18}$. L denotes the length of the pore (*i.e.* the length of the CJ crystal along the z -axis).

$$1 - \left(\frac{4}{3}\pi R^3\right) \cdot q(z) \cdot N_A = \frac{R_p^2}{R_{p_0}^2} \quad (\text{Eq. I.24})$$

The volume of an individual spherical guest molecule is taken as $\frac{4}{3}\pi R^3$. Multiplying this by Avogadro's number (N_A) yields the volume consumed per mole of guest molecules. Multiplying this by the local concentration of adsorbed species $q(z)$ [mol / volume] yields a unit-less fraction corresponding to the volume fraction consumed by guest. Subtracting the consumed volume fraction from Equation S21 yields the free volume fraction. Simplify and rearrange to obtain the effective pore radius (CHAPTER 2 Eq. 2.8).

$$R_p = R_{p_0} \left[1 - \left(\frac{4}{3}\pi R^3\right) q(z) N_A \right]^{0.5} \quad (\text{Eq. I.25})$$

We can plug this relationship into the empirical function that describes the reduction to the pore diffusion when the guest molecule radius (R) is a significant fraction of the effective pore radius (R_p).

$$\lambda = R/R_p \quad (\text{Eq. I.26})$$

$$\lambda(q(z)) = R / \left\{ R_{p_0} \left[1 - \left(\frac{4}{3}\pi R^3\right) q(z) N_A \right]^{0.5} \right\} \quad (\text{Eq. I.27})$$

$$\begin{aligned} D_p(q(z)) = D_0 & (1 + 1.125\lambda(\ln \lambda) - 1.56034\lambda + 0.528155\lambda^2 \\ & + 1.91521\lambda^3 - 2.81903\lambda^4 + 0.270788\lambda^5 \\ & + 1.10115\lambda^6 - 0.435933\lambda^7) \end{aligned} \quad (\text{Eq. I.28})$$

See Figure I.9 for the plot of D_p verses R_p

© I.5 EQUILIBRIUM CONSTANT AND GIBB'S FREE ENERGY

Regarding CHAPTER 2 Equation 2.4, there are numerous reports discussing the appropriate units or lack thereof for the equilibrium constant (K) when determining the change in standard Gibb's free energy (ΔG°). Here, we have adopted the interpretation of Milonjic⁵ to obtain a dimensionless

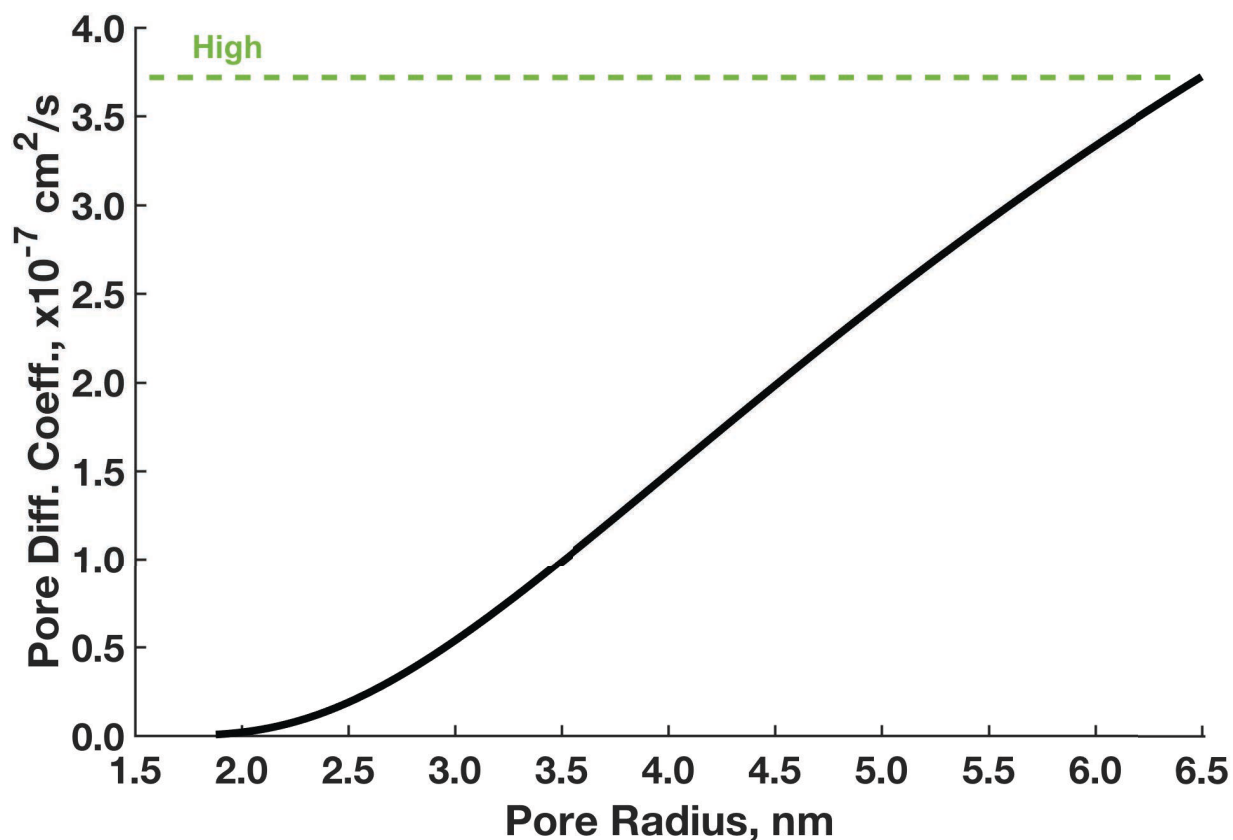


Figure I.9. *Black:* the pore diffusion coefficient (D_p) as a function of effective pore radius (R_p) calculated using Equation I.28 with a maximum R_p of 6.5 nm (13 nm diameter z-axial pores) and a guest molecule radius (R) of 1.54 nm (HYDROPRO¹ prediction). *Green:* highest D_p observed at early times and at low free-solution concentration (C_0). Note: the lowest D_p observed occurs at late time at high C_0 (CHAPTER 2 Figure 2.6) when R_p approaches R .

K by multiplying by 55.5 (molarity of water). This approach was also used by Zhou and Zhou⁶ in their assessment of the appropriate units to be used when calculating the thermodynamics of adsorption from Langmuir equilibrium constants. The work of Zhou and Zhou reveal the following equation to be the most appropriate method for calculating ΔG° from Langmuir constants for liquid-phase adsorption:

$$\Delta G^\circ = -RT \ln(55.5 K_L W_g) \quad (\text{Eq. I.29})$$

Here, the Langmuir equilibrium constant (K_L) has units of L/g, so multiplication by the molecular weight of the adsorbate (W_g) results in units of L/mol. The correction factor 55.5 has units of mol/L to obtain a unitless quantity. From the main text equilibrium adsorption experiment we found the Langmuir equilibrium constant to be 7.51 L/g. The molecular weight of the $\text{Au}_{25}(\text{GSH})_{18}$ adsorbate is 10,456 g/mol. Therefore, the change in standard Gibb's free energy was calculated to be -37.2 kJ/mol.

© I.6 SIZE CHARACTERIZATION OF GOLD NANOCCLUSERS BY DLS

Dynamic light scattering (DLS) was performed in triplicate on $\text{Au}_{25}(\text{GSH})_{18}$ nanoclusters suspended in 20 mM HEPES pH 8.0 at 20° C using a Malvern Zetasizer Nano ZS with 633nm laser. The size distribution by intensity shows two monodisperse peaks with hydrodynamic radii of 1.69 ± 0.09 nm and 89.8 ± 12.4 that correspond to monomeric $\text{Au}_{25}(\text{GSH})_{18}$ nanoclusters and higher order aggregates respectively (Figure I.10 *Left*). However, the size distribution by mass only reveals the monodisperse 1.69 ± 0.09 nm peak corresponding to monomeric $\text{Au}_{25}(\text{GSH})_{18}$ nanoclusters (Figure I.10 *Right*) indicating this is the predominant species in the solution. Therefore, R_h was set to 1.69 nm in the main text and the free diffusion coefficient D_0 was calculated from R_h using the Stokes Einstein relationship (CHAPTER 2 *Eq. 2.7*). This result is

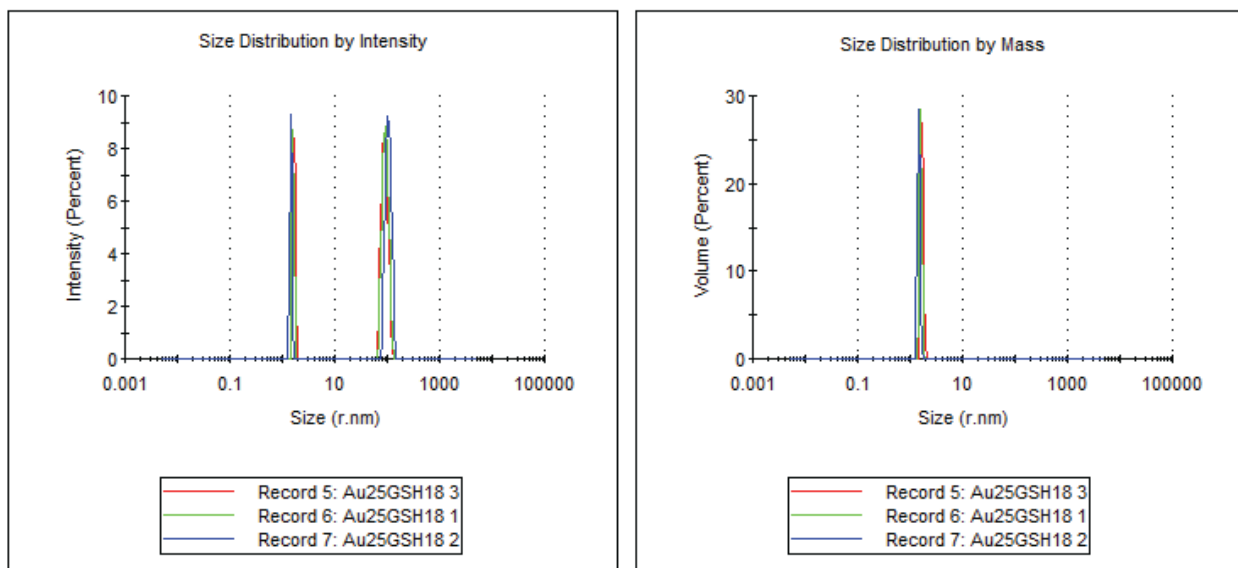


Figure I.10. Au₂₃(GSH)₁₈ nanocluster size data from DLS analysis. *Left:* Size distribution by intensity shows two monodisperse peaks corresponding to monomeric nanoclusters (1.69 ± 0.09 nm) and higher order aggregates (89.8 ± 12.4 nm). *Right:* Size distribution by mass shows only one monodisperse peak corresponding to monomeric nanoclusters (1.69 ± 0.09 nm).

only modestly higher than the HYDROPRO¹ predicted hydrodynamic radius of 1.54 nm, which was retained as the adsorbed guest molecular radius (R).

◎ I.7 HYDROPRO FREE DIFFUSION COEFFICIENT AND GUEST RADIUS

The free diffusion coefficient (D_0) and the radius (R) for Au₂₅(GSH)₁₈ nanoclusters in an aqueous environment was determined from the molecular structure (CHAPTER 2 Figure 2.1)⁷ using the HYDROPRO hydrodynamic bead model.¹ Key HYDROPRO output lines are emphasized in Figure I.11. HYDROPRO parameters and results are as follows. Note: the experimental hydrodynamic radius (R_h) measured by DLS was somewhat larger.

◎ I.8 CJ PROEIN SEQUENCE

```
MKEYTLDKAHTDVGFKIKHLQISNVKGNFKDYSVIDFDPASAEFKKLDVTIKIASVNTENQTR
DNHLQDDFFKAKKYPDMTFTMKKYEKIDNEKGKMTGTLTIAGVSKDIVLDAEIGGVAKGKDGK
EKIGFSLNGKIKRSDFKFATSTSTITLSDDINLNI EVKANEKEGGSHHHHHH* *
```

◎ I.9 CJ DNA SEQUENCE

```
TTAAGAAGGAGATATACATATGAAAAAAGTTCTGCTGAGCAGCCTGGTTGCAGTTAGCCTGCTG
AGTACCGGTCTGTTTGCAAAAGAATATACCCTGGATAAAGCCATACCGATGTTGGCTTTAAAA
TCAAACATCTGCAGATTAGCAATGTGAAAGGCAACTTTAAAGATTATAGCGCAGTGATCGATTT
TGATCCGGCAAGTGCAGAATTCAAAAACTGGATGTGACCATTAAAATCGCCAGCGTGAATACC
GAAAATCAGACCCGTGATAATCATCTGCAGCAGGATGACTTCTTCAAAGCCAAAAAATACCCGG
ATATGACCTTTACCATGAAAAAATACGAGAAAATCGATAACGAAAAGGCAAAATGACCGGCAC
CCTGACCATTGCCGGTGTAGCAAAGATATTGTTCTGGATGCAGAAATTGGTGGTGTGCCCCAA
GGTAAAGATGGCAAAGAAAAAATTGGCTTTAGCCTGAACGGCAAAATCAAACGTAGCGATTTCA
AATTTGCAACCAGCACCAGCACCATTACCCTGAGTGATGACATTAATCTGAACATTGAAGTGAA
AGCCAACGAGAAAGAAGGTGGTAGTCATCACCACCACCATCACTAATAACTCGAGCACCACCAC
CACCACCACTGAGATCCGGCTG
```

 HYDROPRO, Version 10, September 2011
 A. Ortega, D. Amoros, J. Garcia de la Torre,
 "Prediction of hydrodynamic and other solution properties of
 rigid proteins from atomic- and residue-level models"
 Biophys. J. 101, 892-898 (2011).

SUMMARY OF DATA AND RESULTS

This file : Au25GSH18_20C-res.txt
 Case : 1/10/2017 3:11:10 PM
 Structural file : Au25GSH18.pdb

Radius of elements in primary model : 2.84 Angs.
 Type of hydropro calculation : 1
 Temperature: 20.0 centigrade
 Solvent viscosity: 0.01000 poise
 Molecular weight: 10500. Da
 Solute partial specific volume: 0.520 cm³/g
 Solution density: 1.000 g/cm³

Translational diffusion coefficient: 1.394E-06 cm²/s

Radius of gyration: 1.140E-07 cm
 Volume: 1.197E-20 cm³
 Rotational diffusion coefficient: 4.515E+07 s⁻¹

Relaxation time (1): 4.090E-09 s
 Relaxation time (2): 4.083E-09 s
 Relaxation time (3): 4.023E-09 s
 Relaxation time (4): 4.006E-09 s
 Relaxation time (5): 3.986E-09 s

Harmonic mean (correlation) time: 4.037E-09 s
 Intrinsic viscosity: 2.281E+00 cm³/g
 Sedimentation coefficient: 2.882E+00 Svedberg

Center of diffusion (x): 1.739E-07 cm
 Center of diffusion (x): 1.757E-07 cm
 Center of diffusion (x): 1.755E-07 cm

Generalized (6x6) diffusion matrix: (Dtt Dtr)
 (Drt Drr)

1.414E-06	-8.063E-09	-1.110E-08	-6.932E-04	-1.592E-03	-1.473E-03
-7.865E-09	1.417E-06	-6.301E-10	-2.089E-03	-1.152E-02	4.017E-03
-1.130E-08	-4.394E-10	1.412E-06	-1.679E-03	4.312E-03	1.120E-02
-6.932E-04	-2.089E-03	-1.679E-03	4.517E+07	-1.778E+05	-1.137E+06
-1.592E-03	-1.152E-02	4.312E-03	-1.765E+05	4.533E+07	3.111E+05
-1.473E-03	4.017E-03	1.120E-02	-1.136E+06	3.135E+05	4.494E+07

List of equivalent radii

Translational: 1.540E-07

Gyration : 1.472E-07
 Volume : 1.419E-07
 Rotation (1): 1.581E-07
 Rotation (2): 1.580E-07
 Rotation (3): 1.572E-07
 Rotation (4): 1.570E-07
 Rotation (5): 1.567E-07
 Rotation (h): 1.552E-07

Intrinsic viscosity: 1.560E-07
 Longest distance: 1.810E-07
 Longest distance : 3.619E-07 cm

Figure I.11. HYDROPRO output for determining the hydrodynamic parameters of Au₂₅(GSH)₁₈. Important parameters have been highlighted.

Table I.1. Equilibrium adsorption isotherm fit quality. Data were fit to their respective isotherm equations *via* least squares using the Matlab version 9.1.0 Curve Fitting Tool (Natick, MA). Equations were adopted from work done by Xunjun Chen on modeling experimental adsorption isotherm data.⁸ *SSE* refers to the sum of squared errors. *R*² refers to the coefficient of multiple determination. *DFE* refers to the residual degrees of freedom (the number of response values minus the number of fit coefficients). *AdjRSqr* refers to a degree of freedom adjusted *R*² value. *RMSE* refers to the root mean squared error.

	<i>SSE</i>	<i>R</i> ²	<i>DFE</i>	<i>AdjRSqr</i>	<i>RMSE</i>	Equation
Langmuir non-linear	7.448E+04	0.9659	17	0.9639	6.619E+01	$q = q_{max} \frac{K_L C}{(1 + K_L C)}$
Langmuir linear	1.339E-02	0.9846	17	0.9837	2.807E-02	$\frac{C}{q} = \frac{1}{q_{max} K_L} + \frac{C}{q_{max}}$
Freundlich non-linear	1.929E+05	0.9116	17	0.9064	1.065E+02	$q = K_F C^{1/n}$
Freundlich linear	7.219E-01	0.9243	17	0.9198	2.061E-01	$\ln q = \ln K_F + \frac{1}{n} \ln C$

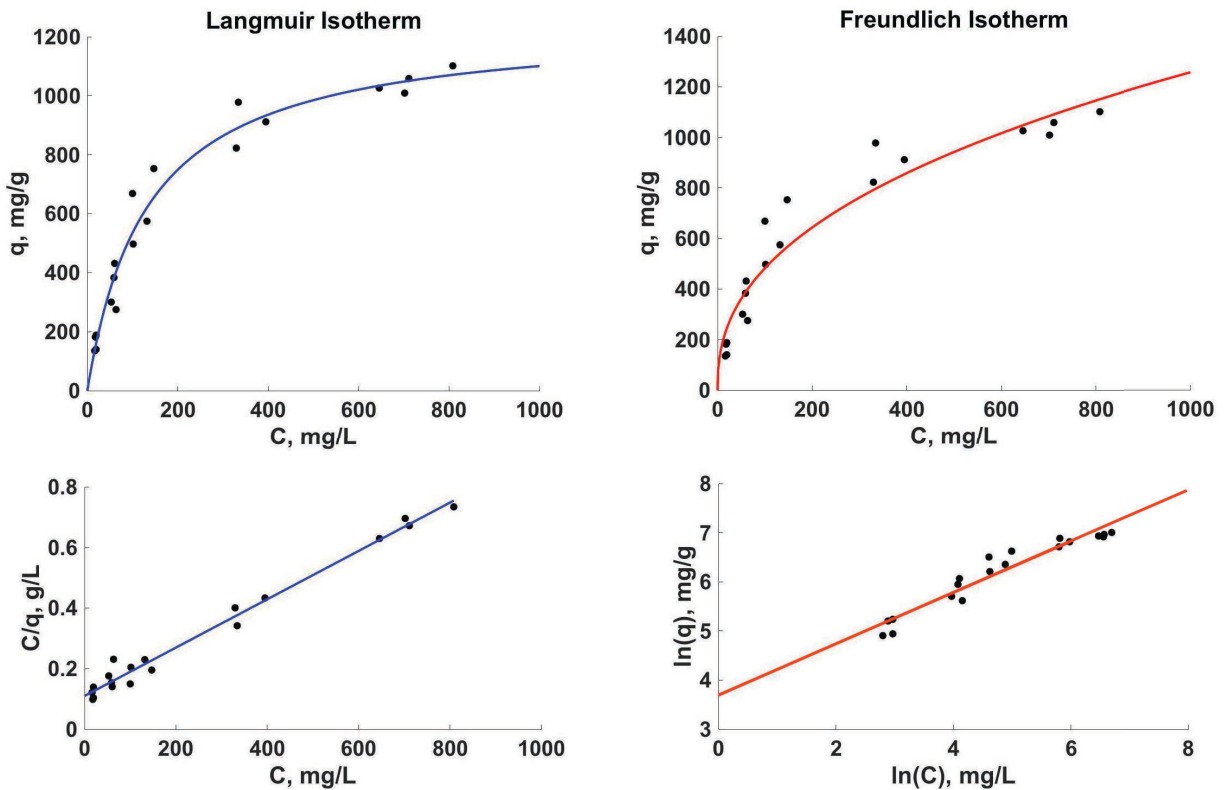


Figure I.12. Comparison of Langmuir (left) and Freundlich (right) non-linear (top) and linear (bottom) equilibrium adsorption isotherms. The fit was slightly superior for the Langmuir isotherm (see Table I.1).

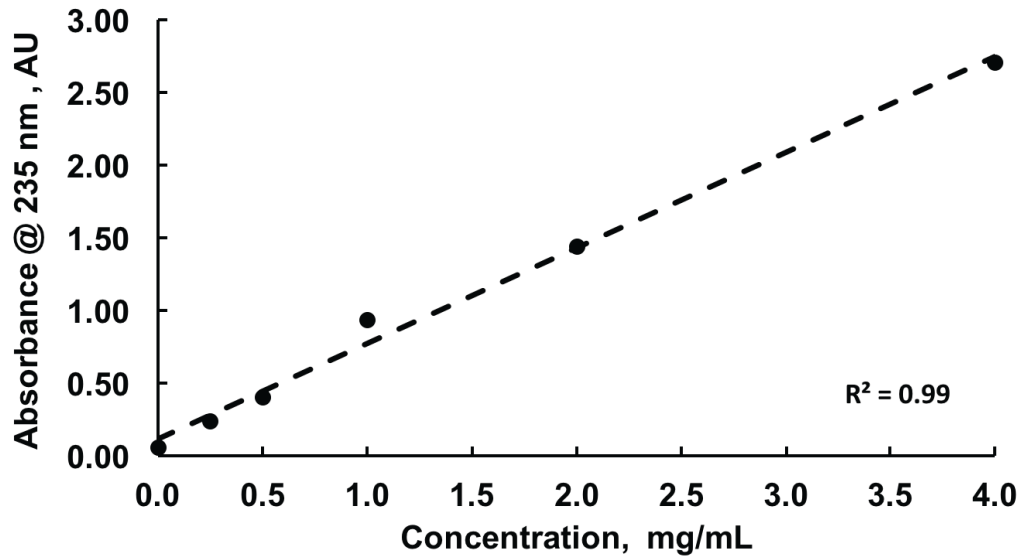


Figure I.13. Absorption standard used to determine the concentration of $\text{Au}_{25}(\text{GSH})_{18}$ nanoclusters in the bulk adsorption equilibrium experiment (Figure I.12 and CHAPTER 2 Figure 2.2)

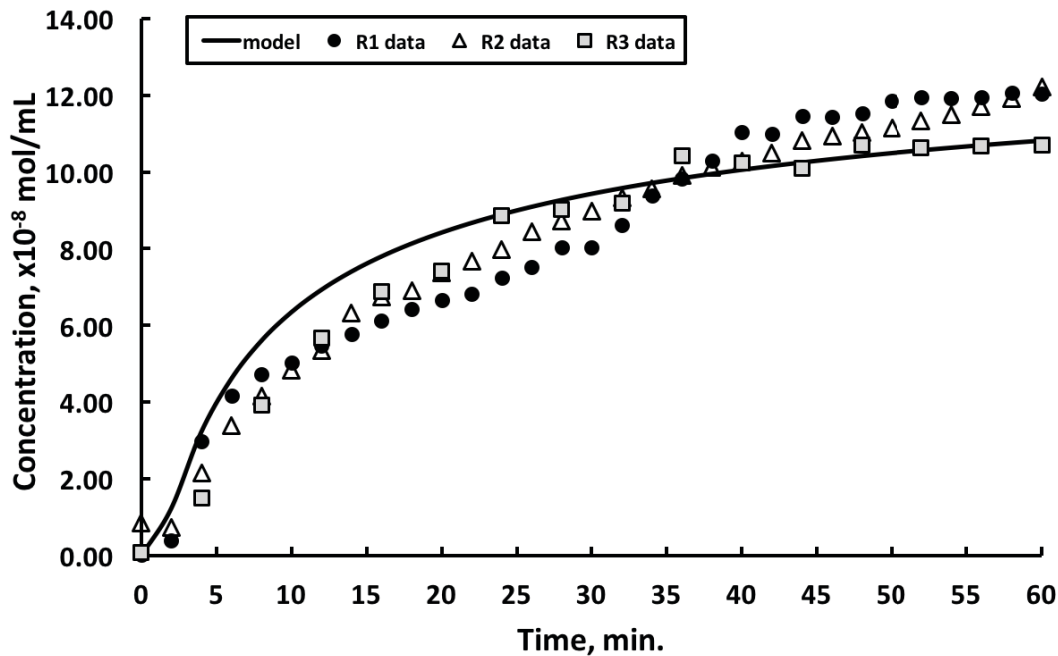


Figure I.14. Effective concentration (C_{0e}) at the crystal surface boundary as a function of time; Replicate data values (R1, R2, and R3) represent the average free-solution concentration at the crystal boundary obtained from confocal images while model values were calculated using Equation I.3 with $x \approx 0.03$.

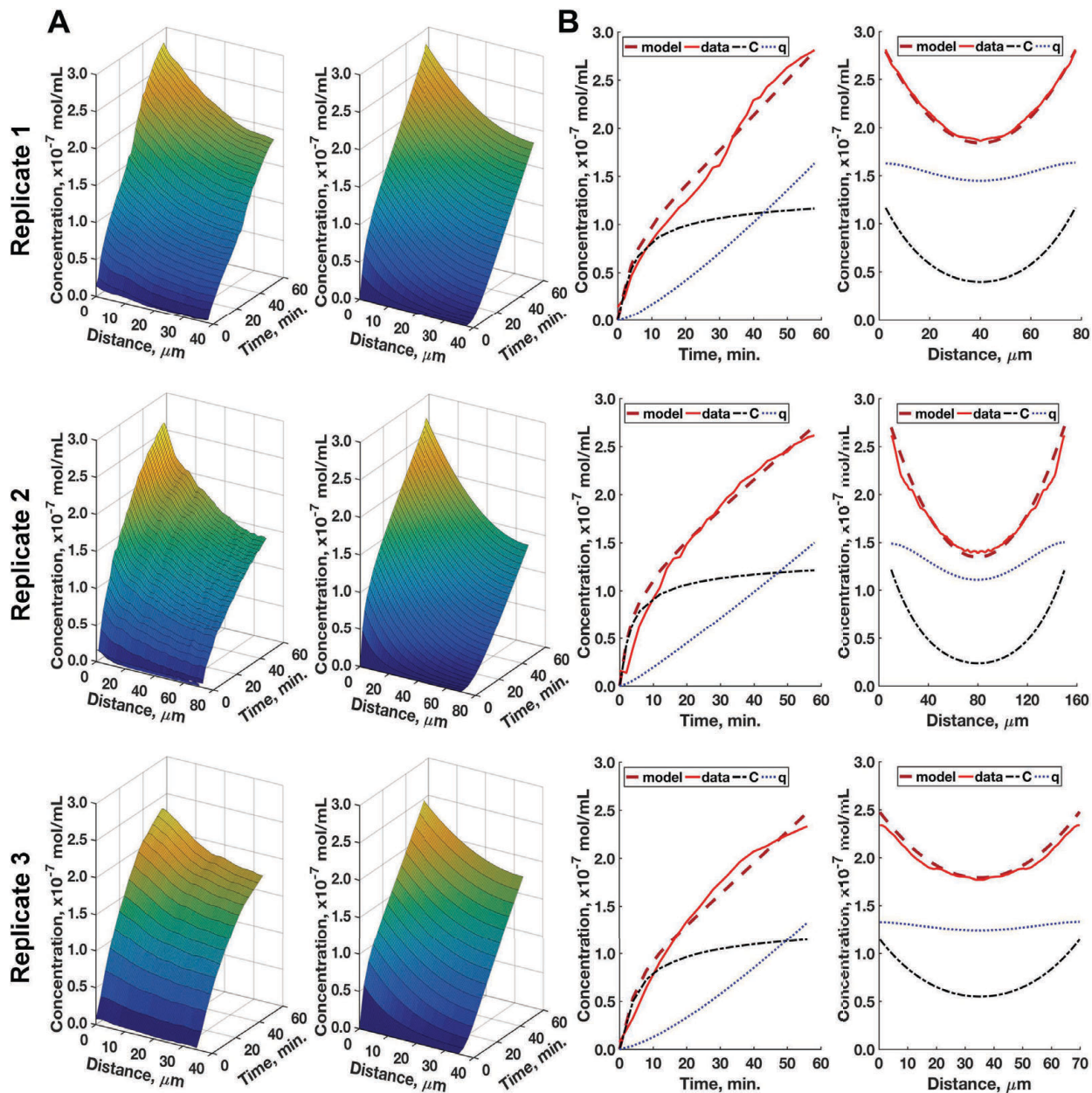


Figure I.15. Individual fits to three replicate 60-minute confocal loading experiments. Fit results can be found in Table 2 of the main text. (A.) Concentration, distance, and time surface plots of the left-hand side ($z = 0$ to $z = L/2$) of replicate diffusion profiles. *Left:* confocal data. *Right:* FEM fit data. (B.) Comparison of replicate FEM fits to the respective experimental confocal data, the fit line represents the sum of C and q . *Left:* data taken just inside the crystal at the boundary ($z = 0$) over the entire 60-minutes. *Right:* data taken at the 60-minute time point over the entire crystal ($z = 0$ to $z = L$).

REFERENCES

- (1) Ortega, A.; Amorós, D.; García de la Torre, J. Prediction of Hydrodynamic and Other Solution Properties of Rigid Proteins from Atomic- and Residue-Level Models. *Biophys. J.* **2011**, *101* (4), 892–898.
- (2) Kowalski, A. E.; Huber, T. R.; Ni, T. W.; Hartje, L. F.; Appel, K. L.; Yost, J. W.; Ackerson, C. J.; Snow, C. D. Gold Nanoparticle Capture within Protein Crystal Scaffolds. *Nanoscale* **2016**, *8* (25), 12693–12696.
- (3) Sanner, M. F.; Olson, A. J.; Spehner, J. C. Reduced Surface: An Efficient Way to Compute Molecular Surfaces. *Biopolymers* **1996**, *38* (3), 305–320.
- (4) *The Mathematics of Diffusion*; Oxford University Press: Oxford, New York, 1980.
- (5) Milonjić, S. K. A Consideration of the Correct Calculation of Thermodynamic Parameters of Adsorption. *J. Serbian Chem. Soc.* **2007**, *72* (12), 1363–1367.
- (6) Zhou, X.; Zhou, X. The Unit Problem in the Thermodynamic Calculation of Adsorption Using the Langmuir Equation. *Chem. Eng. Commun.* **2014**, *201* (11), 1459–1467.
- (7) Rojas-Cervellera, V.; Rovira, C.; Akola, J. How Do Water Solvent and Glutathione Ligands Affect the Structure and Electronic Properties of Au₂₅(SR)₁₈? *J. Phys. Chem. Lett.* **2015**, *6* (19), 3859–3865.
- (8) Chen, X. Modeling of Experimental Adsorption Isotherm Data. *Information* **2015**, *6* (1), 14–22.

APPENDIX II

SUPPORTING INFORMATION

FOR CHAPTER 3

SUPPORTING INFORMATION

CHARACTERIZING THE CYTOTOXICITY OF VARIOUS CROSS-LINKING CHEMISTRIES FOR THE PRODUCTION OF BIOSTABLE LARGE-PORE PROTEIN CRYSTAL MATERIALS

● II.1 REAGENTS

The following chemicals were purchased and used without further purification. From Sigma-Aldrich: dimethylamine borane complex (DMAB), trimethylamine N-oxide (TMAO), glutaraldehyde solution (GA) (25% in H₂O), 1-Ethyl-3-(3-dimethylaminopropyl)carbodiimide (EDC), sodium phosphate dibasic (Na₂HPO₄), potassium phosphate monobasic (KH₂PO₄), ammonium sulfate ([NH₄]₂SO₄), and sodium acetate (CH₃COONa). From VWR: HEPES, glycerol, and bis-tris. From Acros Organics: glyoxal solution (40% in H₂O) referred to as oxaldehyde (OA) throughout this manuscript. From Alfa Aesar: hydroxylamine solution (50% in H₂O) and imidazole. From EMD Millipore: sulfuric acid (H₂SO₄). From PHARMCO-AAPER: Ethyl Alcohol 200 proof. From Fisher Scientific: sodium borate, boric acid, NaCl and KCl. From J.T. Baker: citric acid.

Other reagents from Thermo Scientific and Sigma-Aldrich were used to make mTacsimateTM: 1.83 M malonic acid, 0.25 M sodium citrate, 0.12 M succinic acid, 0.3 M D-L malic acid, 0.4 M acetic acid, 0.5 M sodium formate, and 0.16 M sodium tartrate—titrated to pH 7.5. mTacsimateTM is a modified blend of TacsimateTM from Hampton Research that removes ammonium from the solution, thereby removing primary amines that can interfere with glutaraldehyde and OA cross-linking.

◎ II.2 PROTEIN EXPRESSION, PURIFICATION, AND CRYSTALLIZATION

t Lyophilized hen egg white lysozyme (HEWL) was purchased from Hampton Research (Cat. #: 12650-88-3), used with no further purification, and crystallized per a modified version of a previously reported bulk crystallization method.¹ Three stock solutions were made: 160 g/L NaCl in DI water, 85 g/L HEWL in DI water, and 100 mM sodium acetate pH 4.6 in DI water. HEWL stock solution was stored at 10 °C or lower when not in use. The three stock solutions were added to a single well of a 9 cavity PYREX spot plate in consecutive order: 50 µL sodium acetate solution, 50 µL NaCl solution, and 100 µL HEWL stock solution. The solution mixture was gently pipetted to mix and allowed to incubate without disturbance at room temperature for 24 hours. After 24 hours, lysozyme crystals have grown and are visible in solution and on the surface of the glass plate; longer growth times yielded larger crystals.

The target gene CJ was modified from the gene vector encoding protein CJ0 obtained from the Protein Structure Initiative: Biology-Materials Repository (Genebank ID: cj0420, Protein Data Bank ID: 2fgs). For ease of uniform expression and purification, the CJ0 gene was codon optimized and the periplasmic signaling peptide deleted thereby yielding CJ. The CJ gene was encoded in expression vector pSB3 with a C-terminal 6xHis tag and expressed in *Escherichia coli* BL21(DE3) pLysS cells using a glucose/lactose induction system² at 17° C for 36 hours. Cells were lysed by sonication and the CJ protein purified *via* nickel affinity capture on a HisTrap HPTM column (GE Healthcare). A single chromatography step provided sufficient purity for crystallization. Purified CJ protein was buffer exchanged into 0.15 M NaCl, 10 mM HEPES, and 10% glycerol at pH 7.5, concentrated to 15 mg/mL, and stored at -30° C. CJ-LPCs were grown overnight by sitting drop vapor diffusion at 20° C in 3.3–3.6 M AmSO₄, 100 mM bis-tris at pH 7.0.

◎ II.3 CJ PROTEIN SEQUENCE

MKEYTLDKAHTDVGFKIKHLQISNVKGNFKDYSAVIDFDPASAEFKKLDVTIKIASVNTENQTRDNHLQDDFFKAK
KYPDMTFTMKKYEKIDNEKGKMTGTLTIAGVSKDIVLDAEIGGVAKGKDGKEKIGFSLNGKIKRSDFKFATSTSTIT
LSDDINLNIEVEANEKEGGSHHHHHH

◎ II.4 CJ DNA SEQUENCE

TTAAGAAGGAGATATACATATGAAAAAAGTTCTGCTGAGCAGCCTGGTTGCAGTTAGCCTGCTGAGTACCGGTCTGT
TTGCAAAAAGAATATACCCTGGATAAAGCCCATACCGATGTTGGCTTTAAAATCAAACATCTGCAGATTAGCAATGTG
AAAGGCAACTTTAAAGATTATAGCGCAGTGATCGATTTTGGATCCGGCAAGTGCAGAATTCAAAAACTGGATGTGAC
CATTAAAATCGCCAGCGTGAATACCGAAAATCAGACCCGTGATAATCATCTGCAGCAGGATGACTTCTTCAAAGCCA
AAAAATACCCGGATATGACCTTTACCATGAAAAAATACGAGAAAATCGATAACGAAAAAGGCAAAATGACCGGCACC
CTGACCATTGCCGGTGTAGCAAAGATATTGTTCTGGATGCAGAAATTGGTGGTGTGCCAAAGGTAAAGATGGCAA
AGAAAAAATTGGCTTTAGCCTGAACGGCAAAATCAAACGTAGCGATTTCAAATTTGCAACCAGCACCAGCACCATTA
CCCTGAGTGATGACATTAATCTGAACATTGAAGTGAAAGCCAACGAGAAAGAAGGTGGTAGTCATCACCACCACCAT
CACTAATAACTCGAGCACCACCACCACCACACTGAGATCCGGCTG

◎ II.5 CJ-LPC MATERIAL CROSS-LINKING

In all cases, cross-linking was performed under conditions as similar as possible to the crystal growth conditions to mitigate crystal degradation caused by harsh solution conditions.

◎ II.5.1 Glutaraldehyde (GA)

Prior to cross-linking, crystals were washed by loop transferring them into a 90% mTacsimateTM, 10% glycerol mixture at pH 7.5 for 1 hour to remove residual CJ monomers. Crystals were then transferred into a fresh mixture of 90% mTacsimateTM, 10% glycerol at pH 7.5, and cross-linked for 2 hours by the direct addition of 1% glutaraldehyde and 25 mM DMAB. The cross-linking reaction was quenched by transferring CJ-LPCs into a solution of 0.3 M hydroxylamine, 25 mM DMAB, 0.15 M NaCl, and 0.1 M citric acid at pH 5.0 for 1 hour. After cross-linking and quenching, the crystals were washed and stored in fresh 4.2 M TMAO, 175 mM H₂SO₄ solution at pH 7.5.

☉ II.5.2 Oxaldehyde (OA)

Prior to cross-linking, crystals were washed by loop transferring them into a 90% mTacsimateTM, 10% glycerol mixture at pH 7.5 for 1 hour to remove residual CJ monomers. Crystals were then transferred into a fresh mixture of 90% mTacsimateTM, 10% glycerol at pH 7.5, and cross-linked for 2 hours by the direct addition of 1% OA and 25 mM DMAB. The cross-linking reaction was quenched by transferring CJ-LPCs into a solution of 0.3 M hydroxylamine, 25 mM DMAB, 0.15 M NaCl, and 0.1 M citric acid at pH 5.0 for 1 hour. After cross-linking and quenching, the crystals were washed and stored in fresh 4.2 M TMAO, 175 mM H₂SO₄ solution at pH 7.5.

☉ II.5.3 1-Ethyl-3-(3-dimethylaminopropyl)carbodiimide (EDC)

Prior to cross-linking, crystals were washed by loop transferring them into a 4.2 M TMAO, 175 mM H₂SO₄ solution at pH 7.5 for 1 hour to remove residual CJ monomers. After washing, crystals were transferred into a fresh mixture of 4.2 M TMAO, 175 mM H₂SO₄ at pH 7.5 containing 100 mM EDC, 50 mM imidazole and cross-linked for 1 hour. Crystals were then moved to a second cross-linking mixture of 5.0 M NaCl, 200 mM MES pH 5.5 containing 200 mM EDC, 100 mM imidazole, 50 mM sodium malonate and cross-linked for an additional 2 hours. The cross-linking reaction was quenched by transferring CJ-LPCs into 5.0 M NaCl, 100 mM Borate buffer pH 10.0 for 30 min. After cross-linking and quenching, the crystals were washed and stored in fresh 4.2 M TMAO, 175 mM H₂SO₄ solution at pH 7.5.

☉ II.6 HEWL MATERIAL CROSS-LINKING

In all cases, cross-linking was performed under conditions as similar as possible to the crystal growth conditions to mitigate crystal degradation caused by harsh solution conditions.

⊙ **II.6.1 Glutaraldehyde (GA)**

Prior to cross-linking, crystals were washed by loop transferring them into 2.5 M NaCl, 50 mM sodium acetate pH 4.6 for 15 minutes to remove residual HEWL monomers. Crystals were then transferred into a fresh mixture of 2.5 M NaCl, 50 mM sodium acetate pH 4.6 containing 10% glutaraldehyde and cross-linked for 2 hours. The cross-linking reaction was quenched by transferring HEWL crystals into a solution of 0.3 M hydroxylamine, 25 mM DMAB, 0.15 M NaCl, and 0.1 M citric acid at pH 5.0 for 1 hour. After cross-linking and quenching, the crystals were washed and stored in fresh 2.5 M NaCl, 50 mM sodium acetate pH 4.6.

⊙ **II.6.2 Oxaldehyde (OA)**

Prior to cross-linking, crystals were washed by loop transferring them into 2.5 M NaCl, 50 mM sodium acetate pH 4.6 for 15 minutes to remove residual HEWL monomers. Crystals were then transferred into a fresh mixture of 2.5 M NaCl, 50 mM sodium acetate pH 4.6 containing 10% oxaldehyde and cross-linked for 2 hours. The cross-linking reaction was quenched by transferring HEWL crystals into a solution of 0.3 M hydroxylamine, 25 mM DMAB, 0.15 M NaCl, and 0.1 M citric acid at pH 5.0 for 1 hour. After cross-linking and quenching, the crystals were washed and stored in fresh 2.5 M NaCl, 50 mM sodium acetate pH 4.6.

⊙ **II.6.3 1-Ethyl-3-(3-dimethylaminopropyl)carbodiimide (EDC)**

Prior to cross-linking, crystals were washed by loop transferring them into 2.5 M NaCl, 50 mM MES buffer at pH 5.5 for 15 minutes to remove residual HEWL monomers. After washing, crystals were transferred into a fresh mixture of 2.5 M NaCl, 50 mM MES buffer at pH 5.5 containing 100 mM EDC, 50 mM imidazole, and cross-linked for 1 hour. Crystals were then moved to a second cross-linking mixture of 2.5 M NaCl, 200 mM MES buffer at pH 5.5 containing 200 mM EDC, 10 mM imidazole, 50 mM sodium malonate and cross-linked for an additional 2 hours. The cross-

linking reaction was quenched by transferring HEWL crystals into 2.5 M NaCl, 100 mM Borate buffer pH 10.0 for 30 min. After cross-linking and quenching, the crystals were washed and stored in fresh 2.5 M NaCl, 50 mM sodium acetate pH 4.6.

☉ II.7 EXPERIMENTAL PROTOCOLS

☉ II.7.1 Stereomicroscopy Imaging

To monitor potential changes in the macroscopic crystal morphology and surface structure, all cross-linked CJ-LPCs and HEWL crystals were imaged using a Motic SMZ168 Series Stereo Zoom Microscope immediately following cross-linking (CHAPTER 3 Figure 3.2 *pre-incubation*) and again after a 24-hour incubation with HDFa cells (CHAPTER 3 Figure 3.2 *post-incubation*) at 37° C with 5% CO₂

No macroscopic degradation of crystal structure or changes in morphology were observed in any of the cross-linked CJ-LPC samples (CJ/GA, CJ/OA, and CJ/EDC) immediately following cross-linking when compared to washed non-cross-linked (NCL) CJ-LPCs. In addition, none of the cross-linked CJ-LPC samples demonstrated substantial macroscopic degradation of crystal structure or changes in morphology after incubation with HDFa cells. However, CJ/NCL samples completely dissolved after incubation with HDFa cells. This data indicates that all three cross-linking chemistries are necessary and sufficient to stabilize the macroscopic crystal morphology and surface structure of CJ-LPCs.

In contrast, after initial cross-linking of HEWL crystals, substantial cracks were observed in the EDC cross-linked crystals (HEWL/EDC) and slight cracking in the OA cross-linked crystals (HEWL/OA). After incubation with HDF cells HEWL/NCL and HEWL/EDC crystals completely dissolved while HEWL/OA crystals demonstrated severe cracking and disintegration. No substantial macroscopic degradation of crystal structure or substantial changes in morphology

were observed in HEWL crystals cross-linked with GA. This data indicates that only GA is sufficient to stabilize the macroscopic crystal morphology and surface structure of HEWL crystals.

☉ II.7.2 Scanning Electron Imaging

The size distribution of fragmented crystals was determined using a JEOL JSM-6500F field emission scanning electron microscope equipped with a Thermo Electron energy dispersive X-ray spectrometer (EDS). Multiple SEM images were stitched together using Fiji^{3,4} to form a large tagged image file (Figure II.1A) of a desiccated 1-2 μL drop of fragmented CJ-LPC material suspended in pure H_2O . A binary image (Figure II.1B) was then created and processed using particle analysis in Fiji to generate particle size data which was quantified *via* histogram plotting tools in MATLAB version 9.1.0 (Natick, MA) (Figure II.1C).

☉ II.7.3 CJ Crystal X-ray Diffraction (XRD) and Data Processing

All CJ-LPC materials were loop transferred into cryoprotectant (4.2 M TMAO, 175 mM H_2SO_4 pH 7.5) and soaked for at least 5 minutes prior to flash freezing in a cryogenic nitrogen stream at 100 K. The diffraction quality was then assessed using a Rigaku Compact HomeLab with a micro-focus X-ray generator and a Pilatus 200K detector based on a 15-frame data collection strategy; each frame was separated by a 2.0° omega offset and exposed for 60 seconds. Reflection data was indexed and scaled using HKL-3000 software (HKL Research Inc.). See Tables II.1-II.5 for scale output logs for CJ-LPC. The high-resolution estimates for all CJ-LPCs was based on a signal to noise ratio above two ($Ave. I / Ave. Err \geq 2.0$). Refer to CHAPTER 3 Figure 3.3 for representative diffraction patterns and a summary of the high-resolution estimates for each CJ-LPC material type.

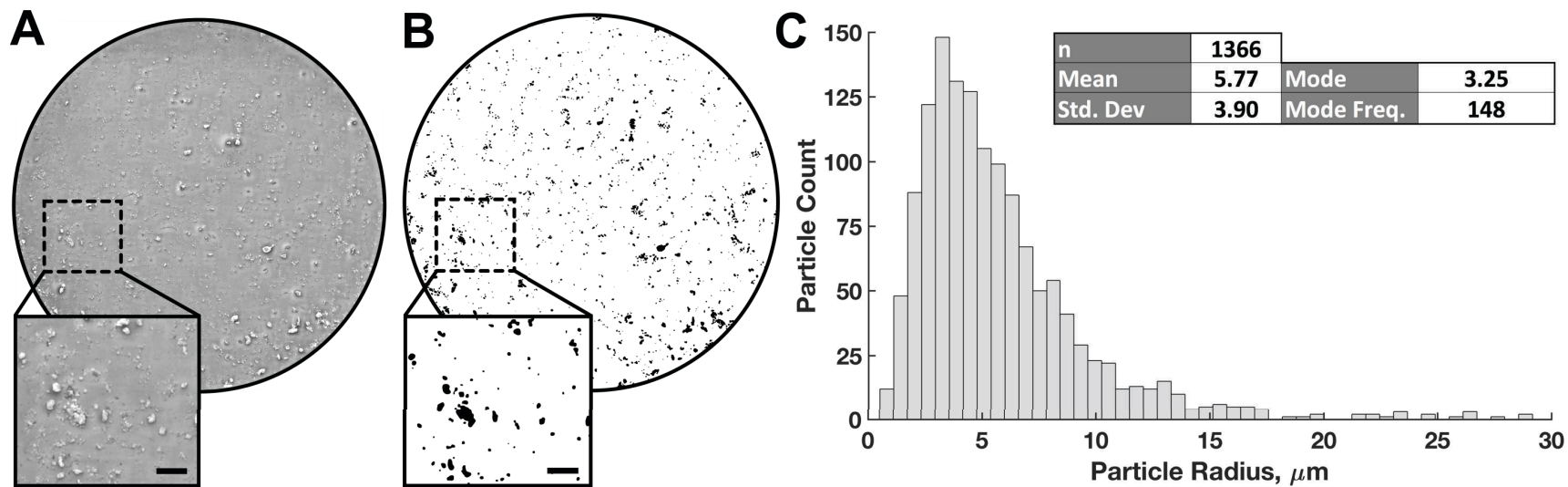


Figure II.1. (A) SEM image mosaic composed of 41 images showing fragmented CJ-LPCs. Panel: close-up of particles. *Scale Bar:* 50 μm . (B) Binary image of (A), used for particle analysis. (C) Histogram of particle spherical radii calculated from total particle area. *Panel:* size statistics.

Table II.1. X-ray diffraction scale output logs for non-cross-linked CJ-LPCs prior to incubation with HDFa cells; *Green Highlight*: high-resolution estimate.

Non-Cross-Linked (NCL) C1						Non-Cross-Linked (NCL) C2						Non-Cross-Linked (NCL) C3					
Lower, Å	Upper, Å	Ave. I	Ave. Err	CC1/2	CC*	Lower, Å	Upper, Å	Ave. I	Ave. Err	CC1/2	CC*	Lower, Å	Upper, Å	Ave. I	Ave. Err	CC1/2	CC*
50.0	7.86	30.3	1.4	0.878	0.967	50.0	7.86	29.5	1.4	0.994	0.998	50.0	7.86	31.5	1.5	0.996	0.999
7.86	6.24	19.6	1.2	0.984	0.996	7.86	6.24	17.5	1.1	0.966	0.991	7.86	6.24	14.4	1.2	1.000	1.000
6.24	5.46	19.9	1.4	0.985	0.996	6.24	5.46	18.7	1.3	0.981	0.995	6.24	5.46	16.0	1.4	0.990	0.998
5.46	4.96	23.6	1.6	0.989	0.997	5.46	4.96	22.0	1.4	0.859	0.961	5.46	4.96	18.9	1.7	-0.986	0.000
4.96	4.60	20.8	1.5	2.462	1.193	4.96	4.60	20.8	1.5	0.000	0.000	4.96	4.60	21.0	1.9	-0.986	0.000
4.60	4.33	23.3	1.7	2.462	1.193	4.60	4.33	22.4	1.7	0.972	0.993	4.60	4.33	19.6	2.4	-0.986	0.000
4.33	4.11	25.8	2.0	0.929	0.981	4.33	4.11	15.7	1.7	0.998	1.000	4.33	4.11	17.9	2.4	-0.986	0.000
4.11	3.94	25.1	2.1	0.931	0.982	4.11	3.94	23.3	2.1	0.694	0.905	4.11	3.94	14.8	2.6	0.996	0.999
3.94	3.78	21.7	2.3	0.833	0.953	3.94	3.78	19.6	2.2	0.888	0.970	3.94	3.78	19.1	3.0	0.404	0.759
3.78	3.65	16.7	2.2	0.552	0.844	3.78	3.65	15.2	2.2	0.981	0.995	3.78	3.65	15.8	3.3	0.994	0.998
3.65	3.54	12.1	2.2	0.571	0.853	3.65	3.54	12.2	2.2	0.945	0.986	3.65	3.54	13.1	3.0	0.879	0.967
3.54	3.44	14.5	2.2	0.822	0.950	3.54	3.44	12.5	2.0	0.713	0.913	3.54	3.44	11.1	3.1	0.006	0.107
3.44	3.35	10.1	2.1	0.880	0.968	3.44	3.35	10.0	2.1	0.832	0.953	3.44	3.35	9.2	2.9	0.198	0.575
3.35	3.27	8.0	2.2	0.723	0.916	3.35	3.27	8.7	2.2	0.810	0.946	3.35	3.27	8.1	3.1	0.567	0.851
3.27	3.19	8.1	2.2	0.827	0.951	3.27	3.19	6.8	2.1	0.748	0.925	3.27	3.19	7.9	3.0	0.805	0.944
3.19	3.12	6.4	2.1	0.731	0.919	3.19	3.12	6.5	2.1	0.743	0.923	3.19	3.12	7.0	3.0	0.461	0.794
3.12	3.06	6.3	2.2	0.827	0.952	3.12	3.06	5.9	2.1	0.485	0.808	3.12	3.06	6.2	3.0	0.428	0.774
3.06	3.00	5.3	2.2	0.757	0.928	3.06	3.00	4.9	2.1	0.544	0.840	3.06	3.00	5.0	3.0	0.704	0.909
3.00	2.95	4.5	2.3	0.533	0.834	3.00	2.95	4.4	2.2	0.437	0.780	3.00	2.95	4.9	3.0	0.043	0.286
2.95	2.90	5.4	2.3	0.527	0.831	2.95	2.90	4.5	2.1	0.506	0.820	2.95	2.90	5.1	2.9	0.221	0.602

Table II.2. X-ray diffraction scale output logs for EDC cross-linked CJ-LPCs prior to incubation with HDFa cells; *Green Highlight*: high-resolution estimate.

EDC Pre-incubation C1						EDC Pre-incubation C2						EDC Pre-incubation C3					
Lower, Å	Upper, Å	Ave. I	Ave. Err	CC1/2	CC*	Lower, Å	Upper, Å	Ave. I	Ave. Err	CC1/2	CC*	Lower, Å	Upper, Å	Ave. I	Ave. Err	CC1/2	CC*
50.0	7.86	18.2	1.0	0.995	0.999	50.0	7.86	20.0	1.0	0.99	1.00	50.0	7.86	17.3	0.9	0.991	0.998
7.86	6.24	12.3	0.9	0.975	0.994	7.86	6.24	11.3	0.9	0.93	0.98	7.86	6.24	9.5	0.7	0.954	0.988
6.24	5.46	13.0	1.1	0.956	0.989	6.24	5.46	11.0	1.1	0.93	0.98	6.24	5.46	10.0	0.8	0.966	0.991
5.46	4.96	15.2	1.3	0.897	0.973	5.46	4.96	13.3	1.3	0.97	0.99	5.46	4.96	12.2	1.0	0.944	0.985
4.96	4.60	15.4	1.3	0.897	0.973	4.96	4.60	14.2	1.4	0.92	0.98	4.96	4.60	12.2	1.1	0.947	0.986
4.60	4.33	15.9	1.5	0.961	0.990	4.60	4.33	13.6	1.7	-1.00	0.00	4.60	4.33	14.5	1.2	0.866	0.963
4.33	4.11	17.2	1.7	1.000	1.000	4.33	4.11	12.1	1.8	1.00	1.00	4.33	4.11	12.2	1.3	0.870	0.965
4.11	3.94	16.7	1.9	0.899	0.973	4.11	3.94	11.3	2.0	0.96	0.99	4.11	3.94	13.0	1.4	0.765	0.931
3.94	3.78	16.2	2.0	0.662	0.893	3.94	3.78	10.0	2.1	0.77	0.93	3.94	3.78	11.2	1.5	0.692	0.904
3.78	3.65	12.9	1.9	0.757	0.928	3.78	3.65	8.2	2.1	0.99	1.00	3.78	3.65	9.5	1.5	0.890	0.971
3.65	3.54	12.0	2.1	0.795	0.941	3.65	3.54	7.5	2.1	0.99	1.00	3.65	3.54	8.7	1.5	0.849	0.958
3.54	3.44	11.9	2.1	0.961	0.990	3.54	3.44	6.0	2.1	0.63	0.88	3.54	3.44	8.2	1.5	0.722	0.916
3.44	3.35	9.1	2.0	0.657	0.890	3.44	3.35	4.6	2.1	1.00	1.00	3.44	3.35	6.3	1.5	0.673	0.897
3.35	3.27	7.3	2.0	0.680	0.900	3.35	3.27	4.7	2.0	0.27	0.65	3.35	3.27	5.2	1.4	0.493	0.813
3.27	3.19	7.6	2.1	0.578	0.856	3.27	3.19	4.1	2.0	0.80	0.94	3.27	3.19	5.7	1.5	0.562	0.848
3.19	3.12	5.9	2.1	0.782	0.937	3.19	3.12	3.3	2.0	0.80	0.94	3.19	3.12	4.7	1.4	0.676	0.898
3.12	3.06	5.6	2.1	0.705	0.909	3.12	3.06	2.7	2.0	-1.00	0.00	3.12	3.06	3.6	1.4	0.656	0.890
3.06	3.00	4.8	2.2	0.537	0.836	3.06	3.00	2.8	2.1	0.00	0.00	3.06	3.00	3.5	1.4	0.391	0.750
3.00	2.95	3.9	2.2	-0.037	0.000	3.00	2.95	2.3	2.1	1.00	1.00	3.00	2.95	2.8	1.4	0.439	0.781
2.95	2.90	3.4	2.2	0.164	0.531	2.95	2.90	2.3	2.1	1.00	1.00	2.95	2.90	2.5	1.3	0.190	0.565

Table II.3. X-ray diffraction scale output logs for EDC cross-linked CJ-LPCs after incubation with HDFa cells; *Green Highlight*: high-resolution estimate.

EDC Post-incubation C1						EDC Post-incubation C2						EDC Post-incubation C3					
Lower, Å	Upper, Å	Ave. I	Ave. Err	CC1/2	CC*	Lower, Å	Upper, Å	Ave. I	Ave. Err	CC1/2	CC*	Lower, Å	Upper, Å	Ave. I	Ave. Err	CC1/2	CC*
50.0	9.1	20.5	1.0	0.999	1.000	50.0	9.1	15.5	0.9	0.992	0.998	50.0	9.1	30.1	1.4	0.990	0.998
9.10	7.23	6.9	0.8	0.983	0.996	9.10	7.23	7.6	0.8	0.980	0.995	9.10	7.23	10.0	1.0	0.973	0.993
7.23	6.32	4.6	0.8	0.905	0.975	7.23	6.32	4.5	0.9	0.873	0.966	7.23	6.32	7.1	1.0	0.939	0.984
6.32	5.74	4.8	0.9	0.925	0.980	6.32	5.74	5.6	1.0	0.830	0.952	6.32	5.74	7.4	1.2	0.939	0.984
5.74	5.33	4.5	1.0	0.902	0.974	5.74	5.33	5.3	1.2	0.858	0.961	5.74	5.33	7.0	1.2	0.855	0.960
5.33	5.02	4.4	1.1	0.922	0.980	5.33	5.02	6.9	1.3	0.824	0.950	5.33	5.02	7.0	1.4	0.805	0.944
5.02	4.77	5.8	1.2	0.702	0.908	5.02	4.77	7.5	1.5	0.753	0.927	5.02	4.77	7.6	1.4	0.952	0.988
4.77	4.56	5.9	1.3	0.702	0.908	4.77	4.56	8.6	1.7	0.888	0.970	4.77	4.56	9.3	1.6	0.932	0.982
4.56	4.38	6.0	1.4	0.950	0.987	4.56	4.38	7.8	1.8	0.848	0.958	4.56	4.38	9.3	1.8	1.000	1.000
4.38	4.23	5.1	1.6	0.749	0.925	4.38	4.23	5.9	1.9	0.736	0.921	4.38	4.23	6.9	1.9	1.000	1.000
4.23	4.10	3.5	1.7	0.327	0.702	4.23	4.10	4.9	2.0	0.336	0.709	4.23	4.10	6.6	2.2	0.523	0.829
4.10	3.98	3.8	1.8	0.532	0.833	4.10	3.98	4.6	2.2	0.610	0.870	4.10	3.98	5.9	2.3	0.615	0.873
3.98	3.88	3.8	1.9	0.569	0.852	3.98	3.88	4.4	2.2	0.469	0.799	3.98	3.88	4.5	2.4	0.721	0.915
3.88	3.78	3.6	2.0	0.406	0.760	3.88	3.78	4.5	2.3	0.161	0.526	3.88	3.78	5.3	2.5	0.727	0.917
3.78	3.70	3.7	2.0	-0.090	0.000	3.78	3.70	4.4	2.4	0.337	0.710	3.78	3.70	4.7	2.6	0.363	0.730
3.70	3.62	3.0	2.0	-0.076	0.000	3.70	3.62	3.8	2.4	0.361	0.728	3.70	3.62	4.5	2.7	0.565	0.850
3.62	3.55	2.7	1.9	-0.051	0.000	3.62	3.55	2.6	2.4	0.521	0.828	3.62	3.55	3.3	2.6	0.565	0.850
3.55	3.48	2.4	1.8	-0.249	0.000	3.55	3.48	2.3	2.4	0.109	0.443	3.55	3.48	3.0	2.5	0.652	0.888
3.48	3.42	1.9	1.8	-0.249	0.000	3.48	3.42	2.2	2.4	-0.202	0.000	3.48	3.42	2.1	2.5	0.961	0.990
3.42	3.36	2.5	1.7	-0.610	0.000	3.42	3.36	2.1	2.3	-0.019	0.000	3.42	3.36	2.4	2.5	0.961	0.990

Table II.4. X-ray diffraction scale output logs for OA cross-linked CJ-LPCs prior to incubation with HDFa cells; *Green Highlight*: high-resolution estimate.

Oxaldehyde (OA) Pre-incubation C1						Oxaldehyde (OA) Pre-incubation C2						Oxaldehyde (OA) Pre-incubation C3					
Lower, Å	Upper, Å	Ave. I	Ave. Err	CC1/2	CC*	Lower, Å	Upper, Å	Ave. I	Ave. Err	CC1/2	CC*	Lower, Å	Upper, Å	Ave. I	Ave. Err	CC1/2	CC*
50.0	9.10	39.6	1.6	0.994	0.999	50.0	9.10	44.3	1.6	0.998	0.999	50.0	9.10	20.8	1.1	0.999	1.000
9.10	7.23	11.2	0.9	0.974	0.993	9.10	7.23	15.8	1.0	0.977	0.994	9.10	7.23	13.3	1.2	0.691	0.904
7.23	6.32	7.8	1.0	0.952	0.988	7.23	6.32	8.3	0.9	0.935	0.983	7.23	6.32	7.6	1.2	0.947	0.986
6.32	5.74	7.8	1.0	0.922	0.979	6.32	5.74	9.0	1.1	0.939	0.984	6.32	5.74	11.5	1.4	0.281	0.663
5.74	5.33	7.8	1.2	0.942	0.985	5.74	5.33	9.0	1.2	0.922	0.980	5.74	5.33	9.8	1.5	0.524	0.829
5.33	5.02	7.9	1.2	0.925	0.980	5.33	5.02	9.4	1.3	0.870	0.965	5.33	5.02	10.6	1.7	0.943	0.985
5.02	4.77	10.1	1.5	0.948	0.987	5.02	4.77	12.5	1.6	0.879	0.967	5.02	4.77	10.2	1.9	-1.000	0.000
4.77	4.56	10.3	1.5	0.943	0.985	4.77	4.56	13.0	1.7	0.919	0.979	4.77	4.56	14.2	2.1	1.000	1.000
4.56	4.38	8.3	1.6	0.753	0.927	4.56	4.38	10.5	1.9	0.883	0.969	4.56	4.38	12.1	2.3	1.000	1.000
4.38	4.23	8.0	1.7	0.831	0.953	4.38	4.23	9.6	2.0	0.709	0.911	4.38	4.23	10.3	2.4	1.000	1.000
4.23	4.10	7.1	1.9	0.836	0.954	4.23	4.10	8.5	2.2	0.799	0.942	4.23	4.10	7.8	2.5	0.823	0.950
4.10	3.98	5.7	1.9	0.941	0.985	4.10	3.98	6.7	2.2	0.531	0.833	4.10	3.98	6.9	2.6	0.598	0.865
3.98	3.88	5.0	2.1	0.526	0.831	3.98	3.88	5.8	2.5	0.790	0.940	3.98	3.88	7.4	2.9	0.529	0.832
3.88	3.78	5.2	2.2	0.423	0.771	3.88	3.78	5.7	2.5	0.148	0.508	3.88	3.78	6.9	2.9	0.199	0.577
3.78	3.70	4.7	2.2	0.188	0.563	3.78	3.70	5.5	2.5	0.545	0.840	3.78	3.70	6.0	3.0	0.277	0.659
3.70	3.62	4.4	2.2	0.397	0.754	3.70	3.62	3.8	2.7	0.258	0.640	3.70	3.62	5.1	3.0	-0.258	0.000
3.62	3.55	3.4	2.2	0.525	0.830	3.62	3.55	2.8	2.5	0.258	0.640	3.62	3.55	3.9	2.9	0.180	0.553
3.55	3.48	3.6	2.2	-0.304	0.000	3.55	3.48	2.5	2.6	0.340	0.712	3.55	3.48	3.8	2.8	0.180	0.553
3.48	3.42	3.7	2.2	0.015	0.172	3.48	3.42	2.3	2.6	-0.197	0.000	3.48	3.42	3.1	2.8	-0.256	0.000
3.42	3.36	2.5	1.9	-0.057	0.000	3.42	3.36	2.6	2.5	0.262	0.645	3.42	3.36	4.7	2.8	-0.368	0.000

Table II.5. X-ray diffraction scale output logs for OA cross-linked CJ-LPCs after incubation with HDFa cells; *Green Highlight*: high-resolution estimate.

Oxaldehyde (OA) Post-incubation C1						Oxaldehyde (OA) Post-incubation C2						Oxaldehyde (OA) Post-incubation C3					
Lower, Å	Upper, Å	Ave. I	Ave. Err	CC1/2	CC*	Lower, Å	Upper, Å	Ave. I	Ave. Err	CC1/2	CC*	Lower, Å	Upper, Å	Ave. I	Ave. Err	CC1/2	CC*
50.0	9.10	36.3	1.9	0.995	0.999	50.0	9.10	36.0	1.9	0.991	0.998	50.0	9.10	36.7	2.1	0.999	1.000
9.10	7.23	13.0	1.3	0.979	0.995	9.10	7.23	12.3	1.3	0.992	0.998	9.10	7.23	13.1	1.4	0.989	0.997
7.23	6.32	8.0	1.3	0.991	0.998	7.23	6.32	8.6	1.3	0.980	0.995	7.23	6.32	9.5	1.4	0.933	0.983
6.32	5.74	9.5	1.4	0.808	0.945	6.32	5.74	9.9	1.4	0.908	0.976	6.32	5.74	10.0	1.5	0.917	0.978
5.74	5.33	7.7	1.4	0.968	0.992	5.74	5.33	8.2	1.5	0.721	0.915	5.74	5.33	8.1	1.5	0.903	0.974
5.33	5.02	9.0	1.6	0.778	0.935	5.33	5.02	8.7	1.7	0.988	0.997	5.33	5.02	8.3	1.6	0.824	0.951
5.02	4.77	9.5	1.6	0.860	0.962	5.02	4.77	9.0	1.8	0.999	1.000	5.02	4.77	10.9	1.7	0.884	0.969
4.77	4.56	11.2	1.8	0.692	0.904	4.77	4.56	10.5	2.0	0.868	0.964	4.77	4.56	12.0	2.0	0.000	0.000
4.56	4.38	10.6	1.9	0.990	0.997	4.56	4.38	10.2	2.1	0.868	0.964	4.56	4.38	10.9	2.0	1.000	1.000
4.38	4.23	7.6	2.0	0.291	0.672	4.38	4.23	7.1	2.3	0.868	0.964	4.38	4.23	10.6	2.5	1.000	1.000
4.23	4.10	7.0	2.1	0.291	0.672	4.23	4.10	6.1	2.3	0.868	0.964	4.23	4.10	7.4	2.4	1.000	1.000
4.10	3.98	7.0	2.3	0.291	0.672	4.10	3.98	6.7	2.7	0.868	0.964	4.10	3.98	7.6	3.0	1.000	1.000
3.98	3.88	7.2	2.5	0.291	0.672	3.98	3.88	8.0	3.1	1.000	1.000	3.98	3.88	7.6	3.2	0.905	0.975
3.88	3.78	5.2	2.7	0.706	0.910	3.88	3.78	6.9	3.0	0.768	0.932	3.88	3.78	6.5	3.1	0.905	0.975
3.78	3.70	5.4	2.5	0.706	0.910	3.78	3.70	5.4	3.0	0.768	0.932	3.78	3.70	5.7	3.0	0.000	0.000
3.70	3.62	4.8	2.6	0.706	0.910	3.70	3.62	4.8	3.4	1.000	1.000	3.70	3.62	6.5	3.3	0.000	0.000
3.62	3.55	3.1	2.6	0.706	0.910	3.62	3.55	3.5	3.4	1.000	1.000	3.62	3.55	3.7	3.1	0.000	0.000
3.55	3.48	4.3	2.7	0.706	0.910	3.55	3.48	4.3	3.5	1.000	1.000	3.55	3.48	4.8	3.0	0.000	0.000
3.48	3.42	4.2	2.5	0.706	0.910	3.48	3.42	2.7	3.8	1.000	1.000	3.48	3.42	4.5	3.1	0.000	0.000
3.42	3.36	4.7	2.9	0.281	0.662	3.42	3.36	5.5	4.1	0.000	0.000	3.42	3.36	6.9	3.4	0.000	0.000

⊙ **II.7.4 HEWL Crystal X-ray Diffraction (XRD) and Data Processing**

All HEWL materials were loop transferred into 2.5 M NaCl, 50 mM sodium acetate pH 4.6 and soaked for at least 5 minutes prior to flash freezing in a cryogenic nitrogen stream at 100 K. The diffraction quality was then assessed using a Rigaku Compact HomeLab with a micro-focus X-ray generator and a Pilatus 200K detector based on a 15-frame data collection strategy; each frame was separated by a 2.0° omega offset and exposed for 60 seconds. Reflection data was indexed and scaled using HKL-3000 software (HKL Research Inc.). See Tables II.6-II.8 for scale output logs for HEWL data and Tables II.1-II.5 for CJ-LPC data. The high-resolution estimates for all HEWL crystals was based on a signal to noise ratio above two (*Ave. I / Ave. Err* ≥ 2.0). Refer to CHAPTER 3 Figure 3.3 for representative diffraction patterns and a summary of the high-resolution estimates for each HEWL material type.

⊙ **II.7.5 Adult Human Dermal Fibroblast (HDFa) Cell Culture**

Adult human dermal fibroblast cells were purchased from Thermo Fisher (Cat. #: C0135C) and cultured in freshly supplemented medium 106 (Thermo Fisher Cat #: M106500) at 37° C with 5% CO₂.

⊙ **II.7.6 Human Macrophage (MV-4-11) Cell Culture**

Human macrophage cells were purchased from ATCC (Cat. #: CRL-9591) and cultured in freshly supplemented Iscove's Modified Dulbecco's Medium (IMDM) from ATCC (Cat. #: 30-2005) at 37° C with 5% CO₂.

⊙ **II.7.7 HDFa Incubation Stability Tests**

HDFa cells (passage number: 4) were plated at 15,000 cells per well (150,000 cells/mL) in a 96-well plate and allowed to adhere for 24 hours at 37° C with 5% CO₂. After the initial 24-hour incubation period, the various CJ-LPC and HEWL crystals were added to individual wells and

Table II.6. X-ray diffraction scale output logs for non-cross-linked HEWL crystals prior to incubation with HDFa cells; *Green Highlight*: high-resolution estimate.

Non-Cross-Linked (NCL) C1						Non-Cross-Linked (NCL) C2						Non-Cross-Linked (NCL) C3					
Lower, Å	Upper, Å	Ave. I	Ave. Err	CC1/2	CC*	Lower, Å	Upper, Å	Ave. I	Ave. Err	CC1/2	CC*	Lower, Å	Upper, Å	Ave. I	Ave. Err	CC1/2	CC*
50.0	5.29	516.3	16.3	0.998	1.000	50.0	5.29	586.2	18.0	0.998	0.999	50.0	5.29	416.9	13.8	0.999	1.000
5.29	4.20	406.8	14.2	0.995	0.999	5.29	4.20	784.0	25.1	0.997	0.999	5.29	4.20	500.5	16.8	0.996	0.999
4.20	3.67	261.8	10.5	0.995	0.999	4.20	3.67	826.6	27.7	1.000	1.000	4.20	3.67	402.7	14.3	0.999	1.000
3.67	3.33	370.8	14.3	0.995	0.999	3.67	3.33	855.7	28.2	0.974	0.993	3.67	3.33	476.9	17.2	0.999	1.000
3.33	3.10	264.2	11.6	1.218	1.048	3.33	3.10	633.4	21.6	0.994	0.998	3.33	3.10	377.5	13.4	0.991	0.998
3.10	2.91	116.8	6.7	0.993	0.998	3.10	2.91	388.6	14.1	0.993	0.998	3.10	2.91	274.4	10.3	0.996	0.999
2.91	2.77	114.5	6.8	0.994	0.998	2.91	2.77	274.8	10.5	0.997	0.999	2.91	2.77	206.7	8.2	0.994	0.999
2.77	2.65	96.1	6.6	0.986	0.996	2.77	2.65	256.1	9.7	0.998	0.999	2.77	2.65	239.3	9.2	0.999	1.000
2.65	2.54	70.2	5.4	0.958	0.989	2.65	2.54	204.7	8.1	0.990	0.997	2.65	2.54	152.6	6.5	0.996	0.999
2.54	2.46	56.2	5.1	0.872	0.965	2.54	2.46	192.8	7.8	0.994	0.998	2.54	2.46	119.6	5.6	0.990	0.998
2.46	2.38	53.1	5.0	0.938	0.984	2.46	2.38	161.9	7.0	0.990	0.997	2.46	2.38	108.6	5.4	0.992	0.998
2.38	2.31	38.1	4.6	0.893	0.971	2.38	2.31	157.9	7.0	0.978	0.994	2.38	2.31	96.6	5.1	0.986	0.997
2.31	2.25	36.4	4.5	0.869	0.964	2.31	2.25	144.7	6.6	0.991	0.998	2.31	2.25	91.1	5.1	0.987	0.997
2.25	2.20	31.3	4.5	0.965	0.991	2.25	2.20	130.6	6.4	0.958	0.989	2.25	2.20	87.8	5.2	0.973	0.993
2.20	2.15	28.6	4.5	0.747	0.925	2.20	2.15	117.5	5.9	0.984	0.996	2.20	2.15	78.0	4.9	0.976	0.994
2.15	2.10	21.0	4.5	0.697	0.906	2.15	2.10	122.4	6.2	0.994	0.998	2.15	2.10	75.2	4.9	0.992	0.998
2.10	2.06	16.7	4.7	0.176	0.548	2.10	2.06	66.5	4.0	0.999	1.000	2.10	2.06	60.5	4.3	0.992	0.998
2.06	2.02	15.4	4.4	0.584	0.859	2.06	2.02	85.7	4.9	0.969	0.992	2.06	2.02	57.6	4.5	0.975	0.994
2.02	1.98	12.8	4.2	0.365	0.731	2.02	1.98	75.5	4.7	0.965	0.991	2.02	1.98	47.2	4.2	0.933	0.983
1.98	1.95	11.5	4.1	0.670	0.896	1.98	1.95	65.0	4.5	0.968	0.992	1.98	1.95	37.6	3.9	0.979	0.995

Table II.7. X-ray diffraction scale output logs for EDC cross-linked HEWL crystals prior to incubation with HDFa cells; *Green Highlight*: high-resolution estimate.

Glutaraldehyde (GA) Pre-incubation C1						Glutaraldehyde (GA) Pre-incubation C2						Glutaraldehyde (GA) Pre-incubation C3					
Lower, Å	Upper, Å	Ave. I	Ave. Err	CC1/2	CC*	Lower, Å	Upper, Å	Ave. I	Ave. Err	CC1/2	CC*	Lower, Å	Upper, Å	Ave. I	Ave. Err	CC1/2	CC*
50.0	5.29	449.2	15.0	0.999	1.000	50.0	5.29	344.3	11.4	0.999	1.000	50.0	5.29	278.1	9.0	0.997	0.999
5.29	4.20	430.5	14.9	0.999	1.000	5.29	4.20	292.7	10.2	0.998	1.000	5.29	4.20	201.1	6.8	0.990	0.998
4.20	3.67	392.1	14.0	0.997	0.999	4.20	3.67	212.7	8.1	0.998	0.999	4.20	3.67	166.6	6.1	0.998	1.000
3.67	3.33	333.5	12.4	0.999	1.000	3.67	3.33	188.0	8.1	0.997	0.999	3.67	3.33	157.2	6.1	0.950	0.987
3.33	3.10	220.5	8.8	0.997	0.999	3.33	3.10	117.7	5.7	0.995	0.999	3.33	3.10	87.5	3.8	0.993	0.998
3.10	2.91	164.3	7.1	0.992	0.998	3.10	2.91	73.4	4.4	0.990	0.997	3.10	2.91	54.3	2.9	0.993	0.998
2.91	2.77	109.1	5.5	0.992	0.998	2.91	2.77	48.4	3.8	0.980	0.995	2.91	2.77	40.6	2.7	0.978	0.994
2.77	2.65	98.0	5.3	0.983	0.996	2.77	2.65	42.9	4.0	0.757	0.928	2.77	2.65	37.1	2.8	0.980	0.995
2.65	2.54	79.2	4.8	0.977	0.994	2.65	2.54	24.2	3.4	0.913	0.977	2.65	2.54	23.8	2.4	0.724	0.917
2.54	2.46	63.4	4.3	0.980	0.995	2.54	2.46	21.3	3.2	0.940	0.985	2.54	2.46	16.9	2.3	0.638	0.883
2.46	2.38	53.4	4.2	0.977	0.994	2.46	2.38	16.5	3.2	0.883	0.969	2.46	2.38	16.1	2.4	0.893	0.971
2.38	2.31	52.3	4.1	0.991	0.998	2.38	2.31	14.1	3.2	0.877	0.967	2.38	2.31	10.9	2.5	0.721	0.915
2.31	2.25	45.5	4.0	0.927	0.981	2.31	2.25	10.7	3.2	0.746	0.925	2.31	2.25	15.0	2.9	1.000	1.000
2.25	2.20	39.5	3.9	0.962	0.990	2.25	2.20	11.9	3.5	0.497	0.815	2.25	2.20	15.2	3.1	-1.000	0.000
2.20	2.15	31.4	3.9	0.946	0.986	2.20	2.15	7.9	3.3	0.586	0.859	2.20	2.15	7.6	2.9	-0.203	0.000
2.15	2.10	28.6	3.9	0.873	0.966	2.15	2.10	8.2	3.4	0.614	0.872	2.15	2.10	6.9	3.1	0.521	0.827
2.10	2.06	27.1	4.0	0.886	0.969	2.10	2.06	12.1	3.7	0.128	0.477	2.10	2.06	13.6	3.7	0.521	0.827
2.06	2.02	19.7	3.7	0.942	0.985	2.06	2.02	4.8	3.2	0.283	0.664	2.06	2.02	6.0	3.2	0.521	0.827
2.02	1.98	17.2	3.6	0.777	0.935	2.02	1.98	3.7	3.1	0.294	0.674	2.02	1.98	5.4	3.3	0.521	0.827
1.98	1.95	15.4	3.4	0.146	0.504	1.98	1.95	3.2	3.0	0.242	0.625	1.98	1.95	5.3	3.2	0.521	0.827

Table II.8. X-ray diffraction scale output logs for EDC cross-linked HEWL crystals after incubation with HDFa cells; *Green Highlight*: high-resolution estimate.

Glutaraldehyde (GA) Post-incubation C1						Glutaraldehyde (GA) Post-incubation C2						Glutaraldehyde (GA) Post-incubation C3					
Lower, Å	Upper, Å	Ave. I	Ave. Err	CC1/2	CC*	Lower, Å	Upper, Å	Ave. I	Ave. Err	CC1/2	CC*	Lower, Å	Upper, Å	Ave. I	Ave. Err	CC1/2	CC*
50.0	5.29	268.0	9.1	0.999	1.000	50.0	5.29	334.2	11.8	0.998	0.999	50.0	5.29	225.2	8.2	0.998	1.000
5.29	4.20	192.4	7.6	0.996	0.999	5.29	4.20	243.4	9.4	0.996	0.999	5.29	4.20	175.4	6.9	0.998	0.999
4.20	3.67	144.5	6.5	1.000	1.000	4.20	3.67	222.9	9.3	0.982	0.995	4.20	3.67	159.9	6.9	0.998	1.000
3.67	3.33	119.2	6.2	0.000	0.000	3.67	3.33	144.2	7.6	0.991	0.998	3.67	3.33	102.0	5.3	0.979	0.995
3.33	3.10	84.0	5.1	0.973	0.993	3.33	3.10	81.1	5.7	0.996	0.999	3.33	3.10	64.6	4.4	0.994	0.998
3.10	2.91	51.1	4.1	0.000	0.000	3.10	2.91	54.0	5.1	0.952	0.988	3.10	2.91	38.5	3.7	0.972	0.993
2.91	2.77	31.8	3.6	0.000	0.000	2.91	2.77	34.8	4.6	0.941	0.985	2.91	2.77	23.4	3.3	0.900	0.973
2.77	2.65	32.5	3.7	1.000	1.000	2.77	2.65	30.5	4.6	0.766	0.931	2.77	2.65	22.4	3.7	0.810	0.946
2.65	2.54	20.0	3.4	1.000	1.000	2.65	2.54	18.7	4.3	0.859	0.961	2.65	2.54	14.9	3.4	0.859	0.961
2.54	2.46	15.7	3.2	1.000	1.000	2.54	2.46	15.7	4.3	0.871	0.965	2.54	2.46	11.5	3.4	0.854	0.960
2.46	2.38	14.2	3.2	0.476	0.803	2.46	2.38	12.5	4.4	0.701	0.908	2.46	2.38	8.4	3.4	0.617	0.873
2.38	2.31	9.5	3.1	0.104	0.434	2.38	2.31	9.6	4.5	0.575	0.854	2.38	2.31	7.2	3.6	0.459	0.793
2.31	2.25	12.6	3.4	-0.860	0.000	2.31	2.25	9.0	4.8	0.338	0.711	2.31	2.25	6.6	3.7	0.593	0.863
2.25	2.20	8.2	3.3	0.966	0.991	2.25	2.20	6.9	4.8	-0.052	0.000	2.25	2.20	7.2	3.9	0.315	0.692
2.20	2.15	6.9	3.2	0.305	0.684	2.20	2.15	6.3	4.7	0.255	0.637	2.20	2.15	5.1	3.9	0.385	0.746
2.15	2.10	5.0	3.2	0.683	0.901	2.15	2.10	5.7	4.7	0.259	0.642	2.15	2.10	3.9	3.9	0.258	0.641
2.10	2.06	4.7	3.1	0.683	0.901	2.10	2.06	8.4	4.8	-0.035	0.000	2.10	2.06	5.4	4.1	-0.473	0.000
2.06	2.02	3.4	3.0	0.837	0.955	2.06	2.02	3.7	4.6	0.355	0.724	2.06	2.02	3.6	4.0	-0.076	0.000
2.02	1.98	3.2	3.0	0.837	0.955	2.02	1.98	3.8	4.5	0.072	0.366	2.02	1.98	2.7	3.9	-0.077	0.000
1.98	1.95	2.7	3.1	0.018	0.190	1.98	1.95	3.0	4.3	0.221	0.602	1.98	1.95	2.3	3.7	0.754	0.927

allowed to incubate for 24 hours at 37° C with 5% CO₂ to test the stability of the crystals under cell culture conditions. After 24 hours, the crystal morphology and surface structure was analyzed *via* stereomicroscopy (CHAPTER 3 Figure 3.2) and the molecular order of the crystals was analyzed using XRD on a Rigaku HomeLab (Tables II.1-II.8 and CHAPTER 3 Figure 3.3).

☉ II.7.8 Crystal Fragmentation by Sonication

Evidence has been found that increasing the surface area of potentially toxic mesoporous solids may lead to increases in the cytotoxic response *in vitro*.⁵ Therefore, to maximize the potential of observing a cytotoxic response in the LDH assay, we used high surface area fragmented CJ-LPC and HEWL protein crystals. Large quantities of small ($5.8 \pm 3.9 \mu\text{m}$) fragmented crystals were generated by sonicating hundreds of large (100-500 μm) non-cross-linked protein crystals (Figure II.1). Large protein crystals were first washed by loop transferring them into their respective wash conditions to remove residual monomers: CJ-LPCs were washed for 1 hour in 90% mTacsimateTM, 10% glycerol mixture at pH 7.5 for aldehyde cross-linking and 4.2 M TMAO, 175 mM H₂SO₄ solution at pH 7.5 for EDC cross-linking, HEWL crystals were washed for 15 minutes in 2.5 M NaCl, 50 mM sodium acetate pH 4.6. After washing all crystals were then loop transferred into fresh wash solutions and slowly sonicated on ice. Fragmented crystals were then cross-linked per the same cross-linking protocol as their large CJ-LPC and HEWL crystal counterparts (see sections II.5 and II.6). Note that in the case of fragmented protein crystals, the fragments were too small to loop transfer, thus dialysis was used as an alternative means to transfer the crystals into new solution conditions. After cross-linking and quenching all reactions, the fragmented crystals were sterilized by dialysis into their respective wash conditions containing 20% EtOH followed by dialysis transfer into sterile 1x PBS and either sterile supplemented cell culture media (HDFa cells) or double deionized water (MV-4-11 cells).

⊙ **II.7.9 Live/Dead Staining**

To validate the LDH cytotoxicity results, cells from the control well (no materials added) and cells from wells containing 400 $\mu\text{g}/\text{mL}$ of cross-linked protein crystal material were taken and stained using the Live/Dead Viability Kit for Mammalian Cells from Thermo Scientific (Cat. #: L3224). Calcein was used to reveal living cells and ethidium homodimer to reveal dead cells. Fluorescent images of the control cells as well as the cells incubated with CJ/OA and CJ/EDC materials were taken on an Olympus IX73 fluorescent light microscope while the cells incubated in both GA cross-linked materials (CJ/GA and HEWL/GA) were taken on a Nikon DIAPHOT 300 light microscope with MetaMorph version 7.7 software. All images were taken using the 470 nm and 595 nm excitation lasers to excite live (green) and dead (red) cells respectively. Results indicate no substantial differences between the control cells and the CJ/EDC or CJ/OA cells (CHAPTER 3 Figure 3.4C-3.4E) while both CJ/GA and HEWL/GA cells show approximately 50% cell death (CHAPTER 3 Figure 3.4F & 3.4G). These results agree with the quantitative LDH cell viability results (CHAPTER 3 Figure 3.4A & 3.4B).

⊙ **II.7.10 Lactate Dehydrogenase (LDH) cytotoxicity Assay**

The short-term cytotoxic response of human cells to various cross-linked protein crystal materials was quantified by measuring the LDH activity in the cell culture medium of HDFa and MV-4-11 human cell lines. HDFa cells (passage number: 3) were plated at 150,000 cells/mL (15,000 cells per well) in a 96-well plate and allowed to adhere for 24 hours at 37° C with 5% CO₂. After the initial 24-hour incubation, the culture medium was aspirated and replaced with fresh medium (negative control) or medium containing various concentrations (1, 50, 100, 200, and 400 $\mu\text{g}/\text{mL}$) of fragmented protein crystal material: non-cross-linked (CJ/NCL &

HEWL/NCL), GA cross-linked (CJ/GA & HEWL/GA), OA cross-linked (CJ/OA), or EDC cross-linked (CJ/EDC). The cells were then incubated for an additional 24 hours at 37° C with 5% CO₂.

The LDH assay had to be adjusted slightly for MV-4-11 cells due to the fact that they are a suspended culture. First, either sterile double distilled water (negative control) or sterile double distilled water containing 400 µg/mL of fragmented protein crystal material: non-cross-linked (CJ/NCL & HEWL/NCL), GA cross-linked (CJ/GA & HEWL/GA), OA cross-linked (CJ/OA), or EDC cross-linked (CJ/EDC) were added to a 96-well culture plate and allowed to desiccate for 24 hours in a laminar flow hood. After the initial 24-hour desiccation period, MV-4-11 cells (passage number: 3) were added to each well at a concentration of 150,000 cells /mL and incubated for 24 hours at 37° C with 5% CO₂.

After 24-hours of incubation with the materials the cell culture medium was removed from each sample well and the LDH activity measured using the Pierce LDH Cytotoxicity Assay Kit from Thermo Scientific (Cat. #: 88953). Percent cell viability was calculated using the following equation:

$$\% \text{ Cell Viability} = 100 - \frac{(\text{CJ Treated LDH Activity} - \text{Spontaneous LDH Activity})}{(\text{Maximum LDH Activity} - \text{Spontaneous LDH Activity})} \times 100$$

(Eq. II.1)

Where the *Spontaneous LDH Activity* refers to the cell samples with no material present while the *Maximum LDH Activity* refers to complete cell death triggered by the addition of 10 µL of lysis buffer. Results can be found in CHAPTER 3 Figure 3.4A.

☉ II.7.11 Nitrite Detection Assay

The potential for human macrophage activation caused by short-term contact with various protein crystal materials was investigated by quantifying the total nitrite/nitrate concentration in the media of MV-4-11 cells using the Nitric Oxide Colorimetric Assay from Roche (Cat. #:

11756281001). The cell culture for this assay was set up the same as that of the LDH cytotoxicity assay. Cells were incubated for 24-hours at 37° C with 5% CO₂ in the presence of 400 µg/mL fragmented protein crystal material. Media was taken from each well and all nitrate in the solution was converted to nitrite by the enzyme nitrate reductase in the presence of NADPH. Results show that MV-4-11 cells incubated with each of the various protein crystal materials produced similar nitrite levels as MV-4-11 cells that were incubated in the absence of material (cells only) (CHAPTER 3 Figure 3.5B). This indicates that none of the protein crystal materials alone could activate the release of nitric oxide from MV-4-11 human macrophages.

☉ II.7.12 Endotoxin Assay

Endotoxins are produced by certain gram-negative bacterium such as *Escherichia coli* (*E. coli*). Considering that CJ proteins used in this study were expressed in *E. coli*, it was necessary to measure the endotoxin levels present in the various steps of CJ-LPC material preparation. This was done using the Pierce LAL Chromogenic Endotoxin Quantitation Kit from Thermo Scientific (Cat. #: 88282). See Figure II.2 for the endotoxin standard. Each step of the material preparation (protein purification, crystallization, and cross-linking) helps to remove residual endotoxins as seen in Figure II.3.

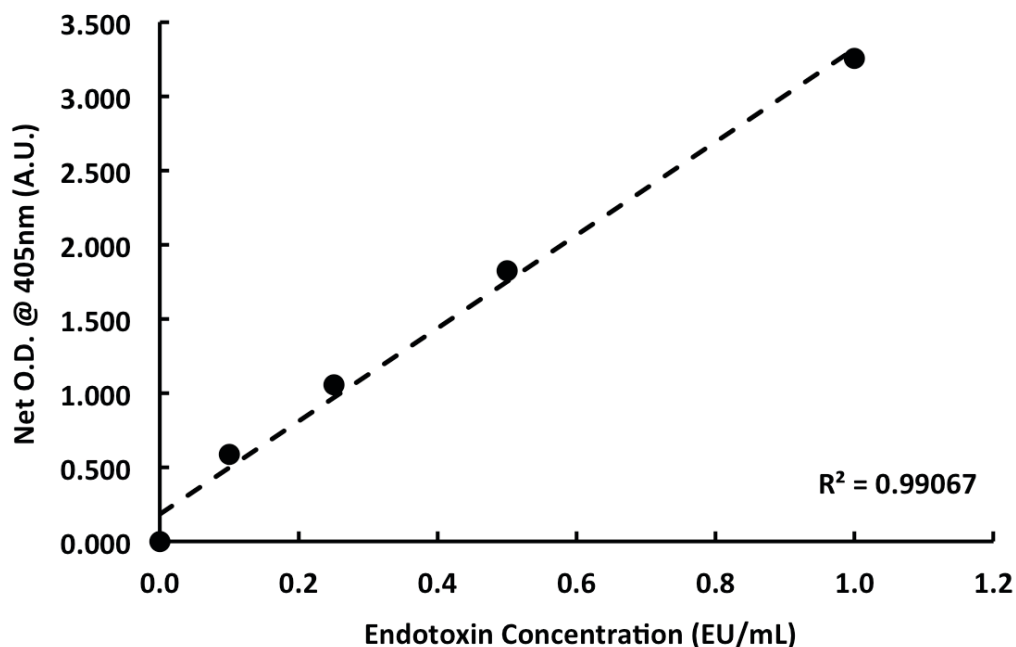


Figure II.2. Endotoxin standard.

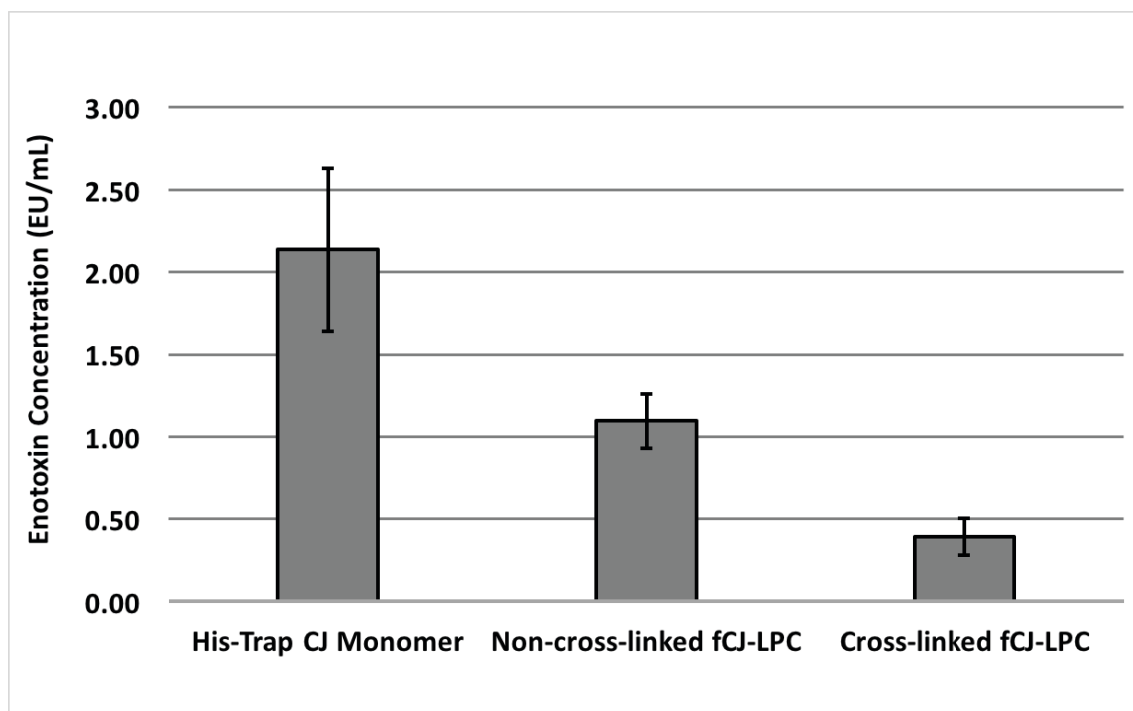


Figure II.3. Endotoxin levels at various stages of CJ-LPC material preparation. Endotoxin concentration is presented using endotoxin units (EU) per milliliter. *Error Bars:* standard deviation, n=3. Note that fragmented CJ-LPCs (fCJ-LPCs) were used for the non-cross-linked sample while OA cross-linked fCJ-LPCs were used for the cross-linked samples.

REFERENCES

- (1) Hekmat, D.; Hebel, D.; Schmid, H.; Weuster-Botz, D. Crystallization of Lysozyme: From Vapor Diffusion Experiments to Batch Crystallization in Agitated MI-Scale Vessels. *Process Biochem.* **2007**, *42* (12), 1649–1654.
- (2) Studier, F. W. Protein Production by Auto-Induction in High Density Shaking Cultures. *Protein Expr. Purif.* **2005**, *41* (1), 207–234.
- (3) Preibisch, S.; Saalfeld, S.; Tomancak, P. Globally Optimal Stitching of Tiled 3D Microscopic Image Acquisitions. *Bioinformatics* **2009**, *25* (11), 1463–1465.
- (4) Schindelin, J.; Arganda-Carreras, I.; Frise, E.; Kaynig, V.; Longair, M.; Pietzsch, T.; Preibisch, S.; Rueden, C.; Saalfeld, S.; Schmid, B.; et al. Fiji: An Open-Source Platform for Biological-Image Analysis. *Nat. Methods* **2012**, *9* (7), 676–682.
- (5) Ducheyne, P.; Healy, K.; Hutmacher, D. E.; Grainger, D. W.; Kirkpatrick, C. J. *Comprehensive Biomaterials*; Newnes, **2015**.

APPENDIX III

SUPPORTING INFORMATION

FOR CHAPTER 4

SUPPORTING INFORMATION

TEXTILE FUNCTIONALIZATION BY POROUS PROTEIN CRYSTAL CONJUGATION AND GUEST MOLECULE LOADING

◎ III.1 REAGENTS

The following chemicals were purchased and used without further purification. From Sigma-Aldrich: acetone, 1,1'-carbonyldiimidazole (CDI), dimethylamine borane complex (DMAB), trimethylamine N-oxide (TMAO), glutaraldehyde solution (GA) (25% in H₂O), sodium phosphate dibasic (Na₂HPO₄), sodium hypophosphite monohydrate, potassium phosphate monobasic (KH₂PO₄), and ammonium sulfate ([NH₄]₂SO₄). From VWR: HEPES and bis-tris. From Acros Organics: glyoxal (oxaldehyde) solution (40% in H₂O), carbonylhydrazide. From EMD Millipore: sulfuric acid (H₂SO₄), and sodium acetate. From Tokyo Chemical Industry Co.: adipic acid dihydrazide (AAD). From Fisher Scientific: sodium borate, NHS-fluorescein, sulforhodamine 101 (non-reactive), NaCl, and KCl. From J.T. Baker: citric acid. From Chemodex: sulforhodamine 101 acid chloride (TexasRed). From Hampton Research: lyophilized hen egg white lysozyme (HEWL).

◎ III.2 CJ VARIANT EXPRESSION AND PURIFICATION

The target gene CJ was modified from the gene vector encoding protein CJ0 obtained from the Protein Structure Initiative: Biology-Materials Repository (Genebank ID: cj0420, PDB Code: 2FGS). For ease of uniform expression and purification, the CJ0 gene was codon optimized and the periplasmic signaling peptide deleted thereby yielding CJ. The CJ gene was encoded in expression vector pSB3 with a C-terminal 6xHis tag and expressed in Escherichia coli C41-DE3 cells. 1 mL of turbid starter culture was added to 500 mL Terrific Broth (TB) with 100 mg/mL kanamycin and incubated at 37° C with shaking at 250 rpm until lightly turbid (~2.5-3 hours). Protein expression was induced with 0.4 mM isopropyl β-D-1-thiogalactopyranoside (IPTG)

followed by overnight (~16 hour) incubation at 25° C with shaking at 250 rpm. Cells were lysed by sonication and the CJ protein purified *via* gravity Ni-NTA affinity capture followed by ammonium sulfate ($[\text{NH}_4]_2\text{SO}_4$) precipitation. Purified CJ protein was buffer exchanged into 0.5 M $[\text{NH}_4]_2\text{SO}_4$, 10 mM HEPES, and 10% glycerol at pH 7.4, concentrated to ~40 mg/mL, and stored at -30° C.

☉ III.2.1 CJ Protein Sequence

MKEYTLDKAHTDVGFKIKHLQISNVKGNFKDYSAVIDFDPASAEFKKLDVTIKIASVNTENQTRDNHLQQD
DFFKAKKYPDMTFTMKKYEKIDNEKGKMTGTLTIAGVSKDIVLDAEIGGVAKGKDGKEKIGFSLNGKIKRS
DFKFATSTSTITLSDDINLNIEVEANEKEGGSHHHHHH

☉ III.2.2 CJ DNA Sequence

TTAAGAAGGAGATATACATATGAAAAAAGTTCTGCTGAGCAGCCTGGTTGCAGTTAGCCTGCTGAGTA
CCGGTCTGTTTGCAAAAAGAATATACCCTGGATAAAGCCCATACCGATGTTGGCTTTAAAATCAAACAT
CTGCAGATTAGCAATGTGAAAGGCAACTTTAAAGATTATAGCGCAGTGATCGATTTTGATCCGGCAAG
TGCAGAATTCAAAAAACTGGATGTGACCATTAAAATCGCCAGCGTGAATACCGAAAATCAGACCCGT
GATAATCATCTGCAGCAGGATGACTTCTTCAAAGCCAAAAAATACCCGGATATGACCTTTACCATGAA
AAAATACGAGAAAATCGATAACGAAAAAGGCAAAATGACCGGCACCCTGACCATTGCCGGTGTTAGC
AAAGATATTGTTCTGGATGCAGAAATTGGTGGTGTGCCAAAGGTAAAGATGGCAAAGAAAAAATTG
GCTTTAGCCTGAACGGCAAAATCAAACGTAGCGATTTCAAATTTGCAACCAGCACCAGCACCATTACC
CTGAGTGATGACATTAATCTGAACATTGAAGTGAAAGCCAACGAGAAAGAAGGTGGTAGTCATCACC
ACCACCATCACTAATAACTCGAGCACCACCACCACCACCCTGAGATCCGGCTG

☉ III.3 CRYSTALLIZATION

☉ III.3.2 HEWL Batch Crystallization

Three stock solutions were made: 160 g/L NaCl in DI water, 85 g/L HEWL in DI water, and 100 mM sodium acetate pH 4.6 in DI water. HEWL stock solution was stored at 10 °C or lower when not in use. The three stock solutions were added to a single well of a 9 cavity PYREX spot plate in consecutive order: 50 μL sodium acetate solution, 50 μL NaCl solution, and 100 μL HEWL

stock solution. The solution mixture was gently pipetted to mix and allowed to incubate without disturbance at room temperature for 24 hours. After 24 hours, visible lysozyme crystals could be seen in solution and on the surface of the glass plate; longer growth times yielded larger crystals.

☉ III.3.2 CJ Batch Crystallization

Approximately 40 mg/mL CJ was mixed with 3.4 M $[\text{NH}_4]_2\text{SO}_4$, 40 mM bis-tris pH 6.5 in a PYREX spot plate well at a protein to precipitant ratio of 2.7:1 at a total volume of 185 μL . Plates were incubated at 15 °C. After 24 hours, CJ-LPCs have grown and are visible in solution.

☉ III.4 CROSS-LINKING AND TRACE-LABELING

☉ III.4.1 HEWL Crystals

After crystallization, HEWL crystals adhere to the well surface of the PYREX spot plate. Mother liquor was removed from the crystallization well by pipette (being careful not to disturb the immobilized crystals) and replaced with 56 g/L NaCl, 50 mM sodium acetate pH 4.6 for 30 minutes to remove excess HEWL monomers. The crystallization well solution was replaced with fresh 56 g/L NaCl, 50 mM sodium acetate pH 4.6 and crystals were crosslinked for 30 minutes at room temperature by direct addition of glutaraldehyde yielding a 5% (v/v) concentration in the crystallization well. Cross-linking reaction quench and crystal trace-labeling were achieved by replacing crystallization well solution with 0.25 M carbonyldiimidazole, 0.25 mM NHS-fluorescein, 100 mM DMAB in 1x PBS pH 7.5. HEWL crystals were removed from the surface of the PYREX spot plate by gentle scraping and stored in fresh 4.2 M TMAO, 0.175 M H_2SO_4 at pH 7.5.

☉ III.4.2 CJ-LPCs

After crystallization, CJ-LPCs do not adhere to the surface of the PYREX spot plate wells. Thus, all crystals and mother liquor in the crystallization well were transferred to a microcentrifuge tube by pipette. CJ-LPCs remaining in the well after the initial transfer were transferred by rinsing

out with 4.2 M TMAO, 0.175 M H₂SO₄ pH 7.5. Crystals in solution were centrifuged on a bench top centrifuge for 2 minutes. The supernatant was then replaced with fresh 4.2 M TMAO, 0.175 M H₂SO₄ pH 7.5. This process was repeated twice at 10-minute intervals. Light agitation was used to break up crystal pellet after the final sedimentation. Crystals were then crosslinked for 3 minutes at room temperature by direct addition of glutaraldehyde or oxaldehyde at 5% (v/v) final concentration. The cross-linking reaction was quenched and crystals trace-labeled by replacing the cross-linking solution with 0.25 M carbohydrazide, 0.25 mM NHS-fluorescein, 100 mM DMAB in 1x PBS pH 7.5.

☉ III.5 FABRIC ATTACHMENT CHEMISTRY

☉ III.5.1 Citric Acid Textile Treatment

1" x 1" cotton fabric test swatches were placed in 2% (w/v) sodium borate solution for 1 hour at 90 °C and subsequently rinsed with 1x PBS pH 7.5 at room temperature. Groups of 6 fabric swatches were placed in 50 mL centrifuge tubes containing 25 mL 7% citric acid, 5% sodium hypophosphite and vortexed for 1 hour. Swatches were dab-dried with Kimwipes® and incubated on aluminum foil (shiny side facing swatches) in an oven at 85° C and 160° C for 5 minutes at each temperature. Citric-acid-treated intermediate fabric swatches were used for further chemistries within 24 hours.

☉ III.5.2 CDI Textile Treatment

Citric acid intermediate swatches were washed twice with new, pure acetone. Before swatches dried, 0.25 g/mL CDI in acetone was pipetted directly onto 5 evenly distributed treatment locations (~12 mm diameter) on each fabric swatch and immediately sealed in an incubation apparatus with Parafilm® (Figure III.1). Swatches were incubated for 3 hours at room temperature and washed

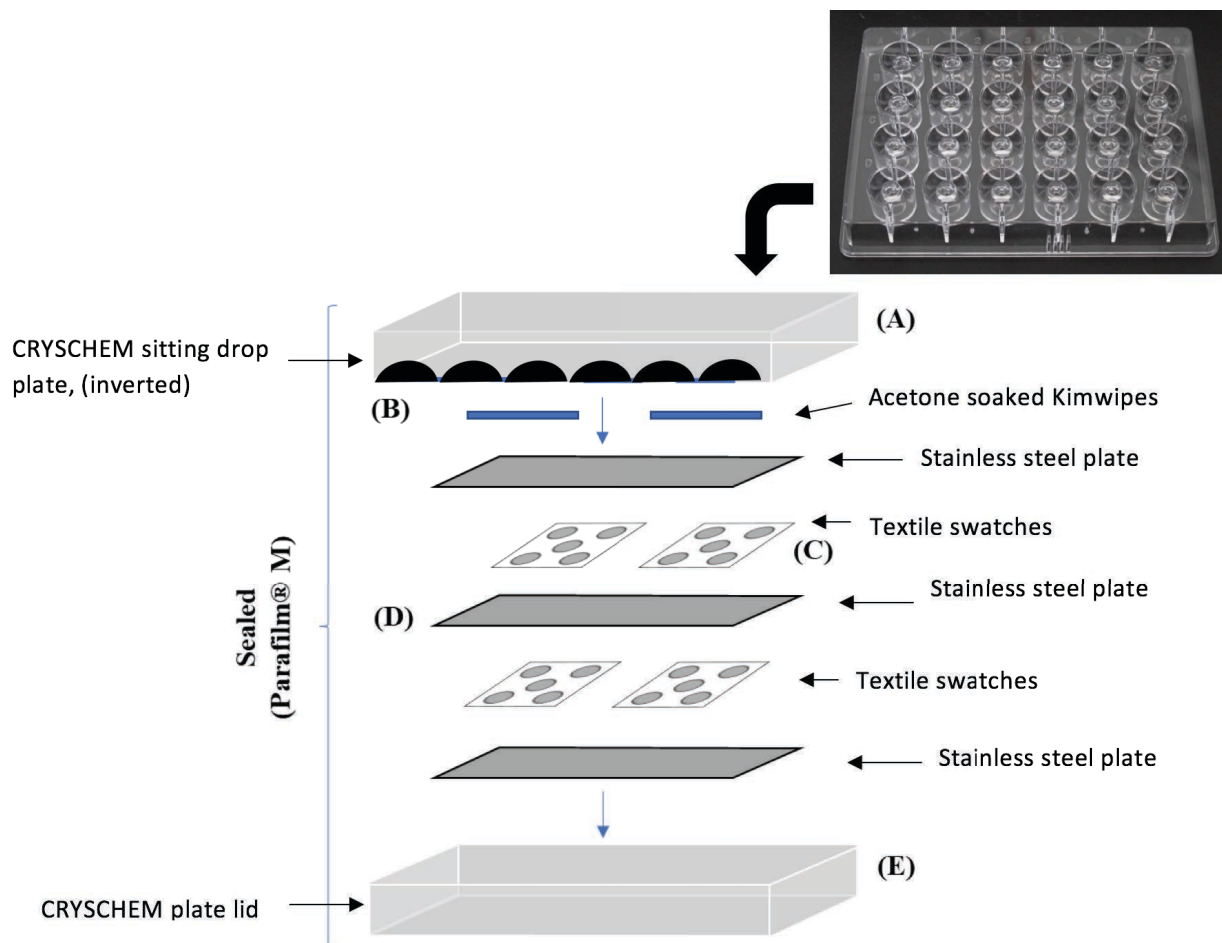


Figure III.1. CDI treatment incubation in “sandwich” apparatus: (A) 24-well sitting drop crystallization plate. (B) Kimwipes® saturated with acetone to prevent drying. (C) Fabric swatches activated with CDI at 5 evenly distributed locations. (D) Stainless steel plate to provide weight and prevent corrosion of plastic crystallization plate. (E) Crystallization plate cover.

twice with acetone after incubation. CDI-treated intermediate swatches were used for further chemistries within 24 hours.

☉ **III.5.3 AAD Textile Treatment**

CDI-intermediate fabric swatches were vortexed in 1 M AAD, 20 mM HEPES pH 8.0 for 3 hours at room temperature and subsequently rinsed with 20 mM HEPES pH 8.0. AAD-treated intermediate swatches were used for further chemistries within 24 hours.

☉ **III.5.4 Crystal Attachment to CDI-Intermediate Fabric**

40 μ L of crosslinked protein crystals (either variant) in 20 mM HEPES pH 8.0 were pipetted onto treatment locations of CDI-intermediate fabric swatches and allowed to incubate overnight at room temperature in an airtight container.

☉ **III.5.5 Crystal Attachment to AAD-Intermediate Fabric**

Protein crystals (either variant) were transferred to 20 mM HEPES pH 8.0. Glutaraldehyde (or oxaldehyde) was added to the crystal mixture to achieve a 2.5% (v/v) concentration in solution. After gentle mixing, the cross-linker and protein crystal solution was pipetted onto the treatment locations of AAD-intermediate fabric swatches, placed in a sealed “sandwich” apparatus (as seen in Figure III.1), and allowed to incubate at room temperature overnight.

☉ **III.6 CRYSTAL RETENTION TESTING AND IMAGING**

The Crystal attachment retention was tested using a modified version of the colorfastness laundering protocol AATC Test Method 61-2013 1A.¹ Test Method 1A (45-minute duration) is meant to simulate the color change due to 5 careful hand-washes. Each fabric swatch containing conjugated crystals was subjected to a 15-minute accelerated laundering machine pre-wash in a steel lever-lock canister containing 200 mL DI H₂O and 10 steel beads to remove excess non-covalently attached crystals from the fabric surface. Swatches were then washed for a total of 60

minutes (15 minute increments) at $40 \pm 2^\circ \text{C}$ in steel-lever canisters containing 200 mL DI H₂O, 0.74 g powder detergent, and 10 steel beads.

Crystal retention was quantified before and after each 15-minute wash increment (including pre-wash) by imaging on a Typhoon FLA 7000 fluorescent scanner at 473 nm and 10 μm resolution. Images were analyzed using the Fiji software package² to detect and count points of fluorescent intensity corresponding to retained trace-labeled crystals (Figure III.2). Raw and normalized retention data is shown in Tables III.1—III.4.

Control samples were prepared in which either the cotton fabric was not activated with citric acid (CA) to add carbocyclic acid groups to the surface of the cotton (-CA), or they did not receive CDI treatment (-CDI sample). Control swatches were imaged both before and after the DI H₂O rinse (Figure III.3A & III.3B). These images reveal substantial loss of protein crystal material in both control samples with near zero crystal retention. These results indicate CA activation and CDI treatment are critical in completing the CDI-only conjugation reaction. Similarly, CA activated fabric treated with GA (instead of CDI) showed near-zero crystal retention (Figure III.3C), indicating that the improved retention seen in the CDI+AAD+GA conjugation scheme is not simply due to the addition of GA alone.

© III.7 CRYSTAL GUEST LOADING

To remove weakly adsorbed crystals, all fabric samples used for loading were subject to a 10-minute hand-shaken pre-wash in a steel lever-lock canister containing 200 mL DI H₂O and 10 steel beads. Fluorescence and DIC imaging was done using a Nikon Eclipse Ti spinning-disk confocal microscope with an AndoriXon Ultra 897U EMCCD camera.

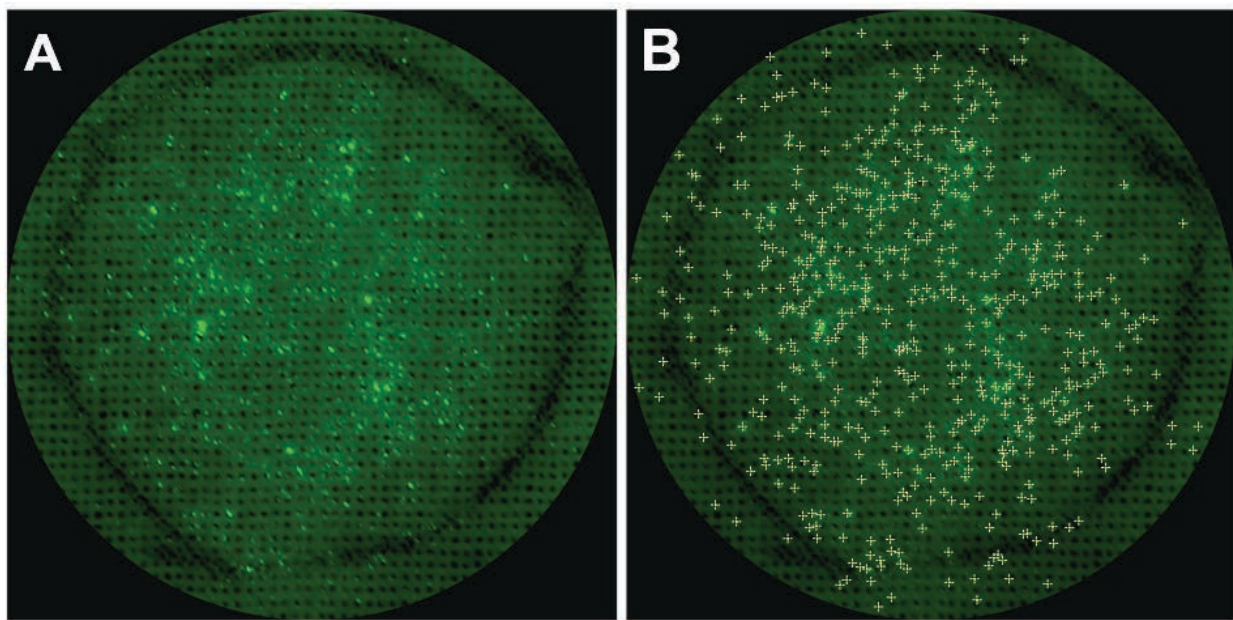


Figure III.2. (A) Representative Typhoon image showing fluorescently labeled crystals. (B) Detection and quantification of crystal puncta using Fiji software.

Table III.1. HEWL crystal retention using CDI-only conjugation.

		Time (min.)	R1	R2	R3	R4	R5	
		0	191	177	175	178	180	Total Count
		15	121	134	107	116	121	
		30	91	95	89	66	75	
		45	68	78	55	45	48	
Ave.	Std. Dev.	60	52	52	42	15	23	
100	0	0	100	100	100	100	100	Norm. Percent
66.5	5.6	15	63.4	75.7	61.1	65.2	67.2	
46.2	6.8	30	47.6	53.7	50.9	37.1	41.7	
32.6	7.6	45	35.6	44.1	31.4	25.3	26.7	
20.4	9.2	60	27.2	29.4	24.0	8.4	12.8	

Table III.2. HEWL crystal retention using CDI+AAD+GA conjugation.

		Time (min.)	R1	R2	R3	R4	R5	
		0	476	517	365	335	517	Total Count
		15	319	380	249	216	376	
		30	283	319	190	180	314	
		45	216	286	156	152	282	
Ave.	Std. Dev.	60	182	266	150	123	207	
100	0	0	100	100	100	100	100	Norm. Percent
66.5	5.6	15	67.0	73.5	68.2	64.5	72.7	
46.2	6.8	30	59.5	61.7	52.1	53.7	60.7	
32.6	7.6	45	45.4	55.3	42.7	45.4	54.5	
20.4	9.2	60	38.2	51.5	41.1	36.7	40.0	

Table III.3. CJ-LPC retention using CDI+AAD+OA conjugation.

		Time (min.)	R1	R2	R3	R4	R5	
		0	139	127	142	159	151	Total Count
		15	75	76	72	69	107	
		30	48	66	69	54	79	
		45	50	85	61	54	72	
Ave.	Std. Dev.	60	42	53	53	43	64	
100	0	0	100	100	100	100	100	
66.5	5.6	15	54.0	59.8	50.7	43.4	70.9	Norm. Percent
46.2	6.8	30	34.5	52.0	48.6	34.0	52.3	
32.6	7.6	45	36.0	66.9	43.0	34.0	47.7	
20.4	9.2	60	30.2	41.7	37.3	27.0	42.4	

*Red data point indicates an outlier that was removed from the average and standard deviation.

Table III.4. CJ-LPC retention using CDI+AAD+GA conjugation.

		Time (min.)	R1	R2	R3	R4	R5	
		0	659	861	497	393	685	Total Count
		15	525	633	335	295	524	
		30	433	543	276	236	445	
		45	332	433	216	198	365	
Ave.	Std. Dev.	60	293	379	202	163	309	
100	0	0	100	100	100	100	100	
66.5	5.6	15	79.7	73.5	67.4	75.1	76.5	Norm. Percent
46.2	6.8	30	65.7	63.1	55.5	60.1	65.0	
32.6	7.6	45	50.4	50.3	43.5	50.4	53.3	
20.4	9.2	60	44.5	44.0	40.6	41.5	45.1	

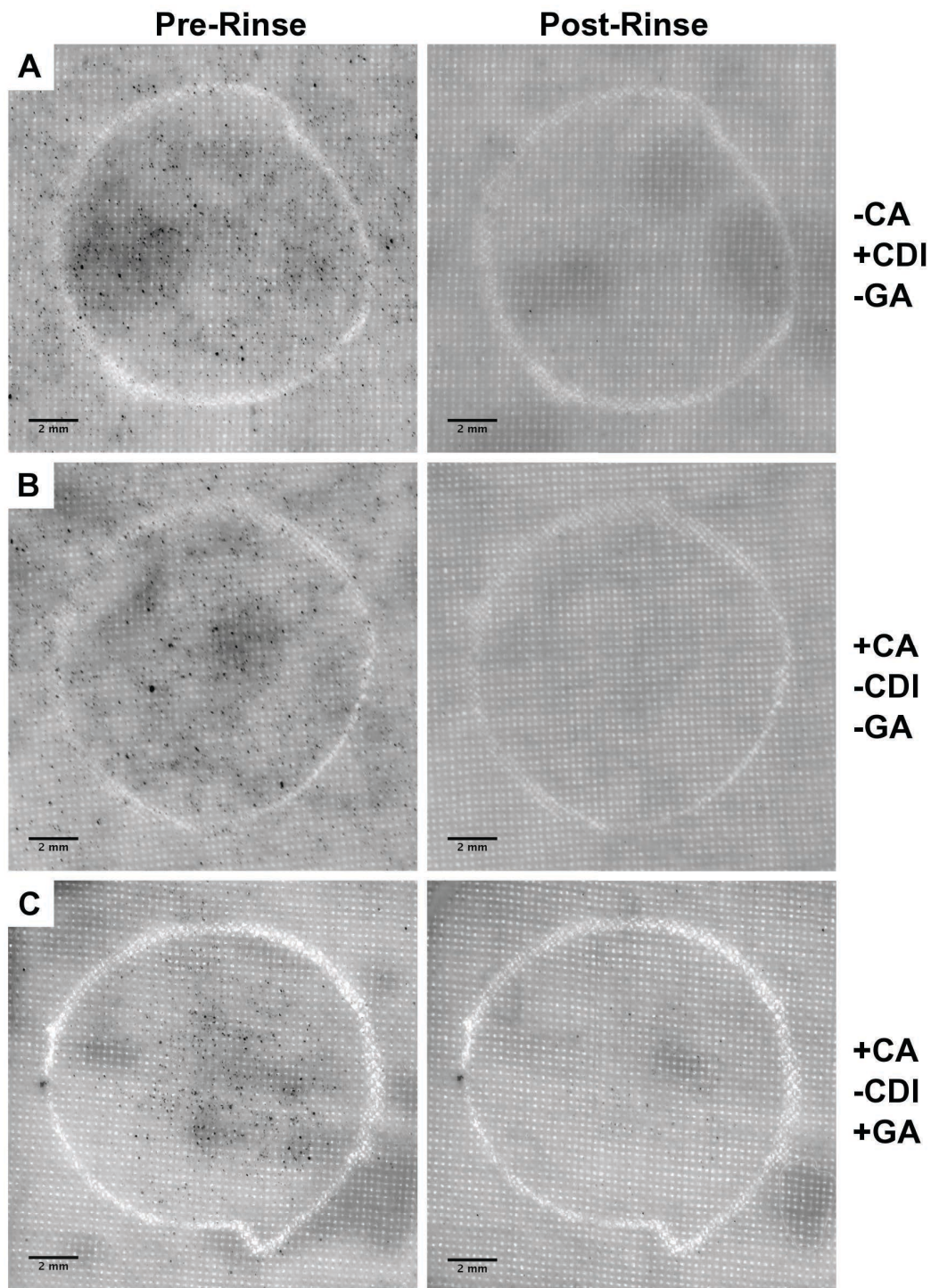


Figure III.3. Control samples for protein crystal conjugation to cotton fabric. *Left:* pre H₂O rinse; *Right:* post DI H₂O rinse, note: samples were not subjected to any laundering time. GA cross-linked, quenched, and NHS-fluorescein trace-labeled HEWL crystals were used in all samples. (A) Cotton not activated with citric acid. (B) Cotton not treated (conjugated) with CDI. (C) Cotton activated with citric acid and treated (conjugated) with GA.

⊙ III.7.1 Sulforhodamine 101 Loading into HEWL Crystals

Rinsed fabric samples containing conjugated HEWL crystals labeled with NHS-fluorescein were placed in 50 mM HEPES, 150 mM NaCl, 10% Glycerol pH 7.5 and imaged under brightfield light (DIC), 488 nm laser light (HEWL fluorescein) and 561 nm laser light (to test for crystal, see CHAPTER 4 Figure 4.4A *Left*). Next, the fabric samples were added to 500 μ L sulforhodamine 101 in 50 mM HEPES, 150 mM NaCl, 10% Glycerol pH 7.5 and incubated for 24 hours in a sealed vessel protected from light. After incubation, the fabric was briefly rinsed with pure water to remove residual guest molecules. Differential interference contrast (DIC) and fluorescent (488 nm & 561 nm) confocal images taken again to demonstrate guest molecule co-localization (CHAPTER 4 Figure 4.4A *Right*).

⊙ III.7.2 Sulforhodamine-Labeled P450 Loading into CJ-LPCs

Rinsed fabric samples containing conjugated CJ-LPCs labeled with NHS-fluorescein were placed in 50 mM HEPES, 150 mM NaCl, 10% Glycerol pH 7.5 and imaged under brightfield light(DIC), 488 nm laser light (CJ-LPC fluorescein) and 561 nm laser light (to test for crystal intrinsic fluorescence), see CHAPTER 4 Figure 4.4B *Left*. After imaging, the buffer was removed and 500 μ L of 50 mM HEPES, 150 mM NaCl, 10% Glycerol pH 7.5 containing cytochrome P450 labeled with sulforhodamine 101 acid chloride (NHS-TexasRed) was added directly to fabric samples. Time-lapse imaging was immediately started using the same settings as before. Images were taken every 2 minutes for 36 minutes, see Figure III.4.

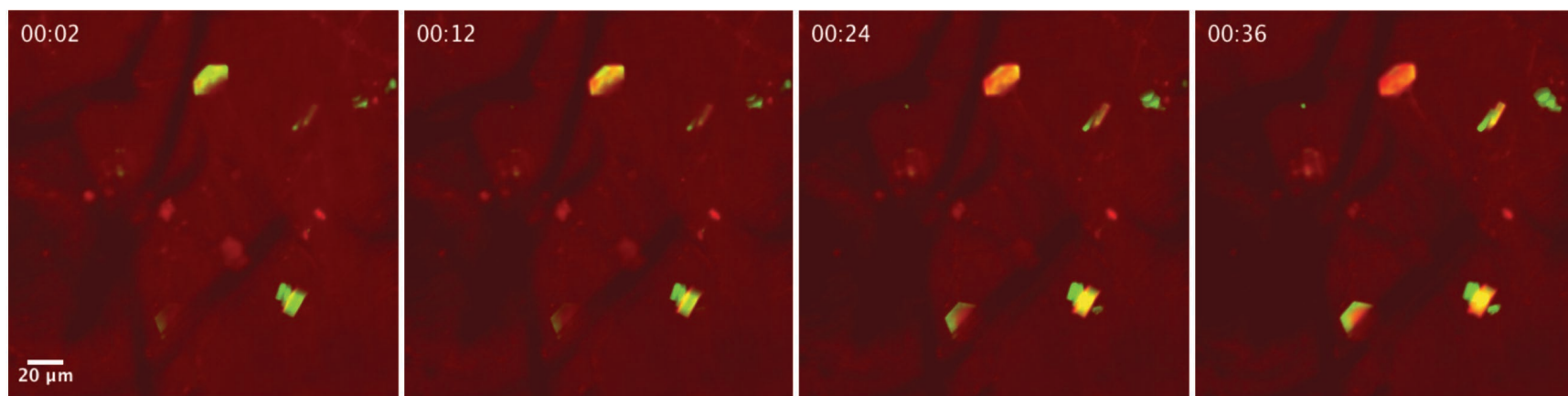


Figure III.4. Time-lapse images of sulforhodamine-labeled P450 (red) loading into GA cross-linked CJ-LPCs (green) conjugated to cotton fabric using a CDI+AAD+GA conjugation scheme over the course of 36 minutes.

REFERENCES

- (1) American Association of Textile Chemists and Colorists. AATCC Test Method 61-2013.
AATCC Tech. Manual 2014 **2013**.
- (2) Schindelin, J.; Arganda-Carreras, I.; Frise, E.; Kaynig, V.; Longair, M.; Pietzsch, T.;
Preibisch, S.; Rueden, C.; Saalfeld, S.; Schmid, B.; et al. Fiji: An Open-Source Platform
for Biological-Image Analysis. *Nat. Methods* **2012**, 9 (7), 676–682.